Unbiased analysis of adipocyte volumes and numbers in a porcine model of diet-induced obesity using quantitative stereology and 3D light sheet fluorescence microscopy

von Denise Natalie Theobalt

Inaugural-Dissertation zur Erlangung der Doktorwürde

der Tierärztlichen Fakultät der Ludwig-Maximilians-Universität

München

Unbiased analysis of adipocyte volumes and numbers in a porcine model of diet-induced obesity using quantitative stereology and 3D light sheet fluorescence microscopy

von Denise Natalie Theobalt

aus Gräfelfing

München 2022

Aus dem Zentrum für Klinische Tiermedizin der Tierärztlichen Fakultät
der Ludwig-Maximilians-Universität München

Lehrstuhl für Allgemeine Pathologie und Pathologische Anatomie

Arbeit angefertigt unter der Leitung von: Univ.-Prof. Dr. Rüdiger Wanke
Mitbetreuung durch: Dr. med. vet. habil. Andreas Parzefall

Gedruckt mit Genehmigung der Tierärztlichen Fakultät
der Ludwig-Maximilians-Universität München

Dekan:	Univ.-Prof. Dr. Reinhard K. Straubinger, Ph.D.
Berichterstatter:	Univ.-Prof. Dr. Rüdiger Wanke
Korreferenten:	Univ.-Prof. Dr. Joris Peters
	Priv.-Doz. Dr. Joachim C. Manning
	Priv.-Doz. Dr. Simone M.-L. Renner
	Priv.-Doz. Dr. Sven Reese

Tag der Promotion: 12. Februar 2022

TABLE OF CONTENTS

INDEX OF ABBREVIATIONS

AACE:	American Association of Clinical Endocrinology
AHA:	American Heart Association
AMPK:	5' adenosine monophosphate-activated protein kinase
ASP:	Acylation-stimulating protein
ATMs:	Adipose tissue macrophages
ATP:	Adenosine triphosphate
BABB:	Benzyl alcohol/benzyl benzoate
BAI:	Body adiposity index
BAT:	Brown adipose tissue
BMI:	Body mass index
BMP:	Bone morphogenetic protein
BP:	Blood pressure
CAFs:	Cancer-associated fibroblasts
cAMP:	Cyclic adenosine monophosphate
CCD:	Charge-coupled device
C/EBPs:	CCAAT-enhancer-binding proteins
CLARITY:	Cleared lipid-extracted acryl-hybridized rigid immunostaining/*in situ* hybridization-compatible tissue hydrogel
CLS:	Crown-like structures
CLSM:	Confocal laser scanning microscopy
CNN:	Convolutional neural network
CoA:	Coenzyme A
CRISPR/Cas:	Clustered regularly interspaced short palindromic repeats/ CRISPR-associated
CtBPs:	C-terminal-binding proteins
CUBIC:	Clear, unobstructed brain imaging cocktails and computational analysis
CVD:	Cardiovascular disease
DAMPs:	Damage-associated molecular patterns
DIO:	Diet-induced obesity
ECi:	Ethyl cinnamate
EGIR:	European Group for the Study of Insulin Resistance

ER:	Endoplasmic reticulum
FBS:	Fetal bovine serum
FFAs:	Free fatty acids
FOV:	Field of view
GH:	Growth hormone
GLUT4:	Glucose transporter 4
GM:	Göttingen minipigs
GMA/MMA:	Glycolmethacrylate/methylmethacrylate
HDL:	High density lipoprotein
HE:	Haematoxylin-eosin
HFHE:	High-fat/high-energy
Hh:	Hedgehog
HIF-1α:	Hypoxia inducible factor-1α
HMGB1:	High mobility group box 1
HSL:	Hormone-sensitive lipase
IDF:	International Diabetes Federation
iDISCO:	Immunolabeling-enabled 3D imaging of solvent-cleared organs
IFG:	Impaired fasting glucose
IGF1:	Insulin-like growth factor 1
IGT:	Impaired glucose tolerance
IL-6:	Interleukin-6
IL-8:	Interleukin-8
IL-10:	Interleukin-10
IR:	Insulin resistance
IRS-1:	Insulin receptor substrate 1
IUR:	Isotropic uniform random
JNK:	c-Jun-N-terminal kinase
KI:	Knock-in
Laser:	Light amplification by stimulated emission of radiation
LMU:	Ludwig-Maximilians-Universität
LPL:	Lipoprotein lipase
LSFM:	(Laser) light sheet fluorescence microscopy
MCP1:	Monocyte chemoattractant protein 1
MetS:	Metabolic syndrome

MHO:	Metabolically healthy obese
MONW:	Metabolically obese normal-weight
MSC:	Mesenchymal stem cell
NA:	Numerical aperture
NCEP/ATP III:	National Cholesterol Education Program's Adult Treatment Panel III
NF-κB:	Nuclear factor-kappa B
NHLBI:	National Heart, Lung and Blood Institute
NIR:	Near-infrared
NST:	Non-shivering thermogenesis
PACT:	Passive clarity technique
PGC-1α/ß:	Peroxisome proliferator-activated receptor gamma coactivator 1-alpha/beta
PPARγ:	Peroxisome proliferator-activated receptor-γ
PRDM16:	PR domain-containing protein-16
RI:	Refractive index
SA:	Spherical aberration
SASP:	Senescent-associated secretory phenotype
SAT:	Subcutaneous adipose tissue
s.c.:	Subcutaneous
SeeDB:	See deep brain
SERCA1a:	Sarco(endo)plasmic reticulum Ca^{2+} ATPase 1a
SLN:	Sarcolipin
SOCS3:	Suppressor of cytokine signalling 3
STAT 3:	Signal transducer and activator of transcription 3
SUR:	Systematic uniform random
SVF:	Stromal vascular fraction
T2D:	Type 2 diabetes mellitus
TAGs:	Triacylglycerides
TNF-α:	Tumour necrosis factor alpha
TNFR1:	Tumour necrosis factor receptor 1
UCP1:	Uncoupling protein 1
UCP3:	Uncoupling protein 3
VAI:	Visceral adiposity index

VAT:	Visceral adipose tissue
visc.:	Visceral
VUR:	Vertical uniform random
WAT:	White adipose tissue
WC:	Waist circumference
WHO:	World Health Organization
WHtR:	Waist-to-height-ratio
Wnt:	Wingless-related integration site
2PM:	2-photon microscopy
3DISCO:	3D imaging of solvent-cleared organs

I Introduction

Obesity is regarded as a primary health threat in the 21st century. It affects not only the quality of life on physiological basis, but also psychologically and economically, irrespective of cultural, financial or ethnic background [1]. The number of overweight (body mass index, BMI ≥ 25 kg/m²) and obese (BMI > 30 kg/m²) humans in industrial and emerging countries has been rising for years with a total of 650 million adults and more than 124 million children globally being obese in 2016 [2]. With the recent trend continuing, an estimated 57.8% of the world's adult population could be overweight or obese by the year 2030 [3]. Simultaneously to this development, the incidences of obesity-associated diseases like type 2 diabetes mellitus, arteriosclerosis with increased risk for cardiovascular complications such as heart attack and stroke, susceptibility to infection and depression are continuously increasing [4-8]. The elevated risk of developing these chronic diseases is primarily due to obesity-associated metabolic changes which, when occurring together, are referred to as metabolic syndrome (*i.e.,* combined occurrence of cardiovascular risk factors characterised by *inter alia* visceral obesity, insulin resistance ± glucose intolerance, dyslipidaemia, hypertension and a pro-inflammatory state on local (*i.e.,* adipose tissue) and systemic level, which also increase the risk for development of type 2 diabetes mellitus) [4-6, 9, 10]. These changes are much more correlated to the regional adipose tissue distribution than the total fat mass [11, 12]. Especially accumulation of visceral adipose tissue enhances the risk of metabolic alterations, whereas subcutaneous fat tissue in the gluteofemoral region even seems to have protective functions [9, 13, 14]. Transplantation experiments have shown that this difference is based on intrinsic properties of the adipose tissue depots [15]. It is considered that the adaptability of the adipose tissue to the positive energy balance at the cellular level plays a major role [16]. Adipocyte hyperplasia is suggested to be important for the maintenance of physiological tissue function, whereas hypertrophy, as it occurs mainly in visceral adipocytes, may lead to dysfunctional fat cells [15, 16]. These findings probably also explain the higher susceptibility of visceral adipocytes to cell death compared to subcutaneous adipocytes [16]. In order to investigate factors relevant for the pathogenesis and treatment of obesity and obesity-associated diseases, several animal models are used in translational obesity research [17]. In addition to the classic rodent models

(*e.g.,* mice, rats), large animal models (*e.g.,* pigs) have been developed in recent years that more adequately reflect the changes occurring in human patients [18, 19]. Adequate methods for quantitative morphological analysis of adipose tissue samples obtained from these animal models are of great importance to gain valuable insights in pathogenesis relevant quantitative morphological alterations on adipocyte level. Crucial morphological parameters, such as the volume, mean volume and number of adipocytes in a specific adipose tissue depot, can be analysed by light microscopy in histological 2D sections of adipose tissue samples. Design-based quantitative stereological analysis methods are considered the gold standard for quantitative morphological analyses in histological tissue sections and allow the unbiased estimation of all morphological structural parameters (*i.e.,* volumes, surfaces, lengths and numbers) of cells and other tissue structures of interest in representative and adequately processed tissue samples [20-23]. The determination of, for example, mean volumes and numbers of cells allow the differentiation of hypertrophic and hyperplastic growth patterns [24, 25]. Although morphological changes of adipocytes, as for instance in volume, play a key role in the pathogenesis of obesity and associated diseases such as the metabolic syndrome, there are so far only a few studies on adipocytes using quantitative stereological methods, as they may involve complex and time-consuming procedures with regard to tissue sampling (*i.e.,* strict sampling designs), tissue processing (*i.e.,* plastic embedding, generation of thin (serial) sections) and analysis (*e.g.,* physical disector) [26-29]. In contrast, novel 3D imaging methods such as (laser) light sheet fluorescence microscopy (LSFM) of optically cleared (*i.e.,* transparent) tissue samples allow for a much faster and partially automated analysis of the three-dimensional morphology of biological tissues [30, 31]. Optically cleared tissue samples are directly, *i.e.,* without physical sectioning, imaged in 3D using a (laser) light sheet fluorescence microscope. Visualization of complex structures, such as the vascular network of murine fat tissue depots or microvessels in whole murine brains, have already been demonstrated using LSFM [32, 33]. In addition to direct 3D visualisation, quantitative morphological parameters of tissue samples can be directly evaluated by digital 3D image analysis, which has already been successfully applied for counting murine kidney glomeruli, analysing the distribution and interaction of immune cells with *Aspergillus fumigatus* in lungs of mice and determining the volume and surface of fish gill lamellae, for instance [30,

34-36]. 3D image analysis could therefore also significantly simplify the determination of adipocyte volumes and numbers compared to the aforementioned 2D section-based unbiased quantitative stereological analysis methods.

The present study addresses the applicability of LSFM-based quantitative morphological analyses for the unbiased determination of morphological adipocyte parameters in subcutaneous and visceral adipose tissue depots of a recently established porcine model of diet-induced obesity [37] (see **Section II Objective of the present work**). The results of this work were published in the journal "*PLoS One"* in 2021 (see also **Section IV Publication**) [38]. The obtained data provide valuable insights into the type (*i.e.,* hyperplasia, hypertrophy, or both) and the extent of volume increase in each adipose tissue depot. Furthermore, the analyses provide important information about the differences in the size distribution of adipocytes within the depots, as well as the mean and maximum individual fat cell volumes in lean and obese pigs in the subcutaneous and visceral fat depot.

II Objective of the present work

The present study was designed to evaluate the suitability of laser light sheet fluorescence microscopy (LSFM) as a new and elegant tool for the unbiased and comparable determination of adipocyte volumes and numbers to characterise obesity-related alterations of adipocyte growth patterns in representatively sampled subcutaneous and visceral adipose tissue depots of a recently established porcine diet-induced obesity model [37]. Unbiased quantitative stereological analyses, which represent the gold standard for estimation of quantitative morphological parameters in histological tissue sections [20-22] were independently performed on adipose tissue specimen of the same animals and fat tissue depots to verify the accuracy of the results obtained by the LSFM analysis. In future studies, LSFM-based analyses might allow for the comprehensive characterisation of adipocyte morphology and, in combination with other analysis techniques such as multi-omics, help to relate obesity-associated morphological adipocyte alterations to potentially concomitant alterations in adipocyte function, all in all contributing to a better understanding of the pathogenesis of obesity and obesity-associated (metabolic) alterations.

III Scientific background

1 Anthropometric measurements of obesity in humans

The accumulation of an abnormal or excessive amount of adipose tissue that may impair the health of the affected individual is defined as overweight or obesity, respectively [2]. The body mass index (BMI) is used worldwide to classify the nutritional status of humans [39]. The weight in kilograms of an individual is divided by its height in meters squared [40]. According to the definition of the world health organization (WHO), adults with a BMI ≥ 25 kg/m² are considered to be overweight, whereas a BMI of 30 kg/m² or higher is defined as obesity [2]. Children and adolescents between two and 18 years of age are excluded from this index [40]. Its easy-to-use calculation and the possibility of making comparisons at population level due to the non-inclusion of age, gender and other factors make the BMI an international standard method. However, it is this superficial calculation basis that limits its power and renders the BMI only a rough guidance [2, 41]. In patients with an increased (*e.g.,* athletes) or decreased (*e.g.,* elderly with sarcopenia) lean body mass the BMI is of low accuracy [2, 42]. Additionally, this index also does not take adipose tissue distribution into account, although it has a much higher impact on the development of obesity-associated diseases as the total fat mass [11]. Furthermore, there are also differences between individual ethnic groups. Comparing the occurrence of metabolic disorders in different ethnic groups, for the identical prevalence the BMI is 30 kg/m² for Caucasians, 24.5 kg/m² for Chinese Americans and 23.3 kg/m² for South Asians [43]. In 2000, the WHO criteria for overweight and obesity were therefore redefined for the Asia-Pacific region as BMI ≥ 23 kg/m² and ≥ 25 kg/m², respectively [44].

In addition to the BMI, other anthropomorphic measures that better reflect the distribution and total amount of adipose tissue have been established [41]. Waist circumference (WC) is also commonly used in clinical praxis as it is easy to determine and seen as a valuable parameter for both adipose tissue distribution and associated dysfunction. Compared to the WC, the waist-to-height-ratio (WHtR) is less correlated to insulin concentration and only a few studies have examined its potential yet [42]. In 2011, Bergman *et al.* [45] introduced the body adiposity index (BAI), which includes hip circumference and height. It is supposed to directly estimate the percentage of body fat of individuals without adjustments for sex or age

[45, 46]. However, gender independence was questioned by a recent study in which BAI correlated positively with glucose and insulin concentrations only in men [42]. The visceral adiposity index (VAI), calculated from anthropometric (WC, BMI) and metabolic (high density lipoprotein (HDL) cholesterol and triglyceride concentration) parameters, is strongly correlated with serum glucose concentrations and the visceral adipose tissue amount and could be a useful tool in detection of cardiometabolic risk factors once cut-off values are established [42].

2 Adipose tissue

2.1 Adipose tissue morphology

In general, there are three types of adipose tissue. The white adipose tissue (WAT) is organized in different depots, which can be subdivided into two major anatomic regions: subcutaneous adipose tissue and visceral (*i.e.,* subserous) adipose tissue. The porcine WAT is of pure white colour, whereas in other animal species and humans the colour ranges from white to white-yellowish, depending on the amount of exogenous lipophilic pigments (*e.g.,* carotenoids) accumulated in the fat tissue [47-49]. The WAT contains mature adipocytes, blood vessels, noradrenergic fibres, fibroblasts, preadipocytes and immune cells (*e.g.,* macrophages) [50]. In WAT adipocytes, the lipids form a single droplet ("unilocular"), which occupies almost the entire intracellular space, ousting the cell organelles and the nucleus to the rim of the cell. This gives the adipocytes a "seal ring" appearance in tissue sections [47, 50, 51]. A dense capillary network, which is essential for the rapid supply of stored energy (see **Chapter 2.2.1**) and the function of adipose tissue as an endocrine organ (see **Chapter 2.2.2**), surrounds each fat cell. The WAT has several metabolic functions, including fast storage and mobilization of lipids, thermoregulation and fluid balance, as well as mechanical functions (structural fat) in for example kidney (*capsula adiposa*), eye (retrobulbar fat pad) and bone marrow [47, 50].

Besides the WAT there is the brown adipose tissue (BAT). It is characterised by a variety of different sized lipid droplets ("multilocular") and a high amount of mitochondria in the cytoplasm of the adipocytes, which are on average smaller compared to the WAT [50]. The high content of cytochrome in the mitochondria of the fat cells and the high vascularization of the tissue are responsible for its brownish colour. The BAT is mainly found in birds and rodents (*e.g.,* in the shoulder girdle), but can also account for up to 5% of body fat in new-born mammals and 1% of body

weight in neonate humans [47, 50]. In contrast to small mammals such as rodents, brown adipocytes in large mammals lose their unique ultrastructural and molecular properties during childhood, which is why BAT cannot be found in adult individuals [50]. In humans, BAT was long assumed to be absent in adults as well, until in 2009, metabolically active BAT was demonstrated in a majority of adults (primarily in supraclavicular, para-aortic, and retroperitoneal fat depots) [52-58]. The main function of the brown adipose tissue is energy storage primarily for non-shivering thermogenesis (NST). The mitochondrial uncoupling protein 1 (UCP1), which is exclusively expressed in the BAT, responds to adrenergic stimulation and uncouples the proton transit across the inner mitochondrial membrane from adenosine triphosphate (ATP) synthesis by acting as an ion channel to allow protons to re-enter the mitochondrial matrix (which would otherwise pass through ATP-synthase). Thus, the energy stored in the proton motor force is not used to produce ATP but is released as heat [50, 59-61]. In humans, stimulation of BAT (*e.g.,* by repeated cold exposure) is discussed as a possible therapy for obesity and diabetes, as it seems to be associated with a high metabolic activity (*e.g.,* 50 g of BAT could account for as much as 20% of daily resting energy expenditure in adults, when maximally stimulated) and improved metabolic parameters such as insulin sensitivity [16, 52, 53, 61, 62]. In contrast to many large mammals and humans, the UCP1 is inactivated in pigs due to gene deletion of exons 3 to 5, an event that occurred about 20 million years ago [63-66]. This results in poor thermoregulation, especially in piglets, an increased susceptibility to cold and, consequently, increased neonatal mortality, in many but not all pig species [63, 65, 66]. Wild boars, for example, build thermoprotective nests for birth, which is unique among the ungulates [65, 67]. Additionally, Nowack *et al.* (2019) showed that, next to shivering, muscle NST plays an important role in thermoregulation of wild boar piglets [67]. The ATP hydrolysis of the sarco(endo)plasmic reticulum Ca^{2+} ATPase 1a (SERCA1a), which transports Ca^{2+} ions from the cytosol into the sarcoplasmic reticulum, is uncoupled from the actual transmembrane transport of Ca^{2+} by the regulatory protein sarcolipin (SLN) [67-69]. This results in Ca^{2+} ions being released back into the cytosol by SERCA1a (so-called slippage), and the energy generated by ATP hydrolysis is completely released as heat, as no transport of Ca^{2+} ions takes place [67, 70, 71]. However, Lin *et al.* (2017) demonstrated, that piglets of cold-adapted pig species such as the Tibetan pig and the Min pig are able to control their body temperature independent

of shivering and muscle NST [64]. Following cold exposures, these piglets are able to recruit beige fat cells (*i.e.,* a third type of fat cells/tissue, see also below) in the subcutaneous WAT, which express increased levels of uncoupling protein 3 (UCP3). This protein is also associated with an elevated uncoupled cellular respiration, indicating an UCP3 induced, UCP1 independent thermogenesis in these piglets. In contrast, piglets of cold-sensitive Bama pigs, for instance, are not able to recruit this type of fat cells [64, 66]. Of note, the gene expression of UCP1 can be restored in pigs by genetically engineering to test effects of the protein on metabolism in obesity and diabetes research (see **Chapter 4.2**), as well as to enhance animal welfare and reduce economic loss in agricultural production, for example [61, 72].

The third type of fat is called beige or “brite” (*i.e.,* brown in white) adipose tissue. It refers to UCP1 expressing, thermogenetic active adipocytes, which appear in localizations characteristic for WAT [73]. This process is called “browning” of WAT and can be caused by long-term cold exposure, $ß_3$-adrenergic stimulation (mimicking the thermogenic effects of cold) or chronic PPARγ activation [60, 74-76]. In humans and mice, beige adipocytes display an intermediate morphology, varying between unilocular and multilocular, and have either energy storage or UCP1 induced thermogenetic function. Both the morphology and the function are depending on the environmental conditions (*e.g.,* a predominantly thermogenetic phenotype in cold environment) [73, 76-78]. In certain pig species, such as the Tibetan pig, beige adipocytes perform UCP3 dependent thermogenesis, as described above [64].

2.2 Function of white adipose tissue

2.2.1 Lipid storage (lipogenesis) and mobilization (lipolysis)

The main function of the white adipose tissue is the storage of excess energy in form of triacylglycerides (lipogenesis), which can be mobilized (lipolysis) again in times of need (*e.g.,* hunger, sleep or long-term physical strain) [79].

In times of sufficient energy supply, WAT-adipocytes store fat, which is mostly derived from blood circulation, in form of triacylglycerides (TAGs) in a cytosolic lipid droplet, a process referred to as lipogenesis [80]. Free fatty acids (FFAs) can enter the adipocyte via fatty acid transporters (*e.g.,* CD36), whereas TAGs must first be broken down into fatty acids and glycerol by lipoprotein lipase (LPL), a membrane-

bound enzyme in adipocytes and capillary endothelium. After uptake into the adipocyte, fatty acids are again synthesized to TAGs through esterification. An additional source of stored lipids is the *de novo* synthesis in adipocytes [81, 82]. Since most of the stored fat is derived from the blood, LPL represents a key regulator of fat accumulation [81, 83]. Insulin stimulates the activity of the enzyme, whereas catecholamines, growth hormone (GH) and testosterone (in male) reduce it [83-87]. Along with induction of LPL, insulin also enhances the secretion of acylation-stimulating protein (ASP), which upregulates the TAG re-esterification in the adipocyte to prevent accumulation of FFAs in the microcirculation after TAGs are broken down via the LPL [83]. Overall, insulin is the only hormone that promotes lipogenesis and fat storage. Besides the induction of LPL, it promotes the uptake of glucose into the adipocyte, which is needed to synthesize TAGs. Lipogenesis is inhibited by catecholamines [88].

There are differences in fat storage between distinct adipose tissue depots, which are further enhanced in obesity [89]. Subcutaneous and visceral adipose tissue together store about 50% of dietary fat in sedentary adults [89-91]. Dietary fats are stored more efficiently in visceral than in subcutaneous adipose tissue depots in men, but *vice versa* in women [12, 83, 91]. They store more fat in subcutaneous fat depots than men do, especially in lower-body obesity (*i.e.,* gluteofemoral region) [89, 92, 93].

Mobilization of stored lipids (lipolysis) takes place at the surface of the lipid droplet [94]. In case of energy deficiency, the rate-limiting enzyme hormone-sensitive lipase (HSL) of the adipocytes is activated to degrade TAGs and subsequently supply especially liver, heart, skeletal muscles and kidneys with FFAs for ß-oxidation and glycerine for glycolysis or gluconeogenesis (liver) [80, 88].

Lipolysis is promoted by catecholamines. They increase the level of cyclic adenosine monophosphate (cAMP) and thus activate the HSL. In the opposite direction, insulin lowers the amount of cAMP, thereby deactivating the enzyme [80, 88]. However, the antilipolytic effect of insulin is weakened with increasing size of the subcutaneous and visceral adipocytes, as they become insulin resistant (see **Chapter 2.4**) [89, 95]. In line with this, diet and exercise, which lead to a reduction in fat cell size, have a positive effect on the regulation of lipolysis via insulin, whereas liposuction was reported to not significantly impact the insulin sensitivity in adipose

tissue, liver or skeletal muscle, since it only reduces the total number of subcutaneous adipocytes with no changes in the visceral adipose tissue mass or the size of the remaining adipocytes [89, 96-98]. Exercise additionally was demonstrated to upregulate lipolysis in the subcutaneous adipose tissue [89, 99]. Overall, visceral adipocytes demonstrate a higher sensitivity towards catecholamine-induced lipolysis and are less sensitive to the antilipolytic effect of insulin, as compared to subcutaneous adipocytes [83, 100, 101]. Furthermore, Jepson *et al.* (1992) [102] showed that intermediate lipid metabolites, such as oleid acid and oleyl coenzyme A (CoA), also function as lipolysis regulators by inhibiting the HSL activity [80, 102]. Additionally, pro-inflammatory cytokines, such as interleukin-6 (IL-6) and tumour necrosis factor-α (TNF-α), stimulate lipolysis, the latter may further provoke adipocyte insulin resistance. The secretion of these cytokines from macrophages and adipocytes is promoted by the low-grade inflammation in the adipose tissue of obese individuals (see **Chapter 3.2**) [80, 103-105].

Reaching the adipocyte expansion limit and/or dysregulation of lipolysis can lead to accumulation of FFAs and their toxic metabolites in ectopic tissues (*i.e.,* lipotoxicity, lipid-derived metabolic alterations) such as skeletal muscle, liver or heart, causing a local inflammatory reaction as well as systemic insulin resistance (*inter alia* due to ectopic pancreatic fat impairing ß-cell function) and an increased risk of type 2 diabetes mellitus (see **Chapter 3.2**) [80, 106-110].

2.2.2 Adipose tissue as endocrine organ

Until the discovery of leptin by Friedman's group in the 1990s, adipose tissue was thought to serve only as energy storage [79, 111-113]. However, the tissue has been revealed as an endocrine organ, secreting a variety of endocrine active proteins (adipokines), such as leptin, adiponectin, TNF-α and IL-6, thereby influencing not only the adipose tissue itself, but also whole-body metabolism and insulin sensitivity [79, 114, 115].

Leptin is a peptide hormone encoded by the gene OBS (*obese*), which is mainly expressed in adipocytes [113, 114]. It reduces food intake mainly via interaction with neurons located in the mediobasal hypothalamus (hence also known as "satiety hormone") and plays an important role in regulating energy and fat metabolism in humans and mammals [109, 116]. In human obesity, high levels of leptin are

characteristic, which may be explained by the increased secretion (up to seven times higher in obese compared to lean individuals) of leptin from large adipocytes [114, 117, 118]. The absence of the hormone's physiological effects (*i.e.,* reduction in food intake and weight loss) suggests leptin resistance in obese individuals [114, 119]. Metabolically relevant tissues, such as skeletal muscle, are suggested to be primarily affected by leptin resistance, which can ultimately lead to impaired regulation of fatty acid metabolism. The important mediator of leptin resistance in skeletal muscle is the suppressor of cytokine signalling 3 (SOCS3), which blocks 5' adenosine monophosphate-activated protein kinase (AMPK) signalling [114, 120-123]. The underlying mechanisms of central leptin resistance are not known yet. One possible explanation might be an altered transport through the blood-brain barrier, which was demonstrated in mice and seems to be reversible with weight loss [119, 124, 125].

Adiponectin is produced exclusively in the adipose tissue [126, 127]. In humans, the plasma concentration is negatively correlated with fat mass, *i.e.,* with increasing obesity, adiponectin levels are reduced [114, 128]. Adiponectin has a positive impact on total body insulin sensitivity. In line with this, low serum levels are associated with type 2 diabetes mellitus [114, 126, 129]. In mice, adiponectin stimulates fatty acid oxidation in the adipose tissue and skeletal muscle via AMPK signalling, thereby reducing the amount of FFAs in these tissues [114, 126, 129-132]. Activation of AMPK improves the insulin sensitivity in murine muscle cells *in vitro* through reduction of inhibitory serine phosphorylation of insulin receptor substrate-1 (IRS-1) [114, 133]. Adiponectin also has an anti-inflammatory effect. It suppresses the secretion of pro-inflammatory cytokines such as TNF-α and IL-6 in adipocytes and macrophages and promotes the release of the anti-inflammatory cytokine interleukin-10 (IL-10) by macrophages [134-137]. In addition, it shifts macrophage polarization from pro-inflammatory classically activated (M1) macrophages to anti-inflammatory alternatively activated (M2) macrophages and inhibits differentiation of myeloid progenitor cells [134, 138, 139].

Adipose tissue derived TNF-α is primarily produced by adipose tissue macrophages (ATMs). Due to an increased infiltration of macrophages in the fat tissue during obesity (see **Chapter 3.2**), TNF-α levels are elevated in an obese state [114, 140]. This cytokine has a negative impact on insulin action in adipose tissue and

hepatocytes through molecular mechanisms such as upregulation of SOCS3 expression and activation of c-Jun-N-terminal kinase (JNK), leading to inhibition of IRS-1 [114, 141-143]. Furthermore, TNF-α was demonstrated to stimulate lipolysis and reduces the hepatic and skeletal muscle fatty acid oxidation. The subsequent accumulation of FFAs and toxic bioactive lipids (*e.g.,* diacylglycerol) can also inhibit the function of IRS-1 and thus reduce insulin sensitivity in these organs (see **Chapter 2.2.1**) [114, 144-149].

Approximately 10% - 35% of plasma IL-6 concentration derives from white adipose tissue, where it is mainly produced by cells of the stromal vascular fraction (SVF, *i.e.,* cells in the aqueous fraction after experimental enzymatic digestion of adipose tissue, such as preadipocytes, lymphocytes and macrophages). Adipocytes themselves only account for about 10% of total IL-6 production in the fat tissue [150-153]. In obese individuals, Fried *et al.* (1998) demonstrated a 3-fold higher production of IL-6 in visceral adipose tissue, compared to subcutaneous fat tissue [153]. Similar to TNF-α, IL-6 inhibits the insulin signalling pathway in adipose tissue and liver by upregulating the expression of SOCS3 in obese individuals [114, 154-156].

2.3 Adipogenesis, transdifferentiation and dedifferentiation of adipocytes

The adipogenesis of brown and white adipose tissue takes place at different times in life. BAT develops already in utero, reaching its maximum around birth, whereas WAT mainly grows post-natal and gradually increasing its size over time [74, 157, 158]. This is partly because new-born humans and many new-born large mammals rely on heat production from non-shivering thermogenesis (see **Chapter 2.1**), which takes place in the BAT under energy expenditure especially in the initial hours after birth [59, 60, 74, 158]. White adipocytes, on the other hand, are specialised in storing energy in form of triglycerides, which can be mobilised as free fatty acids in times of need (see **Chapter 2.2.1**) [60, 74, 158, 159].

Both white and brown mature adipocytes develop from pluripotent (*i.e.,* not yet determined to a certain tissue type) mesenchymal stem cells (MSCs) located in the vascular stroma of adipose tissue as well as in the bone marrow [160-163]. Although both adipose tissue types originate from the mesenchyme, they develop from two different MSC lineages. White adipocytes originate from Myf5-negative precursor

cells, brown adipocytes from Myf5-expressing myogenic precursor cells, which also hold the potential to differentiate into myocytes [74, 164].

The adipogenesis can be divided in two well-defined phases. The first, commitment or determination phase, is activated by signals, which *in vivo* have not been identified yet, and restricts the stem cell to the adipocyte lineage, ultimately leading to the conversion of the MSCs into white or brown preadipocytes. This cell type is morphologically undistinguishable from the MSC but has lost its potential to differentiate into other cells (*e.g.,* myocytes, chondrocytes, osteocytes) [157, 160-163].

In vitro, pluripotent C3H10T1/2 cells have been used as a reliable MSC model to study adipogenesis. They can be activated by factors such as bone morphogenetic proteins (BMP4, BMP2) and wingless-related integration site (Wnt; additionally inhibiting the differentiation phase), whereas the expression of Hh (hedgehog) is inhibitory, although its role in adipogenesis is not well-defined yet [161, 163, 165-168].

In the following terminal differentiation phase, the preadipocyte adopts characteristics of a mature white (*e.g.,* single, almost cell-filling lipid droplet) or brown (*e.g.,* multiple lipid droplets, high number of mitochondria) adipocyte and acquires the ability to transport and synthesize lipids, to secrete specific proteins, obtains its insulin sensitivity and produce adaptive heat, respectively [50, 60, 157]. This process is similar in both WAT and BAT and is regulated by a number of different transcription factors, with peroxisome proliferator-activated receptor-γ (PPARγ) and CCAAT-enhancer-binding proteins (C/EBPs) like C/EBPα playing a central part [157, 169]. While C/EBPα plays a major role in the differentiation of WAT, BAT development is independent of its expression [74, 157, 158, 170]. Here, PR domain-containing protein-16 (PRDM16) appears to be the main regulator that initiates the commitment to the brown fat cell lineage [60, 74, 158, 164, 171, 172]. This zinc-finger protein can simultaneously promote the induction of genes for the "brown" phenotype (*i.e.,* genes associated with mitochondrial biogenesis, oxidative phosphorylation, and oxidation of lipids) and suppress corresponding genes of WAT by interacting with either peroxisome proliferator-activated receptor gamma coactivator 1-alpha/beta (PGC-1α/ß) or C-terminal-binding proteins (CtBPs), respectively [74, 158, 172].

Gold standard for investigating the second phase in culture is the murine 3T3-L1 preadipocyte cell line. The exposure of G_1-growth-arrested preadipocytes with adipogenetic inducers like fetal bovine serum (FBS), insulin-like growth factor 1 (IGF1; insulin is also possible, but IGF1 induces in much lower concentrations) and dexamethasone, causes the preadipocytes to re-enter the cell cycle about 16 to 20 hours later and undergo one or two rounds of mitosis (mitotic clonal expansion), a necessary step in differentiation [157, 163, 169]. After the cells exit the cell cycle, they change from fibroblastic to adipocyte morphology and acquire functions of mature adipocytes. White fat cells start to accumulate triacylglycerides (TAGs), which is accompanied by an increased expression of enzymes for fatty acid and TAG biosynthesis [163, 173]. Brown fat cells express high amounts of UCP1 (*i.e.,* thermogenin), the central mediator for non-shivering thermogenesis in humans and a variety of animals, except pigs (see **Chapter 2.1**) [59, 60, 63, 65, 74].

The origin of beige adipocytes has not yet been completely clarified. Some theories suggest that they derive from transdifferentiation of white adipocytes, with a so-called "paucilocular" adipocyte (*i.e.,* UCP1 positive, distribution of lipid droplets intermediate between brown and white adipocytes) being an intermediate form [74, 174]. Furthermore, $ß_3$-adrenergic stimulation is believed to induce transdifferentiation of white fat cells in the inguinal WAT, but differentiation of Myf5-negative progenitor cells in the epididymal WAT of mice [74, 175]. Either way, beige adipocytes do not originate from the same MSC lineage as “classic” brown adipocytes, but from progenitor cells similar to those of white fat cells [66, 74, 164].

Transdifferentiation of white adipocytes can also be observed in pathological conditions such as breast cancer, where cancer cell neighbouring adipocytes transdifferentiate to cancer-associated fibroblasts (CAFs) and subsequently promote tumour progression [176-178].

In a process known as dedifferentiation, mature white adipocytes, as well as other cell types (*e.g.,* Schwann cells), can convert back into less differentiated cells of their respective lineage [177, 179]. The preadipocytes can re-enter the cell cycle, proliferate and finally re-differentiate into mature adipocytes [176]. Dedifferentiation occurs physiologically for example during late pregnancy in the mammary gland, where the adipose tissue gives way to the epithelium. In the course of the involution of the mammary gland after lactation, preadipocytes re-differentiate into mature

adipocytes [176, 177, 180]. The mechanisms that drive dedifferentiation are not well characterised, yet. Modulators that also control adipogenesis, such as PPARγ and Wnt, may play a role [176, 177].

2.4 White adipose tissue remodelling in obesity

A constantly positive energy balance poses great challenges to the adaptability of adipocytes. To provide storage capacity for the increased amount of lipids, adipose tissue can enlarge its volume by increasing the number of adipocytes (hyperplasia) and/or their volume (hypertrophy) [181].

In a study on subcutaneous adipose tissue of 764 individuals, Arner *et al.* (2010) [182] defined hypertrophic adipose tissue by a morphologic parameter based on the difference between the measured adipocyte volume (mean value calculated from the diameter of isolated adipocytes using formulas of Hirsch and Gallian (1968) [183]) and the expected adipocyte volume (based on a curve-linear relationship between adipocyte volume and total body fat mass) [109, 181, 182]. If the adipocyte volume was larger than expected, the value was positive and the adipose tissue was classified as hypertrophic; if the value was negative (*i.e.,* the volume was smaller than expected), the adipose tissue was classified as hyperplastic. Pronounced hyperplasia or hypertrophy was indicated by large absolute values. In addition, they demonstrated that the number of adipocytes (determined by dividing the total amount of body fat by the mean adipocyte weight, which in turn was calculated from fat cell diameter) and the adipocyte volume were negatively correlated, and 70% fewer adipocytes were generated per year in hypertrophic than in hyperplastic subcutaneous adipose tissue [109, 182].

To maintain tissue function, the remodelling processes are accompanied by numerical and/or functional changes in various stromal vascular cells. In their entirety, these events are summarized as adipose tissue remodelling [79]. Adipocyte hyperplasia seems to result in a healthy expansion of fat tissue by evenly distributing the excess lipids to newly differentiated fat cells, whereas adipocyte hypertrophy ultimately leads to dysfunctional adipocytes promoting an unhealthy tissue expansion [29, 109, 184]. For example, adipocytes reaching their expansion limit (which is determined by the extracellular matrix) become lipid-overloaded and insulin resistant (due to impaired trafficking of glucose transporter 4 (GLUT4) to the plasma membrane) [109, 185-188]. Additional alterations which can occur in the

course of an unhealthy adipose tissue expansion are disturbed adipogenesis, mitochondrial dysfunction, and disturbed cytokine secretion, which lead to local and systemic inflammation [109, 189]. Furthermore, studies on murine and human adipose tissue indicate that the increased size of adipocytes, as well as changes in the microenvironment of the fat tissue (*i.e.,* mechanical and oxidative stress, hypoxia), initiate adipocyte apoptosis [11, 186, 190-192].

Knittle *et al.* (1979) analysed the growth of adipose tissue in children and adolescents [193]. For this purpose, they determined the cell size (defined as lipid content in µg per cell) in the subcutaneous fat of 288 children between four and 18 years of age using the method described by Hirsch and Gallian (1968) [183] and estimated the total number of fat cells from the total body fat (body weight minus lean body mass) and the mean fat cell size [193]. The authors of the study concluded from the collected findings that adipose tissue expands in children and adolescents mainly due to an increase in adipocyte number, with obese individuals developing significantly more fat cells than lean individuals. However, especially in children between six months and one year of age, there is also an increase in fat cell size up to almost adult levels, which decreases to previous levels between one and two years of age [193]. Early studies suggested that in human adults, adipose tissue solely expands via increase in fat cell size (except in severe obesity) [194-196]. Currently it is believed that, in humans, both types of remodelling mechanisms occur and depend on the adipose tissue depot.

Hypertrophy occurs mainly in the visceral depot (VAT), whereas the subcutaneous adipose tissue depot (SAT) increases its volume mainly through hyperplasia [15, 16]. For example, Joe *et al.* (2009) showed that following a high-fat diet, C57BL/6 mice demonstrate a significantly higher increase in adipocyte diameters in visceral adipose tissue compared to the respective subcutaneous fat depots [15]. They suggested that the difference in adipose tissue expansion might be caused by a higher number of progenitor cells (determined via limiting dilusion analysis) in the SAT compared to the VAT [15]. The increased number of dysfunctional adipocytes in the visceral adipose tissue depot may also explain its association with an increased risk of obesity-associated diseases [15]. However, adipogenesis in SAT seems to be impaired in chronic states of obesity, enabling the adipose tissue depot to only minimally counteract the metabolic alterations by *de novo* adipogenesis

[197]. In contrast, VAT is suggested to have a higher hyperplastic capacity compared to SAT [16]. This has been observed in “AdipoChaser” mice, which reacted to positive energy balance with hypertrophic VAT within four weeks, followed by adipocyte hyperplasia after two months. Subcutaneous adipose tissues, however, demonstrated only a negligible amount of adipogenesis [197].

Both Spalding *et al.* (2008) [181] and Andersson *et al.* (2014) [198] demonstrated that in case of severe weight loss (induced by bariatric surgery), however, subcutaneous and visceral fat depots demonstrate a decrease in adipocyte size (mean cell volume, calculated from the diameter of isolated adipocytes), whereas the number of fat cells (division of total amount of body fat by the mean adipocyte weight calculated from fat cell diameter) remains constant [181, 198]. Observations on rats and humans suggest, that subsequent regain of weight occurs mainly through refilling of mature adipocytes and only partly due to an increase in fat cell number [185, 199-201].

Obesity also promotes senescence of the adipose tissue, which physiologically only occurs in old age [202]. In the latter, this irreversible process is activated, among other things, by the fact that the telomeres (*i.e.,* repetitive nucleotide sequence at the end of linear chromosomes) become shorter with each cell division due to a lack of telomerase activity. This triggers a DNA damage reaction, which in turn activates the tumour suppressor protein p53 and its downstream transcriptional target, the cyclin-dependent kinase inhibitor $p21^{CIP1/WAF1}$, which subsequently leads to cell cycle arrest and insulin resistance [202-204]. The expression of p53 is also increased in adipose tissue of obese individuals, promoting adipocyte senescence [202, 203, 205]. Visceral adipose tissue seems more affected than subcutaneous adipose tissue. Characteristics of senescent adipose tissue include impaired lipid metabolism, inflammation, insulin resistance and a so-called senescent-associated secretory phenotype (SASP) (*i.e.,* secretion of high levels of inflammatory cytokines, growth factors, and matrix-remodelling proteases), which ultimately contribute to the progression of adipose tissue dysfunction [202].

3 Metabolic syndrome

3.1 Definition and prevalence of the metabolic syndrome

The metabolic syndrome (MetS), also known as syndrome X, insulin resistance syndrome, and hypertriglyceridemic waist, refers to the combined occurrence of various metabolic alterations within an individual that increases the risk of cardiovascular diseases (CVD) and type 2 diabetes mellitus (T2D) [4, 5, 206]. How much this risk increases depends on the alterations occurring simultaneously and the additional individual risk factors of the affected human [4]. The metabolic alterations include glucose intolerance, insulin resistance (IR), central obesity, hypertension and atherogenic dyslipidaemia (including elevated serum triglycerides and reduced HDL cholesterol) [4, 206]. These components seem to have an additive effect, which elevates the risk for T2D and CVD the more components occur together [5]. Although the MetS was already described in the 1920s, there has long been no uniform set of criteria (*i.e.,* which alterations must occur in combination and how they are defined). It was not until 1998 that the WHO took the initiative to develop a uniform and internationally recognized definition, which will be adapted according to the current state of knowledge. In terms of the essential components (glucose intolerance, insulin resistance, central obesity, hypertension, dyslipidaemia), it agrees with the definitions that the National Cholesterol Education Program's Adult Treatment Panel III (NCEP/ATP III) and the European Group for the Study of Insulin Resistance (EGIR) postulated shortly afterwards. In detail, however, the definitions differ in terms of cut-off points and the combination of the individual components [206]. According the WHO criteria, for diagnosis of MetS the presence of impaired glucose tolerance, type 2 diabetes mellitus and/or insulin resistance and two additional risk factors is required [207]. The EGIR definition also requires insulin resistance plus two additional risk factors, whereas the NCEP/ATP III definition does not necessarily imply the diagnosis of IR, but more generally requires the presence of three out of five factors as diagnostic criteria [206]. In 2003, the American Association of Clinical Endocrinology (AACE) proposed another definition. They suggested elevated triglycerides, reduced HDL cholesterol, elevated blood pressure, and elevated fasting glucose as the identifying criteria. Although central obesity is a major risk factor for both T2D and CVD, it is not mentioned as a criterion [206]. In contrast to the previously mentioned definitions,

no fixed number of existing criteria is specified here, but left to clinical judgment [4]. In 2005, the International Diabetes Federation (IDF) published a modified version of the NCEP/ATP III definitions. In this version, the presence of abdominal obesity rather than IR is required (together with two other components), as they are strongly correlated, and IR is much more laborious to measure. In contrast to the other definitions, the threshold values for abdominal obesity are specified for different ethnic groups. The list of required additional components is the same as in the NCEP/ATP III version [4]. In the same year, the National Heart, Lung and Blood Institute (NHLBI) in collaboration with the American Heart Association (AHA) also presented a set of criteria. It retains the ATP III criteria except for a few minor changes [4]. A detailed summary of the different criteria is provided in **Table 1**. Although the introduction of a set of criteria facilitates diagnosis, the variety of different definitions still makes it difficult to compare prevalence for the metabolic syndrome across countries or even research groups [206]. As a result, the global prevalence of the metabolic syndrome varies between 20% and 45% and is expected to reach 53% until 2035 [41, 208]. In addition to the set of criteria used, the prevalence of the MetS also depends highly on the age of an individual. In Iran, for example, the prevalence is <10% for both men and women aged 20-29 years but increases to 38% and 67%, respectively, in individuals aged 60-69 years. Similar findings were observed in the French and US population [206, 209, 210]. Even within the same age range, the prevalence varies in both men and women. For example, in studies using the NCEP/ATPIII criteria, prevalence of 8% to 20% in men and 7% to 43% in women was reported for age 20 and higher [206, 211].

Table 1. Set of criteria for the definition of the metabolic syndrom by different associations

	WHO (1998)	NCEP - ATP III (2001)	EGIR (2002)	AACE (2003)	IDF (2005)	AHA/NHLBI (2005)
Requirement	IGT, T2D and/or insulin resistance **+** *Two or more of the following:*	*Any three of the following:*	Hyperinsulinemia / IR **+** *Two or more of the following:*	IGT or IFG **+** *Any of the following:*	Abdominal obesity (ethnicity and gender specific) WC ≥ 94 cm (♂) WC ≥ 80 cm (♀) **+** *Two or more of the following:*	*Three or more of the following:*
Additional components	Central adiposity WC > 94 cm Waist-to-hip ratio > 0.90 (♂) Waist-to-hip ratio > 0.85 (♀) **+/-** BMI > 30kg/m²	WC ≥ 102 cm (♂) WC ≥ 88 cm (♀)	WC ≥ 94 cm (♂) WC ≥ 80 cm (♀)	BMI ≥ 25 kg/m²		WC ≥ 102 cm (♂) WC ≥ 88 cm (♀)
	TG ≥ 150 mg/dL **+/-** HDL-C < 35 mg/dL (♂) HDL-C < 39 mg/dL (♀)	TG ≥ 150 mg/dL **+/-** HDL-C < 40 mg/dL (♂) HDL-C < 50 mg/dL (♀)	TG ≥ 150 mg/dL **+/-** HDL-C < 39 mg/dL	TG ≥ 150 mg/dL **+** HDL-C < 40 mg/dL (♂) HDL-C < 50 mg/dL (♀)	TG ≥ 150 mg/dL **+/-** HDL-C < 40 mg/dL (♂) HDL-C < 50 mg/dL (♀)	TG ≥ 150 mg/dL HDL-C < 40 mg/dL (♂) HDL-C < 50 mg/dL (♀) **or** Drug treatment for elevated TG / reduced HDL-C
	BP ≥ 140/90 mmHg	BP ≥ 130/85 mmHg	BP ≥ 140/90 mmHg **or** Antihypertensive medication	BP ≥ 130/85 mmHg	BP ≥ 130/85 mmHg **or** Antihypertensive medication	BP ≥ 130/85 mmHg **or** Antihypertensive drug treatment (if history of hypertension)
	Microalbuminuria > 30mg/g	Glucose > 110 mg/dL*	IGT or IFG (no Diabetes)	IGT or IFG (no Diabetes)	Fasting glucose ≥ 100 mg/dL **or** Drug treatment for elevated glucose	Fasting glucose ≥ 100 mg/dL **or** Drug treatment for elevated glucose
	Impaired glucose regulation or diabetes, insulin resistance					

AACE, American Association of Clinical Endocrinologists; AHA/NHLBI, American Heart Association/National Heart, Lung and Blood Institute; BMI, body mass index; BP, blood pressure; EGIR, European Group for the Study of Insulin Resistance; HDL-C, HDL cholesterol; IDF, International Diabetes Federation; IFG, impaired fasting glucose; IGT, impaired glucose tolerance; NCEP-ATP III, National Cholesterol Education Program - Adult Treatment Panel III; T2D, type 2 diabetes mellitus; TG, triglycerides; WC, waist circumference; WHO, World Health Organization.
*modified in 2004 to be ≥ 100mg/dL according to the updated IFG definition

This table was compiled by Theobalt (2021) based on the data available in the literature [4, 5, 41, 206, 207, 209].

3.2 Pathogenesis of the metabolic syndrome

The aetiology of the metabolic syndrome is manifold [206]. Major underlying risk factors are physical inactivity and a diet high in carbohydrates and fat, since they contribute to two of the essential components of the MetS, central obesity and insulin resistance [5]. The pathogenesis linking obesity with the metabolic alterations defining the metabolic syndrome are complex.

The adipose tissue is the main organ to store excess energy in form of neutral fats [79]. Especially in chronic obesity, alterations in the adipose tissue remodelling may occur, which can lead to disturbed adipogenesis and may also have an effect on the endocrine function of the adipose tissue, resulting in altered adipokine secretion and, consequently, in local and systemic inflammation as well as local and systemic insulin resistance (see **Chapters 2.2.2** and **2.4**) [79, 189, 212]. Additional characteristics of dysfunctional adipose tissue might be insufficient angiogenesis, hypoxia and fibrosis [213-217].

In hypertrophic adipose tissue, the adipokine secretion changes from a balanced level of anti-inflammatory (adiponectin) and pro-inflammatory adipokines (*e.g.,* leptin) to a predominantly pro-inflammatory one [218-222]. This shift is mediated through a variety of mechanisms. Maury *et al.* (2010), for example, demonstrated an elevated responsiveness of *in vitro* cultured omental adipocytes of obese subjects to TNF-α (*in vivo* secreted by the SVF), which was mediated by an upregulation of tumour necrosis factor receptor 1 (TNFR1), followed by an increased activity of nuclear factor-kappa B (NF-κB), and in turn an increased production of different pro-inflammatory adipokines [223]. Additionally, *Adiponectin* mRNA expression is downregulated in adipocytes with endoplasmic reticulum (ER) stress caused by hypoxia, as Hosogai *et al.* (2007) demonstrated in 3T3-L1 adipocytes [221]. Macrophage infiltration also plays a crucial role in the development of a predominantly pro-inflammatory phenotype and is further described below [140, 223].

The pro-inflammatory cytokines can alter the insulin signalling in adipose tissue and liver via inhibition of IRS-1 (see **Chapter 2.2.2**), which subsequently leads to local and systemic IR [109, 143, 156]. Furthermore, they can recruit additional immune cells to the adipose tissue and thus stimulate local inflammation [189]. Leptin, for example, can directly increase the production of mediators such as TNF-α, IL-6,

interleukin-8 (IL-8) and monocyte chemoattractant protein1 (MCP1) in resident ATMs, which recruit T-cells and macrophages (up to 40% of the SVF of VAT in obese individuals, compared to 10% - 15% in VAT of lean individuals) and thus promote, and subsequently sustain, a local and systemic inflammation [140, 189, 218, 224]. These macrophages originate mainly from monocytes circulating in the blood, which differentiate into M1 ATMs once they arrive in the adipose tissue [140, 189, 225]. They similarly secrete pro-inflammatory cytokines that maintain the adipose tissue inflammation, as well as chemokines that again recruit new macrophages [109]. The degree of macrophage infiltration is significantly and positively correlated with the average adipocyte cross-sectional area in murine and human white adipose tissue (WAT) as shown by Weisberg *et al.* [140] in 2003 [140, 226]. In mice and human, most macrophages are found in areas of adipocyte death (see **Chapter 2.4**), where they surround the dead cells (so-called crown-like structures, CLS) to phagocyte cell remnants, especially the possibly cytotoxic lipid droplet [225, 227]. It is assumed that the chronic inflammation is sustained by the macrophages' clearing up processes [226, 227]. However, the clearance of the adipocyte remnants by ATMs is (at least initially) important for adipose tissue remodelling and differentiation of new adipocytes [225, 227]. Furthermore, the dead adipocytes contribute to the local tissue inflammation by activating the immune system via direct recruitment and/or activation of macrophages, or the release of damage-associated molecular patterns (DAMPs), such as high mobility group box 1 (HMGB1), for example [190, 227, 228].

Besides their pro-inflammatory effect, TNF-α and IL-6 are also involved in the downregulation of GLUT4, the main insulin-responsive glucose transporter in adipocytes. Together with impaired insulin signalling via inhibition of IRS-1, this results in reduced insulin-stimulated glucose transport and metabolism in adipose tissue [115, 154, 212]. Consequently, basal lipolysis is increased since insulin cannot exert its anti-lipolytic effect [229, 230]. Besides this, TNF-α itself can stimulate lipolysis via reduction of HSL- and perilipin expression [146, 147, 231, 232]. The latter, a protein coating the intracellular lipid droplet, regulates the accessibility for HSL to the surface of the droplet [94, 231, 232]. These mechanisms all in all result in hyperinsulinemia, hyperglycaemia, and hyperlipidaemia [229, 230].

Following increased lipolysis in hypertrophic adipocytes, large amounts of FFAs are released into the circulation, which can trigger various inflammatory signalling pathways in both adipocytes and macrophages [109, 233]. For example, FFAs bind to Toll-like receptor 2 of *inter alia* adipocytes and macrophages, leading to the activation of NF-κB and JNK signalling pathways [109, 223, 234-237]. This in turn increases the synthesis and secretion of many chemokines (*e.g.,* MCP1) in adipocytes, as well as inhibitory serine phosphorylation of IRS-1, all in all contributing to proinflammatory macrophage infiltration and IR [109, 235, 236].

Furthermore, local hypoxia due to reduced capillary density, as shown by Pasarica *et al*. (2009) [238], which determined the number of capillaries per millimetre adipose tissue section area in human abdominal fat, or an increased oxygen consumption (due to uncoupled respiration) by the hypertrophic adipocytes can trigger local adipose tissue inflammation [109, 238, 239]. Subsequently, hypoxia inducible factor-1α (HIF-1α) is activated, which stimulates *inter alia* expression of pro-inflammatory cytokines in macrophages [109, 239, 240].

It is important to note that the localization of adipose tissue plays a central role in its metabolic effects. Especially increased storage of lipids in visceral adipose tissue depots seems to be closely related to IR, T2D and CVD. The underlying causes have not yet been clarified. Increased lipolysis activity or the secretion of factors particularly affecting insulin sensitivity could potentially be involved [212].

In conclusion, the major trigger of obesity-associated complications lies in the alteration of adipose tissue plasticity, which is followed by an inadequate response of the adipose tissue depots to the energy overflow and subsequently to systemic metabolic alterations [109].

3.3 Diagnosis and therapy of the metabolic syndrome

The clinical symptoms of the metabolic syndrome highly depend on the combination of components that occur in each affected individual, which can make it difficult to detect the syndrome at an early stage. The diagnosis is based on the definition criteria mentioned in **Table 1** (see **Chapter 3.1**). The ATP III criteria (and their variations) are suited for clinical practice, whereas the initial WHO definition is primarily suitable for scientific purposes [206].

The treatment of the metabolic syndrome is multifactorial [241]. The first-line therapeutic goal in individuals with MetS is to treat all abnormal metabolic components and thus reduce the risk for diabetes and CVD, if not already present [4, 242]. Due to their additive effect, the therapy of one or two of the components could already have a positive effect [5]. Pharmacotherapy is used when metabolic alterations such as high levels of HDL cholesterol, hypertension and hyperglycaemia are not reversible through lifestyle changes alone or require immediate treatment [4, 242].

The long-term therapeutic goal, which is also the most important preventive measure, consists primarily in the reduction of the underlying metabolic risk factors, above all obesity, since the metabolic syndrome almost never manifests without some degree of obesity and effective weight loss improves all metabolic disturbances. A healthy diet (*inter alia* reduced saturated fats, cholesterol and salt, increased amount of fruits, vegetables and whole grains), more physical activity and an early and long-lasting reduction in adipose tissue mass (especially in visceral fat depots) can help to control obesity and the complications associated with it, including insulin resistance [4, 206, 242]. The importance of an early therapy and prevention is also reflected in the fact that over 75% of obese children stay obese in adulthood whereas only 10% of normal weight become obese later in life [181].

3.4 Metabolically healthy obese

Although the changes on adipocyte level occur in every obese individual, impaired adipose tissue remodelling does not appear homogeneously, and obesity will not necessarily cause insulin resistance and an increased risk for metabolic complications [109]. A subgroup of about 10 - 30% of obese individuals is currently referred to as “metabolically healthy obese” (MHO) [243]. Despite increased subcutaneous adipose tissue depots, they exhibit insulin sensitivity, reduced adipose tissue inflammation, reduced visceral adipose tissue expansion, as well as normal physiology and hormone profiles [109, 244]. However, the factors that compose this rather healthy phenotype are yet to identify. For this reason, there is currently no uniform definition of this subtype, which together with other factors such as lifestyle, sex and age leads to considerable variations in the prevalence of MHO [41, 243, 244]. In European obese individuals the prevalence of MHO is higher in women than in men [243]. This might be explained by the differences in adipose

tissue distribution between both sexes. Although women often have a higher proportion of total and/or subcutaneous fat compared to men, they still have less of the visceral fat associated with metabolic risk factors [244]. One of the most important factors for the higher levels of insulin sensitivity of MHOs compared to obese individuals seems to be the small share of VAT in their total body fat. Since hypertrophic adipocytes have a negative influence on insulin sensitivity (see **Chapter 2.4**), investigating volume and number of adipocytes in different adipose tissue depots may be critical in explaining the higher insulin sensitivity observed in MHOs [245]. In addition, an early onset of obesity may lead to a number of compensatory metabolic adjustments that allow for normal insulin sensitivity [245]. Although this subgroup displays a (temporarily) healthy metabolism, other obesity-associated co-morbidities like osteoarthritis, respiratory diseases and psychological abnormalities are still present and may reduce the quality of life [9]. According to long-term studies, however, this metabolic state seems to be only a transient condition [109, 246]. About one third of MHO individuals develop diabetes and cardiovascular diseases over time [247]. Compared to metabolically unhealthy obese, MHOs are on average younger and have less abdominal adiposity [248]. Following Appleton *et al.* (2013), MHOs of younger age with lower central adiposity show about the same degree of risk to develop diabetes or cardiovascular diseases compared to metabolically healthy normal weight individuals over a period of five to ten years [247]. In general, metabolically healthy obese individuals have an intermediate risk for developing obesity-associated diseases between metabolically healthy normal weight and unhealthy obese individuals [245, 248, 249]. This obesity “phenotype” is therefore not as healthy as its name suggests and should not be considered a harmless condition [9, 248]. One of the most common therapeutic approaches against obesity, weight-loss intervention, does not appear to improve individual metabolic risk factors in MHOs, but in some cases has rather a paradoxical effect [243]. This includes declined energy expenditure and increased symptoms of depression, which can ultimately lead to weight regain [248, 250]. However, "weight-loss" is a very general term regarding the different adipose tissue depots possibly affected by it. Since not all fat tissue depots have negative effects on the metabolism (*e.g.,* subcutaneous adipose tissue), a targeted fat loss towards a more beneficial fat distribution would be a possible approach [248]. Understanding

the underlying causes of the MHO phenotype can help to gain valuable insights into the pathophysiology of obesity-related diseases [243].

3.5 Metabolically obese normal-weight

In contrast to MHOs, there are non-obese individuals (*i.e.,* individuals with normal weight and BMI) who have metabolic disorders that are characteristic for obesity [245]. These metabolically obese normal-weight (MONW) individuals (also referred to as metabolically abnormal normal-weight individuals or normal-weight obesity) show increased levels of visceral adipose tissue, insulin resistance, hyperinsulinemia and dyslipidaemia which may result in an increased risk for type 2 diabetes mellitus and cardiovascular disease [245, 251]. The factors leading to this increased risk profile have not yet been clarified, but abnormal distribution of body fat seems to play an important role in these individuals [245].

However, since MONW individuals generally appear healthy due to their normal BMI and young age, metabolic disorders and CVD are frequently undetected, usually being diagnosed only after several years. Therefore, early detection and treatment of the metabolic alterations could prevent an exacerbation of symptoms [245].

4 Animal models of obesity and obesity-associated alterations

The aim of translational medicine is to translate discoveries of fundamental research into clinical application, whether for prevention, diagnosis or therapy [252]. For a long time, a wide variety of animal models were used for this purpose. The animal species used in experimental models in obesity research range from rodents to larger animals such as pigs, each of them with individual advantages and disadvantages. Since the development of obesity is a multifactorial process in which, among other things, a large number of different genes are involved, animal models in obesity research can be divided into two major categories [253]. On the one hand, genetically modified animals, and on the other hand, animals that have been exposed solely to an obesity-enhancing environment, for example, high-calorie diet leading to diet-induced obesity (DIO) [253]. The latter are believed to reflect more precisely the obesity-associated changes in humans [17, 253, 254].

4.1 Rodent models of obesity and obesity-associated alterations

Traditionally, obesity research has primarily used rodent models to study disease mechanisms and to treat obesity-associated alterations [253]. The short reproduction intervals of the species used (*i.e.,* mice, rats) resulting in high numbers of offspring, the availability of a large number of genetically modified strains, the relatively short duration of the experiments and the cost-effective animal husbandry are among the reasons for this [17, 255].

The *db/db*-mouse has become well known as a monogenetic (*i.e.,* a causal mutation linked to one gene) model for obesity, dyslipidaemia and type 2 diabetes mellitus. Animals of this model display a spontaneous autosomal recessive mutation (sequence insertion) in the gene for the hypothalamic receptor of the satiety hormone leptin (*Lepr*), which leads to leptin resistance and in consequence to high levels of the hormone itself, since there is no impaired synthesis [17, 253, 256, 257]. Phenotypically, they resemble the *ob/ob*-mouse, in which leptin synthesis is prematurely terminated due to a spontaneous mutation in the leptin gene (*Obs*), resulting in a hormone deficiency, but they show more severe hyperglycaemia. The *db/db*-mouse is also characterised by hyperphagia, reduced energy expenditure, decreased linear growth due to growth hormone deficiency, infertility and insulin resistance, which leads *inter alia* to early-onset morbid obesity and type 2 diabetes mellitus [17, 253]. At cellular level, *db/db*-mice have approximately 11 times larger adipocyte section areas in subcutaneous and visceral adipose tissue compared to wild-type mice, with subcutaneous adipocytes appearing to be considerably larger than visceral ones. Both depots also show changes at the ultrastructural adipocyte level (*e.g.,* thinning of the cytoplasmic rim, cholesterol crystals) which are highly suggestive of cellular stress [226].

Another murine model for leptin receptor deficiency is the genetically engineered *s/s*-mouse [253]. To generate this model, Bates *et al.* (2003) used homologous gene targeting to exchange the gene for the leptin receptor, which physiologically encodes the amino acid tyrosine at position 1138 (Tyr1138), with an allele that encodes serine (Ser1138) instead. The translated leptin receptor is normally expressed but unable to activate the transcription factor signal transducer and activator of transcription 3 (STAT3), which primarily mediates the effect of leptin on energy homeostasis. However, other leptin signals are correctly mediated by the

receptor, making the *s/s*-mouse a more specific model for leptin receptor defects [258]. Homozygous (*s/s*) mice of this model demonstrate hyperphagia, insulin resistance and obesity, but in contrast to the *db/db*-mouse, they are fertile and develop a physiological body length as well as less hyperglycaemia [253, 258].

Sprague-Dawley rats are used as an DIO/polygenetic model of obesity. They develop, as most other animals, an obese phenotype when exposed to a high-fat diet [253]. In a semi-quantitative analysis of histological adipose tissue sections, Rojas *et al.* (2018) showed an increase in section profile size of subcutaneous fat cells compared to adipocytes of retroperitoneal and gonadal adipose tissue [259]. Marques *et al.* (2016) demonstrated an increase in adipocyte section profile areas in mesenteric adipose tissue in a quantitative analysis using ImageJ software [260]. Generally, there is a significant variation in phenotypes in outbred strains of Sprague Dawley rats due to different breeding histories, which makes comparison and generalization of results obtained in this DIO-model difficult [261, 262]. Although most of the characteristics of the metabolic syndrome (*e.g.,* insulin resistance, dyslipidaemia and hypertension) could be observed in these animals, there are studies that demonstrated an obese phenotype in rats of this model, but only slight obesity-associated changes, thus resembling rather the phenotype of metabolically healthy obese humans [259-261].

However, due to low life expectancy and numerous anatomical and physiological differences to humans, classic laboratory rodent models are often unable to adequately reflect the full spectrum of disease-associated changes occurring in humans [18, 19].

The rodent models described here represent only a small selection of monogenetic and DIO/polygenetic models of obesity and obesity-associated alterations. For further examples, the interested reader is referred to Kleinert *et al.* (2018) [263], Lutz and Woods (2012) [253], Panchal and Brown (2011) [264], and Tschöp and Heiman (2001) [265].

4.2 Porcine models of obesity and obesity-associated alterations

Pigs serve as important large animal models of human biology [18, 266]. They demonstrate high similarities to humans in anatomy (*e.g.,* organ size, gastrointestinal anatomy), physiology (*e.g.,* omnivore, human-like food choice, eating behaviour and digestion), metabolism (*e.g.,* lipoprotein metabolism) and pathology (*e.g.,* obesity associated with insulin resistance, dyslipidaemia and atherosclerotic lesions) [17, 18, 61, 267]. Especially the resemblances in feeding behaviour and digestion make it possible to study the effects of a diet on the metabolism in pigs [267]. However, it should be noted that the response to dietary interventions also depends on the genetic background [61]. Ossabaw pigs, for example, develop significantly more pronounced forms of metabolic syndrome than Yucatan pigs on a high-fat diet [268]. These pigs represent the feral descendants of domestic pigs abandoned by sailors on Ossabaw Island (Georgia, USA) about half a millennium ago, which over time regained a "thrifty genotype" due to the more meagre food supply and increased physical activity in their new environment. Today, this causes Ossabaw pigs to be prone to obesity when put on a high-calorie diet in combination with low physical activity [61, 269, 270]. Early sexual maturity, all season breeding, multiple offspring and a short generation interval additionally qualifies pigs as large animal models in translational medicine [18].

Advanced techniques for genetic engineering of pigs, including clustered regularly interspaced short palindromic repeats/CRISPR-associated (CRISPR/Cas) technology, can be used to create porcine models for studying specific mechanisms of disease processes [19, 61]. For example, pigs with a restored UCP1 expression are used as animal models in obesity and diabetes research. The UCP1 knock-in (KI) pigs show, among others, changes in the thermogenesis and adipocyte metabolism, as well as signs of increased lipolysis [61, 72].

Besides the genetically modified models, porcine DIO models are of great importance. Pigs, like humans, are omnivorous and ingest their food discontinuously throughout the day, making it easy to generate a metabolism mimicking "Western lifestyle" with a variety of different diets. For example, a diet rich in energy combined with saturated fats and carbohydrates such as fructose can trigger characteristics of the metabolic syndrome in pigs [61].

Such a DIO-“minipig model” of the metabolic syndrome has recently been developed by Renner *et al.* (2018) [37]. These Göttingen minipigs (GM) were fed an experimental diet (high-fat/high-energy; HFHE) over a period of 70 weeks, which they were offered *ad libitum* for the final 15 weeks. At the end of the trial, the HFHE-fed minipigs (aged 3 years) had more than doubled their body weight compared to restrictively fed, age-matched control pigs, thus developed a pronounced obesity in subcutaneous and visceral adipose tissue depots, and furthermore showed metabolic changes (*i.e.,* increased plasma cholesterol, triglyceride and free fatty acid levels, impaired glucose tolerance and insulin resistance) that are regularly observed in humans in the context of the metabolic syndrome. In addition, the obese minipigs displayed multifocal, marked adipose tissue necrosis and severe inflammatory alterations, which occurred in the visceral fat tissue depots, but were not observed in the subcutaneous adipose tissue. At the level of light microscopy, there was no histomorphological evidence of adipose tissue inflammation or necrosis in the subcutaneous and visceral depots of lean pigs, nor in the subcutaneous fat depots of obese pigs. In contrast, the morphological findings in the visceral fat depots of the obese animals ranged from focal acute necrosis of single fat cells to large areas of extensive adipocyte necrosis and massive chronic inflammatory cell infiltration (*inter alia* macrophages, lymphocytes and plasma cells). Of particular notice was the drastic increase of the adipocyte section profile areas in these depots compared to the ones in the subcutaneous depots as well as compared to the section profile areas in both SAT and VAT of lean GM [37].

The porcine models described here represent only a small selection of monogenetic and DIO/polygenetic models of obesity and obesity-associated alterations. For further examples, the interested reader is referred to Renner *et al.* (2020) [61] and Kleinert *et al.* (2018) [263].

5 Methods for determination of adipocyte sizes/volumes and adipocyte numbers

Changes in the regional distribution of adipose tissue (especially increase in visceral fat tissue) as well as in the morphology of adipocytes (hyperplasia and/or hypertrophy) during weight gain play a major role in the development of obesity-associated diseases [109]. The detection of even the most subtle variations in, for example adipocyte volume or number, is therefore of fundamental importance in translational research.

A wide spectrum of techniques has been described in the last decades to quantify different adipocyte parameters [20, 21, 29, 183, 271-274]. The methods differ regarding the preparation of the tissue samples and the analysis method used.

5.1 Analysis of isolated adipocytes

5.1.1 Isolation of adipocytes

Isolated fat cells can be obtained by incubating fat tissue samples with collagenase [271]. Subsequently, the suspension is centrifuged, resulting in an adipocyte fraction in the top of the centrifuge tube, or the cells in the suspension are fixed with glutaraldehyde followed by the separation of adipocytes via filtration through a nylon screen [183, 272, 275]. The collagenase method is a gentle method to extract fat cells from the tissue [29]. However, centrifugation, mesh separation and collagenase digestion might cause fat cell damage [183, 271]. The latter affects especially hypertrophic adipocytes, whose large lipid droplet makes the cell fragile, possibly resulting in breakage of the cell and release of triglycerides [29, 183].

Isolated fat cells can also be obtained without prior collagenase digestion of the tissue by fixing fat pieces in osmium tetroxide. Subsequently, the suspension is filtered through a nylon net, larger pieces are carefully rubbed by hand first. The advantage of this method, compared to the use of collagenases, is that it is appropriate for all cell sizes [183]. Disadvantages are the high toxicity of osmium tetroxide and the fact that it may cause cell swelling, which can lead to a possible overestimation of the cell size [183, 271, 274].

It should be noted that adipocytes, despite their icosahedral/tetracaidecahedronic shape in histological sections, adopt an approximately spherical shape when isolated, which might be hard to distinguish from lipid droplets [183, 276, 277].

5.1.2 Analysis of sizes/volumes and numbers of isolated adipocytes

The number of isolated fat cells can be counted using a haemocytometer [272]. The diameters of isolated adipocytes can be determined either manually using a microscope equipped with a scale or from images of the individual fat cells using a software [183, 272, 274, 276]. Advantages and disadvantages of these methods are summarized in **Chapter 5.2**.

The Coulter Counter represents a method to determine both the number and the size of unfixed or fixed isolated adipocytes [183, 274]. The cells pass through a capillary opening, which changes the electrical resistance between two electrodes. Thus, the number of fat cells per unit volume can be determined [183]. Subsequently, the adipocyte volume can be achieved. Hirsch and Gallian (1968), for example, calculated the average adipocyte size (µg lipid/cell) by dividing lipid weight of a comparable sample by the adipocyte number [183]. Maroni *et al.* (1990) multiplied the midpoint of previously set channels by the number of adipocytes contained therein to determine the mean cell diameter [274]. With the Coulter Counter it is possible to evaluate large numbers of cells (up to 10.000) with a wide size spectrum (about 20 µm to 300 µm in diameter). However, it is debated whether cell debris can bias the results for small adipocytes (*i.e.,* false positive measurements) [29].

A more recent approach to analyse isolated adipocytes is flow cytometry [273, 278]. Here, a detector measures the scattered light or fluorescence signal of individual cells passing a laser beam [279]. The forward scatter (FSC) provides information about the relative size of cells, the side scatter (SSC) about the granularity of the cell [278, 279]. In addition to a rapid evaluation of large quantities of adipocytes, flow cytometry allows for sorting adipocytes (up to 250 µm in diameter) of the same sample by size and for detection of fat cell sub-populations in adipose tissue depots such as UCP1 expressing adipocytes in WAT [29, 278, 280]. Disadvantages of flow cytometry are the high acquisition costs and the need for specialised staff [271].

5.2 Morphometric analysis of adipocyte profiles in histological sections of adipose tissue samples

One of the most common methods for generating adipose tissue sections is paraffin embedding, sectioning, and haematoxylin-eosin (HE)-staining of fat tissue samples [281, 282]. Major advantages are the easy and swift feasibility, and the applicability of various tissue staining methods [282]. However, paraffin embedding causes a profound, irregular, and inconsistent tissue shrinkage, which negatively affects quantitative morphological analysis of dimensional parameters [282, 283].

Further techniques are frozen sectioning or plastic embedding (*e.g.,* in glycolmethacrylate/methylmethacrylate; GMA/MMA) [38, 281, 282]. Frozen sections are faster to prepare than paraffin sections and are particularly suitable for immunohistochemical staining [282]. Moreover, unlike paraffin sections, they display virtually no shrinkage in the X-Y plane [20]. Plastic embedding also causes only little tissue shrinkage compared to paraffin embedding. Additionally, it allows for the generation of thin (serial) sections. Disadvantages are the increased time required to produce the sections and the fact that immunohistochemistry protocols often don’t work satisfactorily in sections of plastic embedded medium due to poor antibody penetration. Immunohistochemical labelling of cells on the surface of the sections, however, can be achieved using special techniques [20, 282].

For a long time, histological sections were only subjected to qualitative evaluation. It is based on the human visual system, which is very skilled at recognising patterns (*e.g.,* inflammatory infiltrates), but has difficulties in assessing quantitative properties, such as differences in size or density of structures [284, 285]. In this context, de Groot *et al.* (2005) [286] showed that pathologists were unable to detect a significant reduction in total hippocampal neuron number of more than 30% in qualitative histological examinations of murine brain sections [286, 287]. It is generally assumed that, depending on the tissue, a deviation of at least 25-40% must occur in order to be recognised by the examiner [20, 21, 287]. Furthermore, the solely qualitative and semi-quantitative (*i.e.,* classification of changes into degrees of severity) observations are difficult to reproduce due to their subjectivity and vary strongly between different examiners [284, 285, 288, 289]. For objective and reproducible detection of quantitative morphological changes (not visible to the

naked eye), which may be subtle but pathogenesis-relevant, it is therefore essential to carry out measurements using quantitative morphological methods [21, 285, 287].

Planimetric methods (*i.e.,* 2D morphometric analysis of histological section profiles) are often used for determination of *e.g.,* mean adipocyte section diameters/-areas and numbers of cell section profiles per area unit of the histological tissue section. These two-dimensional morphometric parameters can be obtained quickly and with little effort either manually using a microscope equipped with a ruler or via different semiautomated image analysis softwares, such as ImageJ [271, 290-292]. However, when analysing 2D histological sections to determine 3D parameters such as volumes or numbers of particles (such as cells), each three-dimensional tissue sample is reduced to a two-dimensional tissue section, causing a loss of dimensional information [293, 294]. This means that each structure with the dimension *n* is represented in the tissue section by an image with *n-1* dimensions (*e.g.,* volumes become profiles, lines become points, numbers are no longer represented) [284, 293]. In addition, tissue shrinkage may occur, whose extent depends on the tissue, its processing and the respective embedding medium [20, 282, 283, 295]. As mentioned above, analysing these two-dimensional sections with common histological methods generates prompt results with little effort. However, these methods often neglect important structural properties of the examined tissue (anisotropy, *i.e.,* uneven distribution of shape, size, distribution and orientation of cells within the respective tissue) and the embedding-related tissue shrinkage [23, 294]. Results such as the cell numbers and -areas/diameters obtained from two-dimensional histomorphometric measurements of cell section profiles are neither equivalent nor directly related to cell volumes and numbers [21, 284, 296]. For example, the size of the section profile area of an adipocyte not only depends on its volume but also on the orientation of section plane cutting through it [23, 285]. Larger particles do also have a higher probability of being sectioned more than once when generating histological sections of a sample, which will lead to an overestimation of total cell numbers in the tissue when counting cell section profiles [296]. Additionally, it is not possible to derive individual cell volumes or cell size distributions in the respective reference compartment from two-dimensional morphometric parameters obtained in single histological sections [297].

5.3 Quantitative stereological analyses of histological adipose tissue sections

Stereology is defined as a set of methods that allows for obtaining information about 3D structures (such as cells) based on their 2D projections in (histological) sections [284, 298, 299]. As opposed to morphometry (*i.e.,* measurement of morphological structures), which is always a quantitative, but not necessarily a three-dimensional analysis, stereological analyses are always three-dimensional, but can be both quantitative and qualitative (*e.g.,* 3D-reconstruction of an object from serial sections) [284, 285].

Model-based quantitative stereological methods are based on *a priori* assumptions on, for example, the shape and size of structures in the respective reference compartment, as well as their shape- and size distribution [284, 293, 298]. For example, the shape of cells might be assumed as spheres or rotational ellipsoids. Although model-based quantitative stereological methods may yield estimates that are very close to reality they can also differ significantly from the actual structure and are therefore considered inherently biased [284].

In contrast, the application of design-based stereology, which is solely dependent on a correct sampling design and without assumptions about *e.g.,* shape, size and size distribution of structures, allows for the unbiased determination of all quantitative morphological parameters of three-dimensional structures in histological sections of representative and adequately processed tissue samples and is considered gold standard for quantitative morphological analyses in histological tissue sections [20-23, 294].

Design-based quantitative stereological analysis methods are based on statistical sampling principles and stochastic geometry that guarantee unbiased estimation of three-dimensional quantitative parameters in two-dimensional tissue sections with statistically defined and tolerable error probabilities [23, 300]. The methods include *inter alia* the application of (systematic) random sampling techniques and, if shrinkage-sensitive parameters (*e.g.,* numerical volume density) are of interest, the determination of the embedding related tissue shrinkage ahead of the estimation of relevant parameters with distinct stereological test systems and probes, all in all allowing for an accurate and precise quantification and comparison of even subtle structural alterations in the tissue that are not visible to the naked eye [20, 23, 293].

Random sampling designs imply the sampling from strictly randomly chosen locations in the reference compartment. This guarantees that each location has the same, random chance to be actually sampled and is therefore representative of the entire reference compartment [20, 21, 23, 301]. Of note, it is not necessary to know about the size, shape, orientation, or spatial distribution of the structures of interest within the reference compartment when using these sampling strategies [302]. The so-called systematic uniform random (SUR) sampling (a form of random sampling design) additionally significantly improves the efficiency (*i.e.,* required minimum of samples) of tissue sampling (see **Supplemental Figure S1** of publication) [21, 301]. Unbiased quantitative stereological analyses require the application of these (systematic) random sampling designs not only when sampling tissue specimen, but also on each subsequent sampling level (*i.e.,* from tissue sample to fields of view) [21].

To counteract the above-mentioned loss of dimensional information, each parameter is analysed with a specific stereological probe. The dimensions of the parameter and the probe used must add up to at least three. Volumes, for example, which have three dimensions are therefore determined with points, as they have no dimension, whereas the number, a dimensionless quantity, can only be determined in a test volume (*e.g.,* physical disector) [23, 294]. This ensures that the 3D tissue space is represented in the results. Furthermore, stereological probes are always positioned at random onto the sections to guarantee a random interaction with the structure of interest [23]. In order to estimate certain quantitative stereological parameters, namely length and surface area densities of anisotropic structures, the section plane orientation must be randomised as well, since these structures have a preferred direction in the 3D tissue leading to the influence of section plane orientation on the section profile [20, 23, 28, 285]. For example, isotropic uniform random (IUR) sections, *i.e.,* section planes randomised in all three dimensions of space, are adequate for the determination of virtually all quantitative stereological parameters including surfaces and lengths [20, 21, 283, 285, 303]. Commonly used methods for generation of IUR sections include the “orientator” [304, 305], where the orientation of the section plane is randomized relative to the tissue sample and the “isector” [306], where the position of the tissue sample is randomized relative to the position of the section plane [283, 303-306]. Also suitable are vertical uniform random (VUR) sections, which are randomised around a fixed vertical axis

determined by the experimentator [283, 303]. They are preferred for tissues with layered structures and natural surfaces (*e.g.,* skin, stomach, urinary bladder), because there is no complete loss of orientation as is the case with IUR sections. VUR sections can be used to estimate the same parameters possible in IUR sections except for lengths, which require section plane randomisation in all three dimensions of space [21, 283, 285, 303, 307].

The results obtained in quantitative stereological analyses are estimates of density values such as volume- and numerical volume densities, *i.e.,* the proportional volume and number of structures within the respective reference compartment (*e.g.,* the organ or tissue compartment). However, drawing conclusions directly from relative stereological parameters may be misleading (so called “reference trap” [308]), since it ignores the fact that not only quantitative changes of the structure of interest but also of the reference compartment influence the relative value. For example, an increase or decrease in the volume of the reference compartment alone may change the relative value and thus suggest a quantitative change of the structure of interest, even though it has remained constant. Conversely, a concordant change in the volume of the target structure and reference compartment may lead to a constant relative value and thus "hide" a quantitative change of the structure of interest [23, 28, 285, 308]. Therefore, the relative values must be translated into absolute values (*i.e.,* multiplication of the relative values with total volume of the corresponding reference compartment) for final evaluation [23, 28, 308]. An exception is the fractionator, as this method allows for the determination of the total number of structures of interest (*e.g.,* adipocytes) without prior estimation of the numerical volume density and thus is independent of tissue shrinkage [21, 309].

The major advantage of unbiased quantitative stereological analysis is the ability to accurately estimate relevant morphological cell parameters. However, the application of these methods remains complex and time intense. Due to the strict sampling design stereological methods cannot be applied retrospectively, *i.e.*, if the tissue of interest has already been sampled in another way, and therefore require detailed planning beforehand [23, 28, 297].

Design-based quantitative stereological analysis methods have already been applied occasionally in adipose tissue research. Cuéllar *et al.* (2005), for example, estimated quantitative stereological parameters (volume density/numerical volume density/mean volume of adipocytes in fat tissue) in biopsies of human fat autografts to analyse their survival rate [26]. In 2006, Aslan *et al.* analysed the effect of a high-fat diet on quantitative parameters of murine omental adipocytes using quantitative stereological analysis methods including the physical disector [27]. In her doctoral thesis, Dr. Lina Nagel (2013) determined the mean adipocyte volume in different fat tissue depots of lean and obese male neutered felines to gain initial insights into possible depot-specific growth patterns that may be related to obesity-associated diseases in cats [310].

5.3.1 Determination of the total volume of adipose tissue depots

A direct method for determining the total volume of adipose tissue depots (*i.e.,* the reference compartment) is to measure the liquid displaced by the submerged adipose tissue (Archimedes' principle) [311]. However, using this method for measuring comparatively large porcine adipose tissue depots is very cumbersome and requires correspondingly large experimental equipment [283]. Furthermore, this method requires a very precise preparation, as any structures/tissues that are not adipose tissue will falsify the measurement result [28].

More conveniently, the total volume of adipose tissue depots can be determined by means of the respective weight and density of the fat tissue [28, 303, 311]. The latter can be determined using the submersion method described by Scherle in 1970, which is based on the liquid displacement of a submerged sample (Archimedes' principle) [311]. The adipose tissue density is calculated from the weight of the submerged fat tissue sample and its volume, which is again calculated from the weight of the liquid displaced by the submerged tissue and its density [28, 303, 311]. Similar to direct volumetry via Archimedes' principle, this method also requires very precise preparation in order to prevent falsification of the measurement results [28].

A stereological approach to determine total adipose tissue depot volumes is the Cavalieri principle [28, 283, 303]. The adipose tissue depot is sectioned exhaustively in parallel equidistant (*i.e.,* equal section thickness *t*) serial sections starting at random point in the first interval of *t*. Subsequently, each adipose tissue slab is consistently placed on the same side (*i.e.,* all on left or right side) and the area of

each section profile is measured by point counting, *i.e.,* by superimposing a cross-grid and counting the points hitting the section profile of the adipose tissue slabs (each point is associated with an area, which is defined by the size of the grid and the number of crosses). The estimated total adipose tissue depot volume is calculated by multiplying the sum of the section profile areas with the mean thickness of the fat tissue slabs [28, 283]. The Cavalieri principle is also applicable to CT/MRI sectional images of fat tissue depots [303].

5.3.2 Determination of embedding-related tissue shrinkage

When processing tissue samples for histological examination (and for LSFM analysis, see **Chapter 5.4.2**), tissue shrinkage may occur, particularly due to fixation and embedding (*i.e.,* embedding-related tissue shrinkage), the extent of which can be expressed as linear tissue shrinkage factor f_s [282, 283, 298].

To determine the extent of tissue shrinkage occurring during fixation of the sample, the volume of the sample before and after fixation can be measured by Archimedes' principle (see **Chapter 5.3.1**) [312].

For estimation of embedding-related tissue shrinkage, the area of the section surface is determined before and again after embedding of the tissue sample by point counting (see **Chapter 5.3.1**) or planimetric measurements (see **Supplemental Figure S3** of publication). It is important to measure the first complete tissue section possible, *i.e.,* as soon as the tissue border is completely visible, since the sample might change its shape further into sectioning [283, 300]. Alternatively, the volume of the sample prior and post embedding can be determined by the weight and density of the sample, and the principle of Cavalieri, respectively (see **Chapter 5.3.1**) [34, 300]. This is especially useful, when determination of section areas prior embedding is not possible due to the architecture of the sample, as it applies to fish gills for example [34].

The linear tissue shrinkage factor is calculated from the section profile areas respectively volumes of the tissue samples after embedding and the corresponding section profile areas respectively volumes of the same tissue samples before embedding [283, 299].

5.3.3 Determination of volume density and total volume of adipocytes in adipose tissue depots

The volume density and the deduced total volume of adipocytes in adipose tissue depots can be estimated from the fractional area density of fat cell section profile areas and the section area of the tissue sample in representative SUR-sampled specimen (principle of Delesse) [21, 313]. The volume density of adipocytes in the respective adipose tissue depot can efficiently be determined by point counting using adequately spaced cross grids superimposed on the respective sections. The total volume of adipocytes in the adipose tissue depot is calculated by multiplying the volume density of adipocytes in the respective adipose tissue depot with the total volume of the fat depot (see **Supplemental Figure S2** of publication) [23]. Since the volume density is a dimensionless parameter it is therefore independent of embedding-related tissue shrinkage and can conveniently be estimated using standard paraffin sections, as well as in cryo-sections (given a presumed equal shrinkage of adipocytes and non-adipocyte tissue compartments, *i.e.,* no differential shrinkage) [282, 298].

5.3.4 Determination of numerical volume density and total number of adipocytes in adipose tissue depots

The numerical volume density and the deduced total number of adipocytes in adipose tissue depots have to be estimated in a three-dimensional test system, such as the disector, since the dimensions of the parameter (number = 0) and the probe (volume = 3) used must add up to at least three [23, 314]. In the physical disector, two consecutive parallel (physically separate) sections (reference and look up section) and an unbiased counting frame form the three-dimensional test field. For generation of thin serial sections with constant section thickness, plastic resin is the embedding medium of choice, avoiding the irregular and inconsistent tissue shrinkage occurring during paraffin embedding and enabling for exact measurement of factual section thickness [20, 282, 315]. Additionally, thinner sections can be achieved compared to paraffin embedding, which reduces bias due to overprojection (“Holmes effect”) and allows for physical disectors with low disector heights to quantify small objects, such as cell nuclei [20, 285, 315]. To estimate the numerical volume density of adipocytes in the respective fat tissue depot and following this determine the absolute numbers of adipocytes in the respective adipose tissue depot, a counting frame of known area is superimposed at random

on SUR-sampled fields of view (FOV) in the reference section and unique tissue structures (*e.g.,* adipocyte nuclei), which appear here but not in the corresponding FOV in the look up section are counted (*Q*-) (see **Figure 6** of publication). This ensures that every particle is counted only once and prevents overrepresentation of (large) cells [23, 309]. To double the efficiency, the counting process can be repeated with interchanged roles of the reference- and look-up section [309, 316]. Dividing the counted number of adipocyte nuclei with the disector volume provides an estimate of the numerical volume density of adipocytes in the respective adipose tissue depot, which subsequently must be corrected for embedding-related tissue shrinkage (see **Chapter 5.3.2**) [21, 23, 298, 309]. The disector volume is calculated by multiplying the area of the adipose tissue (*i.e.,* reference compartment) superimposed by the counting frame (determined by point counting) with the disector height *h* (*i.e.,* distance between the reference and look up section) [21, 23, 309]. The latter should be less than the height of the object to be counted and is considered optimal at around $^1/_3$ to $^1/_4$ of the linear orthogonal projection of the counted particles [20, 314, 315]. The knowledge of the factual section thickness is essential for the determination of the disector height and thus the accuracy of the physical disector, as it often deviates from the nominal section thickness (*i.e.,* the section thickness set at the microtome). The factual section thickness can be determined by orthogonal re-embedding [317-319] or, more practicable, by spectral reflectance measurement [315]. The total number of adipocytes in the adipose tissue depot is determined by multiplying the numerical volume density of the adipocytes in the respective adipose tissue depot with the total volume of the reference compartment (*i.e.,* the total volume of the fat depot) [21, 23, 309].

The optical disector is based on the same principle. However, instead of using two physically separate sections, a thin focal plane (< 1 µm) is moved a known distance (*i.e.,* disector height) through one thick section and particles, such as cell nuclei, are counted as soon as they come into focus [23, 309]. The use of a single section entails that neither elaborate serial sections nor a laborious search for corresponding fields of view in the look up section are necessary, making the method fast and easy to use. Additionally, the higher section thickness allows the three-dimensional cell structure to be viewed. However, with increasing section thickness a complete stain penetration, required to clearly identify the tissue components, becomes more difficult [23]. Since part of the cells can be extracted

during sectioning (known as “lost caps”), guard zones at the top and bottom of the section have to be excluded from analysis [23, 282, 320].

The physical/optical disector method is often combined with fractionator sampling (also known as physical/optical fractionator), which allows for a direct determination of the number of structures in the reference compartment (*i.e.,* without prior determination of the numerical volume density) independent of embedding-related tissue shrinkage and section thickness [23, 309, 315, 321]. Here, the total number of the structure of interest is determined in a sample with known sample fraction and subsequently multiplied by the inverse of the sampling fraction to estimate the total number of the structure of interest in the reference compartment (*i.e.,* determination of the volume of the reference compartment is not necessary) [23, 309, 321].

5.3.5 Determination of mean adipocyte volumes

The mean volume of adipocytes in an adipose tissue depot can be calculated by dividing the volume density of adipocytes in the respective adipose tissue depot by the shrinkage corrected numerical volume density of the adipocytes in the adipose tissue depot.

The point sampled intercept estimator can be used to directly estimate the volume weighted (*i.e.,* the probability of a cell being sampled depends on its volume) mean volume in single IUR or VUR sections (*i.e.,* no disector is required). Isotropic lines with uniform random points are superimposed on the tissue sections and cells hit by a point are sampled. Subsequently, the distance between the two intersections of the line passing through that point and the cell boundary is determined and used to calculate the mean volume [20, 21, 321].

Further unbiased quantitative stereological estimators for mean particle volume, such as the nucleator and the planar rotator, are described in detail elsewhere [322, 323].

5.3.6 Determination of individual adipocyte volumes

The determination of individual adipocyte volumes can be performed following the principle of Cavalieri [20, 21, 301]. The embedded adipose tissue sample is sectioned exhaustively in parallel equidistant serial sections starting at random point in the first interval of *t*. Subsequently, section profile areas of a previously sampled individual adipocyte are measured by superimposing a cross-grid and counting the

points hitting the section profile of the adipocyte or by planimetric measurements. The evaluation of 10 to 15 sections is sufficient for accurate estimation of the individual volume. The individual adipocyte volume is calculated by multiplying the sum of the section profile areas with the average distance between them (*i.e.,* section thickness times section interval) [20, 21, 23, 301]. A major drawback of this method is the requirement of a large number of serial sections, especially when analysing large cells, such as adipocytes. Additionally, the identification and analysis of each adipocyte section profile is quite cumbersome.

Another way to determine individual cell volumes is the optical vertical/isotropic rotator [20, 324]. This method is performed on either vertical or isotropic sections and the cells are sampled using the optical disector [309, 324]. The estimate is based on intersections between a 3D line grid and the boundary of the cell [324]. For more detailed information the interested reader is referred to Tandrup *et al.* (1997) [324]. A major advantage of this method is the possibility to obtain the size distribution of the examined cells [20].

5.4 Light sheet fluorescence microscopy (LSFM) of optically cleared adipose tissue samples

Laser light sheet fluorescence microscopy (LSFM) is a deep tissue imaging technique which is usually performed on optically cleared tissue samples without physical sectioning, allowing also for whole organ imaging [31]. It provides the opportunity to three-dimensionally visualize functional structures in their biological environment [325]. Optical tissue clearing reduces the impairment caused by strong light absorption and scattering occurring in such thick tissue samples. By means of different processing steps, the refractive index (RI, dimensionless number that describes the ratio of the wavelength of light in a vacuum to the wavelength of light in the respective material/medium and is dependent on the frequency of the light [326]) of the tissue and that of the surrounding medium are homogenized, rendering the sample clear (see **Chapter 5.4.1**). Afterwards a thin light sheet of adjustable wavelength illuminates the sample from the side, whereupon fluorescent signals emerge from the sample (*e.g.,* autofluorescence, fluorescence labelled antibodies) and are captured by a digital camera (see **Chapter 5.4.2**). In contrast to other fluorescence-based optical section methods, such as confocal laser scanning microscopy (CLSM) or two-photon microscopy (2PM), which provide only a very

limited FOV, in LSFM the entire (optical) section plane is available [31]. Besides generating digital 2D sections with high imaging rates, LSFM also allows for a digital three-dimensional reconstruction of the sample with micrometre resolution [30]. Originally invented by Siedentopf and Zsigmondy in 1903 [327] for the visualization and size determination of gold particles, light sheet microscopy has been undergoing several technical developments in the past decades and LSFM now makes it possible to gain a better understanding of the tissue morphology and address questions, that can only be solved in comprehensive 3D-images of relevant functional structures, organs or intact specimens [31, 327]. For example, Chi *et al.* (2018) used LSFM imaging and digital image analysis to study beige adipose tissue biogenesis and quantify the sympathetic neurite density in murine subcutaneous and visceral adipose tissue depots [328]. Furthermore, in 2020, Kennel *et al.* performed a 3D reconstruction of the entire vascular network inside inguinal fat pads of C57BL/6J mice using LSFM [32]. Most recently, Geng *et al.* (2021) combined laser light sheet fluorescence microscopy and deep learning (*i.e.,* convolutional neural network, CNN) to identify and analyse macrophage microenvironment in crown-like structures in reconstructed 3D images of VAT of lean and obese C57BL/6 mice. The CNN was used for identification and segmentation of CLS in the 3D images, whereas their size and number were determined using a digital image analysis software [329].

5.4.1 Optical tissue clearing

The opaque structure of almost every biological tissue is a limiting factor in microscopy in general, especially in deep-tissue imaging. The various tissue constituents absorb (*e.g.,* haemoglobin and myoglobin) and scatter (*e.g.,* fibres with high refractive index surrounded by interstitial fluid with low refractive index) the light impinging on the sample, which leads to a reduced light penetration and following this a limited imaging depth [31, 325]. Both effects occur simultaneously and are depending on the wavelength. Although a near-infrared (NIR) wavelength can reduce absorption and scattering of light, optical tissue clearing is far more effective, rendering a large specimen highly transparent. This makes a combination of LSFM and tissue clearing methods inevitable. The basic principle in the various clearing protocols is to remove interfering tissue constituents, homogenize the refractive index and thereby preserve the three-dimensional tissue structure as well as already

present fluorophores [31]. There exist a variety of different tissue clearing protocols, which can be divided into three groups.

The organic solvent-based clearing methods require an initial dehydration and lipid solvation, followed by a RI adjustment using an organic clearing agent with approximately the same RI as the treated tissue [31, 326]. No specific clearing device is needed, and the tissue must be *ex vivo* immunolabeled ahead of clearing [31]. Examples of this group are the BABB (benzyl alcohol/benzyl benzoate) [330] protocol and a modified version of it, the 3DISCO (3D imaging of solvent-cleared organs) [325, 331-333] protocol [31]. The latter leads to an improved tissue transparency and a better preservation of fluorescent proteins. Since most of these proteins require an aqueous medium to continue to fluoresce, samples whose endogenous fluorescence needs to be visualized must be imaged quickly due to the dehydration step [31]. The protocols are easy to use, simple to reproduce, can be combined with various labelling methods (*e.g.,* transgenic expression of fluorophores or antibody labelling) and has been successfully applied to various rodent organs [31, 332]. Disadvantages of these protocols are the high toxicity of some of the solvents, a considerable degree of clearing-associated tissue shrinkage during the dehydration (see **Chapter 5.4.2**), and the possible quenching of signals from fluorescent proteins [326, 334, 335].

The second group are the aqueous-based clearing methods. The aqueous phase of the sample is replaced with water-soluble compounds (*e.g.,* fructose) whose RI is above 1.45 to increase the refractive index of the aqueous phase within the tissue [31]. Examples are the FRUIT [336] and SeeDB (see deep brain) [337] protocols [31]. In almost all protocols lipids are preserved, which allows for lipid targeting [31]. Exceptions are Sca*l*e [338] and CUBIC (clear, unobstructed brain imaging cocktails and computational analysis) [339, 340], which use urea and detergents to adjust RI [31]. The application of these protocols is simple, but the degree of transparency is limited [31].

The hydrogel-based protocols represent the third group. Biological tissues are chemically transformed into stable hydrogel tissue hybrids thereby maintaining the protein arrangement. The lipids are removed either passively (*i.e.,* incubation in detergent solution) or actively (*i.e.,* electrophoresis). Since this method does not affect RI, it must be adjusted in a further step [31]. Examples of this group are the

CLARITY (cleared lipid-extracted acryl-hybridized rigid immunostaining/*in situ* hybridization-compatible tissue hydrogel) [341] and PACT (passive clarity technique) [342] protocols [31].

For a comprehensive overview of various clearing methods in terms of the duration of the clearing process, the clearing-associated tissue shrinkage, the possible toxicity of the chemicals used, and the degree of antibody penetration for immunolabelling, the interested reader is referred to the excellent reviews by Gómez-Gaviro *et al.* (2020) [335], Ueda *et al.* (2020) [343], Feuchtinger *et al.* (2016) [31], and Richardson and Lichtman (2015) [326].

5.4.2 Principle of LSFM of optically cleared tissue samples

The LSFM allows for two- and three-dimensional visualization of whole tissue samples up to the size of several cm³. Once the tissue sample is optically cleared (see **Figure 2** of publication), a light sheet of adjustable wavelength illuminates a plane of a few micrometre thickness (~ 5µm) through the entire sample (*i.e.,* the focus plane) [31]. The light sheet is usually generated by a laser (light amplification by stimulated emission of radiation) and a cylindrical lens and illuminates the sample either from one side or from two opposite sides (see **Figure 3** of publication). The latter is especially useful in larger samples, as the overlapping light sheets compensate for the gradual decrease of the laser light [332]. The light excites the fluorophores within the focus plane and the emitting light is detected perpendicular to the illumination axis by a camera and by means of a linked computer system [31]. The lateral image resolution is determined by the numerical aperture (NA) of the imaging objective lens alone. The axial resolution is additionally influenced by the thickness of the light sheet with thinner light sheets improving the axial resolution [344, 345]. Since only the focus plane is illuminated, the photo-bleaching of fluorophores as well as the scattering effect are reduced to a minimum [332]. A pinhole as used in CLSM or 2PM to exclude fluorescence outside the focal plane is therefore not necessary in LSFM [31, 346]. The fluorescence signals can originate from the autofluorescence of the tissue components, from *in vivo* administered fluorescent-labelled substances, the expression of fluorescent reporter molecules or from fluorescence-labelled primary and/or secondary antibodies [31].

By moving the tissue sample through the light sheet along the vertical axis in defined z-increments, a series of section planes, each individually and exclusively illuminated, is generated [31, 332]. This so-called z-stack can be converted into a digital 3D image of the tissue sample via digital 3D reconstruction (including 3D volume rendering) (see **Figures 1** + **4**, and **Supplemental Video S1** of publication). The reconstructed digital 3D image can be viewed and further analysed, using suitable software tools, which can also include tools for morphometric measurements of individual cells based on pixel/voxel analyses [31, 347]. The “magic wand” tool (arivis Vision4D), for example, allows for the rapid analysis of various morphometric cell parameters, such as the individual cell volume and surface area [347].

The precise determination of object volumes (*e.g.,* individual adipocyte volumes) depends on the accurate reconstruction of the 3D image from the z-stacks (*i.e.,* the digital reconstruction must precisely reflect the volume of the imaged object). Variations between the nominal and factual z-step size (*i.e.,* an untrue vertical scaling) and imaging artifacts may cause distortion of object shapes and their corresponding volumes in the reconstructed 3D images [348]. Differences between the refractive indices (RI) of the sample and the surrounding medium (clearing/mounting medium), the RIs of the surrounding medium and the objective (*e.g.,* watery solution and oil immersion objective), as well as between different lens elements inside a fluorescence microscope result in spherical aberration (SA), leading to the aforementioned imaging artifacts [348]. Lens-induced spherical aberration occurs when peripheral and central lens parts do not converge the light at the same point [348]. SA caused by an RI mismatch affects the imaging in three different ways: dim and blurry images due to non-converging of the light rays at the image plane, shifting of the nominal focus position due to refraction of rays increasingly entering from peripherally, and distortion of the z-axis due to non-uniform movement of the objective (or stage) and the focal plane resulting in artificially elongated (RI immersion medium > RI sample) or compressed (RI immersion medium < RI sample) 3D images [348].

Possible shape and volume distortions can be avoided using appropriate technical equipment, such as SA-corrected optical components and precisely adjusted instrument settings (*e.g.,* correct calibration of z-step height). Additionally, the use

of dipping caps for air objectives and immersion media with an RI similar to the RI of the cleared tissue sample prevent the development of SA due to RI-mismatch. If it is not possible to completely avoid an RI-mismatch, the 3D images have to be corrected for axial distortion [348]. For more detailed information on the calculation of correction factors the interested reader is referred to Diel *et al.* (2020) [348].

Additionally, processing-induced alterations of the tissue volume must be considered to obtain unbiased analysis results [28, 282]. For instance, many optical tissue clearing protocols (especially organic solvent-based ones), can cause different extents of tissue shrinkage [326, 349, 350]. 3DISCO clearing, for example, can lead to a considerably large shrinkage of the cleared tissue samples of up to 50% [334]. In contrast, organic solvent-based iDISCO+ (immunolabeling-enabled 3D imaging of solvent-cleared organs) [351] protocol, and the non-toxic solvent-based ECi (ethyl cinnamate) [35] protocol were reported to cause only little tissue shrinkage, whereas organic solvent-based AdipoClear [352] and aqueous-based SeeDB [337] were found to not cause any clearing-associated tissue shrinkage [35, 334, 335, 337, 349, 351]. The extend of tissue shrinkage can be quantified by determining the volume of the samples both before and after the clearing procedure using the submersion method (see **Chapter 5.3.2**) [34, 283, 303, 311]. Subsequently, the corresponding linear tissue shrinkage factor can be estimated and used to correct shrinkage-sensitive quantitative morphological parameters, such as individual cell volumes [283, 298, 299].

The 3D visualization and determination of object volumes and other quantitative parameters via digital image analyses are also influenced by the general handling of the tissue samples, especially in tissues with soft consistency such as adipose tissue. Effects that influence the cell or tissue structure, such as compression or mechanical distortion of the material, should be strictly avoided during the entire course of the experiment (from sample collection to the actual analysis) by generally handling the tissue specimens very carefully.

IV Publication

N. Theobalt, I. Hofmann, S. Fiedler, S. Renner, G. Dhom, A. Feuchtinger, A. Walch, M. Hrabě de Angelis, E. Wolf, R. Wanke, A. Blutke (2021). Unbiased analysis of obesity related, fat depot specific changes of adipocyte volumes and numbers using light sheet fluorescence microscopy. PLoS One, 16(3):e0248594

The numeration of the sections in the following publication is independent of the chapter order in this thesis.

PLOS ONE

RESEARCH ARTICLE

Unbiased analysis of obesity related, fat depot specific changes of adipocyte volumes and numbers using light sheet fluorescence microscopy

Natalie Theobalt[1], Isabel Hofmann[1¤a], Sonja Fiedler[1], Simone Renner[2,3,4], Georg Dhom[2,3¤b], Annette Feuchtinger[5], Axel Walch[5], Martin Hrabě de Angelis[4,6], Eckhard Wolf[2,3,4,7], Rüdiger Wanke[1], Andreas Blutke[5¤c]*

1 Institute of Veterinary Pathology at the Center for Clinical Veterinary Medicine, Ludwig-Maximilians-Universität München, Munich, Germany, **2** Gene Center and Department of Veterinary Sciences, Chair for Molecular Animal Breeding and Biotechnology, Ludwig-Maximilians-Universität München, Munich, Germany, **3** Department of Veterinary Sciences, Center for Innovative Medical Models (CiMM), Ludwig-Maximilians-Universität München, Oberschleißheim, Germany, **4** German Center for Diabetes Research (DZD), Neuherberg, Germany, **5** Research Unit Analytical Pathology, Helmholtz Zentrum München, Neuherberg, Germany, **6** Institute of Experimental Genetics, Helmholtz Zentrum München, Neuherberg, Germany, **7** Laboratory for Functional Genome Analysis (LAFUGA), Gene Center, Ludwig-Maximilians-Universität München, Munich, Germany

¤a Current address: Bavarian Health and Food Safety Authority, Oberschleißheim, Germany
¤b Current address: Bavarian Food Safety and Veterinary Control Authority (KBLV), Oberding, Germany
¤c Current address: Institute of Experimental Genetics, Helmholtz Zentrum München, Neuherberg, Germany
* andreas.parzefall@helmholtz-muenchen.de

OPEN ACCESS

Citation: Theobalt N, Hofmann I, Fiedler S, Renner S, Dhom G, Feuchtinger A, et al. (2021) Unbiased analysis of obesity related, fat depot specific changes of adipocyte volumes and numbers using light sheet fluorescence microscopy. PLoS ONE 16(3): e0248594. https://doi.org/10.1371/journal.pone.0248594

Editor: Konradin Metze, University of Campinas, BRAZIL

Received: November 12, 2020

Accepted: March 1, 2021

Published: March 16, 2021

Data Availability Statement: The data underlying this study is available on Dryad (doi:10.5061/dryad.8gtht76nt).

Funding: NT, IH, and SF receive a PhD-stipend of the Hanns-Seidel-Stiftung e.V., Munich, Germany. The funders had no role in study design, data collection and analysis, decision to publish, or preparation of the manuscript.

Competing interests: The authors have declared that no competing interests exist.

Abstract

In translational obesity research, objective assessment of adipocyte sizes and numbers is essential to characterize histomorphological alterations linked to obesity, and to evaluate the efficacies of experimental medicinal or dietetic interventions. Design-based quantitative stereological techniques based on the analysis of 2D-histological sections provide unbiased estimates of relevant 3D-parameters of adipocyte morphology, but often involve complex and time-consuming tissue processing and analysis steps. Here we report the application of direct 3D light sheet fluorescence microscopy (LSFM) for effective and accurate analysis of adipocyte volumes and numbers in optically cleared adipose tissue samples from a porcine model of diet-induced obesity (DIO). Subcutaneous and visceral adipose tissue samples from DIO-minipigs and lean controls were systematically randomly sampled, optically cleared with 3DISCO (3-dimensional imaging of solvent cleared organs), stained with eosin, and subjected to LSFM for detection of adipocyte cell membrane autofluorescence. Individual adipocytes were unbiasedly sampled in digital 3D reconstructions of the adipose tissue samples, and their individual cell volumes were directly measured by automated digital image analysis. Adipocyte numbers and mean volumes obtained by LSFM analysis did not significantly differ from the corresponding values obtained by unbiased quantitative stereological analysis techniques performed on the same samples, thus proving the applicability of LSFM for efficient analysis of relevant morphological adipocyte parameters. The results of the present study demonstrate an adipose tissue depot specific plasticity of adipocyte

growth responses to nutrient oversupply. This was characterized by an exclusively hypertrophic growth of visceral adipocytes, whereas adipocytes in subcutaneous fat tissue depots also displayed a marked (hyperplastic) increase in cell number. LSFM allows for accurate and efficient determination of relevant quantitative morphological adipocyte parameters. The applied stereological methods and LSFM protocols are described in detail and can serve as a guideline for unbiased quantitative morphological analyses of adipocytes in other studies and species.

Introduction

Worldwide, the prevalence of obesity and its sequelae, such as the metabolic syndrome (MetS), is constantly rising [1]. Particularly visceral adiposity and the development of an associated local and systemic inflammatory response are key determinants in the pathogenesis of the human MetS [2,3]. In translational research, various experimental obesity models of different species are used to study obesity related metabolic derangements and their role in the pathogenesis of adiposity related diseases [4]. In addition to "classic" rodent models of adiposity, also diverse large animal models (LAM) are increasingly used due to their physiological and metabolic similarities to humans [4,5]. Göttingen minipigs (GM) with diet induced obesity (DIO) exhibit severe subcutaneous and visceral adiposity, diverse metabolic dysregulations, such as disturbed glucose tolerance, and develop manifest histopathological adipose tissue inflammation, which is restricted to the visceral adipose tissue [6]. Understanding of the pathogenesis-relevant processes in the adipose tissue during development of obesity and the MetS requires a joint consideration of histomorphological changes, such as adipocyte hypertrophy/hyperplasia and alterations of the cellular tissue composition due to infiltration of inflammatory cells, as well as associated molecular alterations, such as differential abundances of inflammatory cytokines and lipokines in the adipose tissue. Relevant morphological changes of adipocytes in developing or manifest obesity are best characterized by unbiased quantitative analyses of the number, the volume, and the mean volume of adipocytes in a defined adipose tissue depot. These parameters allow for an objective identification, definition, and comparison of already subtle quantitative morphological alterations of cells [7–9], such as adipocytes, *e.g.*, by differentiation of hyperplastic and hypertrophic adipocyte growth patterns [10,11]. Quantitative parameters of adipocyte morphology can thus also help to interpret the results of *e.g.*, lipidomic, transcriptomic, proteomic, or metabolomic profiling analyses of adipose tissue samples [12]. A thorough analysis of obesity related changes in adipose tissue samples should therefore also include quantitative morphological analyses. The generally accepted "gold-standard" for quantitative morphological analyses in histological tissue sections are so-called "unbiased quantitative stereological" analysis methods, combined with (systematic) random sampling methods [13,14]. Unbiased quantitative stereological analyses are capable to provide assumption-free, accurate and precise estimates of quantitative morphological parameters (*i.e.*, volumes, surfaces, lengths, numbers) of the examined tissue structures of interest with known error probabilities by analysis of adequately sampled and oriented histological sections, using appropriate stereological probes [7–9,15,16]. In various biomedical research disciplines, such as neurosciences or nephrology, unbiased quantitative stereological analysis methods have become an indispensable component in studies involving quantitative analyses of histomorphological tissue features [13,17,18]. However, application of unbiased quantitative stereological methods is often regarded quite time consuming and cumbersome, since these methods

usually require the observance of strict sampling designs and often use special histotechniques, such as plastic embedding and preparation of thin sections [16].

Here, we report the application of 3D light sheet florescence microscopy (LSFM) of optically cleared adipose tissue samples as a simple, fast and elegant approach to characterize the relevant quantitative changes of adipose tissue and adipocyte morphology in different adipose tissue depots of the DIO minipig model. LSFM of optically cleared tissue specimen is a rapidly evolving imaging technique [19–21], allowing for direct 3D imaging of cellular details in tissue samples up to the size of several cm^3, *e.g.*, to visualize complex vascularization patterns of organs, tumor samples [22,23], or adipose tissue depots [24]. For LSFM, the tissue specimens are cleared, *i.e.*, made optically transparent, using a variety of different possible methods and protocols. The cleared samples are then directly (without physically sectioning) imaged in 3D, using a laser light sheet fluorescence microscope. Here, a light sheet of defined laser light wavelength is generated, which illuminates a few microns thin plane of the sample. Fluorescent signals induced within this tissue plane, either by autofluorescence of distinct tissue structures, or by fluorescent marker molecules introduced into the tissue (*e.g.*, by transgene expression of fluorescent molecules, fluorescence labelled antibodies, lectins or exogenously administered substances), are captured by a camera. As the sample moves through the light sheet, parallel optical fluorescence images are captured, corresponding to the position of the light sheet in the sample. The resulting image stack can be computed to create a digital volume rendered 3D reconstruction of the sample that can be viewed, virtually rotated and sectioned in all three dimensions of space, using appropriate software programs, which may also include tools for digital morphometric image analysis in 3D [20]. **Fig 1** shows a schematic illustration of the LSFM technique for examination of cleared adipose tissue samples. Comprehensive descriptions of the LSFM principle, different clearing methods and applications of LSFM are provided in the pertinent literature [19–21,23,25,26]. In translational obesity research, LSFM has already proven its practicability for 3D imaging of adipose tissue, as well as for the visualization of sympathetic innervation, vascular networks, or inflammatory foci in cleared (murine) adipose tissue samples, using specific fluorescence labelled antibodies or lectins [24,27]. The swift and direct visualization of 3D tissue structures by LSFM, and the direct measurability of morphological features of these structures by digital 3D-image analysis could also efficiently simplify analyses of adipocyte volumes and numbers, which can, so far, only be determined unbiasedly using comparably elaborate and time-consuming quantitative stereological analysis methods. The present study was designed to evaluate the suitability of LSFM-based quantitative morphological analyses to provide accurate (*i.e.*, precise and unbiased) measures of adipocyte volumes and numbers for characterization of obesity-related alterations of adipocyte growth patterns in different adipose tissue depots of the Göttingen minipig DIO model. To prove the accuracy of the LSFM-analysis results, unbiased quantitative stereological analyses were independently performed on representative samples taken from the same animals and adipose tissue depots. The described methods may serve as a guideline for unbiased quantitative morphological analyses of adipose tissue in future studies involving different translational obesity models and experimental animal species, as well as for examination of human adipose tissue specimens.

Materials and methods

Experimental design

Key determinant quantitative morphological parameters of adipocytes (**Table 1**) in subcutaneous (s.c.) and visceral (visc.) adipose tissue depots were determined in obese DIO minipigs and lean control animals, using unbiased quantitative stereological analysis methods, as well as

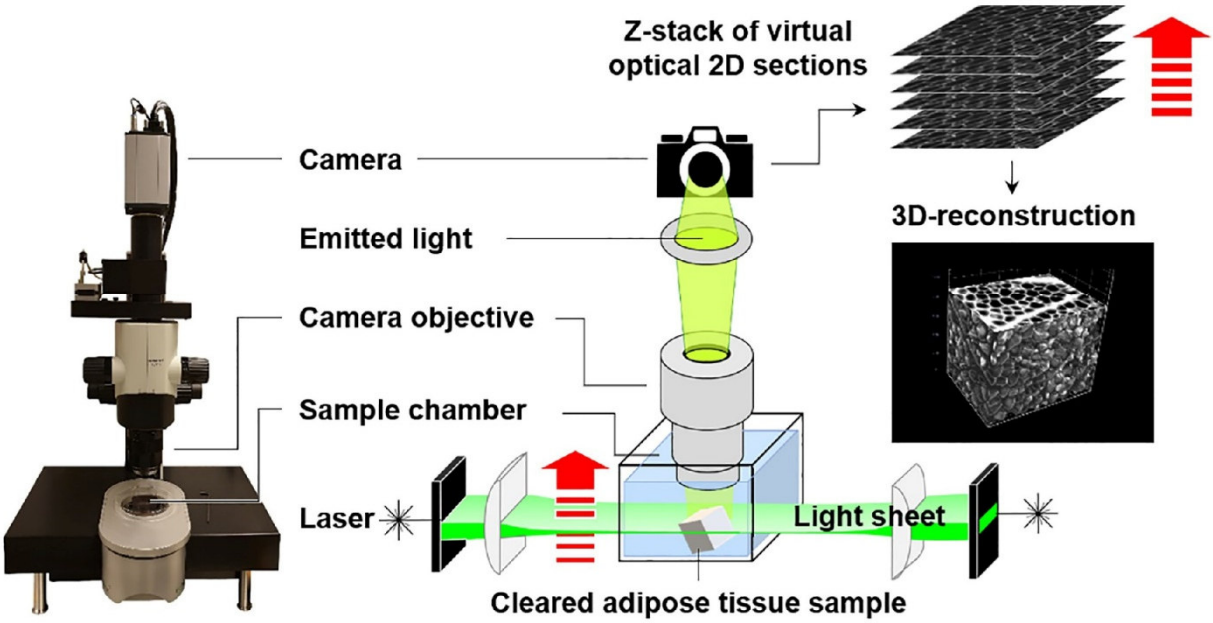

Fig 1. LSFM analysis of cleared adipose tissue samples. An optically cleared adipose tissue sample is placed in the sample chamber of the laser light sheet microscope. A laser light sheet (green) of specific wavelength illuminates the in-focus plane either from one or both sides of the sample. This excites fluorophores within the tissue sample (here: autofluorescence of adipocyte cell membranes) and the emitting light is detected perpendicular to the illumination axis by a digital camera. By moving the sample stepwise (step size: 5 μm) along the vertical axis (red arrow) a series of optical section fluorescence images (z-stack) is acquired, that is used to compute a volume rendered 3D image reconstruction of the adipose tissue sample.

https://doi.org/10.1371/journal.pone.0248594.g001

light sheet fluorescence microscopy (LSFM) based analyses of optically cleared adipose tissue samples. All quantitative morphological analyses were performed on representative adipose tissue samples, generated by systematic uniform random (SUR) sampling [8,28]. The volume densities and the total volumes of adipocytes in the adipose tissue were determined in hematoxylin and eosin (HE) stained standard paraffin sections and calculated from the fractional areas of adipocyte cross section profiles within adipose tissue sections and the total volume of the respective adipose tissue depots [8].

For LSFM-based quantitative morphological analyses, SUR sampled adipose tissue samples were optically cleared according to an established 3DISCO (3 dimensional imaging of solvent cleared organs) protocol [25] and post-stained with eosin to enhance the autofluorescence signal intensity of (adipocyte) cell membranes for LSFM. 2D optical fluorescence image stacks of the cleared samples acquired by LSFM were computed to digital 3D reconstructions of the

Table 1. Analyzed quantitative morphological parameters of adipocytes.

Abbreviation	Parameter
$V_{(ATD)}$	Volume of the adipose tissue depot (ATD)
$V_{V(AC/ATD)}$	Volume density of adipocytes in an adipose tissue depot
$V_{(AC,ATD)}$	Total volume of the adipocytes in an adipose tissue depot
$N_{V(AC/ATD)}$	Numerical volume density of adipocytes in an adipose tissue depot
$N_{(AC,ATD)}$	Total number of adipocytes in an adipose tissue depot
$\bar{v}_{(AC,ATD)}$	Mean volume of adipocytes in an adipose tissue depot
$V_{i(AC,ATD)}$	Individual cell volume of an adipocyte in an adipose tissue depot

https://doi.org/10.1371/journal.pone.0248594.t001

samples, using a standard imaging and analysis software. Quantitative morphological analyses of LSFM images for determination of adipocyte numbers and volumes were performed, using the same stereological probes for unbiased sampling and counting of cells as applied in unbiased quantitative stereological analyses. The numerical volume densities of adipocytes within their corresponding adipose tissue depots were determined, using the disector method [8,29]. The total number of adipocytes per adipose tissue depot was calculated from their numerical volume density and the total volume of the respective adipose tissue depot. Individual adipocyte volumes were directly measured in volume rendered 3D reconstructions of the adipose tissue samples, using automated 3D digital image analysis. The mean cellular adipocyte volumes were calculated from the individual volumes and the number of analyzed adipocytes.

The results of the LSFM-based quantitative morphological analyses were verified by unbiased quantitative stereological analysis techniques, using the physical disector method [8,29] with isotropic uniform random (IUR) sections of plastic embedded SUR adipose tissue samples [8,30–32]. The results of both analysis approaches were statistically compared to evaluate the suitability of LSFM of optically cleared adipose tissue samples for quantitative morphological adipocyte analyses.

Animals

The tissue samples analyzed in the present study were derived from 5 female, ovariectomized, 28 to 30 month old, lean (mean body weight (BW): 46 ± 3 kg) and 6 obese (mean BW: 113 ± 6 kg) Göttingen minipigs. These animals had been euthanized and necropsied in the course of a previously published study on the DIO minipig model [6]. All animal experiments were conducted according to the German Animal Welfare Act and the ARRIVE guidelines and Directive 2010/63/EU, and with approval of the ethics committee of the Government of Upper Bavaria and its permission (permission number: AZ 55.2-1-54-2532-60-2015). Pigs were anesthetized by intramuscular injection of ketamine (Ursotamin, Serumwerke Bernburg, 20 mg/kg BW) and azaperone (Stresnil, Elanco, 2 mg/kg BW) followed by intravenous application of ketamine and xylazine (Xylazin 2%, Serumwerk Bernburg). The animals were then euthanized under anesthesia by intravenous injection of pentobarbital (Release, WDT, at least 450 mg/10 kg BW) and immediately subjected to necropsy.

Volume determination of adipose tissue depots

Two different (white) adipose tissue depots within previously defined anatomical borders [6] were examined, the subcutaneous (s.c.) adipose tissue depot of the back and the visceral (visc.) adipose tissue. The s.c. adipose tissue depot was defined as the subcutaneous adipose tissue covering the dorsal aspect of the back from the first to the last lumbar vertebra, ventrally limited by the plane of the transverse processes of the lumbar vertebrae. The visceral adipose tissue was defined as the subperitoneal adipose tissue attached to the abdominal wall, excluding the omental-, and mesenteric-visceral adipose tissue. At necropsy, these adipose tissue depots were separated mechanically and weighed to the nearest gram. The density of the adipose tissue was determined using the submersion technique, as previously described [6,30,31], and accounted for $\rho = 0.9 \pm 0.02$ g/cm^3 on the average (with no significant differences between different adipose tissue depots in lean and obese pigs). The volumes of the different adipose tissue depots were calculated from their weights and density [6,30,31].

Systematic uniform random (SUR) sampling of adipose tissue specimen

For unbiased quantitative stereological analyses, as well as for LSFM-based quantitative morphological analyses, each 6 representative tissue specimens of approximately 1 cm x 1 cm x 1

cm were systematically uniformly randomly (SUR) sampled from the s.c. and the visc. adipose tissue depots of each pig (S1 Fig), as previously described [6,30]. In the visceral adipose tissue depot, samples were only taken from areas without macroscopically evident inflammatory alterations. The excised tissue samples were fixed in neutrally buffered 4% formaldehyde solution for >12 hours.

Determination of the volume densities and of the total volumes of adipocytes per adipose tissue depot

The formalin-fixed adipose tissue samples destined for unbiased quantitative stereological analyses were bisected. One half of each sample (*i.e.*, 6 s.c. and 6 visc. adipose tissue SUR samples per case) were routinely embedded in paraffin in arbitrary orientation, sectioned and stained with hematoxylin and eosin (HE). The volume density of adipocytes in an adipose tissue depot ($V_{V(AC/ATD)}$) was determined, using the Visiomorph image analysis system with Newcast software (Visiopharm A/S, Denmark). $V_{V(AC/ATD)}$ was calculated as the fractional area of section profiles of adipocytes and the corresponding adipose tissue in 29 ± 5 SUR sampled fields of view at 100x microscopic magnification, using the point counting method (S2 Fig), as described earlier [8,31,33]. Per case, 92 ± 15 points were counted, on the average. The total volume of adipocytes in an adipose tissue depot ($V_{(AC,ATD)}$) was calculated as the product of $V_{V(AC/ATD)}$ and the total volume of the adipose tissue depot ($V_{(ATD)}$).

Sample processing for LSFM-based quantitative morphological analyses

SUR sampled, formalin-fixed adipose tissue specimens were optically cleared (Fig 2), using a slightly modified version of the established 3DISCO protocol [25], with chemicals purchased from Sigma Aldrich, Germany. After washing off the fixation solution in tab water for 2 hours, the samples were processed through series of clearing solutions: 50% tetrahydrofuran (THF, 1h), 50% THF (12h), 70% THF (8h), 80% THF (12h), 100% THF (12h), 100% THF (1h), 100% dichloromethane (DCM, 30 min. until the tissue sample sinks), benzyl alcohol benzyl benzoate (BABB, 10 min.), BABB (20 min.), BABB (30 min). To avoid compression of samples, the samples were placed in individual, sufficiently large containers and cleared in large volumes of the respective clearing solvents (*i.e.*, "free-swimming" samples; tissue-to-solvent ratio approximately 1:20). To increase the autofluorescence signal intensity of adipocyte cell membranes (**Figs 2C and 3**), the cleared tissue samples were then stained with eosin solution (ST Infinity H&E staining system, ref. 3801098, Leica, Germany) for 45 minutes, after rehydrating the samples in a series of 100% isopropyl alcohol (30 min.), and 100%, 96%, 90%, 80%, 70%, 50%

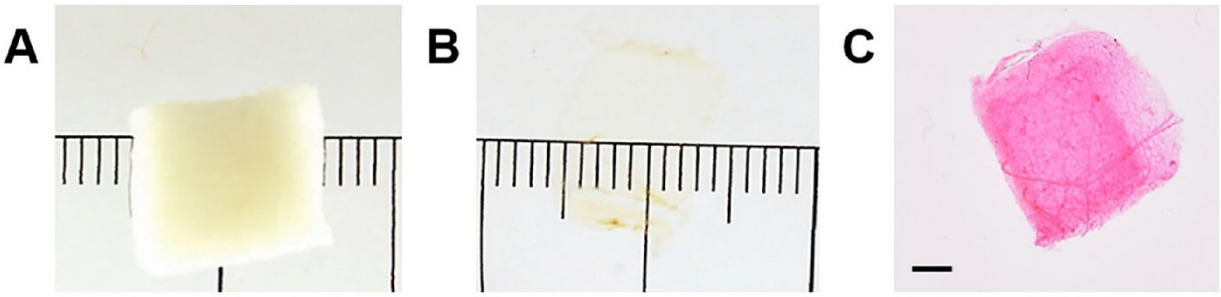

Fig 2. Optical clearing and eosin staining of cleared adipose tissue samples. A. SUR sampled, formalin-fixed adipose tissue sample. **B.** Adipose tissue sample from A after 3DISCO clearing. Note the transparency and the reduced size of the cleared tissue sample, as compared to **A**. **C.** Eosin stained, cleared adipose tissue sample. Bar = 1 mm.

https://doi.org/10.1371/journal.pone.0248594.g002

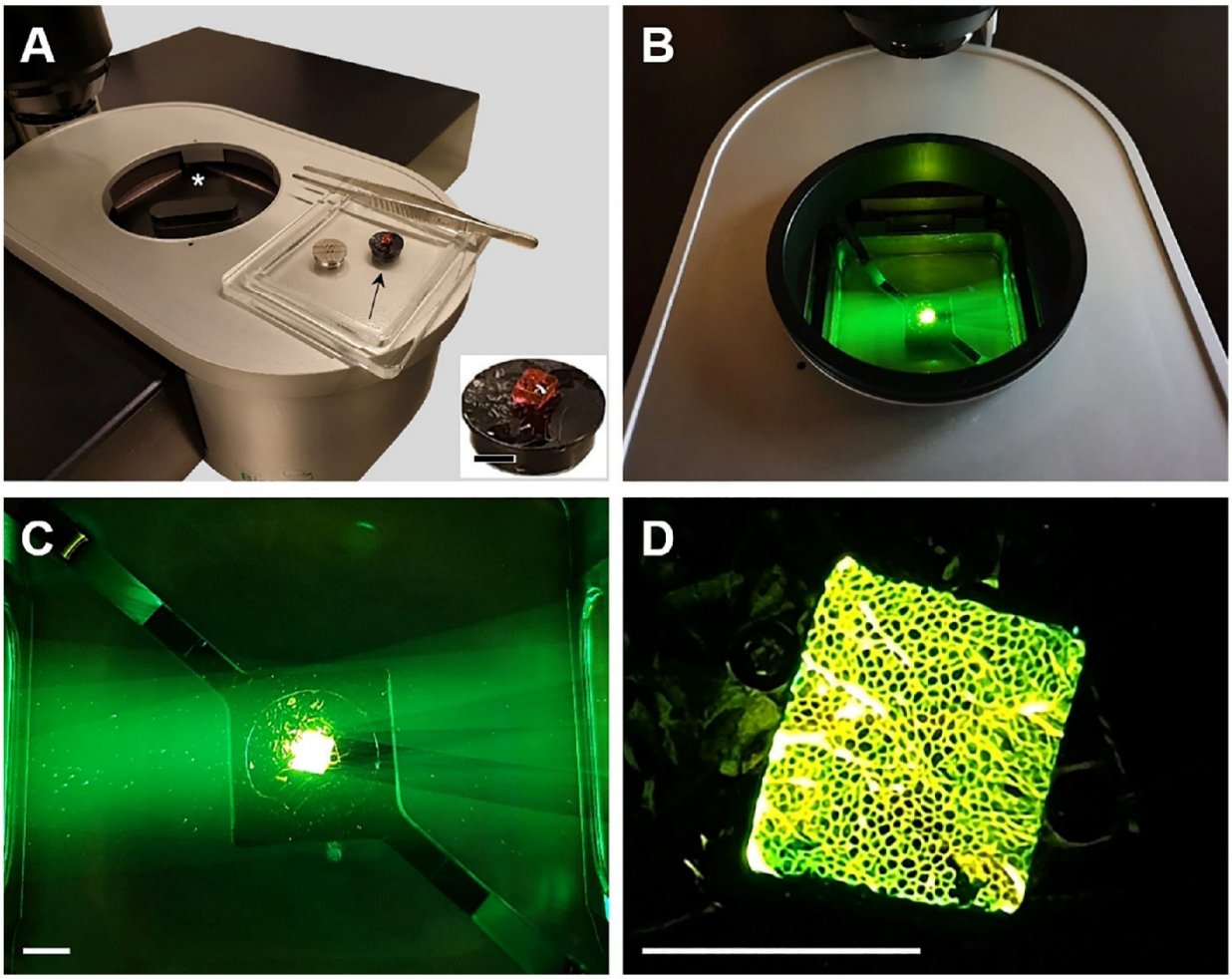

Fig 3. LSFM analysis of 3DISCO cleared, eosin-stained adipose tissue samples. A. Bottom part of the laser light sheet microscope (UltraMicroscope 2, LaVision Biotec). A cleared and eosin-stained adipose tissue sample is mounted on a specimen holder (black arrow). The asterisk marks the sample chamber (closed with a lid). Inset: Detail enlargement of the 3DISCO cleared, eosin-stained adipose tissue sample. **B.** Adipose tissue sample illuminated by a laser light sheet (green light, 520/40 nm) in the sample chamber. **C.** Detail enlargement of **B**. Note the green laser light sheet and the green-yellow autofluorescence of the sample. **D.** Macroscopic picture of the laser illuminated adipose tissue sample. Single adipocytes are already grossly discernible.

https://doi.org/10.1371/journal.pone.0248594.g003

ethanol and tab water (each for 30 min.). The stained adipose tissue samples were rinsed in tab water until the added water remained unstained, and then dehydrated in the same alcohol series applied for rehydration, transferred to BABB, and stored in in BABB in the dark at 4–8˚C until further examination.

The extent of tissue shrinkage associated with the clearing and staining process was calculated from the individual adipose tissue sample volumes of 16 s.c. and visc. adipose tissue samples of lean and obese pigs, determined before and after the clearing/staining procedure, using the submersion technique [30,31,34] with 4% formaldehyde solution (ρ = 1.0165 g/cm^3) or BABB (ρ = 1.0969 g/cm^3) as submersion liquids (at 20˚C).

LSFM and quantitative morphological analyses

For LSFM analysis (**Figs 2–5, S1 Video**), the 3DISCO cleared, eosin-stained adipose tissue samples were examined with an UltraMicroscope II—zoom box configuration (LaVision BioTec GmbH, Germany) with dual side illumination and triple sheet optics on each side generating laser light sheets perpendicular to the direction of detection. The microscope was equipped with a SuperK EXTREME EXW12 white laser (NTK Photonics, Germany) with a wavelength range from 465 to 2400 nm, a 2x objective lens (Olympus MVPLAPO 2X/0.5 NA) combined with an adjusted, custom-made dipping cap (LaVisionBiotec) optimized for liquids with a refractive index of 1.56 ± 0.1, an Olympus MVX-10 zoom body (Olympus, Hamburg, Germany) providing magnification steps from 0.63x to 6.3x, and a Andor Zyla 4.2 Plus sCMOS camera (Oxford Instruments GmbH, Germany). BABB was used as medium. Z-stacks of fluorescence images of 5 μm optical thickness were acquired at 520/40 nm (excitation range) and 585/40 nm (emission range) for detection of autofluorescence (**Fig 4**). With the used objective lens and the applied analysis settings, also a lateral resolution of approximately 5 μm was achieved. 3D volumetric sample reconstruction images (**Fig 4, S1 Video**) were computed, using ImSpector Pro[64] (vers. 5.1.328, LaVision Biotec GmbH, Germany), and arivis Vision4D (vers. 3.0, arivis, Germany) software tools.

For control of the LSFM-image (pixel/voxel-size) scaling and to monitor the realistic rendering of object shapes and volumes in digital 3D-LSFM reconstructions, fluorescently labelled, spherical microbeads (PS-FluoRot 100, batch: PS-FluoRot-Fi274, microParticles GmbH, Germany) with a defined diameter of 99.9 ± 1.8 μm (*i.e.*, similar to the size of adipocytes) were used as control objects. These polystyrene beads are shape- and volume-stable (non-shrinking), resistant to organic and aqueous solvents, have a smooth, non-porous

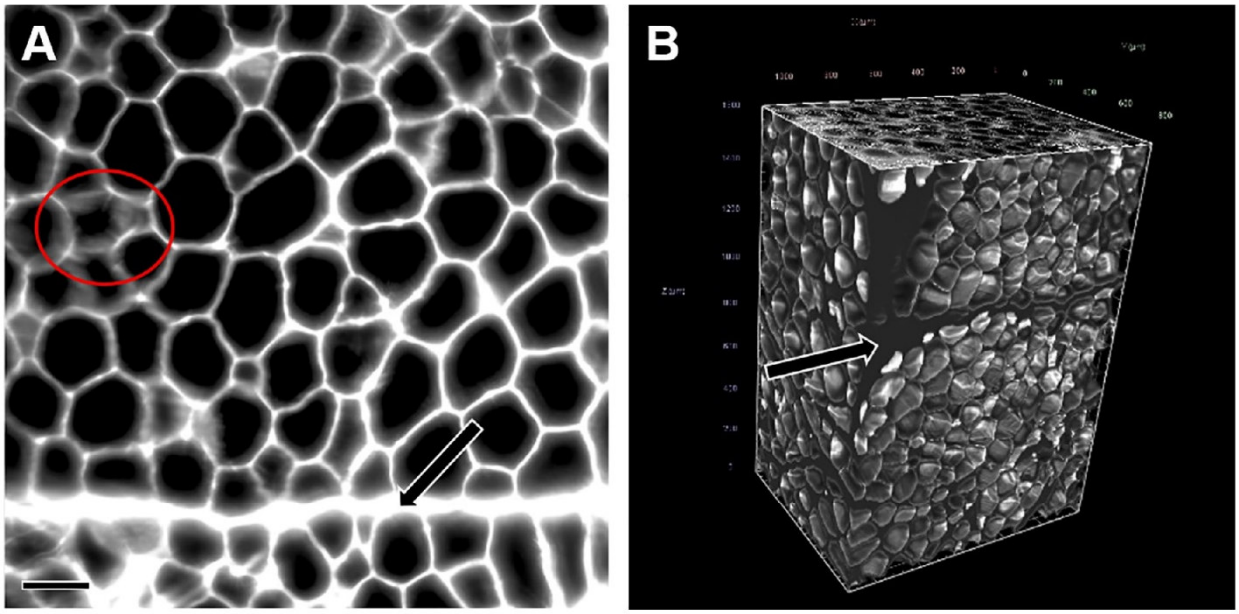

Fig 4. 2D LSFM section image and digital 3D reconstruction of an adipose tissue sample. A. 2D LSFM autofluorescence image from an optical section image stack acquired in a 3DISCO cleared, eosin stained s.c. adipose tissue sample. Autofluorescence signals of adipocyte cell membranes acquired at 585/40 nm (emission range) wavelength (excitation range: 520/40 nm) and are shown in white color. Areas of indistinctly broadened cell membranes (encircled in red) represent tangential sections of cell membranes (adipocyte "tops" or adipocyte "bottoms"). **B.** Digital 3D reconstruction of the s.c. adipose tissue sample, computed from a z-stack of 322 optical section plane images with a step size of 5 μm, containing the image shown in **A**. The 3D reconstruction is freely rotatable and can be virtually sectioned in all directions of space (compare to **S1 Video**). Note the presence of strands of connective tissue traversing through the s.c. adipose tissue sample (arrows in **A** and **B**). Bar = 100 μm.

https://doi.org/10.1371/journal.pone.0248594.g004

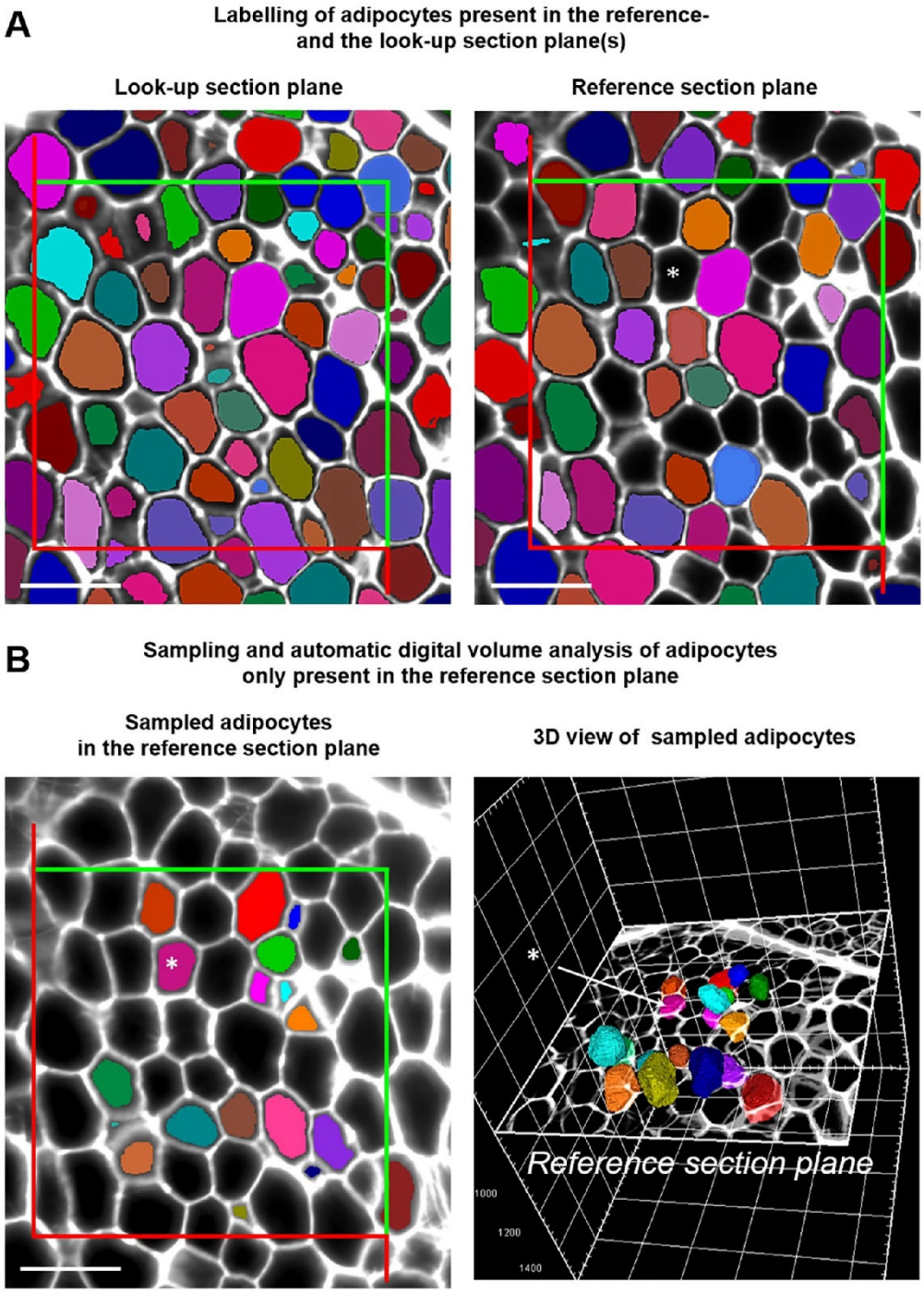

Fig 5. Unbiased number weighted sampling of adipocytes in 3D LSFM image reconstructions of optically cleared adipose tissue samples with the disector for determination of adipocyte numbers and individual adipocyte volumes. A. Randomly sampled 2D optical LSFM autofluorescence image planes (look-up- and reference-section plane) with a defined distance (50 μm). Corresponding fields of view in the look-up section plane and the reference section plane are superimposed with unbiased counting frames. All adipocyte cross section profiles present in the look-up section are marked with the "*Magic Wand*" tool

included in the arivis Vision4D imaging and analysis software and labelled with individual colors. Adipocytes which also occur in the reference section are automatically displayed in the same colors. Section profiles of adipocytes which are sectioned by the reference section plane, but not by the look-up section plane remain unlabelled (black). For illustration purposes, one cross section of an adipocyte that is sectioned by the reference section plane but not by the look-up section plane is highlighted by an asterisk. Adipocytes which are only sectioned by the reference section plane but not by the look-up section plane are than sampled, using unbiased counting frames, *i.e.*, cells are only sampled/counted, if their section profiles are either entirely located within the sampling frame, or if they touch one of the "inclusion" lines (green lines) without touching one of the "exclusion" lines (red). **B**. Disector sampled adipocytes in the 2D reference section plane (left image) and in the 3D LSFM image reconstruction of the adipose tissue sample, virtually sectioned at the level of the disector reference section (right image). The sampled adipocytes are labelled with the "*Magic Wand*" tool, which also calculates the individual adipocyte cell volumes. Individual adipocytes and their corresponding section profiles are shown in corresponding, individual colors. The asterisks mark the same adipocyte as in A. Bars = 200 μm.

https://doi.org/10.1371/journal.pone.0248594.g005

surface, display a refractive index of 1.59 (*i.e.*, similar to the refractive index of BABB (1.56)) and exhibit a red fluorescence at Ex/Em 530nm/607nm. The mean physical ("true") volume of the microbeads (522 ± 28 x10^3 μm^3) was calculated ($V = (4/3)*\pi*r^3$) from their mean diameter and standard deviation (as indicated by the manufacturer and verified by microscopic measurements of 50 randomly selected beads, S4A Fig). For LSFM-imaging, approximately 100 microbeads were immobilized by embedding in a ~0.5 cm^3 cube of agar (Agar-Agar, Kobe I, Carl Roth GmbH & Co KG, Germany). The agar block was fixed in 4% neutrally buffered formaldehyde solution (12 hours) and subsequently processed according to the 3DISCO-clearing protocol described above. The microbead control sample was then imaged and analysed, using the same LSFM-instrument-, image-acquisition-, and analysis-settings, as for analysis of adipose tissue samples. Additionally, the correct calibration of the z-stage drive of the LSFM-instrument was confirmed in regular intervals, using a digital micrometer (RS Components GmbH, Germany). The diameters and volumes of microbeads were measured in the digital LSFM z-stack images and corresponding 3D reconstructions (S4B–S4E Fig) and compared to the "true" physical bead-diameters and -volumes.

For analysis of adipocyte numbers in the adipose tissue depots, the mean adipocyte volumes ($v_{(AC,ATD)}$) and the individual adipocyte volumes ($V_{i(AC,ATD)}$), adipocytes were unbiasedly sampled using the disector method [8,29,35]: from each 2D autofluorescence LSFM image stack, two technically impeccable optical section plane images (a reference section and a look up section) with a distance of 50 μm (*i.e.*, 10 section planes apart) were randomly sampled from the middle third of the image stack. Using the "split screen" function of the arivis Vision4D software, both optical section planes were displayed side by side on the same screen. In both optical section planes, corresponding fields of view were SUR sampled at appropriate magnification. Adipocytes sectioned by the reference section, but absent in the look-up section were identified, using the "*Magic Wand*" tool of the arivis Vision4D software (analysis settings: dark objects, tolerance: 10000), as illustrated in Fig 5. Using unbiased counting frames [7,8,29,36,37] superimposed on the digital images of the corresponding fields of view, 116 ± 23 adipocytes were sampled and counted per adipose tissue depot, on the average. The "*Magic Wand*" tool was also used to directly label individual adipocytes in the volume rendered 3D image reconstruction of the adipose tissue sample, and to measure the individual cell volumes of adipocytes unbiasedly sampled with the disector (based on the number of voxels within the unstained centre of the cell that is completely surrounded by a continuously stained cell membrane). The measured individual adipocyte cell volume values were subsequently corrected for the shrinkage associated with the 3DISCO clearing and eosin staining procedure of the tissue samples. The mean adipocyte volume ($v_{(AC,ATD)}$) was calculated as the mean of the (shrinkage corrected) individual adipocyte volumes measured in all tissue samples from one adipose tissue depot. The total numbers of adipocytes ($N_{(AC,ATD)}$) in the s.c. and visc. adipose tissue depots were calculated from total volume of adipocytes and the corresponding mean adipocyte volume(s).

Verification of LSFM-based quantitative morphological analysis results by unbiased quantitative stereological analyses

For verification of LSFM-based quantitative morphological analysis results, each twelve SUR sampled, formalin-fixed, halved, subcutaneous and visceral adipose tissue samples of lean and obese pigs were randomly sampled and processed for estimation of cell numbers and mean volumes by unbiased quantitative stereological analyses. The adipose tissue samples were processed to generate isotropic uniform random (IUR) sample section planes, using the orientator method, as described previously [6,30–32]. For shape stability and better visual contrast, the fixed adipose tissue samples were encased in ink-blackened agar [30] to avoid mechanical deformation/compression of soft adipose tissue samples during the further processing steps (S3 Fig). The IUR samples were then embedded in glycolmethacrylate/methylmethacrylate (GMA/MMA) plastic embedding medium [38]. From each GMA/MMA embedded tissue block, a series of at least nine consecutive serial sections with a nominal section thickness of 1.00 μm was cut. The factual section thicknesses were measured by spectral reflectometry, as previously described in detail [35] and accounted for 1.34 ± 0.28 μm on the average. The sections were then stained with HE.

The tissue shrinkage associated with the embedding in GMA/MMA was calculated from the quotient of the IUR section plane area of the tissue sample prior to GMA/MMA embedding and the tissue section profile area of the first (complete) section, as described previously (S3 Fig) [31]. On the average, the GMA/MMA embedding related volume shrinkage of adipose tissue samples accounted for 21 ± 0.001%, corresponding to a linear tissue shrinkage factor f_s of 0.93 ± 0.0006. The numerical volume density of adipocytes per adipose tissue depot ($N_{V(AC/ATD)}$) was determined, using the physical disector principle (Fig 6), as described earlier [8,29,35]. From each series of consecutive (nominally) 1 μm thick GMA/MMA sections, two neighboured sections were randomly sampled. In the first section (reference section) 15 ± 8 fields of view were SUR sampled at 200x magnification and superimposed with unbiased counting frames of 300 μm x 300 μm edge length [7,8,29,36,37]. The corresponding section areas in the second section (look-up section) were located, aligned to the reference section, and also superimposed with unbiased counting frames. Using the unbiased counting frames, adipocyte cell nuclei (not adipocytes) were counted (Q^-), if their section profiles were present in the reference section but absent in the look-up section (Fig 6). The counting process was then repeated with interchanged roles of the reference- and look-up sections, thus doubling the efficiency of the counting process. Per adipose tissue depot, 62 ± 12 adipocytes (nuclei) were counted in 242 ± 124 fields of view in 16 ± 3 analyzed pairs of disector sections, on the average. $N_{V(AC/ATD)}$ was then calculated as described in **Eq 1**.

The corresponding coefficients of error (CE) of the numerical volume density estimates, considering the variances originating from the sampling within sections, were calculated as described previously [39] and accounted for 0.1 ±0.01 on the average. The total number of adipocytes in an adipose tissue depot ($N_{(AC,ATD)}$) was calculated as the product of $N_{V(AC/ATD)}$ and $V_{(ATD)}$. The mean volume of adipocytes in an adipose tissue depot ($v_{(AC,ATD)}$) was calculated as the quotient of $V_{V(AC/ATD)}$ / $N_{V(AC/ATD)}$.

Eq 1. Numerical volume density of adipocytes in an adipose tissue depot

$$\mathbf{N_{V(AC/ATD)}} = \left(\frac{\sum \mathbf{Q^-}}{\mathbf{h} * \sum \mathbf{A_{(ATD)}}}\right) * \mathbf{f_s^3}$$

$N_{V(AC/ATD)}$ Numerical volume density of adipocytes (AC) in an adipose tissue depot (ATD).

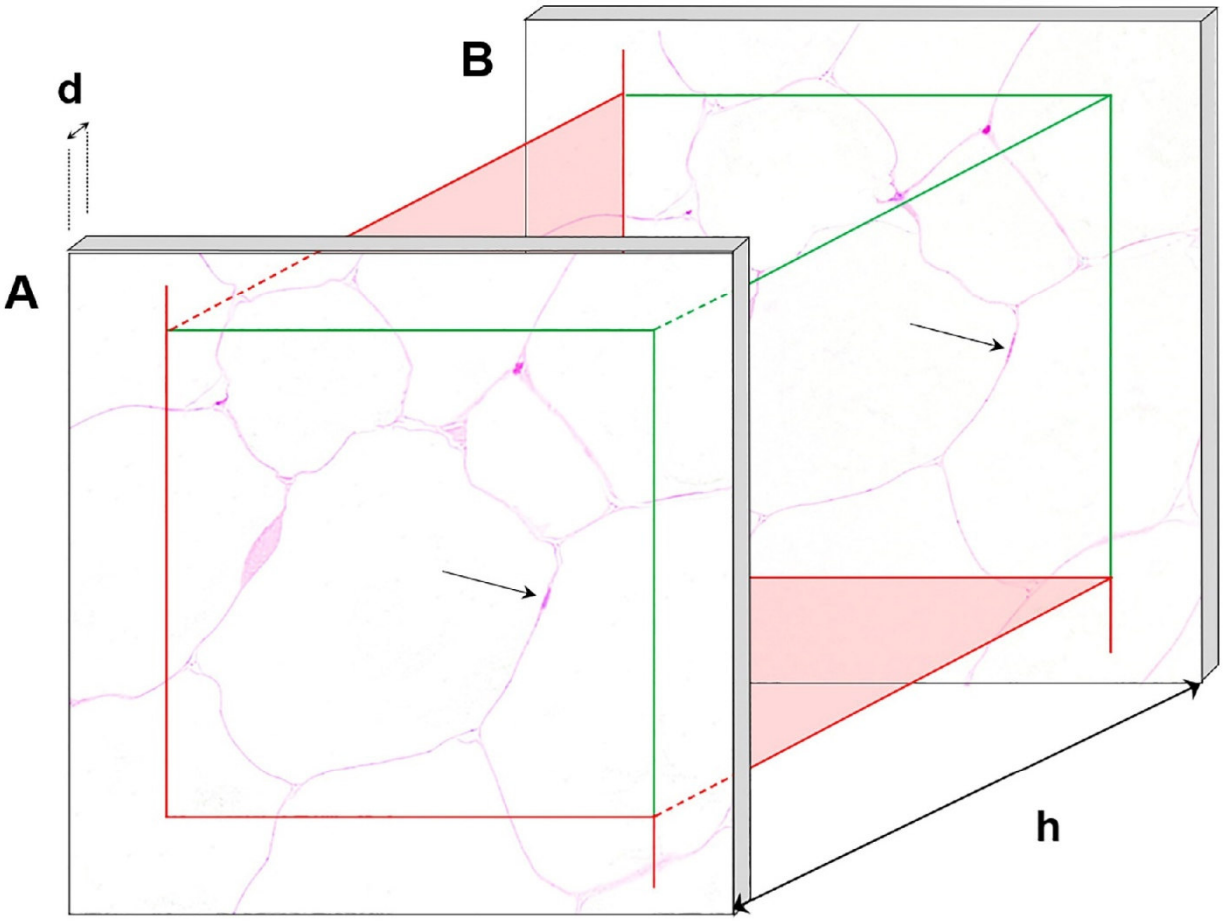

Fig 6. Illustration of the physical disector method for unbiased sampling and counting of adipocytes (nuclei). A physical disector consists of two parallel, corresponding tissue sections (**A**, **B**) of known distance, randomly sampled from a series of consecutive sections. The distance of both sections (*i.e.*, the disector height, h) is defined by the thickness of sections (d), and by the number of sections between them. The aligned (SUR sampled) fields of view are superimposed with unbiased counting frames of known area with exclusion (red) and inclusion lines (green). Thus, a specified tissue volume is defined between both section planes, in which particles, such as cells or cell nuclei, can be unbiasedly sampled and counted independent of their shape, size, or orientation. For analysis of numerical volume densities of (uninuclear) cells, usually cell nuclei are sampled with the physical disector, since they can easily be rediscovered in disector sections with a disector height of approximately one third of the mean minimal nucleus diameter. Using the unbiased counting frames, particles are counted, if they are present within the first (reference) section (**A**) but absent in the second (look-up) section (**B**).

https://doi.org/10.1371/journal.pone.0248594.g006

ΣQ^- Cumulative number of all counted adipocyte cell nuclei (Q^-) in all disectors examined per adipose tissue depot.

h Disector height, *i.e.*, the distance between the reference and the look-up section.

$\Sigma A_{(ATD)}$ Cumulative adipose tissue section area within the unbiased counting frames in all SUR sampled reference section fields of view.

h x $\Sigma A_{(ATD)}$ Cumulative volume of all disectors examined per adipose tissue depot.

f_s Linear tissue shrinkage factor (0.93 for GMA/MMA embedded porcine adipose tissue, and 0.92 for 3DISCO cleared and HE stained porcine adipose tissue).

Histomorphometric measurement of adipocyte cross section profile parameters

In order to also provide histomorphometric measurements of "commonly used" 2D adipocyte section profile parameters, the mean adipocyte section profile-areas, and -(maximal) diameters, as well as the adipocyte section profile-numbers per section area (*i.e.*, the numerical area densities of adipocyte section profiles) were determined in HE-stained IUR-cryo-sections [8,30,32,40] prepared from each three systematically randomly sampled, subcutaneous and visceral adipose tissue samples from 3 lean-, and 3 obese pigs. Per case, an average of 1054 ± 405 adipocyte section profiles were randomly sampled with unbiased counting frames and analyzed using a standard automated image analysis software (Definiens, Germany).

Statistical analyses

Data are presented as means ± standard deviations per group (lean and obese minipigs) and adipose tissue depot (s.c. and visc.). Distribution and variance homogeneity analyses and statistical comparisons between different groups were performed, using GraphPad Prism (version 5.04, GraphPad Software, USA) and Microsoft Excel (Microsoft, USA), with appropriate statistical tests, as indicated.

Results

Total adipocyte volumes in subcutaneous and visceral body fat depots of lean and obese minipigs

The volume densities of adipocytes in the subcutaneous adipose tissue depot ($V_{V/(AC/ATD)}$) did not significantly differ in obese (0.91 ± 0.04%) and lean (0.87 ± 0.04%) minipigs, whereas the volume densities of adipocytes in the visceral adipose tissue depot were significantly increased in obese (0.93 ± 0.02%) *vs*. lean (0.89 ± 0.01%) minipigs.

In both adipose tissue depots, the total adipocyte volume was significantly increased in obese *vs*. lean minipigs, by >860% (s.c.), and by >340% (visc.), respectively (Fig 7A).

LSFM-based quantitative morphological analyses of adipocyte volumes and numbers

LSFM of 3DISCO cleared, eosin-stained adipose tissue samples allowed for an unambiguous autofluorescence detection of continuous adipocyte cell borders and generation of precise 3D sample reconstructions from optical LSFM image stacks, with identification of single adipocytes (**Figs 4 and 5, S1 Video**). The applied clearing/staining procedure was associated with a volume shrinkage of the tissue samples of 21 ± 5.4% (corresponding to a linear tissue shrinkage factor of $f_s = 0.92$) on the average (without significant differences between lean and obese minipigs or s.c. and visc. adipose tissue samples). Using the arivis Vision4D vers. 3.0 imaging and analysis program for generation, viewing, volume rendering, and analysis of 3D tissue sample reconstructions enabled an easy and swift acquisition of individual volumes of adipocytes, unbiasedly sampled with a disector probe.

The correct LSFM-image (pixel/voxel-size) scaling and rendering of object shapes and volumes in digital 3D-LSFM reconstructions was confirmed by imaging and volume analysis of fluorescent microbeads with a defined size comparable to that of adipocytes. In their digital 3D-image reconstructions, the beads appeared as spheres (*i.e.*, retainment of shape, S4 Fig) and the bead volumes determined in their digital 3D-images (534 ± 14 x10^3 μm^3) precisely matched with the "true" bead volumes calculated from their physical diameters (522 ± 28 μm^3), with a mean deviation of under 5% ($p > 0.3$). Compared to 2D section based

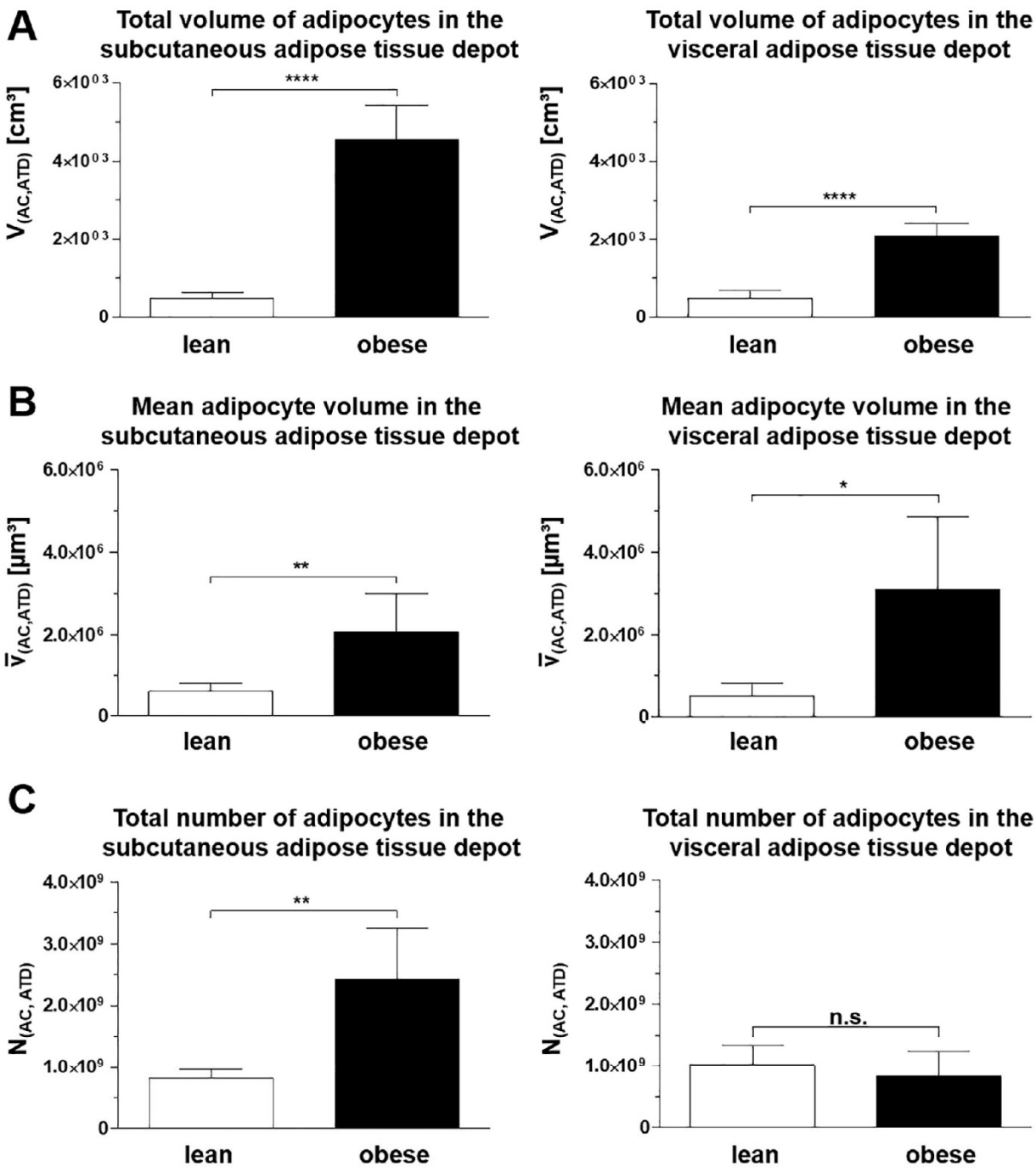

Fig 7. Key determinant quantitative morphological adipocyte parameters in s.c. and visc. adipose tissue depots of lean (n = 5) and obese (n = 6) minipigs. A. The total volumes of adipocytes in the s.c. and the visc. adipose tissue depots were determined from the volume density of adipocytes in the adipose tissue and the total volume of the respective adipose tissue depot. **B, C.** The mean volumes and the total numbers of adipocytes in an adipose tissue depot were obtained by LSFM-based quantitative morphological analyses. Data are means ± standard deviations. t-test. *: $p < 0.05$; **: $p < 0.01$; n.s.: not significant ($p > 0.05$).

https://doi.org/10.1371/journal.pone.0248594.g007

unbiased quantitative stereological analyses, LSFM-based quantitative morphological analyses were associated with considerably lower time- and work-expenditure. This difference was primarily due to the considerably faster sample clearing process and LSFM imaging procedure, as compared to the generation and analysis of histological (serial) sections of plastic embedded tissue samples.

Obesity associated changes of adipocyte numbers and mean volumes in subcutaneous and visceral body fat depots identified by LSFM-based quantitative morphological analyses

In both lean and obese minipigs, respectively, the mean cellular volumes of adipocytes ($v_{(AC,ATD)}$) in the subcutaneous adipose tissue depots were not significantly different from the mean volumes of adipocytes in the corresponding visceral adipose tissue depots of the same animals (paired t-tests; $p > 0.3$).

The adiposity associated increase of the total volumes of both the subcutaneous and the visceral adipose tissue depots in obese *vs*. lean minipigs was consistently associated with significant increases of the mean cellular volumes of adipocytes. On the average, the obesity associated increase of the mean volume of adipocytes in the subcutaneous adipose tissue depot of lean *vs*. obese animals accounted for 361%, and 406% in the visceral adipose tissue depot (Fig 7B).

In the subcutaneous adipose tissue depot, the total number of adipocytes per adipose tissue depot ($N_{(AC,ATD)}$) was also significantly increased in obese *vs*. lean minipigs, accounting for an almost triplication (270% increase) of adipocyte numbers. In the visceral adipose tissue depot, however, the obesity associated increase of the mean cellular volumes of adipocytes in obese *vs*. lean minipigs was not associated with a significant ($p = 0.44$) increase of the total numbers of adipocytes (Fig 7C).

The measured individual adipocyte volumes ($V_{i(AC,ATD)}$) ranged over three decimals from 0.013×10^6 μm^3 to 15.9×10^6 μm^3, with the largest adipocytes being present in the visceral adipose tissue of obese minipigs. Regardless of the increased mean cellular adipocyte volumes in obese *vs*. lean minipigs, the individual adipocyte volumes in both s.c. and visc. adipose tissue samples of lean and obese minipigs were normally distributed (Fig 8).

Verification of LSFM-based quantitative morphological analysis results by unbiased quantitative stereological analyses

The results of the LSFM-based analyses of the absolute numbers of adipocytes in the different adipose tissue depots ($N_{(AC,ATD)}$), and of the mean adipocyte volumes in optically cleared s.c. and visc. adipose tissue samples of lean and of obese minipigs did not significantly differ from the corresponding values obtained by unbiased quantitative stereological analyses (paired t-test; $p > 0.4$). Indeed, the mean percentual deviation of the results obtained by both analysis methods was only 1.04 ± 3.0% for the total numbers of adipocytes, and 1.14 ± 3.1% for the mean volumes of adipocytes in the s.c. and the visc. adipose tissue depots in lean and obese minipigs.

Histomorphometric measurement of adipocyte cross section profile parameters

The mean adipocyte section profile -areas, and -(maximal) diameters in sections of s.c. and visc. adipose tissue depots of obese minipigs (s.c.: 16545 ± 3174 μm^2, and 179 ± 17 μm; visc.: 24196 ± 4796 μm^2, and 207 ± 21 μm) were significantly ($p > 0.05$) increased (by > 200%,

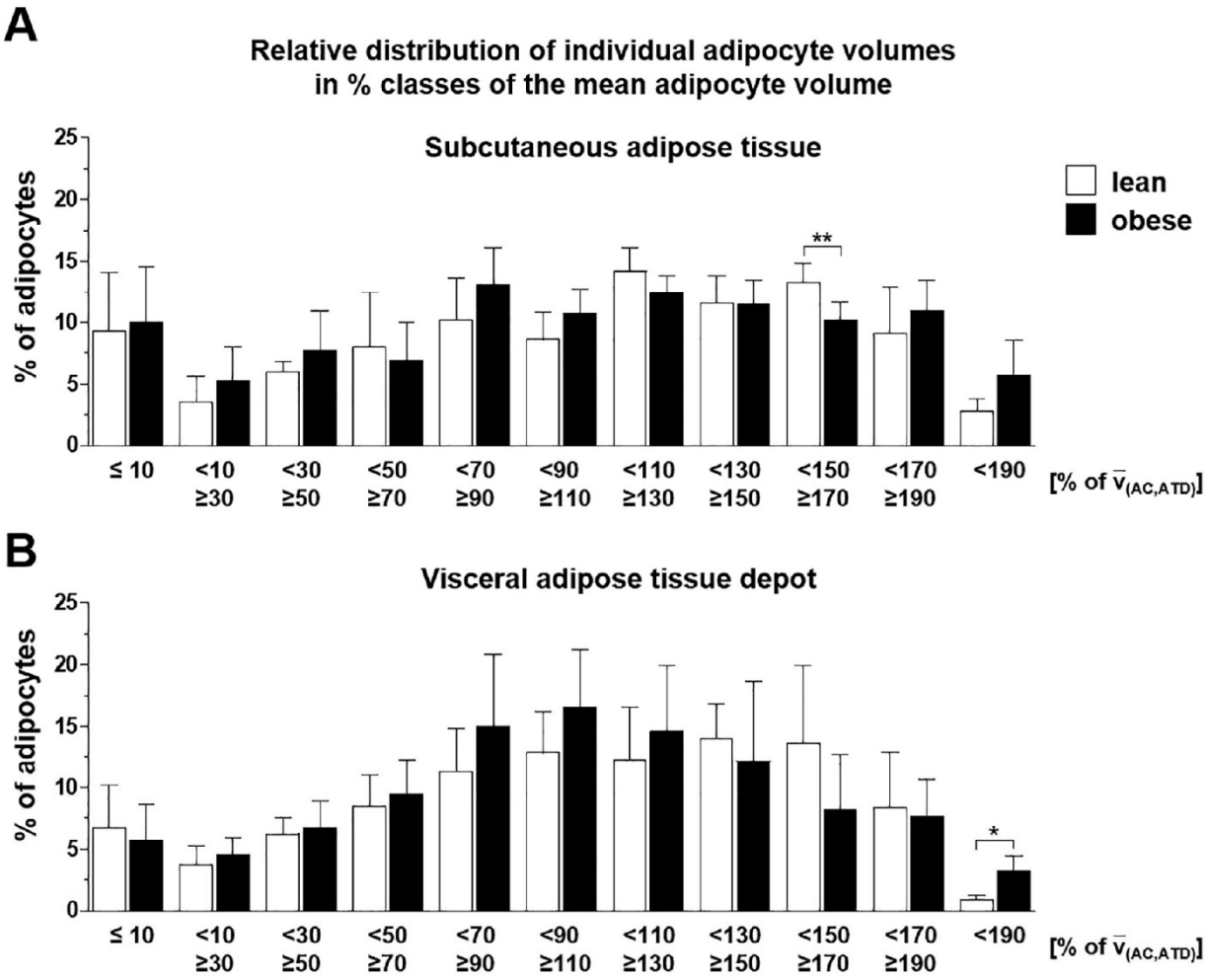

Fig 8. Relative distribution of individual adipocyte volumes in % classes of the mean adipocyte volume in the subcutaneous adipose tissue depot (A) and the visceral adipose tissue depot (B) of lean (n = 5) and obese (n = 6) minipigs (obtained by LSFM-based analyses of optically cleared adipose tissue samples). The bars represent the percentual numbers of adipocytes with individual volumes ranging in 20% classes of the mean adipocyte volume. Data are means ± standard deviations. t-test. *: $p < 0.05$, **: $p < 0.01$.

https://doi.org/10.1371/journal.pone.0248594.g008

respectively by > 150%), as compared to lean control animals (s.c.: 8088 ± 1476 μm^2, and 122 ± 9 μm; visc.: 10548 ± 3031 μm^2, and 139 ± 20 μm). In contrast, the numerical area densities of adipocyte section profiles were significantly higher (> 50%) in lean (s.c.: 1156 ± 189 n/10^6 μm^2; visc.: 769 ± 90 n/10^6 μm^2) than in obese minipigs (s.c.: 557 ± 91 n/10^6 μm^2; visc.: 386 ± 83 n/10^6 μm^2).

Discussion

Discussion of study aims and the general experimental design

The aims of the present study were to evaluate the suitability of LSFM-based quantitative morphological analyses to provide precise and unbiased measures of adipocyte volumes and numbers to characterize obesity-related, fat depot specific alterations of adipocyte growth patterns

in the large animal model (LAM) of diet induced obesity (DIO) in Göttingen minipigs [6]. Methodologically, the use of an LSFM-based approach for quantitative volume- and number-analyses of adipocytes was motivated by the principal advantages of LSFM-analyses, allowing for a quick and straightforward 3D-visualization and morphological analysis of tissue elements in optically cleared, intact (adipose) tissue samples [24,27,41]. Provided the reliability and accuracy of obtained measurement results, LSFM-based analyses thus hold a great potential to efficiently examine relevant quantitative (and qualitative) histomorphological parameters of adipocytes with less effort and analytical travail than conventional quantitative morphological analysis methods that depend on 2D histological sections.

The experimental design of the study was thus conceived to warrant an objective evaluation of the accuracy of LSFM-based quantitative morphological measurement data of adipocyte volumes and numbers. For this, LSFM-measurement data were compared to the results of adipocyte volume and number analyses obtained by unbiased quantitative stereological analysis methods, representing the gold-standard of quantitative histomorphological analyses in biological tissue samples.

To warrant the comparability and unbiasedness of the results obtained by both analysis approaches, representative adipose tissue samples (of identical animals) were generated by systematic uniform random sampling [8,28,30,31,42] and either subjected to LSFM-analysis, or processed for unbiased quantitative stereological analysis. Both analyses approaches used the disector method [8,29,35] for unbiased sampling and analysis of adipocytes, ensuring that the selection of analyzed adipocytes within the examined tissue samples were not biased by the size, shape, and orientation of the adipocytes.

Factors confounding the accuracy of quantitative morphological analysis results in both approaches, such as the embedding-, respectively clearing-related shrinkage of tissue samples [43], incorrect and/or variable factual thicknesses of the analyzed histological sections [35], and potential LSFM-imaging artifacts (leading to a distortion of adipocyte shapes and volumes in digital 3D image reconstructions generated from LSFM-image z-stacks) [44] were precisely determined and corrected, or, respectively, minimized by using adequate technical equipment and defined test-particles as shape/volume-controls.

Discussion of the LAM-DIO model and relevant quantitative histomorphological adipocyte parameters

In the present study, the established LAM of DIO in Göttingen minipigs was used to objectively quantify and characterize obesity related alterations of growth patterns of (unilocular) adipocytes in different adipose tissue depots [6]. Animals of this DIO model reproducibly develop pathogenetically relevant metabolic derangements and histological alterations which are also observed in the human metabolic syndrome (MetS). Due to their body size, minipigs can provide abundant amounts of sample materials, available for extensive analyses by methodologically different approaches. DIO Göttingen minipigs display histomorphologically manifested multifocal adipose tissue inflammation and degeneration, exclusively occurring in the visceral (visc.) adipose tissue, but not in subcutaneous (s.c.) body fat depots [6]. In humans, visceral adiposity and adipose tissue inflammation are associated with many adverse metabolic effects, including insulin resistance [45], dyslipidemia [46], and hypertension [47]. They are also considered to play key roles in the pathogenesis of the (human) metabolic syndrome (MetS) [48], which is also significantly correlated with an increased risk of cardiovascular complications, such as myocardial infarction and stroke [49]. In obese patients with the MetS, as well as in murine DIO models, inflammatory adipose tissue alterations preferentially affect the visceral adipose tissue depot(s) [48]. The inflammation is (histo)morphologically characterized

by increased numbers of lymphocytes and macrophages, along with locally and systemically increased levels of inflammatory cytokines, such as tumor necrosis factor alpha (TNFα) and interleukin 6 (IL-6), partially deriving from adipocytes [48,50]. The abundance levels of free fatty acids and of adipose tissue derived hormones, such as adiponectin and leptin are also altered in obesity and in the MetS [48,51,52]. Since many years, (translational) obesity research is focused on detection and characterization of obesity associated functional and molecular adipose tissue alterations, such as metabolic, lipidomic, transcriptomic and proteomic changes associated with the development of adipose tissue inflammation and the MetS. Different studies also examined morphological changes of adipocytes during development of adiposity, using different analysis approaches [12,53], such as flow cytometry of single isolated adipocytes and morphometric (incl. digital image) analysis of histological sections. These studies indicated a substantial role of adipocyte cell size in health, as well as under disease conditions [12]. In particular, visceral and subcutaneous adipocytes appear to react differentially towards adiposity, indicating a fat depot specific adipocyte growth reaction pattern [12,48], which could be relevant for the development of inflammatory alterations triggering the development of the MetS. However, obesity associated quantitative morphological parameters of adipocytes, such as "adipocyte size", or differences between subcutaneous and visceral adipocytes, have yet not been extensively studied using unbiased quantitative morphological analysis methods.

In obesity-research, 2D-morphometric data obtained by planimetric analysis of adipocyte section profiles in histological sections of adipose tissue samples, such as the mean adipocyte section profile-areas/diameters, or the numbers of adipocyte section profiles per section area, are frequently used to describe adipocyte morphology [53]. These parameters can precisely and quickly be determined in standard histology sections, using digital image analysis software, such as "Image J". Also, in the present study, the obesity-related changes of adipocyte morphology in s.c. and visc. adipose tissue depots of obese *vs*. lean minipigs were associated with significant increases of the mean adipocyte section profile areas and diameters, respectively, with significant decreases of the numbers of adipocyte section profiles per section area. However, 2D histomorphometric measurement data of cell section profiles are, offhand, neither equivalent to, nor can they be directly compared to 3D cell volumes and numbers, which represent inherently different parameters [8,39,54]. 2D histomorphometric measurements of cell section profiles in single histological sections can also not provide information about individual cell volumes, or the distribution of cell sizes in a defined tissue reference compartment. A precise, accurate, and objective characterization and differentiation of obesity-related hyperplastic and hypertrophic adipocyte growth patterns requires, by definition, unbiased measures of quantitative morphological parameters, namely the mean adipocyte volume, and the total number of adipocytes. However, these quantitative morphological parameters can generally not be determined without bias by 2D histomorphometric measurements of cell section profiles in single arbitrarily sampled histological sections [7–9,14,39,54]. Here, unbiased quantitative stereological methods, based on stochastic geometry, are required, representing the "gold-standard" for quantitative morphological analyses of biological tissues in biomedical sciences [7–9,14,33].

Discussion of unbiased quantitative morphological analyses for determination of adipocyte volumes and numbers

The general principles and methodologies of quantitative stereological analyses and applicable sampling strategies have comprehensively been described in several textbooks [7,8,33,55], reviews and studies [9,14–17,28,39,42,54] the interested reader is referred to. Early "model-based" quantitative stereology methods use(d) (model-) assumptions about the shape, the

shape- and size-distribution, the orientation, and the distribution of the examined tissue structures, to estimate their 3D volumes, numbers, surfaces, or lengths in histological sections. These model-based methods are therefore, independent how close the respective estimates may come to reality, inherently biased. In contrast, the accuracy and precision of estimates of stereological parameters obtained by modern, unbiased (design-based, model-free) quantitative stereological methods, such as the methods featured in the present work, do not depend on any model-assumptions, but only rely on adequate sampling designs and stereological probes. To obtain unbiased estimates of 3D morphological parameters of the tissue structures of interest (*e.g.*, cell volumes, surfaces, lengths, and numbers), quantitative stereological analyses depend on "random sampling designs", where samples are taken from strictly randomly selected locations (*i.e.*, each location within a given tissue reference space has the same, random, chance (equiprobability) to be actually sampled) to appropriately generate representative samples that adequately reflect the interested features of the tissue reference compartment they are derived from [7,8,28]. Importantly, random-, or equiprobability-sampling designs do not require any external knowledge, such as size, shape, orientation, or spatial distribution of the objects of interest. The accuracy (error probability) of random sampling designs is predefined by the number and (fractional) size of the selected samples, relative to the size of the reference space, and to the abundance and distribution of the objects of interest within the reference space [42,56]. The efficiency of random sampling designs (*i.e.*, the sampling effort, *i.e.*, the necessary minimal number of samples) can significantly be improved, using systematic uniform random (SUR) sampling strategies [28]. In SUR-sampling designs, samples (of identical size) are selected from their corresponding reference space according to a random starting point but with a fixed, periodic (sampling) interval. SUR-sampling designs are appropriate to unbiasedly determine quantitative morphological features of biological structures. SUR-sampling designs are easy to apply, and, as long as the chosen sampling interval does not accidentally coincide with a cyclical pattern of the sampled structures, they eliminate the risk of preferential selection of objects with distinct properties, such as *e.g.*, large volumes (*i.e.*, a clustered selection, which would bias the obtained quantitative stereological estimates). In unbiased quantitative stereological analyses, SUR sampling designs are generally applied on all levels of sampling, *i.e.*, to sample tissue-specimens, -blocks, and -sections, section fields of view, and test-fields/counting frames, warranting their unbiased representativity [8]. In contrast, "stratified sampling designs", use prior knowledge for specification of particular properties/features to distinguish defined subpopulations of interested structures [42]. In stratified sampling designs, the sample size (and number) is adjusted in relation to *e.g.*, the sizes, staining-intensities, neighborhood conditions, spatial distributions, or interspatial relationships of the objects of interest with distinct other tissue elements. Stratified sampling designs play an important role in image segmentation algorithms and for intensity threshold determination in immunohistochemically stained sections and are often applied in *e.g.*, diagnostic (digital) pathology [42].

Unbiased quantitative stereological analyses estimate 3D morphological parameters (volumes, surfaces, lengths, and numbers of the tissue structures of interest) from their corresponding volume densities. These are determined, using specific test systems, stereological probes, and appropriately oriented 2D sections of the tissue, considering the effects of (potential) anisotropy, preferred orientation and non-uniform distribution of the tissue structure(s) of interest in their reference compartment [7,8]. Volume-, surface-, and length densities can be determined in single 2D tissue sections by appropriate stereological probes. In contrast, unbiased (number weighted) estimations of mean particle volumes and particle numbers require three-dimensional stereological test systems, such as the disector [7–9]. For calculation of absolute quantities, the volume-, surface-, length-, or numerical volume-densities are

multiplied with the total volume of the corresponding reference compartment, which has to be determined in advance [16]. Some quantitative stereological approaches, such as determination of numerical volume densities with the physical disector [8,29], require consideration of the shrinkage of the tissue, associated with the embedding of tissue samples in histological embedding media [43]. Here, plastic embedding media, such as GMA/MMA, are preferable, since they allow preparation of thin sections and cause a precisely determinable, uniform, reproducible, and relatively low embedding related tissue shrinkage, as compared to paraffin embedding [7,35,43]. Regarding the orientation of the analyzed tissue sections, it needs to be noted, that determination of volume densities by point counting and analyses of numerical volume densities of particles with the disector can be performed in arbitrarily oriented sections (provided that unbiased, *i.e.*, representative, randomly sampled sections are analyzed, and that the examined structures of interest and their tissue reference compartment are not affected by differential embedding related shrinkage), whereas other quantitative stereological analysis parameters, such as surface- and length-densities may require a randomization of the section plane orientation [8]. For estimation of surface densities, for example, vertical sampling designs are commonly applied [57], whereas estimates of length densities require sections with random orientation in all three dimensions of space (isotropic uniform random, or IUR sections) [8,32,40,58]. Although determination of $V_{V(AC/ATD)}$ and $N_{V(AC/ATD)}$ do not require IUR sections, it might though be useful to apply IUR sampling designs, since all quantitative stereological parameters can be analyzed in IUR sections, thus allowing for a retrospective analysis of any additional stereological parameters in the same sections, without the necessity to generate new sections with randomized section plane orientations.

The analysis of individual particle volumes, such as individual cell volumes within the tissue, still remains a challenging and extremely laborious task, using unbiased quantitative stereological analysis methods [8]. Indeed, the determination of individual cell volumes (unbiased by the volume of the analyzed cell) within a tissue sample, requires the analysis of the cells section profile areas in approximately equidistant, parallel, serial sections, completely covering the entire vertical extension of the cell (Cavalieri's principle) [8]. Since unilocular adipocytes in white adipose tissue are comparably large cells (with an average diameter of often > 150 μm), this procedure requires the analysis of a large number of serial sections, and is most cumbersome, since identification of corresponding section profiles of the same cell in different sections becomes increasingly difficult, as higher the vertical distance of the two examined sections is. Therefore, individual fat cell volumes determined by unbiased quantitative stereological methods have yet not been reported (whereas, some studies determined individual volumes of adipocytes in single cell suspensions generated by enzymatic separation of adipocytes from adipose tissue samples [12,59]).

In the present study, strict sampling designs were applied for quantitative stereological analyses of adipocyte sizes, numbers, and mean volumes, to characterize the principal obesity associated quantitative morphological alterations of adipocytes in different adipose tissue depots of the examined DIO minipig model. The volume densities of adipocytes in the different adipose tissue depots were determined by point counting in arbitrarily oriented paraffin sections of SUR sampled adipose tissue specimens. In tissues where differential shrinkage is not relevant, this parameter is independent of the extent of embedding related tissue shrinkage and can be determined without greater effort, using standard paraffin sections (volume density determination is of course also possible in sections of plastic embedded tissue samples, or in (virtual) 2D optical LSFM sections, if paraffin sections are not prepared in a given study). For determination of individual adipocyte volumes and the numerical volume densities of adipocytes within their corresponding adipose tissue depots by LSFM-based morphological analysis, the disector method [8,29,35] was chosen, because it warrants an unbiased, number weighted, and

swift sampling of adipocytes for subsequent analyses directly in the volume rendered 3D reconstruction of the LSFM imaged adipose tissue sample. For the confirmative unbiased quantitative stereological analysis approach, the same stereological probe was used, although the physical disector method is often considered technically complex and time consuming, as compared to alternative unbiased quantitative stereological methods, such as *e.g.*, fractionator sampling designs combined with the optical disector and the nucleator [7,8]. In the present study, the physical disector method was, subjectively, still found absolutely suitable for the unbiased quantitative stereological analysis of adipose tissue specimen sampled from large body fat depots. Next to the application of appropriate sampling procedures, there are essentially two relevant, technical factors that must be adequately determined to warrant the accuracy of particle volume- and number estimates obtained by physical disector analyses: the extent of embedding-related tissue shrinkage and the factual thicknesses of the examined sections [30,35]. In the present study, the (soft) adipose tissue samples were shape-stabilized by encasing in agar to prevent mechanical deformation/compression during the embedding process [30]. Embedding-related tissue shrinkage and section-thicknesses were precisely determined using established volumetric measurement methods [30,31], and reflectometric measurement analysis [35], respectively, and correspondingly used for calculation of the numerical volume estimates of adipocytes in their adipose tissue reference compartments. The homogeneity of the extent of 3D-shrinkage related to GMA-MMA-embedding of adipose tissue samples was confirmed by the low standard deviation of shrinkage rates of individual samples.

Discussion of LSFM-based unbiased quantitative morphological analyses of adipocytes

Although the featured unbiased quantitative stereological analysis methods allow for an accurate estimation of relevant morphological adipocyte parameters, the application of these methods remains time intense and cumbersome. It might be for this reason, that unbiased quantitative stereological analyses have only rarely been implemented to characterize adipocyte morphology in previous studies examining human specimens [60], or translational obesity models [61]. Therefore, we tested the applicability of 3D light sheet fluorescence microscopy (LSFM) for quantitative morphological analyses of optically cleared adipose tissue samples, as an efficient alternative to 2D section based unbiased quantitative stereological analysis approaches. To evaluate the comparability of the results of LSFM-based quantitative morphological analyses of cleared adipose tissue samples to the results obtained by unbiased stereological methods, both analysis approaches were performed on adipose tissue specimens SUR sampled from the same adipose tissue depots of the identical pigs. Previously, few other studies have already successfully applied LSFM analyses for examination of distinct quantitative morphological parameters in other types of tissues, *e.g.*, to count the number of glomeruli in murine kidneys [62], to analyse the volume of bronchus associated lymphoid tissue in mice [63], or to determine the volume and surface of fish gill lamellae [64]. A large variety of different techniques for tissue clearing has been developed [65], such as CLARITY, iDISCO, 3DISCO, FRUIT, CLEAR T [20], vDISCO [66], Adipo Clear [27], and ECi [62], optimized for different sample types and various downstream applications. For quantitative morphological analyses of adipose tissue samples, we used the 3DISCO technique [25], since this clearing method works fast and produces firm, dimensionally stable, but easy to cut specimens up to the size of several cubic centimetres. 3DISCO clearing is generally known to cause a considerable shrinkage of the cleared tissue samples [67]. In the present study, however, a constant and regular volume decrease of adipose tissue samples of approximately ~21% was associated with

the applied clearing and staining procedure, as determined by precise volumetric measurement methods. Interestingly, this degree of clearing related tissue shrinkage is approximately the same, as the extent of embedding related tissue shrinkage of GMA/MMA embedded adipose tissue samples (which is generally considered to be beneficially low, as compared to other histological embedding media, such as paraffin). Other solvent based clearing protocols, such as iDISCO+ or Adipo-Clear reportedly cause a generally lower degree of clearing associated tissue shrinkage [27,67,68] than the 3DISCO procedure and have been successfully applied for clearing and 3D LSFM imaging of adipose tissue samples [27]. For quantitative morphological analyses of adipose tissue samples, these clearing protocols might thus represent suitable alternatives to the 3DISCO method.

In 3DISCO cleared adipose tissue samples, the (adipocyte) cell membranes displayed a variably strong autofluorescence at 520/40 nm (excitation range) / 585/40 nm (emission range) wavelength. The automatic digital image analysis of single adipocyte cell volumes in 3D reconstructions of cleared adipose tissue samples depends on the separation of cell membrane staining signals and the unstained inner space of the cell [69]. The adipocyte cell volume is calculated from the number of voxels within the unstained (*i.e.*, optically empty background) centre of the cell that is completely surrounded by a continuously stained cell membrane. In unstained 3DISCO cleared adipose tissue samples, the cell membranes of single adipocytes could often not be detected in complete continuity, thus hindering single cell volume analyses (if the cell membrane staining between two adjacent adipocytes is disrupted, these two cells will be detected as one, thus producing a false individual cell volume measurement value). To enhance the adipocyte cell membrane autofluorescence in the 3DISCO cleared tissue samples, a simple eosin (post) staining was applied. In 3DISCO cleared and eosin-stained samples all adipocyte cell membranes were reliably and sufficiently strong labelled. The samples could straightforwardly be imaged by LSFM at 585/40 nm wavelength (emission range), with a 0.63–10 magnification and a z-step height (*i.e.*, vertical resolution) of 5 μm. A standard LSFM image viewing and analysis software (arivis Vision4D vers. 3.0) was used to generate precise 3D sample reconstructions [69]. After digital adjustment of the staining intensity to limit the width of the stained adipocyte cell membranes to < 1 μm, all individual adipocytes present in the examined tissue sample could be unambiguously identified.

In 3D fluorescence microscopy, the accuracy of quantitative measurements of object volumes in 3D digital images reconstructed from z-stacks of 2D optical (fluorescence) images depends on the accuracy of the 3D image reconstruction, *i.e.*, a precise match of the volumes (and shapes) of the imaged objects and their digital reconstructions. Major factors causing distortion of object shapes (and correspondingly of their measured volumes) in 3D reconstructions of 2D fluorescent image piles (z-stacks) are a nonconformity of the nominal and factual z-step size (*i.e.*, an untrue vertical scaling), and imaging artifacts due to spherical aberration (SA) due to refractive index (RI) differences between the imaged sample and the surrounding medium (clearing/mounting medium, air, objective lens), as well as between different lens elements inside a fluorescence microscope [44]. Light rays passing such RI-mismatched interfaces are focused to different points of the optical axis, causing a shift of the optical focus plane of the imaged object. During z-stack acquisition of fluorescent images, the vertical distance that the imaged object physically moves (*i.e.*, the stage movement) in every z-step, is then different from the movement of the acquired image (focus) planes, leading to artificially distorted (elongated or compressed) 3D object images, and correspondingly to incorrect object volumes [44]. In 3D LSF-microscopy, shape and volume distortions of imaged objects can be generally addressed by using appropriate technical equipment (such as SA-corrected LSFM-objectives) and precisely adjusted instrument settings (precise calibration of z-step height, alignment of light sheet planes, adjustment of light sheet widths and focus settings, *etc.*). SA-imaging

artifacts due to RI-mismatches can be avoided by using dipping lenses (or dipping caps) and immersion media with RIs adapted to the RIs of the cleared tissue samples, and by correction of SA-induced digital image distortion with appropriate algorithms [44]. In a given experiment, a potential distortion of images of biological objects of interest (such as adipocytes) can also be examined by imaging of control (test)-objects with similar properties (shape, size, RI, fluorescence), using the same instrument settings for image acquisition, volume rendering and image analysis. In the present study, diverse technical and methodological precautions were taken to avoid image-distortion and correspondingly incorrect adipocyte volume measurement results, including precise control of the z-step advance, adequate adjustment and control of LSFM-instrument settings and image (pixel/voxel-size) scaling. To minimize SA-imaging artifacts due to RI-mismatches, the objective was equipped with an optimized dipping cap, and the same chemical (BABB, RI: 1.56) [70] was used as solvent for clearing, and as submersion medium for imaging of adipose tissue samples. The realistic rendering of object shapes and volumes in digital 3D-LSFM reconstructions was additionally confirmed by imaging and volumetric image-analysis of fluorescently labelled, spherical, polystyrene (RI: 1.59) microparticles (*i.e.*, comparable to the RI of solvent-cleared tissue samples [44]) with precisely defined diameters of ~100 μm (*i.e.*, comparable to the size of adipocytes), using the exactly same instrument-, image-acquisition, and analysis-settings, as for analysis of the adipose tissue samples.

For determination of $V_{V(AC/ATD)}$ and $N_{V(AC/ATD)}$ in 3D LSFM autofluorescence images of the optically cleared adipose tissue samples, the same stereological probe (*i.e.*, disector analyses in SUR sampled fields of view) was applied, as in the unbiased quantitative stereological analysis approach, ensuring the unbiasedness of the quantitative morphological LSFM measurements.

The used arivis Vision4D (vers. 3.0) imaging and analysis software does not feature integrated specific application tools for SUR sampling, point counting, disector analyses with unbiased counting frames, or other quantitative stereological probes [69] (*therefore, in the view of the authors, a "stereology-add-on" for the arivis Vision4D software would be beneficial*). However, the application of these stereological probes was supported by advantageous functions of the arivis Vision4D software, such as the "split screen" function, or the "*Magic Wand*" tool. The split screen function allowed for a side-by-side view of two analysis windows of the same 3D LSFM dataset, enabling a parallel, independent view of two different, determinable, optical section planes of the identical 3D tissue sample reconstruction for the disector. Combined with the "*Magic Wand*" tool, for labelling of individual cells in the 3D sample reconstruction, an unbiased, number weighed disector sampling of adipocytes could efficiently be performed. The "*Magic Wand*" tool also allowed a rapid analysis of the individual cell volumes (and other quantitative morphometric parameters, such as surface area) of the sampled adipocytes.

The (shrinkage corrected) measurement values of adipocyte numbers and volumes in s.c.- and visc.-adipose tissue samples of lean and obese pigs assessed by LSFM-based analyses and by unbiased quantitative stereological analyses were virtually equal, thus proving the suitability of LSFM-based analyses for precise and unbiased determination of relevant quantitative morphological adipocyte parameters.

Discussion of the advantages of LSFM-based analyses of adipocyte volumes and numbers

In contrast to the elaborate tissue processing and analysis steps associated with 2D section based unbiased quantitative stereological analyses (plastic-embedding of tissue samples, preparation of thin section series, analysis of section thicknesses, physical disector analyses), the

clearing, LSFM imaging and subsequent digital quantitative morphological analyses of adipose tissue samples required significantly less time, workload, and material costs. Particularly, the straightforward disector-sampling process of adipocytes in virtual 3D-adipose tissue reconstructions and the direct digital volume analysis of the sampled adipocytes was (subjectively) far less cumbersome and more certain than the sampling and counting process of adipocyte nuclei in physical disector section pairs. Most remarkably, LSFM analysis also enables unbiased measurements of individual adipocyte volumes. In contrast, determination of individual fat cell volumes with (2D-section-based) quantitative stereological analysis methods has so far not been possible with reasonable technical effort. Due to the (comparably large) size of adipocytes, the applied vertical resolution (step size) of ~5 μm was small enough to provide sufficiently accurate measurements of individual adipocyte cell volumes in 3D LSFM image reconstructions. Thus, for the first time, it is now possible to monitor not only obesity associated changes of the mean adipocyte cell volume within intact tissue samples, but also to detect changes in the size distribution of the adipocytes in a defined adipose tissue depot (which even might not cause a net change of the mean fat cell volume). This way, subpopulations of adipocytes could be identified, which might display differential hyperplastic and hypertrophic growth reaction patterns, metabolic capacities and pro-inflammatory properties in different body fat depots in states of hypercaloric nutrition and developing obesity [12].

Discussion of obesity-associated, fat depot specific alterations of adipocyte growth patterns in the Göttingen minipig DIO model

The results of the present study objectively prove, that the obesity related volume increase of the subcutaneous and visceral adipose tissue depots in DIO Göttingen minipigs is due to different, depot specific adipocyte growth reaction patterns. Adipocytes in the subcutaneous adipose tissue of obese animals displayed a comparatively balanced ratio of hyperplastic (*i.e.*, an increase of cell numbers) and hypertrophic (*i.e.*, an increase of the cell size, characterized by the mean adipocyte volume) growth reaction patterns. In contrast, the adiposity related increase of the visceral adipose tissue depot in obese animals was characterized by a disproportionally marked increase of the mean adipocyte volume, paralleled by an only minimal and insignificant increase of the total number of adipocytes. In the present study, the largest adipocytes in the visceral adipose tissue depot of obese pigs displayed individual cell volumes of more than 15×10^6 μm^3, exceeding the mean volume of subcutaneous adipocytes in obese minipigs by more than 7-fold. The morphologically different growth reaction patterns of subcutaneous and visceral adipocytes during development of obesity might provide a possible explanation for the pathogenesis of the inflammatory lesions exclusively occurring in the visceral adipose tissue. An excessive (individual or general) enlargement of adipocytes might disturb the (mechanical) stability of the adipose tissue and expose enlarged adipocytes to increased shear stress [12,71,72], as soon as a "critical" cell size is reached. This might probably induce altered adipocytokine expression patterns, triggering the development of an inflammatory milieu with activation of resident macrophages and attraction of infiltrating inflammatory cells, or directly lead to adipocyte degradation [12]. Previous studies have already demonstrated a correlation between obesity associated adipocyte cell hypertrophy and impaired insulin mediated glucose uptake and increased lipolysis [73], predicting pathological conditions such as insulin resistance and type 2 diabetes [73–77]. Obesity related adipocyte hypertrophy was also shown to be positively correlated with the expression of inflammatory genes [78], increased pro-inflammatory adipokine secretion (*e.g.*, IL-6, IL-8, MCP-1) [79], and reduced secretion of anti-inflammatory adipokines (*e.g.*, adiponectin), contributing to an increased inflammatory response in adipose tissue [80].

Previous studies have indicated that not only the metabolic state and the pro-inflammatory attributes of hypertrophied adipocytes are altered in states of obesity, but also those of increased proportions of small adipocytes with impaired adipogenesis and/or terminal differentiation [81–83]. In the examined DIO minipig model, the relative size distribution patterns of individual adipocytes in s.c.- and visc.- adipose tissue depots did not considerably vary between lean and obese pigs. These findings indicate a largely homogenous volume increase of individual visceral adipocytes during development of adiposity, exclusively mediated by cellular hypertrophy. In contrast, the normal distribution of individual adipocyte volumes in the subcutaneous adipose tissue of obese minipigs was maintained by balanced hypertrophic and hyperplastic adipocyte growth patterns. Thereby, these findings also demonstrate that significant changes of either cell numbers or cell volumes do not necessarily also manifest in altered size distributions, or *vice versa*.

Limitations of the study

Currently, the technical equipment, the configuration of hardware elements, and the performance capabilities of different LSFM-platforms in different laboratories are not standardized. Different optical parameters of the installed objectives (dry-lenses *vs*. dipping-lenses, different magnification-ranges and numerical apertures, adaption of objectives to immersion liquids of distinct refractive index-ranges, *etc*.), variable light sheet dimensions and geometries, different emission/excitation wavelength ranges, different instrument settings (including z-stage calibration), and camera properties might cause variable image qualities, resolution capacities, and potentially imaging artifacts. These factors can not only impede accurate quantitative measurements of adipocyte volumes, but also hinder a precise reproduction of LSFM-based quantitative morphological measurement results with different LSFM-systems. In a given study, LSFM-based quantitative morphological analyses of different adipose tissue samples should therefore be performed on identically processed tissue samples, using the same LSFM-instrument and analysis settings. Since a standardization of the currently used LSFM-systems and the optical properties of their components is yet not achieved, any studies reporting quantitative morphological measurement data obtained by LSFM-analysis should precisely indicate all relevant technical details of the used LSFM-instrument. Additionally, the experimental design of such studies should schedule LSFM-imaging and analysis of appropriate shape- and volume controls (*i.e*., test objects, such as the fluorescent polystyrene beads used in the present study) to confirm the general correctness of 3D-LSFM measurement results.

As a second seeming limitation of the described LSFM-approach, adipocytes are only identified by their cell-membrane autofluorescence signal (intensified by eosin-staining). Differentiation of adipocytes and other tissue structures, such as vessels, strands of connective tissue (**Fig 4B**), or other cell types, thus solely depends on their characteristic shape. However, this theoretical disadvantage is compensated by the possibility to watch the tissue/cell morphology in 3D. For the purpose of volume analysis of (unilocular) adipocytes in cleared adipose tissue samples, detection of cell-membrane autofluorescence by LSFM (without additional elaborate and expensive cell-type specific labelling procedures) was therefore considered a fast, efficient, and absolutely sufficient approach. However, if cell nuclei or different cell types/tissue structures have to be specifically labeled and analyzed in an LSFM-experiment (*e.g*., for differentiation of different subtypes of uni-or multilocular adipocytes, or inflammatory cells), other appropriate clearing methods and labelling protocols have to be applied and adapted to the given experimental design [27,41].

Finally, the present study examined adipocyte morphology in a pig-model of DIO, whereas the majority of translational obesity research is currently performed using rodent models. The

application of the described LSFM-approach for adipocyte volume- and number analysis in *e.g.*, mice would therefore require an adaption of the used (SUR)-sampling regime to the smaller volume of the examined adipose tissue depots and the corresponding numbers of sampled tissue locations. However, application of the described clearing/staining protocol and the LSFM-imaging- and analysis-procedures is principally also possible in murine adipose tissue samples, as murine and porcine unilocular adipocytes display a similar morphology (S5 Fig) and their cell volumes are principally in the same order of magnitude.

Perspectives of LSFM-based quantitative morphological adipocyte analyses

Next to the determination of adipocyte volumes and numbers in cleared adipose tissue samples, 3D-LSFM analyses also provide the possibility for comprehensive analyses of additional qualitative-, and quantitative morphological adipocyte parameters, such as shape, shape variability, surface, isotropy, *etc.* Alterations of these parameters might also be relevant for adipocyte (dys)function in obesity (*e.g.*, by affecting the shear-stress-stability of hypertrophied adipocytes), and/or used as morphological markers of metabolic disease states in translational obesity models. In future studies, combination the described LSFM-approach for adipocyte volume- and number analyses with additional specific fluorescence labelling and tissue clearing techniques will also allow detailed quantitative and spatial analyses of different cell populations in adipose tissue samples, *e.g.*, by using specific markers of white (unilocular), beige, or brown (multilocular) adipocytes, or different inflammatory cell types.

Conclusion

LSFM-based analyses can be recommended as an elegant and efficient approach for comprehensive quantitative characterization of adipocyte morphology in future studies, probably also in other species. Of note, LSFM of 3DISCO cleared tissue samples can also be combined with other imaging modalities, such as histology, immunohistochemistry, or mass spectrometry imaging, and also works using paraffin-embedded tissue samples, *e.g.*, from pathology archives [84]. The swift determinability of accurate numerical values of adipocyte numbers and (individual) volumes can undoubtedly significantly contribute to increase the effectiveness of a study, *e.g.*, by correlation of quantitative morphological adipocyte parameters with transcript profiling-, proteomic-, lipidomic-, or metabolomic analysis data, or measurements of inflammatory cytokines and hormones analyzed in the same adipose tissue samples, or with systemic marker concentrations, or clinical outcomes. We are currently considering performing such multi-OMICS studies on biobank adipose tissue samples of our DIO minipig model to further clarify the relationship(s) between obesity associated morphological changes of fat cells and their corresponding molecular function profiles in defined adipose tissue depots.

Supporting information

S1 Fig. Systematic uniform random (SUR) sampling for generation of representative adipose tissue samples for downstream quantitative morphological analyses.
(TIF)

S2 Fig. Determination of the volume density and total volume of adipocytes in adipose tissue depots.
(TIF)

S3 Fig. Estimation and correction of embedding related tissue shrinkage.
(TIF)

S4 Fig. Control of correct LSFM-image (pixel/voxel-size) scaling/calibration for realistic object shape- and volume-rendering in digital 3D-LSFM image reconstructions.
(TIF)

S5 Fig. Demonstration of the principal similarity of the morphology of adipocytes in histological sections and LSFM-images from murine and porcine subcutaneous adipose tissue samples.
(TIF)

S1 Video. LSFM 3D reconstruction of a 3DISCO cleared porcine subcutaneous adipose tissue sample.
(MP4)

S1 File. Step-by-step protocol for disector sampling and volume analysis of adipocytes with the arivis Vision4D imaging and analysis software.
(DOCX)

S2 File. Exemplary LSFM-dataset. Downloadable from: doi:10.5061/dryad.8gtht76nt.
(DOCX)

Acknowledgments

The authors thank Lisa Pichl, Nadschman Rahimi, Alex Schubö, Josef Grieser and Marold Handl (LMU) for excellent technical assistance.

Images and drawings/artwork

All images and drawings in the Figures of the present work and the Supporting Information were taken/created by the authors.

Author Contributions

Conceptualization: Natalie Theobalt, Isabel Hofmann, Sonja Fiedler, Simone Renner, Georg Dhom, Annette Feuchtinger, Axel Walch, Martin Hrabě de Angelis, Eckhard Wolf, Rüdiger Wanke, Andreas Blutke.

Data curation: Natalie Theobalt.

Formal analysis: Natalie Theobalt.

Funding acquisition: Simone Renner, Georg Dhom, Martin Hrabě de Angelis, Eckhard Wolf, Rüdiger Wanke, Andreas Blutke.

Investigation: Natalie Theobalt, Andreas Blutke.

Methodology: Natalie Theobalt, Andreas Blutke.

Project administration: Eckhard Wolf, Rüdiger Wanke, Andreas Blutke.

Resources: Simone Renner, Georg Dhom, Annette Feuchtinger, Axel Walch, Martin Hrabě de Angelis, Eckhard Wolf, Rüdiger Wanke.

Software: Natalie Theobalt.

Supervision: Andreas Blutke.

Validation: Natalie Theobalt, Isabel Hofmann, Sonja Fiedler, Eckhard Wolf, Rüdiger Wanke, Andreas Blutke.

Visualization: Natalie Theobalt, Isabel Hofmann, Sonja Fiedler, Andreas Blutke.

Writing – original draft: Andreas Blutke.

Writing – review & editing: Natalie Theobalt, Isabel Hofmann, Sonja Fiedler, Simone Renner, Georg Dhom, Annette Feuchtinger, Axel Walch, Martin Hrabě de Angelis, Eckhard Wolf, Rüdiger Wanke, Andreas Blutke.

References

1. Kelly T., et al., Global burden of obesity in 2005 and projections to 2030. Int J Obes (Lond), 2008. 32 (9): p. 1431–7. https://doi.org/10.1038/ijo.2008.102 PMID: 18607383
2. Porter S.A., et al., Abdominal subcutaneous adipose tissue: A protective fat depot? Diabetes Care, 2009. 32(6): p. 1068–75. https://doi.org/10.2337/dc08-2280 PMID: 19244087
3. Chawla A., Nguyen K.D., and Goh Y.P., Macrophage-mediated inflammation in metabolic disease. Nat Rev Immunol, 2011. 11(11): p. 738–49. https://doi.org/10.1038/nri3071 PMID: 21984069
4. Fuchs T., et al., Animal models in metabolic syndrome. Rev Col Bras Cir, 2018. 45(5): p. e1975. https://doi.org/10.1590/0100-6991e-20181975 PMID: 30379216
5. Aigner B., et al., Transgenic pigs as models for translational biomedical research. Journal of Molecular Medicine, 2010. 88(7): p. 653–664. https://doi.org/10.1007/s00109-010-0610-9 PMID: 20339830
6. Renner S., et al., Metabolic syndrome and extensive adipose tissue inflammation in morbidly obese Göttingen minipigs. Mol Metab, 2018. 16: p. 180–190. https://doi.org/10.1016/j.molmet.2018.06.015 PMID: 30017782
7. Gundersen H.J.G., et al., Stereological principles and sampling procedures for toxicologic pathologists, in Haschek and Rousseaux´s Handbook of Toxicologic Pathology Haschek W.M.e.a., Editor. 2013, Academic Press. INC.: London. p. 215–286.
8. Howard C.V. and Reed M.G., Unbiased Stereology. 2 ed. 2005, Coleraine, UK: QTP Publications. 278.
9. West M.J., Introduction to stereology. Cold Spring Harb Protoc, 2012. 2012(8). https://doi.org/10.1101/pdb.top070623 PMID: 22854572
10. Blutke A., et al., Growth hormone (GH)-transgenic insulin-like growth factor 1 (IGF1)-deficient mice allow dissociation of excess GH and IGF1 effects on glomerular and tubular growth. Physiol Rep, 2016. 4(5). https://doi.org/10.14814/phy2.12709 PMID: 26997624
11. Hoeflich A., et al., Insulin-like growth factor binding protein 2 (IGFBP-2) separates hypertrophic and hyperplastic effects of growth hormone (GH)/IGF-I excess on adrenocortical cells in vivo. FASEB J, 2002. 16(13): p. 1721–31. https://doi.org/10.1096/fj.02-0349com PMID: 12409314
12. Stenkula K.G. and Erlanson-Albertsson C., Adipose cell size: Importance in health and disease. Am J Physiol Regul Integr Comp Physiol, 2018. 315(2): p. R284–R295. https://doi.org/10.1152/ajpregu.00257.2017 PMID: 29641234
13. Madsen K.M., The art of counting. J Am Soc Nephrol, 1999. 10(5): p. 1124–5. PMID: 10232699
14. Wanke R., Stereology—benefits and pitfalls. Exp Toxicol Pathol, 2002. 54(2): p. 163–4. https://doi.org/10.1078/0940-2993-00223 PMID: 12211638
15. Boyce R.W., et al., Design-based stereology: Introduction to basic concepts and practical approaches for estimation of cell number. Toxicol Pathol, 2010. 38(7): p. 1011–25. https://doi.org/10.1177/0192623310385140 PMID: 21030683
16. Tschanz S., Schneider J.P., and Knudsen L., Design-based stereology: Planning, volumetry and sampling are crucial steps for a successful study. Ann Anat, 2014. 196(1): p. 3–11. https://doi.org/10.1016/j.aanat.2013.04.011 PMID: 23769130
17. Nyengaard J.R., Stereologic methods and their application in kidney research. J Am Soc Nephrol, 1999. 10(5): p. 1100–23. PMID: 10232698
18. Pakkenberg B., et al., Editorial: Neurostereology. Front Neuroanat, 2019. 13: p. 42. https://doi.org/10.3389/fnana.2019.00042 PMID: 31057371
19. Elisa Z., et al., Technical implementations of light sheet microscopy. Microsc Res Tech, 2018(81): p. 941–958. https://doi.org/10.1002/jemt.22981 PMID: 29322581
20. Feuchtinger A., Walch A., and Dobosz M., Deep tissue imaging: A review from a preclinical cancer research perspective. Histochem Cell Biol, 2016. 146(6): p. 781–806. https://doi.org/10.1007/s00418-016-1495-7 PMID: 27704211

21. Whitehead L.W., et al., The reinvention of twentieth century microscopy for three-dimensional imaging. Immunol Cell Biol, 2017. 95(6): p. 520–524. https://doi.org/10.1038/icb.2017.36 PMID: 28446796

22. Garvalov B. and Ertürk A., Seeing whole-tumour heterogeneity. Nature Biomedical Engineering, 2017. 1: p. 772–774. https://doi.org/10.1038/s41551-017-0150-5 PMID: 31015596

23. Zhao S., et al., Cellular and molecular probing of intact human organs. Cell, 2020. 180(4): p. 796–812 e19. https://doi.org/10.1016/j.cell.2020.01.030 PMID: 32059778

24. Kennel P., et al., From whole-organ imaging to in-silico blood flow modeling: A new multi-scale network analysis for revisiting tissue functional anatomy. PLoS Comput Biol, 2020. 16(2): p. e1007322. https://doi.org/10.1371/journal.pcbi.1007322 PMID: 32059013

25. Erturk A., et al., Three-dimensional imaging of solvent-cleared organs using 3DISCO. Nat Protoc, 2012. 7(11): p. 1983–95. https://doi.org/10.1038/nprot.2012.119 PMID: 23060243

26. Tanaka N., et al., Whole-tissue biopsy phenotyping of three-dimensional tumours reveals patterns of cancer heterogeneity. Nature Biomedical Engineering, 2017. 1: p. 796–806. https://doi.org/10.1038/s41551-017-0139-0 PMID: 31015588

27. Chi J., et al., Adipo-Clear: A tissue clearing method for three-dimensional imaging of adipose tissue. J Vis Exp, 2018(137). https://doi.org/10.3791/58271 PMID: 30102289

28. Gundersen H.J. and Jensen E.B., The efficiency of systematic sampling in stereology and its prediction. J Microsc, 1987. 147(Pt 3): p. 229–63. https://doi.org/10.1111/j.1365-2818.1987.tb02837.x PMID: 3430576

29. Sterio D.C., The unbiased estimation of number and sizes of arbitrary particles using the disector. J Microsc, 1984. 134(Pt 2): p. 127–36. https://doi.org/10.1111/j.1365-2818.1984.tb02501.x PMID: 6737468

30. Albl B., et al., Tissue sampling guides for porcine biomedical models. Toxicol Pathol, 2016. 44(3): p. 414–20. https://doi.org/10.1177/0192623316631023 PMID: 26883152

31. Blutke A. and Wanke R., Sampling strategies and processing of biobank tissue samples from porcine biomedical models. J Vis Exp, 2018(133). https://doi.org/10.3791/57276 PMID: 29578524

32. Mattfeldt T., et al., Estimation of surface area and length with the orientator. J Microsc, 1990. 159(Pt 3): p. 301–17. https://doi.org/10.1111/j.1365-2818.1990.tb03036.x PMID: 2243364

33. Weibel E.R., Stereological methods. I. Practical methods for biologicalmorphometry. 1979, London: Academic Press.

34. Scherle W., A simple method for volumetry of organs in quantitative stereology. Mikroskopie, 1970. 26 (1): p. 57–60. PMID: 5530651

35. Matenaers C., et al., Practicable methods for histological section thickness measurement in quantitative stereological analyses. PLoS One, 2018. 13(2): p. e0192879. https://doi.org/10.1371/journal.pone.0192879 PMID: 29444158

36. Gundersen H.J., Notes on the estimation of the numerical density of arbitrary profiles: The edge effect. Journal of Microscopy, 1977. 111: p. 219–223.

37. Gundersen H.J., Stereology of arbitrary particles. A review of unbiased number and size estimators and the presentation of some new ones, in memory of William R. Thompson. J Microsc, 1986. 143(Pt 1): p. 3–45. PMID: 3761363

38. Hermanns W., Liebig K., and Schulz L.C., Postembedding immunohistochemical demonstration of antigen in experimental polyarthritis using plastic embedded whole joints. Histochemistry, 1981. 73(3): p. 439–46. https://doi.org/10.1007/BF00495658 PMID: 7035413

39. Slomianka L., Basic quantitative morphological methods applied to the central nervous system. J Comp Neurol, 2021. 529(4): p. 694–756. https://doi.org/10.1002/cne.24976 PMID: 32639600

40. Mattfeldt T., Mobius H.J., and Mall G., Orthogonal triplet probes: An efficient method for unbiased estimation of length and surface of objects with unknown orientation in space. J Microsc, 1985. 139(Pt 3): p. 279–89. https://doi.org/10.1111/j.1365-2818.1985.tb02644.x PMID: 3908688

41. Chi J., et al., Three-Dimensional Adipose Tissue Imaging Reveals Regional Variation in Beige Fat Biogenesis and PRDM16-Dependent Sympathetic Neurite Density. Cell Metab, 2018. 27(1): p. 226–236 e3. https://doi.org/10.1016/j.cmet.2017.12.011 PMID: 29320703

42. Kayser K., et al., Theory of sampling and its application in tissue based diagnosis. Diagn Pathol, 2009. 4: p. 6. https://doi.org/10.1186/1746-1596-4-6 PMID: 19220904

43. Dorph-Petersen K.A., Nyengaard J.R., and Gundersen H.J., Tissue shrinkage and unbiased stereological estimation of particle number and size. J Microsc, 2001. 204(Pt 3): p. 232–46. https://doi.org/10.1046/j.1365-2818.2001.00958.x PMID: 11903800

44. Diel E.E., Lichtman J.W., and Richardson D.S., Tutorial: avoiding and correcting sample-induced spherical aberration artifacts in 3D fluorescence microscopy. Nat Protoc, 2020. 15(9): p. 2773–2784. https://doi.org/10.1038/s41596-020-0360-2 PMID: 32737465

45. Kahn B.B. and Flier J.S., Obesity and insulin resistance. J Clin Invest, 2000. 106(4): p. 473–81. https://doi.org/10.1172/JCI10842 PMID: 10953022

46. Williams P.T. and Krauss R.M., Associations of age, adiposity, menopause, and alcohol intake with low-density lipoprotein subclasses. Arterioscler Thromb Vasc Biol, 1997. 17(6): p. 1082–90. https://doi.org/10.1161/01.atv.17.6.1082 PMID: 9194758

47. Head G.A., et al., Central nervous system dysfunction in obesity-induced hypertension. Curr Hypertens Rep, 2014. 16(9): p. 466. https://doi.org/10.1007/s11906-014-0466-4 PMID: 25090962

48. Tchkonia T., et al., Mechanisms and metabolic implications of regional differences among fat depots. Cell Metab, 2013. 17(5): p. 644–656. https://doi.org/10.1016/j.cmet.2013.03.008 PMID: 23583168

49. IDF, The IDF consensus worldwide definition of the metabolic syndrome, in IDF communications. 2006: Brussels, Belgium.

50. Huh J.Y., et al., Crosstalk between adipocytes and immune cells in adipose tissue inflammation and metabolic dysregulation in obesity. Mol Cells, 2014. 37(5): p. 365–71. https://doi.org/10.14348/molcells.2014.0074 PMID: 24781408

51. Mancuso P., The role of adipokines in chronic inflammation. Immunotargets Ther, 2016. 5: p. 47–56. https://doi.org/10.2147/ITT.S73223 PMID: 27529061

52. Longo M., et al., Adipose tissue dysfunction as determinant of obesity-associated metabolic complications. Int J Mol Sci, 2019. 20(9). https://doi.org/10.3390/ijms20092358 PMID: 31085992

53. Parlee S.D., et al., Quantifying size and number of adipocytes in adipose tissue. Methods Enzymol, 2014. 537: p. 93–122. https://doi.org/10.1016/B978-0-12-411619-1.00006-9 PMID: 24480343

54. Brown D.L., Bias in image analysis and its solution: Unbiased stereology. J Toxicol Pathol, 2017. 30(3): p. 183–191. https://doi.org/10.1293/tox.2017-0013 PMID: 28798525

55. Weibel E.R., Stereological Methods II. Theoretical foundations. 1980, London: Academic Press.

56. Kayser K., et al., AI (artificial intelligence) in histopathology—from image analysis to automated diagnosis. Folia Histochem Cytobiol, 2009. 47(3): p. 355–61. https://doi.org/10.2478/v10042-009-0087-y PMID: 20164018

57. Baddeley A.J., Gundersen H.J., and Cruz-Orive L.M., Estimation of surface area from vertical sections. J Microsc, 1986. 142(Pt 3): p. 259–76. https://doi.org/10.1111/j.1365-2818.1986.tb04282.x PMID: 3735415

58. Nyengaard J.R. and Gundersen H.J.G., The isector: A simple and direct method for generating isotropic, uniform random sections from small specimens. Journal of Microscopy, 1992. 165(3): p. 427–431.

59. Model M.A., Methods for cell volume measurement. Cytometry A, 2018. 93(3): p. 281–296. https://doi.org/10.1002/cyto.a.23152 PMID: 28622449

60. Cuellar E. and Solis L., First use of stereology to quantify the survival of fat autografts. Image Anal Stereol 2005. 24: p. 187–193.

61. Aslan H., et al., Effect of a high fat diet on quantitative features of adipocytes in the omentum: An experimental, stereological and ultrastructural study. Obes Surg, 2006. 16(11): p. 1526–34. https://doi.org/10.1381/096089206778869942 PMID: 17132420

62. Klingberg A., et al., Fully automated evaluation of total glomerular number and capillary tuft size in nephritic kidneys using lightsheet microscopy. J Am Soc Nephrol, 2017. 28(2): p. 452–459. https://doi.org/10.1681/ASN.2016020232 PMID: 27487796

63. Mzinza D.T., et al., Application of light sheet microscopy for qualitative and quantitative analysis of bronchus-associated lymphoid tissue in mice. Cell Mol Immunol, 2018. 15(10): p. 875–887. https://doi.org/10.1038/cmi.2017.150 PMID: 29429996

64. Fiedler S., et al., A practical guide to unbiased quantitative morphological analyses of the gills of rainbow trout (Oncorhynchus mykiss) in ecotoxicological studies. PLoS One, 2020. 15(12): p. e0243462. https://doi.org/10.1371/journal.pone.0243462 PMID: 33296424

65. Azaripour A., et al., A survey of clearing techniques for 3D imaging of tissues with special reference to connective tissue. Prog Histochem Cytochem, 2016. 51(2): p. 9–23. https://doi.org/10.1016/j.proghi.2016.04.001 PMID: 27142295

66. Cai R., et al., Panoptic imaging of transparent mice reveals whole-body neuronal projections and skull-meninges connections. Nat Neurosci, 2018. https://doi.org/10.1038/s41593-018-0301-3 PMID: 30598527

67. Vigouroux R.J., Belle M., and Chedotal A., Neuroscience in the third dimension: Shedding new light on the brain with tissue clearing. Mol Brain, 2017. 10(1): p. 33. https://doi.org/10.1186/s13041-017-0314-y PMID: 28728585

68. Renier N., et al., Mapping of brain activity by automated volume analysis of immediate early genes. Cell, 2016. 165(7): p. 1789–1802. https://doi.org/10.1016/j.cell.2016.05.007 PMID: 27238021

69. arivis-AG, arivis Vision4D Basic Guide, a. AG, Editor. 2018. p. 112.

70. Richardson D.S. and Lichtman J.W., Clarifying Tissue Clearing. Cell, 2015. 162(2): p. 246–257. https://doi.org/10.1016/j.cell.2015.06.067 PMID: 26186186

71. Drenckhan W. and Hutzler S., Structure and energy of liquid foams. Adv Colloid Interface Sci, 2015. 224: p. 1–16. https://doi.org/10.1016/j.cis.2015.05.004 PMID: 26233494

72. Siber A. and Ziherl P., Cellular patterns. 1 ed. 2017: CRC Press.

73. McLaughlin T., et al., Adipose cell size and regional fat deposition as predictors of metabolic response to overfeeding in insulin-resistant and insulin-sensitive humans. Diabetes, 2016. 65(5): p. 1245–54. https://doi.org/10.2337/db15-1213 PMID: 26884438

74. Laforest S., et al., Adipocyte size as a determinant of metabolic disease and adipose tissue dysfunction. Crit Rev Clin Lab Sci, 2015. 52(6): p. 301–13. https://doi.org/10.3109/10408363.2015.1041582 PMID: 26292076

75. Johannsen D.L., et al., Effect of 8 weeks of overfeeding on ectopic fat deposition and insulin sensitivity: Testing the "adipose tissue expandability" hypothesis. Diabetes Care, 2014. 37(10): p. 2789–97. https://doi.org/10.2337/dc14-0761 PMID: 25011943

76. Jacobsson B. and Smith U., Effect of cell size on lipolysis and antilipolytic action of insulin in human fat cells. J Lipid Res, 1972. 13(5): p. 651–6. PMID: 5075509

77. Laurencikiene J., et al., Regulation of lipolysis in small and large fat cells of the same subject. J Clin Endocrinol Metab, 2011. 96(12): p. E2045–9. https://doi.org/10.1210/jc.2011-1702 PMID: 21994963

78. Bahceci M., et al., The correlation between adiposity and adiponectin, tumor necrosis factor alpha, interleukin-6 and high sensitivity C-reactive protein levels. Is adipocyte size associated with inflammation in adults? J Endocrinol Invest, 2007. 30(3): p. 210–4. https://doi.org/10.1007/BF03347427 PMID: 17505154

79. Skurk T., et al., Relationship between adipocyte size and adipokine expression and secretion. J Clin Endocrinol Metab, 2007. 92(3): p. 1023–33. https://doi.org/10.1210/jc.2006-1055 PMID: 17164304

80. Weyer C., et al., Enlarged subcutaneous abdominal adipocyte size, but not obesity itself, predicts type II diabetes independent of insulin resistance. Diabetologia, 2000. 43(12): p. 1498–506. https://doi.org/10.1007/s001250051560 PMID: 11151758

81. McLaughlin T., et al., Inflammation in subcutaneous adipose tissue: Relationship to adipose cell size. Diabetologia, 2010. 53(2): p. 369–77. https://doi.org/10.1007/s00125-009-1496-3 PMID: 19816674

82. McLaughlin T., et al., Subcutaneous adipose cell size and distribution: Relationship to insulin resistance and body fat. Obesity (Silver Spring), 2014. 22(3): p. 673–80. https://doi.org/10.1002/oby.20209 PMID: 23666871

83. McLaughlin T., et al., Enhanced proportion of small adipose cells in insulin-resistant vs insulin-sensitive obese individuals implicates impaired adipogenesis. Diabetologia, 2007. 50(8): p. 1707–15. https://doi.org/10.1007/s00125-007-0708-y PMID: 17549449

84. Blutke A., et al., Light sheet fluorescence microscopy guided MALDI-imaging mass spectrometry of cleared tissue samples. Sci Rep, 2020. 10(1): p. 14461. https://doi.org/10.1038/s41598-020-71465-1 PMID: 32879402

Supporting Information

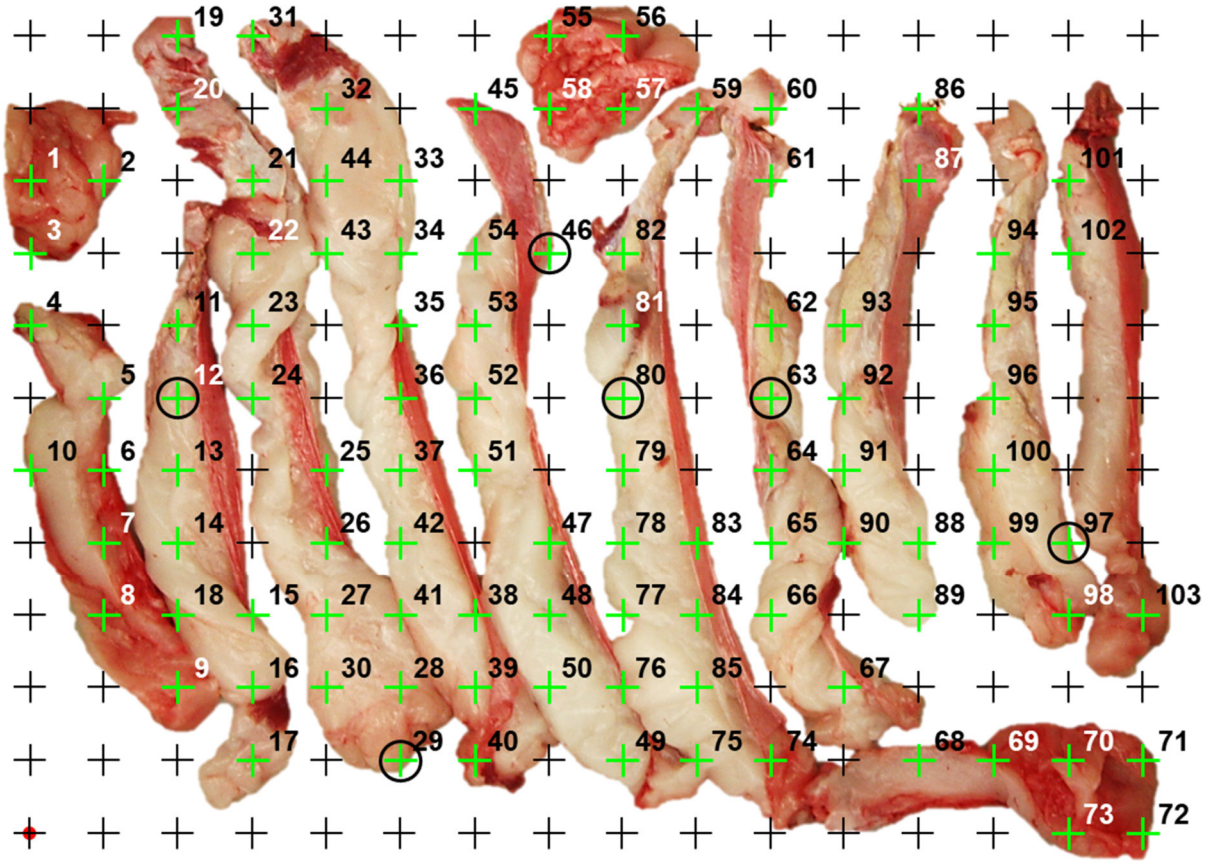

S1 Fig. Systematic uniform random (SUR) sampling for generation of representative adipose tissue samples for downstream quantitative morphological analyses. SUR sampling represents an effective method for generation of representative samples for quantitative stereological analysis (1, 2), *i.e.,* every location within the tissue depot has the same chance to be sampled. In order to generate SUR samples, the whole adipose tissue depot is cut into parallel equidistant slices of approximately 2 cm thickness. All tissue slabs are uniformly laid on either their right or their left side and are then superimposed with an appropriately sized cross grid printed on a plastic transparency. The first sampling location is randomly chosen, whereas all subsequent samples are systematically taken at a previously determined interval (2-5). The outermost left lower cross of the grid is placed over a random point (•) out of the tissue. All crosses hitting the adipose tissue are counted. In the present example, starting on the left side and counting each piece of fat clockwise, 103 crosses hit the tissue. For demonstration, these crosses are numbered and highlighted in green colour. In the present example, six sampling positions are to be sampled. Therefore, every 17th position where a cross hits the adipose tissue is sampled (103 / 6 ≈ 17). The first sampling position is determined randomly in the first interval (1 to 17). This is done using a random number table. In the present example, the position of the 12th cross (N°12) hitting the tissue is randomly sampled as the first sampling site. Next, the position of every seventeenth cross hitting the tissue is systematically sampled. In the present example, these are the positions N°29, 46, 63, 80, and 97 (marked by a circle). The corresponding tissue locations can be tagged by slightly raising the transparency and placing a small piece of clean, blank confetti paper on the surface of the adipose tissue slice using a pair of tweezers. The tissue samples are excised, using a sharp blade. The transparencies may be cleaned, dried, and reused.

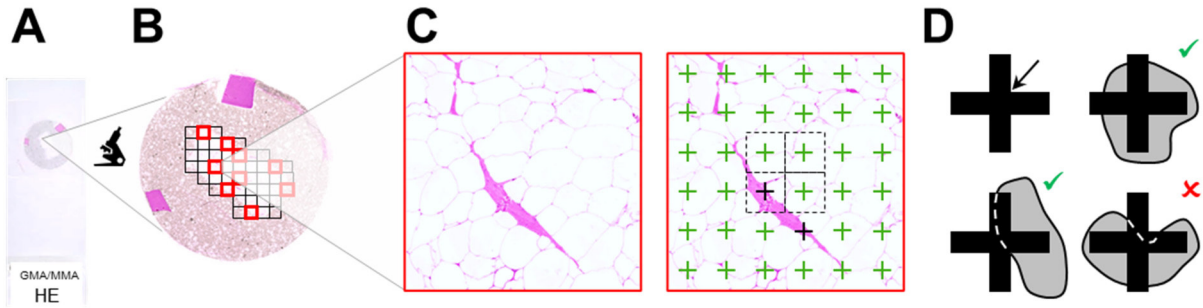

S2 Fig. Determination of the volume density and total volume of adipocytes in adipose tissue depots. The volume density of adipocytes in the adipose tissue (*i.e.,* the proportion of the volume of adipocytes in the adipose tissue volume) and the deduced total volume of adipocytes in a defined adipose tissue depot can be estimated from the fractional area density of fat cell section profiles and the total adipose tissue section area in unbiased sections of the sample (principle of Delesse) (6). The volume density of adipocytes in the adipose tissue ($V_{V(AC/ATD)}$) can efficiently be determined by point counting, using adequately spaced cross grids superimposed on the respective sections. The total volume of adipocytes in an adipose tissue depot ($V_{(AC,ATD)}$) is calculated by multiplying the volume density with the total volume of the fat depot ($V_{(AC,ATD)} = V_{V(AC/ATD)} \times V_{(ATD)}$). To obtain unbiased estimates of the volume density with acceptable error probabilities, the specimens must be SUR sampled, an adequate number of microscopic fields of views (FOV) on appropriate magnification must be examined and an adequate number of points hitting the reference compartment (*i.e.,* adipose tissue) has to be counted. Since the volume density is a dimensionless parameter it is therefore independent of embedding related tissue shrinkage and can conveniently be estimated using standard paraffin sections (assuming equal effects of embedding related shrinkage on adipocytes and other cell types or structural components in the adipose tissue). Using paraffin sections also allows for determination of volume densities of immunohistochemically detectable tissue structures in adipose tissue sections, such as *e.g.,* lymphocytes, macrophages, blood capillaries or nerves. In a given experiment the appropriate number of test points can be read of a nomogram published by Weibel (7, 8). For volume density of adipocytes within the adipose tissue ranging from 85-95%, counting of ~100 points hitting the adipose tissue in all analyzed fields of view in all examined sections per case is sufficient to obtain an estimate with an expected relative probable error of <5% of the mean $V_{V(AC/ATD)}$ (8). In **A**-**C**, the single analysis steps of the estimation of $V_{V(AC/ATD)}$ are schematically illustrated. **A.** Slide with a hematoxylin eosin stained GMA/MMA section of a SUR sampled adipose tissue specimen (for shape-stability and better contrast, the adipose tissue specimen was casted in blackened agar prior to embedding in GMA/MMA). Two pieces of liver tissue were co-embedded for orientation. **B.** Systematic uniform random sampling of fields of view (FOV) for subsequent analysis (indicated by red boxes). **C.** Microscopic view of a sampled FOV (left). An adequately spaced cross grid is superimposed over each FOV (right). Every cross is equal to certain (but not necessarily known) area, indicated as dashed squares surrounding the four central crosses. To determine the fractional area density of adipocyte section profiles in the adipose tissue, the number of crosses hitting the reference compartment (*i.e.,* the adipose tissue) and the number of crosses hitting adipocyte section profiles are counted. In this example, all 36 crosses hit the reference compartment, 34 of them hit adipocyte section profiles (green crosses) and the two remaining ones hit connective tissue (black crosses). The volume density of adipocytes in the adipose tissue depot is calculated from the quotient of the cumulative number of points hitting adipocyte section profiles and the cumulative number of points hitting adipose tissue section profiles in all examined FOVs of all analyzed sections and tissue samples per case ($V_{V(AC/ATD)} = A_{A(AC/ATD)} = \sum Pt_{(AC)} / \sum Pt_{(\cancel{ADT}\ ATD)}$; here: 34/36 = 0.94 ≙ 94 %). **D.** Cross counting rules. A cross is counted only if the upper right inner corner of the vertical and horizontal lines (arrow) covers the section profile of the tissue structure of interest.

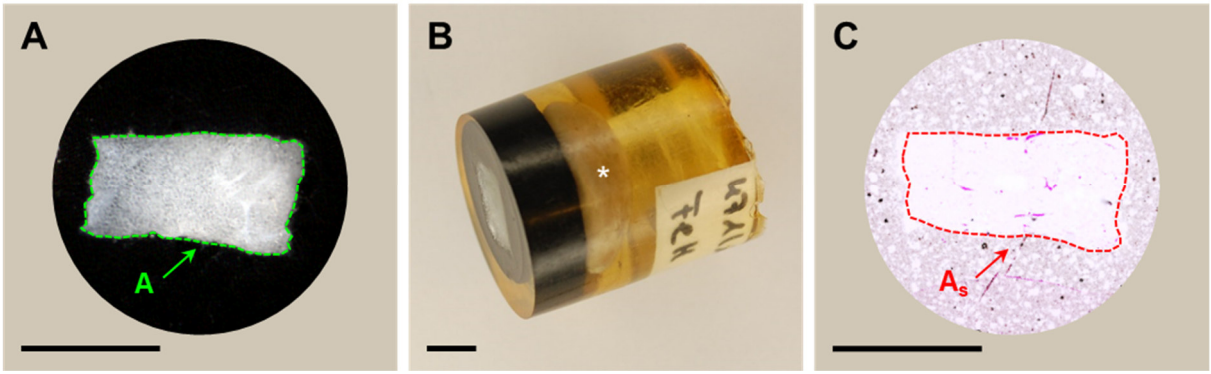

S3 Fig. Estimation and correction of embedding related tissue shrinkage. In paraffin, the most commonly used histological embedding medium, embedding related tissue shrinkage is irregular, inconsistent, and generally high, which makes prediction, monitoring and correction of embedding related tissue shrinkage impossible (3, 4, 9-11). Thus, other embedding media causing lower and homogenous tissue shrinkage such as glycolmethacrylate/methylmethacrylate (GMA/MMA) and diglycidyl ether (Epon) are preferred in distinct quantitative stereological analysis approaches for estimation of shrinkage sensitive morphological parameters (12), such as the physical disector (5, 13, 14) for determination of numerical volume densities of adipocytes in a defined adipose tissue depot. The extend of embedding related adipose tissue shrinkage, expressed as the linear tissue shrinkage factor f_s (3, 15) can be determined from the area of the section surface prior to (**A**), and after (**C**) embedding (A_S). **A.** Scan of a formalin-fixed adipose tissue sample embedded in blackened agar (for contrast and shape stability of the sample). The section area A (marked with green dashed line) of the fat tissue can directly be determined by planimetric measurement, using a commercially available morphometry system. **B.** The same adipose tissue sample after embedding in GMA/MMA. (The asterisk marks a small stone used as a ballast during the embedding procedure). **C.** The first complete histological section cut from the GMA/MMA block is stained with hematoxylin and eosin (HE). The section area A_S (marked with a red dashed line) of the adipose tissue sample, now after embedding related tissue shrinkage, is again determined. The linear tissue shrinkage factor f_s is calculated as $f_s = \sqrt{(A_S/A)}$. Bars = 5 mm.

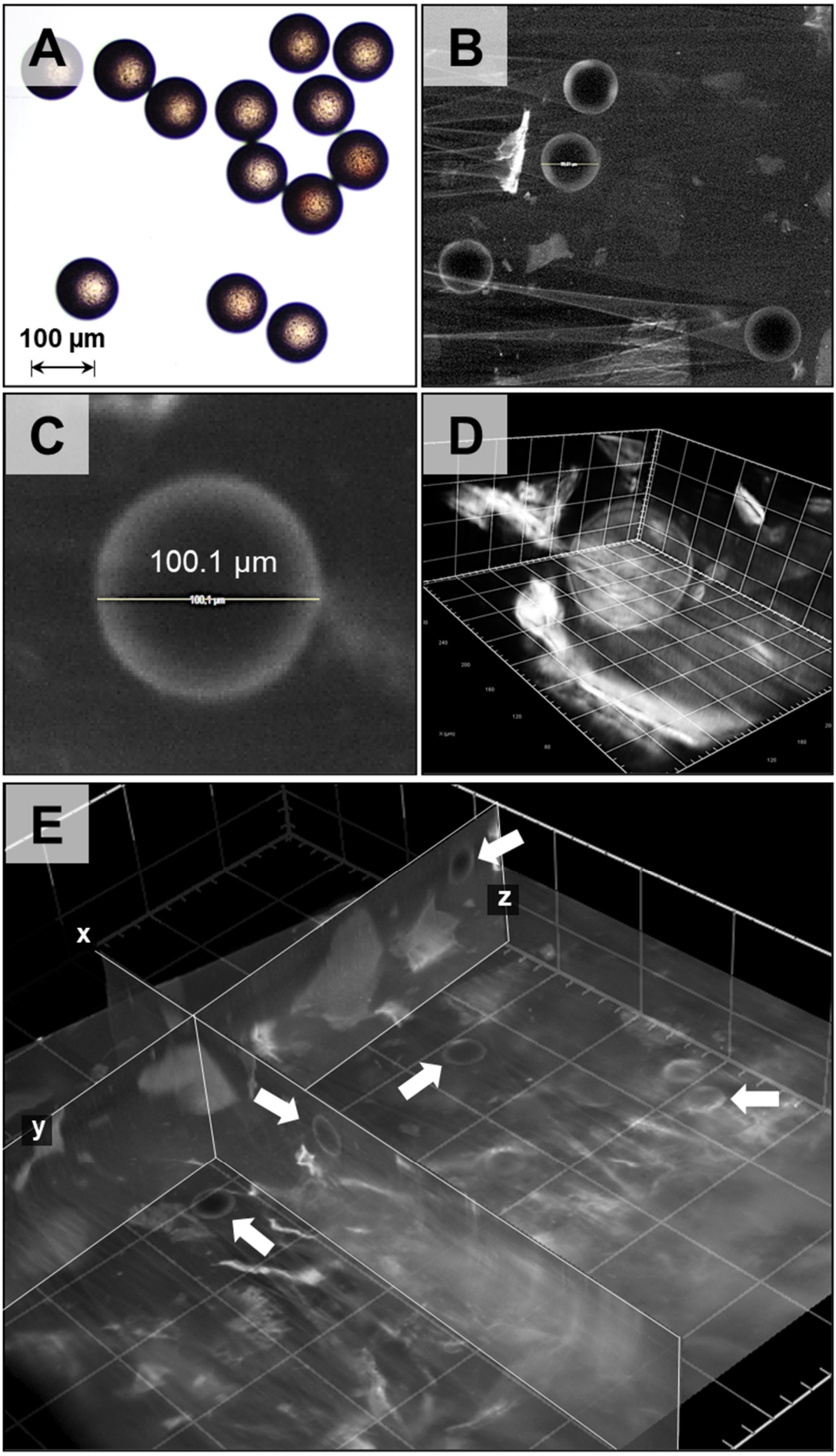
A
100 µm
B
C
100.1 µm
D
E
x
z
y

S4 Fig. Control of correct LSFM-image (pixel/voxel-size) scaling/calibration for realistic object shape- and volume-rendering in digital 3D LSFM image reconstructions. Fluorescence-labelled, spherical, smooth, polystyrene (RI: 1.59) microbeads with a defined diameter of 99.9 ± 1.8 µm (*i.e.,* similar to the size of adipocytes) are used as shape- and volume standards. The beads are shape- and volume stable (*i.e.,* not shrinking) and resistant to organic and aqueous solvents. The microbeads are immobilized by embedding in agar. The agar block is subsequently fixed, optically cleared (3DISCO), imaged in BABB medium (RI: 1.56) and analyzed, using exactly the same LSFM-instrument-, image-acquisition-, and analysis-settings, as used for analysis of adipose tissue samples. Volume measurement results obtained by analysis of digital LSFM-images/3D-image reconstructions are then compared to the "true" volumes of the spherical microbeads, calculated from their physical diameters ($V=(4/3)*\pi*r^3$). **A.** Light microscopic image of microbeads. The beads display uniform spherical shapes and sizes. **B.** Microbead section profiles in 2D optical digital LSFM-images acquired at (Ex/Em) 520/40 nm / 585/40 nm. The "cloudy" fluorescence signals around the beads are derived from flakes in the agar-embedding medium. **B**, **C.** The measured diameter of the equatorial (middle) section profile of the microbead (100 µm) corresponds with its physical diameter, thus confirming the correctness of the (automatically) set pixel-size scaling in x- and y-direction. **D**, **E.** 3D image reconstructions of microbeads generated from a z-stack of 2D fluorescence images with a z-step size of 5 µm. The reconstructed bead images have a uniform spherical shape and size. **D.** 3D image reconstruction of a single microbead. **E.** 3D image reconstruction of agar-embedded microbeads. In all three directions of space (x-y plane, x-z plane and y-z plane), the equatorial microbead image planes display a circular contour, visually confirming the realistic rendering of the spherical shape of the microbeads without artificial distortion (compression or elongation) in z-direction. The correctness of the (automatically) set pixel-size scaling in z-direction (*i.e.,* the z-step height) is additionally confirmed by the mean microbead volume measured in the LSFM-images (534 ± 14 x10³ µm³) that is virtually equal to the mean "true" physical volume (522 ± 28 x10³ µm³) of the microbeads (<5% difference, $p < 0.3$).

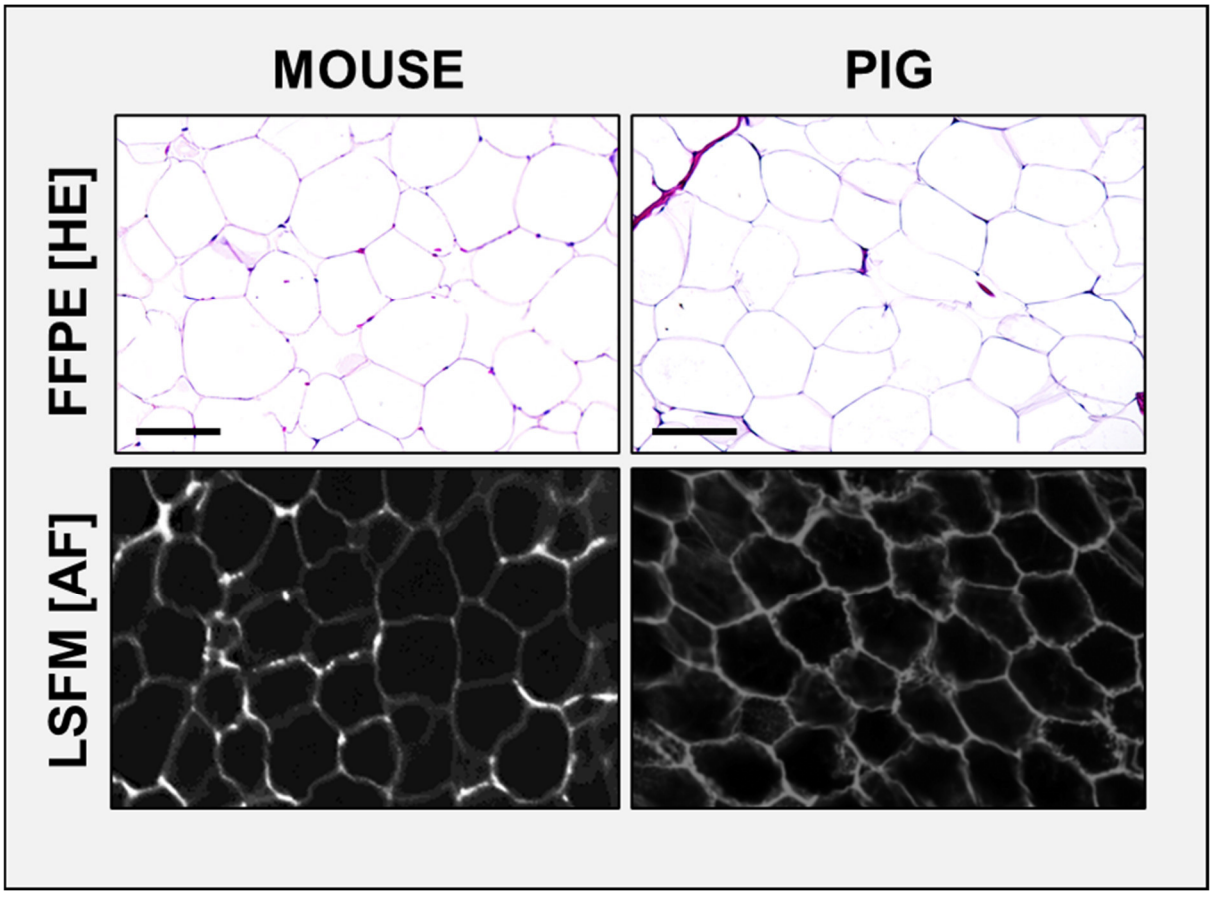

S5 Fig. Demonstration of the principal similarity of the morphology of adipocytes in histological sections and LSFM-images from murine and porcine subcutaneous adipose tissue samples. FFPE: Formalin-fixed and paraffin-embedded tissue section; HE: Hematoxylin and eosin-staining. LSFM: Light sheet fluorescence microscopy; AF: Autofluorescence detection at 585/40 nm wavelength (excitation range: 520/40 nm). Bar = 100 µm.

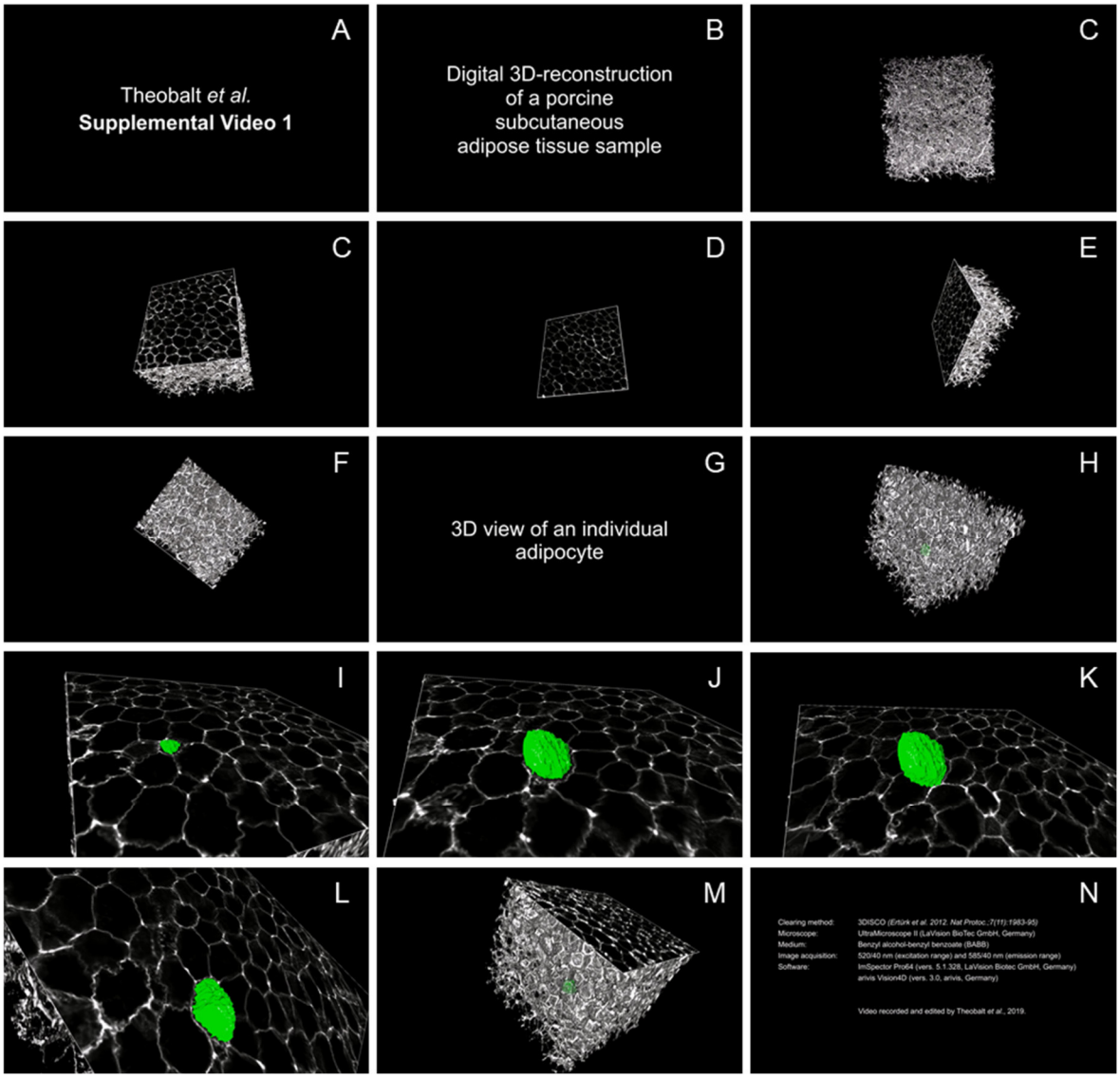

S1 video. LSFM 3D reconstruction of a 3DISCO cleared porcine subcutaneous adipose tissue sample. Autofluorescence signals of (adipocyte) cell membranes are visualized in gray color (*please note that the adipose tissue sample shown here was not post stained with eosin to increase autofluorescence*). Rotating 3D-view and virtual 2D-optical section planes of the adipose tissue sample [0:00-0:28 sec]. An individual adipocyte within the sample is highlighted in green color [0:29-0:43 sec].

Explanatory note. The original S1 video file (MP4) can be downloaded from: https://doi.org/10.1371/journal.pone.0248594.s006. Here, a timeline series (A-N) of screenshots taken from the video is shown. **A.** Title. **B-F.** Rotating image of a 3D reconstructed adipose tissue sample (**C**) with a (virtual) section plane moving through the sample (**D-F**). Adipocyte cell membranes appear as grey lines. **G-M.** 3D-view of an individual adipocyte (highlighted in green color). A virtual section plane moves through the rotating sample, allowing to view the adipocyte shape from all directions. **N.** Credits and additional information.

Step-by-step protocol for unbiased sampling and volume analysis of adipocytes in 3D LSFM image reconstructions, using the arivis Vision4D imaging and analysis software

This protocol describes the generation of 3D LSFM image reconstructions from z-stacks of 2D LSFM-images of cleared adipose tissue samples using the arivis Vision4D (arivis, Germany) imaging and analysis software (I), as well as unbiased sampling of adipocytes with the disector method (II), and the direct 3D digital image analysis of individual adipocyte volumes with the "*Magic Wand*" tool (III). For practical exercise, a training dataset (Supporting Information S2 file) from the present study [containing 181 2D-LSFM-z-stack-images acquired in a 3DISCO-cleared, eosin-stained, s.c. adipose tissue sample of an obese Göttingen minipig at Ex/Em: 520/40nm/585/40nm with a z-step height of 5 µm] can be downloaded from: doi:10.5061/dryad.8gtht76nt.

[The present protocol is only intended to serve as a supporting information protocol describing the application of methods featured in the corresponding publication by Theobalt et al. (2021). The protocol is neither an officially authorized publication of the arivis AG, nor does any of the authors have any commercial association with this company. For more detailed information on the applicability of the software, computer-system requirements, or available trial versions, the interested reader is referred to the arivis Vision4D homepage (https://www.arivis.com/en/), and the arivis Vision4D operation manual and video-tutorials (https://imaging.arivis.com/en/imaging-science/arivis-vision4d-video-tutorials).]

I. Generation of 3D LSFM image reconstructions of cleared adipose tissue samples

I.1) Open the arivis Vision4D imaging and analysis software (version 3.0 or higher).

I.2) Drag-drop the folder with the 2D LSFM z-stack images to the opened arivis Vision4D window. An "*Import files – Assume same structure for all files?*"-window will pop up. Klick "*Yes*". Then a "*Import files –Select import destination*"-window will open. Choose "*New File*", select folder and file name and klick "*OK*" (During import of the training dataset, an "*Import files –Select import scenario and destination*"-window will open. Choose the *"images as planes"* scenario as well as "*New File*", select folder and file name and klick "*OK*"). A pop-up window will appear, showing the progress of image import. The software will create an SIS file (as well as a corresponding "*metadata*" and "*objects*" file) from each imported z-stack. By double-clicking on the SIS file, the imported dataset can be re-opened in the last saved setting (if the corresponding "*metadata*" and "*objects*" files are present in the same folder) without having to import the z-stack again.

I.3) After the image z-stack is loaded, a 2D view of the median image plane will appear (**Screenshot 1A**). Use the "*Zoom to Fit*" button (encircled in red) to display the entire image on the screen. Image properties (gamma-correction, contrast. brightness, color-channels, *etc.*) can be changed using the controllers/sliders displayed in the windows on the right side of the screen. The image plane displayed in the left screen window is set using the slider (red arrow) in the "*Navigator*" window (black arrow). In the presented example, fluorescence signals (of adipocyte membranes) are displayed in the grey-color channel (one channel) in the AUTO-intensity mode (red arrow). By default, the medial image plane of the z-stack (here: N° 147) is displayed.

Usually, the correct pixel size-scaling is automatically directly acquired from the metadata of the imported LSFM-image z-stack file. Using the training dataset S2 file, the correct pixel-scaling might, however, be reset to the default value of 1 µm in each direction of space. Therefore, the correct pixel size scaling for this dataset must be controlled in advance (**Screenshot 1B**). This is done by clicking on the *"Data"* button and then selecting *"Pixel Size"* in the pull-down menu (red arows). Enter the correct pixel sizes for the training dataset S2 file (X: 755,112 nm, Y: 755,112 nm and Z: 5) and klick on "*Change pixel size*" (arrow).

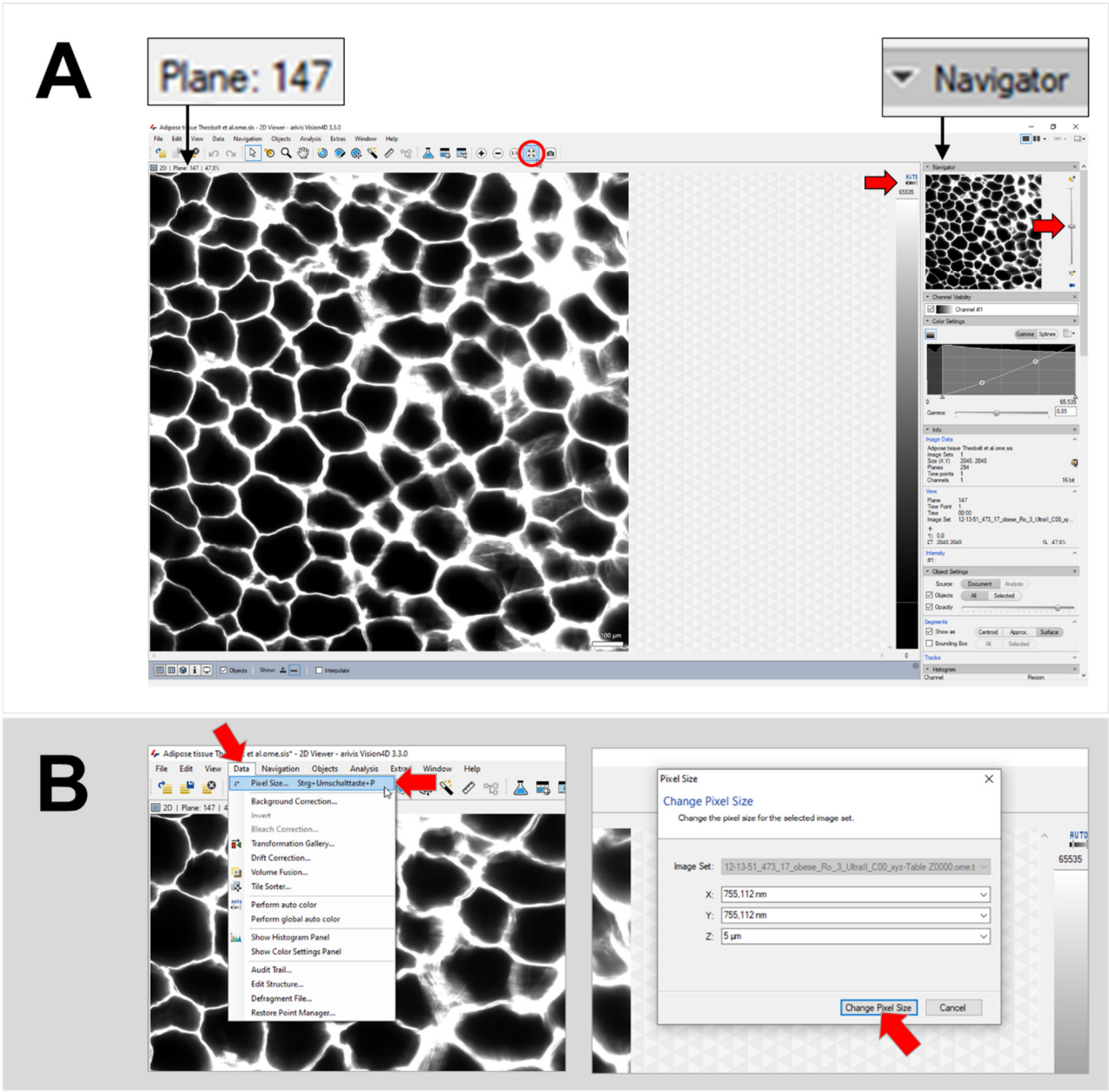

Screenshot 1.

II. Unbiased sampling of adipocytes in 3D LSFM images with the disector method

For measurement of individual cell volumes, adipocytes are unbiasedly sampled in the 3D LSFM image of the adipose tissue sample, using the disector method. This sampling design warrants that the selection of adipocytes is not biased by their volume (size), shape, or orientation (i.e., that the adipocyte volume measurement results are not biased). The principle of the disector method is extensively explained in the main paper.

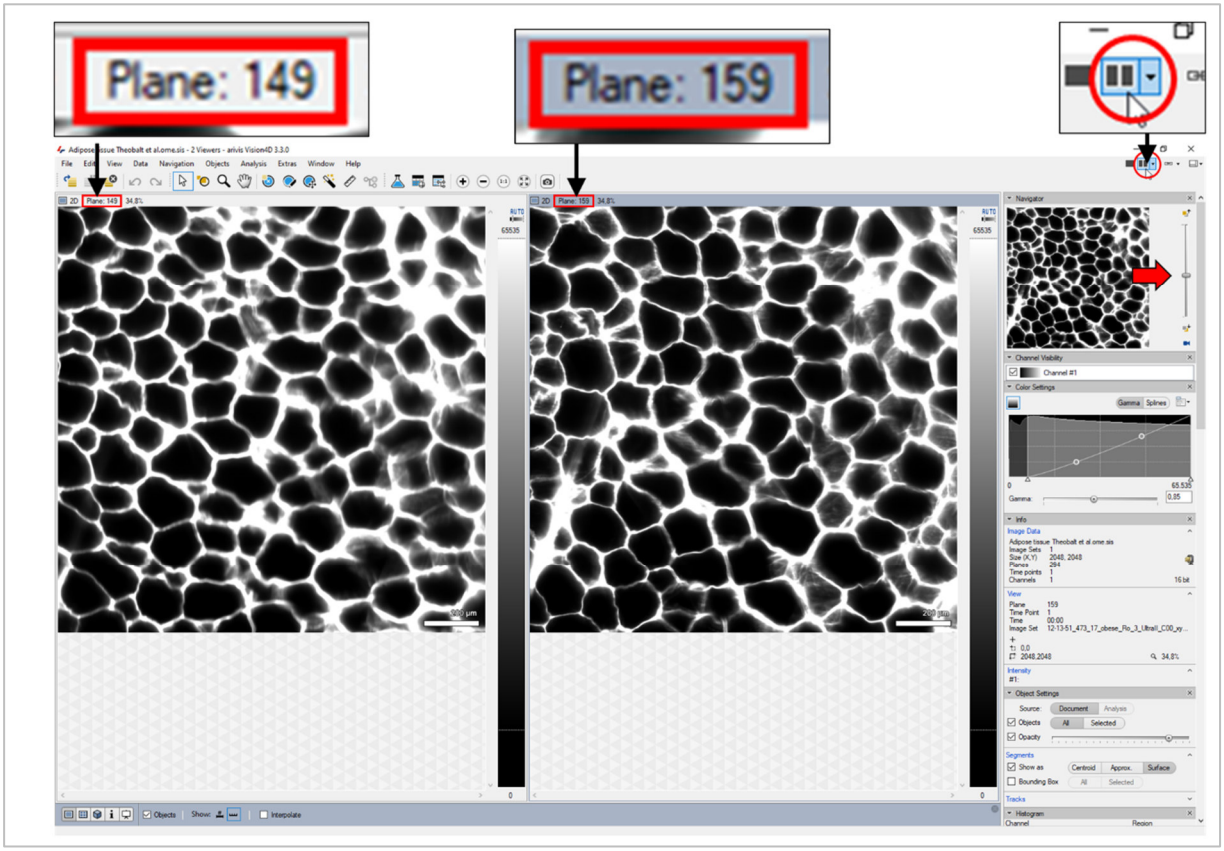

Screenshot 2.

II.1) Select the split-screen modus (encircled in red) for parallel display of two different section planes (**Screenshot 2**). To display both images in the same size, select each window and press the "*Zoom to Fit*" button (see I.3, **Screenshot 1A**).

II.2) Select a random section plane as the disector reference section plane (random sampling can be performed, using a random number table from an internet-random number generator). This section plane should be sampled from the middle of the z-stack (*i.e.,* in a range starting from approximately 40 section planes after the first, and 40 section planes before the last section plane of the image z-stack) to warrant that all section planes of the sampled adipocytes are completely present within the image set. Here, section plane N° 159 (black arrow) is sampled as the reference section plane (right screen window, the darker grey-blue color of the window frame indicates that this window is currently active).

II.3) Then switch to the left screen window (*i.e.,* the second section plane window) and systematically determine the disector look-up section plane considering the applicable disector height (*i.e.,* the distance between the reference- and the disector look-up section plane). The disector height should be approximately 1/3rd of the minimal linear orthogonal projection of the measured objects (*i.e.,* 1/3rd of the minimal adipocyte diameter – here, a disector height of 50 µm was chosen, referring to 10 section planes with an average single section thickness (*i.e.,* z-step height) of 5 µm), and section plane N° 149 was sampled as disector look-up section plane (black arrow). Use the slider in the "*Navigator*" window (red arrow) to move to the determined disector look-up section image plane.

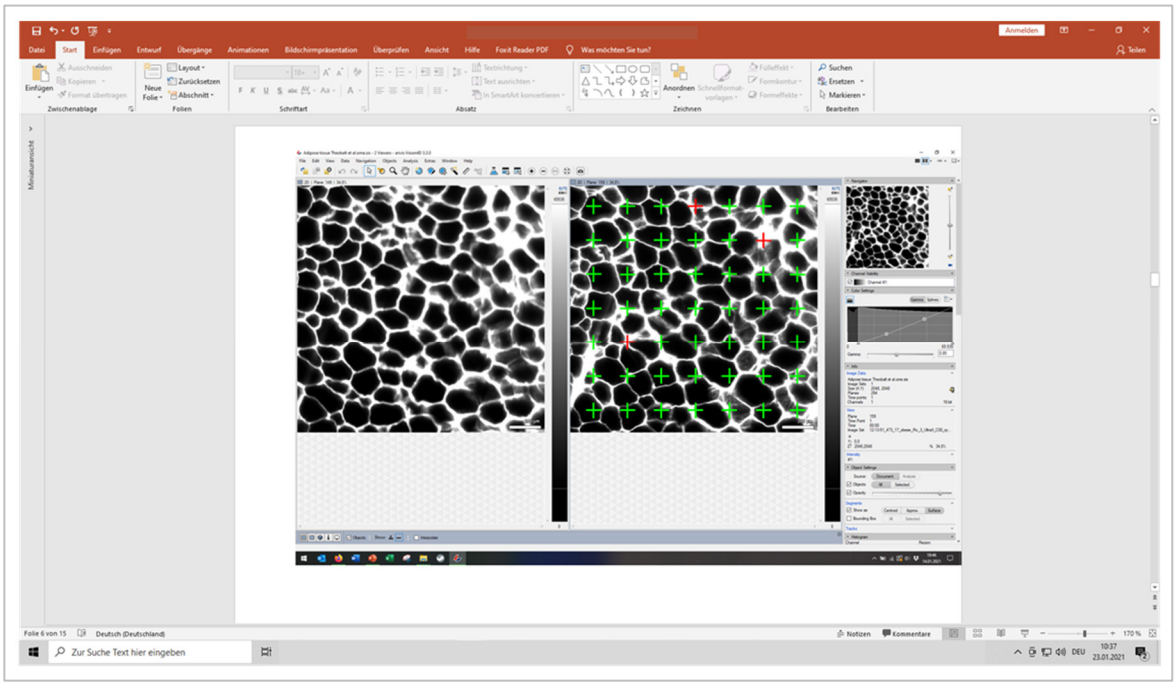

Screenshot 3.

II.4) Optionally (if not performed in paraffin sections) the area density of adipocytes in the adipose tissue can be determined by point-counting for estimation of the volume density of adipocytes in the adipose tissue. Since the arivis Vision4D imaging and analysis software does not provide a tool for superimposing cross grids, a screenshot of the image of the disector-look-up section is copied into another software-application (*e.g.,* Microsoft PowerPoint) and superimposed with a grid of equally spaced test points/crosses (**Screenshot 3**). The number of crosses hitting adipocyte section profiles (green) are counted (points are counted, if the upper right corner of a cross hits the structure of interest, *i.e.,* an adipocyte cross section profile) and this number is related to the total number of crosses hitting the adipose tissue (here, crosses hitting non-adipocyte cross sections within the adipose tissue, such as connective tissue strands, are displayed in red color). Here, 46 crosses of a 7x7 (49) point cross grid hit adipocyte cross section profiles.

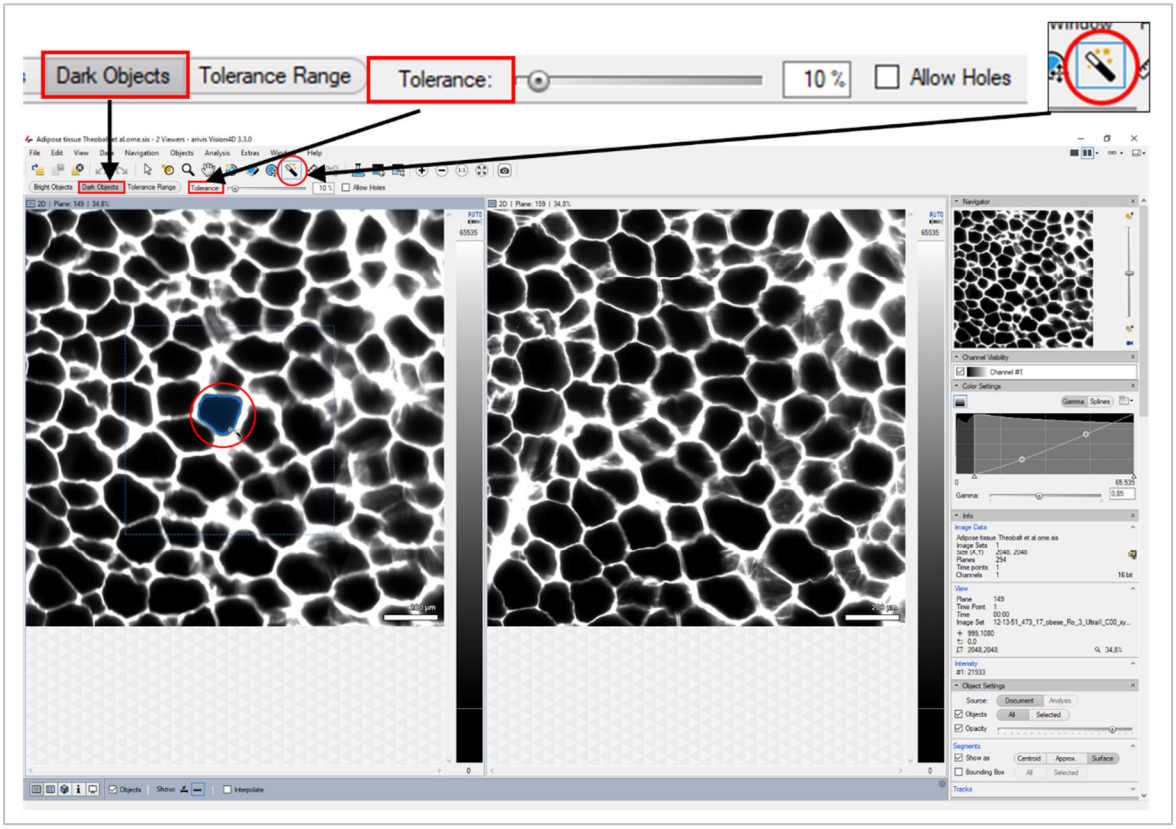

Screenshot 4.

II.5) Select the "*Magic Wand*" tool (encircled in red, **Screenshot 4**) in the disector look up section image plane (N° 149, left screen side). Select the "*Magic Wand*" tool properties "*Dark Objects*" and a "*Tolerance*" of 10% (respectively of another appropriate tolerance level – use the same tolerance level for analysis of all images in all cases of a study). Move the mouse cursor over an adipocyte cross section profile (a square region of interest is shown around the mouse cursor and a preview of the section profile detected by the "*Magic Wand*" tool is displayed in a bluish color when hovering over it with the "*Magic Wand*" tool) and klick inside the black (unstained) center of the cell section profile (encircled in red).

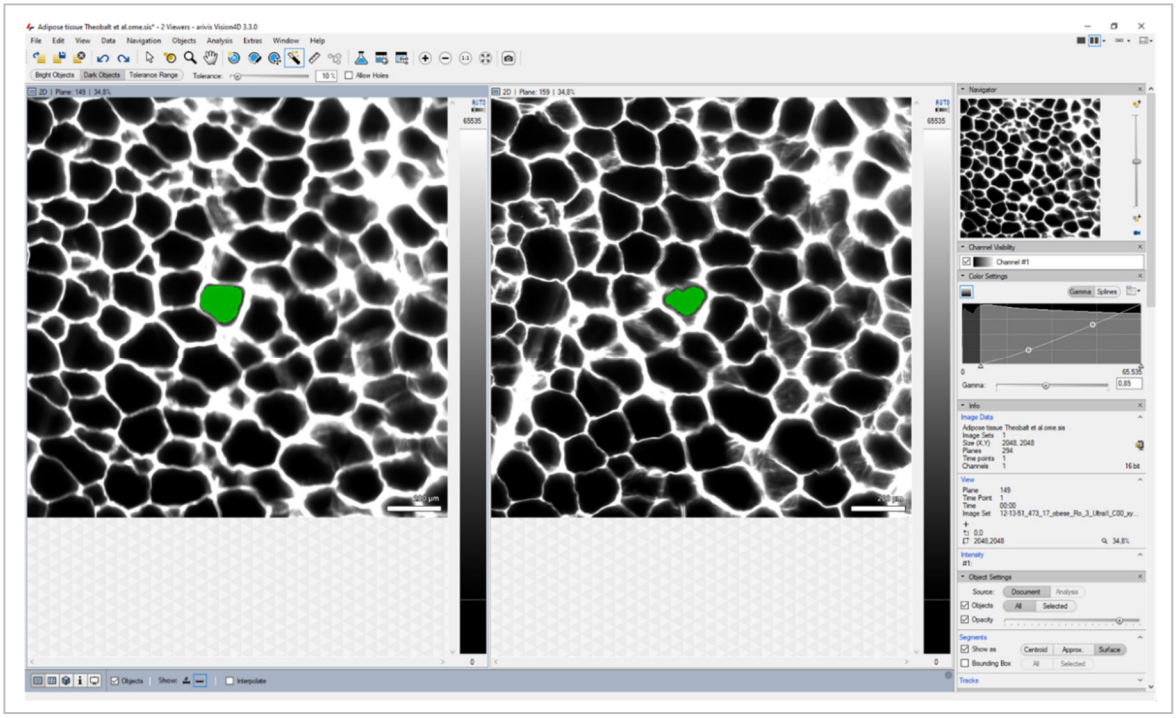

Screenshot 5.

II.6) The "*Magic Wand*" tool will automatically recognize the outer boundaries of the adipocyte cell membrane and label the adipocyte cell section profile areas in all image section levels of that single adipocyte with an individual color, *i.e.,* the profile of the adipocyte tagged in section plane N° 149 will automatically be tagged in the same color in section plane N° 159 (**Screenshot 5**) on right screen side (as well as in all other section planes).

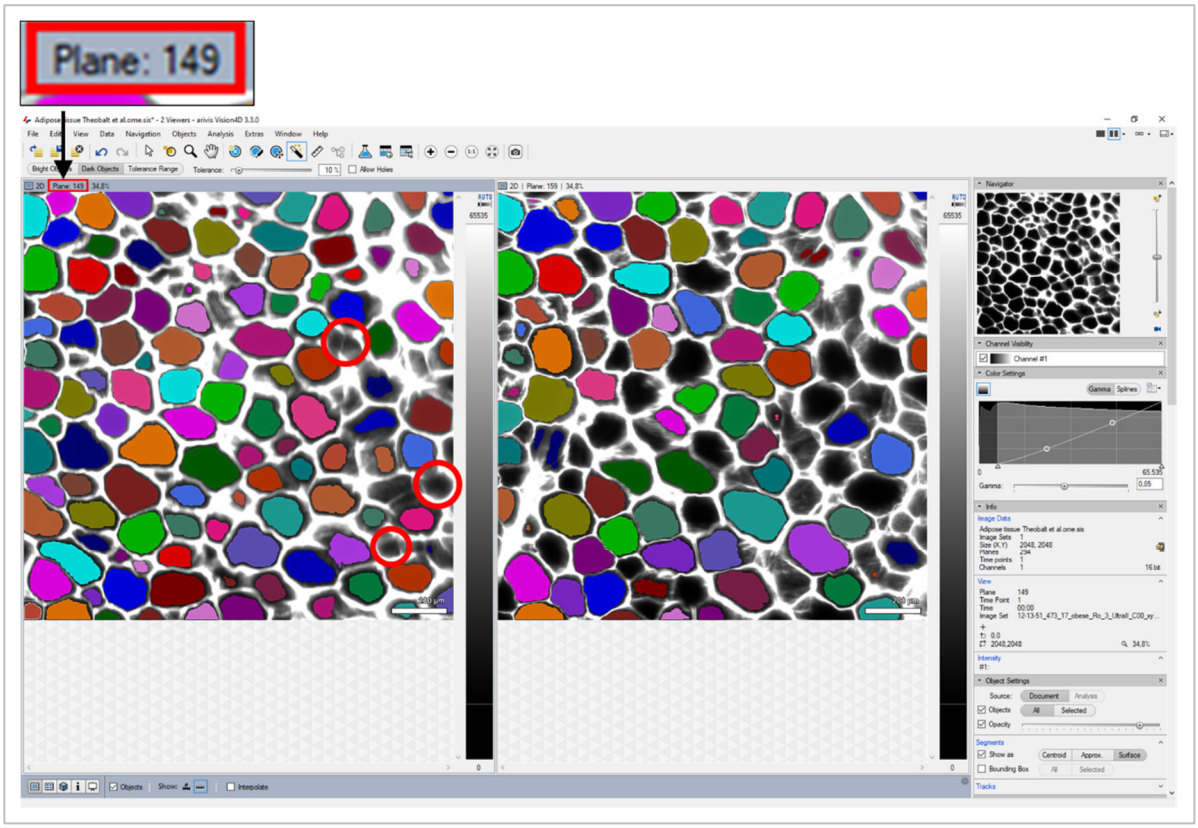

Screenshot 6.

II.7) Tag all adipocyte cross section profiles present in the look up section plane (section plane N° 149, **Screenshot 6**). Adipocytes also sectioned in the reference section plane (image plane N° 159) will automatically appear labeled in the corresponding color. Some adipocyte cross section profiles might apparently remain unlabeled (encircled in red) in the look up section plane (here: plane N° 149) although being tagged with the "*Magic Wand*" tool (**Screenshot 6**). By moving the slider of the "*Navigator*" window it can be controlled if the corresponding cell sections are correctly identified and labelled in upper/lower image section levels. **Screenshot 7** shows image section plane N° 139, where the cell section profiles of adipocytes which were apparently not labelled in section plane N° 149, are correctly labelled (encircled in red).

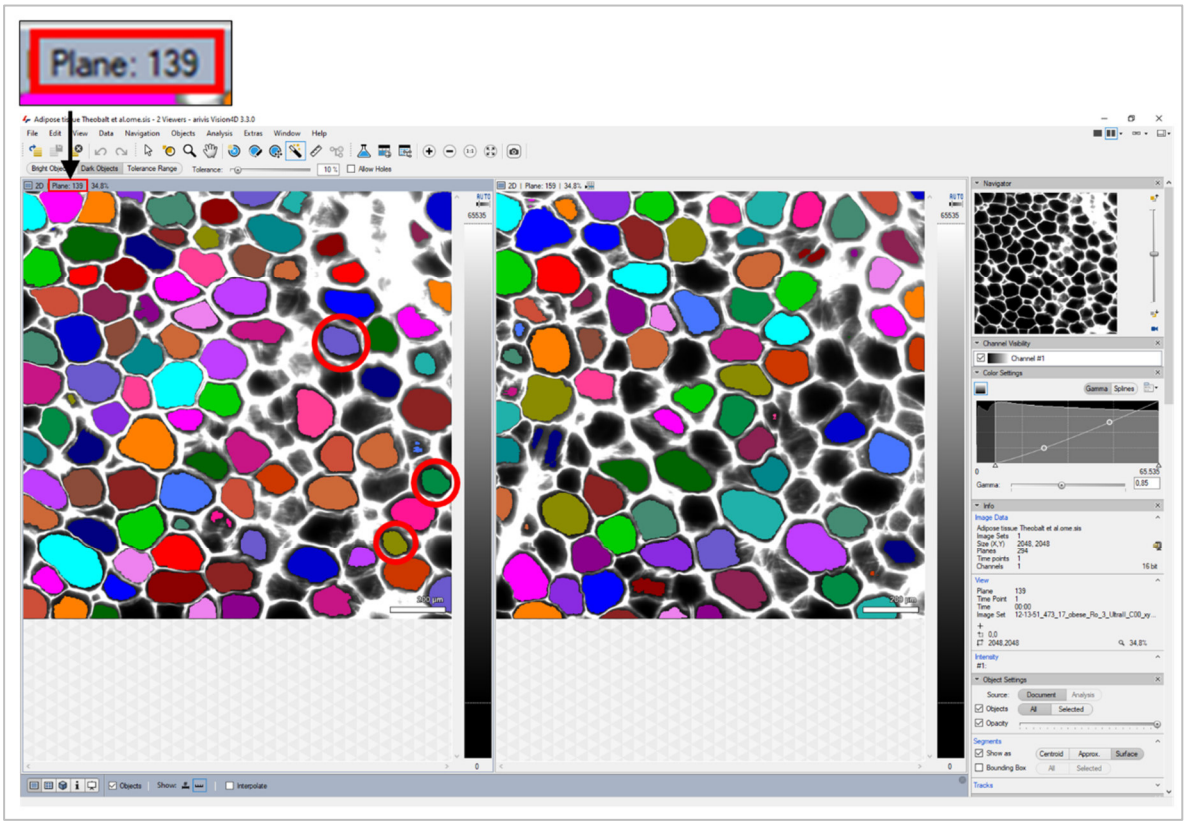

Screenshot 7.

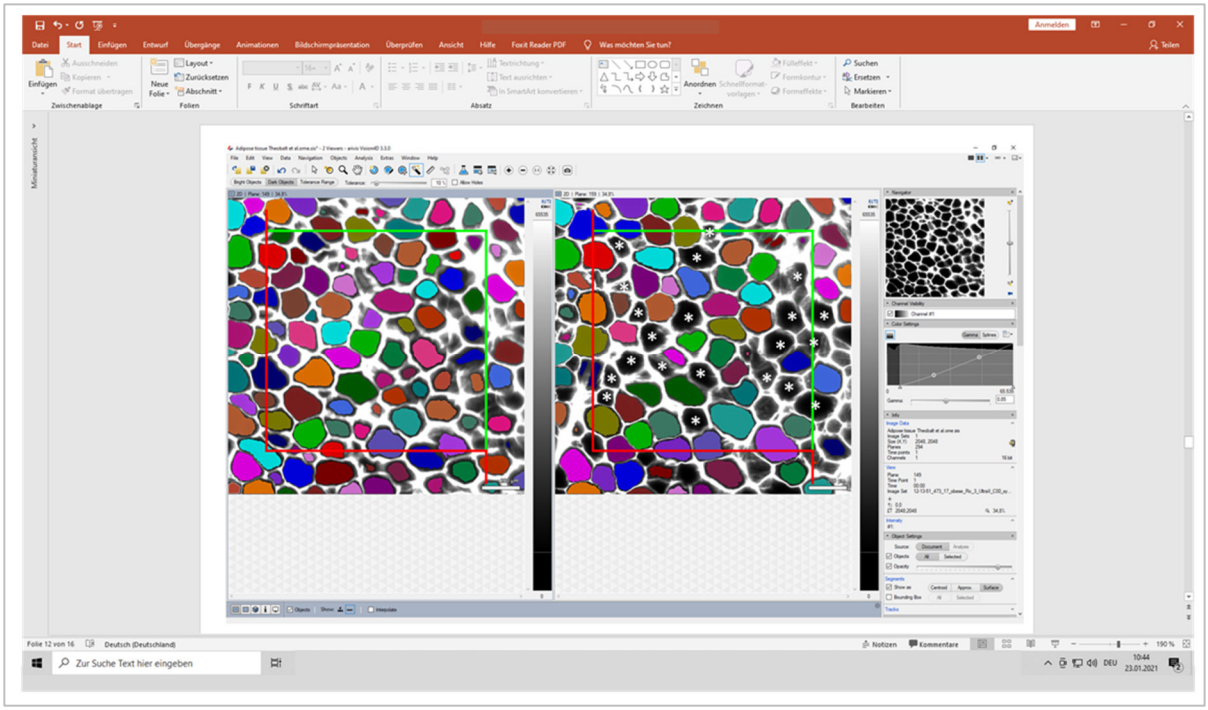

Screenshot 8.

II.8) When all adipocyte cross section profiles present in the look up section plane are tagged with the "*Magic Wand*" tool take a screenshot, copy it into another software-application (*e.g.,* Microsoft PowerPoint), and superimpose an unbiased counting frame (of known area) over a random location of the look up section plane (left screen side). Then also superimpose a second, equally sized unbiased counting frames over the corresponding location of the reference section (right screen side). [The arivis Vision4D imaging and analysis software does not provide a tool for superimposing unbiased counting frames]. Here, the area of the unbiased counting frame is 1165 x 1165 µm² (only relevant if numerical volume densities of adipocytes in the adipose tissue are determined with the disector method). Adipocytes present in the reference section plane but not in the look-up section plane are sampled with the unbiased counting frame (indicated by asterisks), using the (green) "inclusion lines" and (red) "exclusion lines" (**Screenshot 8**).

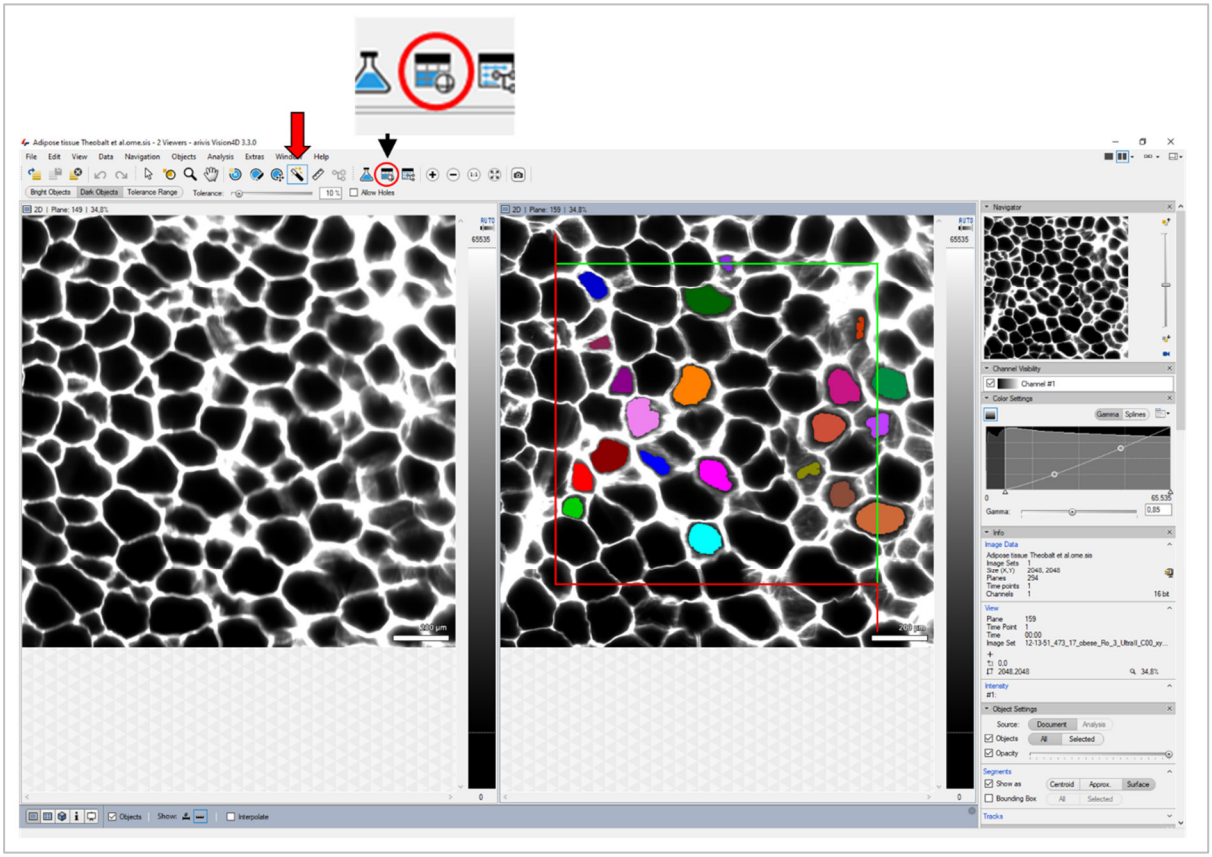

Screenshot 9.

II.9) Move back to the arivis-window. Select the "*Show Objects Table*" button (encircled in red) and mark and delete all so-far tagged "*Magic Wand Objects*" (see III.3, **Screenshot 11**). Then again use the "*Magic Wand*" tool (arrow) to tag the section profiles of the adipocytes in the disector reference section plane sampled with the unbiased counting frame (indicated by asterisks in II.8, **Screenshot 8**) in the previous step. For better visualization, the unbiased counting frame is also superimposed here. In the present disector, 21 adipocytes are sampled.

III. Direct 3D digital image analysis of individual adipocyte volumes

The "Magic Wand" tool is used to directly analyze volumes and other quantitative morphological parameters of the sampled adipocytes. To monitor the correct labelling/tagging of individual adipocytes (i.e., to verify that the analyzed cells are adipocytes, and that only individual adipocytes are analyzed), cells tagged with the "Magic Wand" tool can be inspected in the 3D view of the imaged tissue sample.

III.1) With the reference section plane being active, select the 3D image display (red circle, red arrow in detail enlargement) to view the sampled adipocytes in 3D (**Screenshot 10, A**). Tick "*Objects*" and select "*Surface*" (red circle) for the display of 3D objects (**1**). Move the slider of the control row (**2**) down to see the "*4D Clipping"* panel (**Screenshot 10, B, 3**).

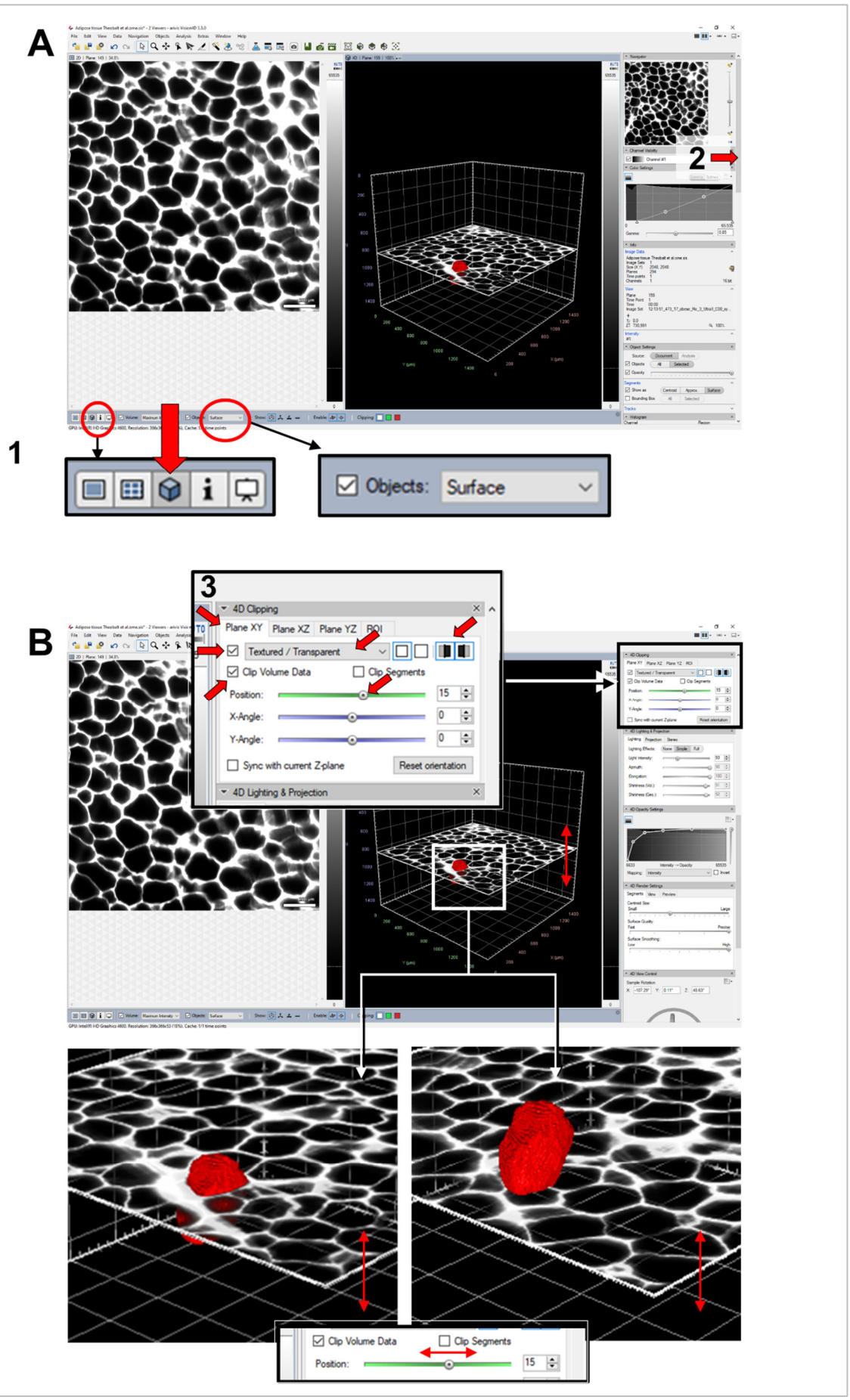

Screenshot 10.

III.2)To view individual adipocytes tagged with the "*Magic Wand*"-tool in 3D, select adipocytes to be displayed in the 3D view from the "*Objects Table*" (III.3, **Screenshot 11**). In **Screenshot 10 B**, the adipocyte (tagged in red color) sampled in the 2D view in **Screenshot 9** is displayed in the 3D-view. For better visualization, use the "*4D Clipping*" panel (**3**) to display a digital clipping plane through the tissue sample, using the indicated settings (red arrows). The position of the clipping plane can be varied, using the "*Position*"-slider. The 3D image of the adipocyte (*i.e.,* the "*Magic Wand Object*") can be freely rotated and viewed from different perspectives. Use this tool to control the completeness of the 3D-labelling of the adipocyte in relation to its cell membrane boundaries (compare to Supporting Information **S1 video**). Control any sampled adipocytes in this way.

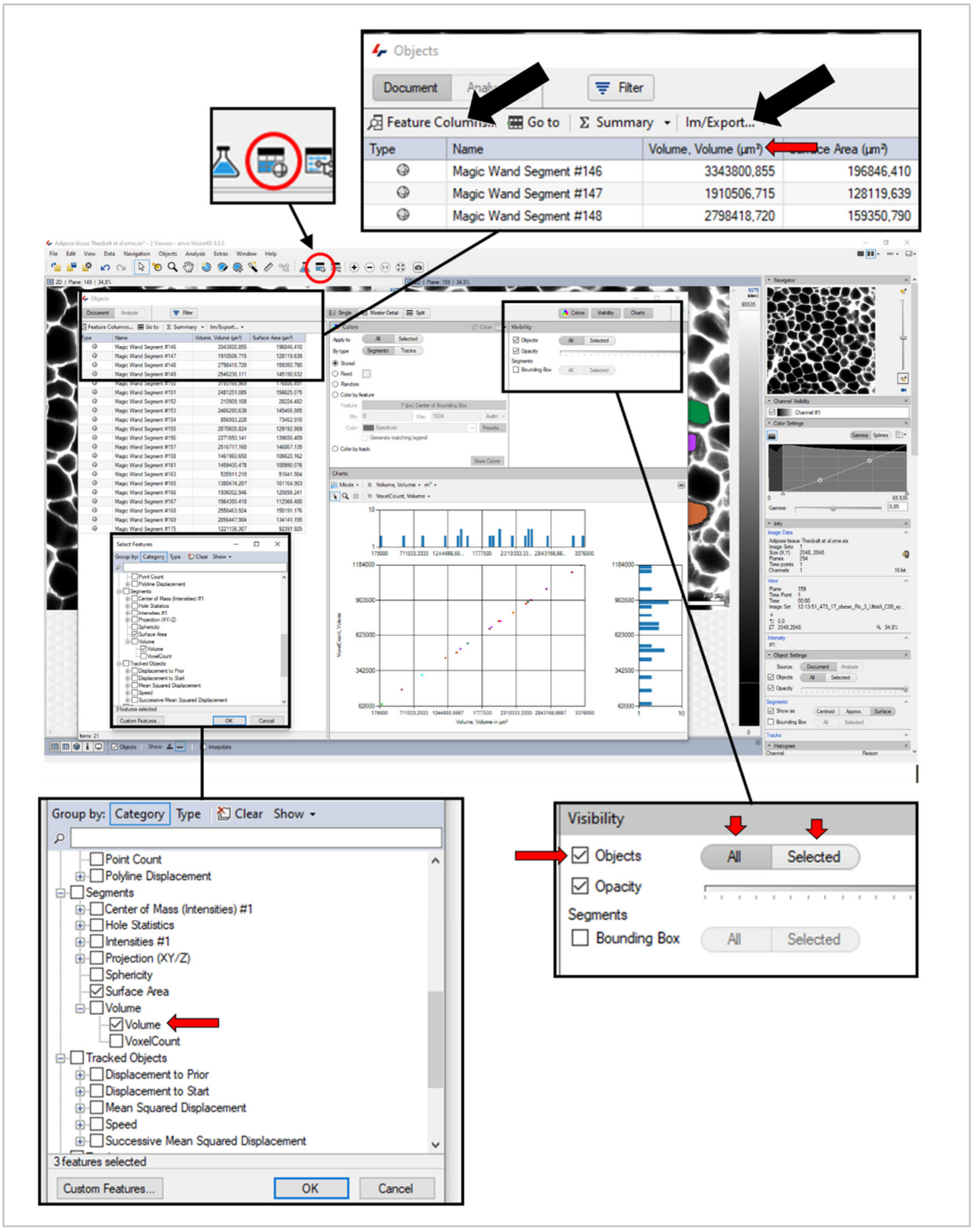

Screenshot 11.

III.3)For selection and analysis of morphometric parameters of unbiasedly sampled adipocytes tagged with the "*Magic Wand*" tool (*i.e.,* "*Magic Wand Objects*") klick the "*Show Objects Table*" button (encircled in red, **Screenshot 11**). The "*Objects Table*" (inset) shows all "*Magic Wand Objects*" (titled as "*Magic Wand Segments*") with their associated morphometric measurement results. The analyzed morphometric parameters can be selected from the "*Feature Columns*" menu (black arrow). In the present example, the parameters of "*Volume*" (red arrow) and "*Surface*" were selected (inset). Tagged adipocytes (*i.e., "Magic Wand Objects"*) can be selected (or deleted) individually in the "*Objects Table*", as groups, or all. Selected "*Magic Wand Objects*" are correspondingly displayed in the 2D/3D viewer(s), as set in the "*Visibility*"-window (inset, red arrows). The analysis results can be exported from the "*Objects Table*" menu (*e.g.,* to Microsoft EXCEL), using the "*Im/Export*"-function (black arrow).

S1 file. Step-by-step protocol for disector sampling and volume analysis of adipocytes with the arivis Vision4D imaging and analysis software. The protocol describes the generation of 3D image-reconstructions from z-stacks of 2D LSFM-images of cleared adipose tissue samples using the arivis Vision4D imaging and analysis software, the subsequent unbiased sampling of adipocytes with the disector method, and direct 3D digital image analysis of individual adipocyte volumes.

S2 file. Exemplary LSFM-dataset. Downloadable from: doi:10.5061/dryad.8gtht76nt. For practical exercise, a z-stack of 181 2D-LSFM-image files from the present study can be downloaded from the URL provided in the paper on the publishers homepage. LSFM images were acquired from a 3DISCO-cleared, eosin-stained, subcutaneous adipose tissue sample of an obese Göttingen minipig, exactly as described in the "Materials and Methods" section (Ex/Em: 520/40nm/585/40nm; z-step size = 5 µm).

Literature

1. Howard CV, Reed MG. Unbiased Stereology. 2 ed. Coleraine, UK: QTP Publications; 2005. 278 p.
2. Gundersen HJ, Jensen EB. The efficiency of systematic sampling in stereology and its prediction. J Microsc. 1987;147(Pt 3):229-63.
3. Albl B, Haesner S, Braun-Reichhart C, Streckel E, Renner S, Seeliger F, et al. Tissue sampling guides for porcine biomedical models. Toxicol Pathol. 2016;44(3):414-20.
4. Blutke A, Wanke R. Sampling strategies and processing of biobank tissue samples from porcine biomedical models. J Vis Exp. 2018(133).
5. Howard CV, Reed MG. Unbiased Stereology. 2 ed. Coleraine, UK: QTP Publications; 2005.
6. Delesse MA. Procédé mécanique pour déterminer la composition des roches. C R Acad Sci Paris 1847;25:544-5.
7. Weibel ER. Stereological methods. I. Practical methods for biologicalmorphometry. London: Academic Press; 1979.
8. Weibel ER. Stereological Methods II. Theoretical foundations. London: Academic Press; 1980.
9. Dorph-Petersen KA, Nyengaard JR, Gundersen HJ. Tissue shrinkage and unbiased stereological estimation of particle number and size. J Microsc. 2001;204(Pt 3):232-46.
10. Gundersen HJG, Mirabile R, Brown D, Boyce RW. Stereological principles and sampling procedures for toxicologic pathologists. In: Haschek WMea, editor. Haschek and Rousseaux´s Handbook of Toxicologic Pathology London: Academic Press. INC.; 2013. p. 215-86.
11. Tschanz S, Schneider JP, Knudsen L. Design-based stereology: Planning, volumetry and sampling are crucial steps for a successful study. Ann Anat. 2014;196(1):3-11.
12. Blutke A, Schneider MR, Wolf E, Wanke R. Growth hormone (GH)-transgenic insulin-like growth factor 1 (IGF1)-deficient mice allow dissociation of excess GH and IGF1 effects on glomerular and tubular growth. Physiol Rep. 2016;4(5):e12709.
13. Matenaers C, Popper B, Rieger A, Wanke R, Blutke A. Practicable methods for histological section thickness measurement in quantitative stereological analyses. PLoS One. 2018;13(2):e0192879.
14. Sterio DC. The unbiased estimation of number and sizes of arbitrary particles using the disector. J Microsc. 1984;134(Pt 2):127-36.
15. Mattfeld T. Stereologische Methoden in der Pathologie. Doerr W, Leonhardt H, editors. Stuttgart-New York: Georg Thieme Verlag; 1990.

V Discussion

The present work was designed to test whether quantitative morphological analyses based on laser light sheet fluorescence microscopy (LSFM) allow for an objective quantification and characterisation of obesity-associated changes of adipocyte morphology and growth patterns in subcutaneous and visceral adipose tissue depots of an established porcine large animal model of diet-induced obesity [37]. The results of the LSFM-based quantitative morphological analyses were verified using design-based quantitative stereological analysis methods, which represent the gold standard for estimation of quantitative morphological parameters in histological tissue sections [20-22].

Obesity is currently regarded as one of the most important health threats worldwide [1]. In parallel with the increase in the number of obese people, diseases such as T2D and CVD are rising, primarily due to obesity-associated metabolic alterations. If several cardiovascular risk factors occur simultaneously (*inter alia* visceral obesity, insulin resistance, dyslipidaemia and a proinflammatory profile), it is referred to as metabolic syndrome [2, 5].

In humans, metabolic alterations correlate rather with the adipose tissue distribution than the total fat mass [11, 12]. In line with this, subcutaneous and visceral adipose tissue depots seem to respond differently to constant energy surplus [16]. Especially an increase in visceral adipose tissue alongside with adipose tissue inflammation is considered to play a key role in the pathogenesis of the (human) MetS [9, 109]. A possible explanation for these *inter*-depot differences might be adipose tissue depot specific growth patterns [16]. Hyperplasia, which mainly occurs in the subcutaneous adipose tissue seems to result in a healthy expansion of fat tissue, whereas hypertrophy may cause cellular stress when reaching the expansion limit, ultimately leading to dysfunctional adipocytes [29, 109, 184, 186].

In translational medicine, a variety of animal models, ranging from rodents to large animals such as pigs, are used [253]. Traditionally, rodents are used in most translational obesity studies [253]. The advantages of a short reproductive interval, simple and inexpensive husbandry and the availability of a large number of genetically different strains are offset by the low life expectancy and large anatomical and physiological differences to humans, which limit the ability of these

models to adequately reflect the full spectrum of obesity-associated changes occurring in human adipose tissue and metabolism [17-19, 255]. Porcine models, however, demonstrate much higher similarities to humans in *inter alia* gastrointestinal anatomy, eating behaviour, and metabolic regulation compared to rodents and can be reproduced comparatively easily due to *inter alia* all season breeding and multiple offspring [17, 18, 61, 267]. Especially pigs with diet-induced obesity are thought to better reflect the obese state in humans compared to monogenetic models such as the *db/db* mouse, since obesity is a multifactorial disease [17, 253, 254]. Total sequencing of the of pig- and Göttingen minipig genome additionally enables for research in genomics, proteomics and metabolomics. However, the use of porcine models is also associated with higher general costs, more elaborate husbandry and lower acceptance in the population compared to rodents [267].

Taking advantage of the beneficial characteristics of porcine models, a recently established DIO Göttingen minipig model [37] was used in the present work to characterise obesity-associated morphological changes on adipocyte level in subcutaneous and visceral adipose tissue depots. Animals of this model develop a pronounced obesity in both adipose tissue depots, as well as metabolic alterations such as an altered lipid profile and insulin resistance that are also observed in the human MetS [37]. Additionally, these obese minipigs display histomorphologically manifest multifocal adipose tissue inflammation in the visceral adipose tissue, which has also been observed in obese human with MetS and murine DIO models [37, 89].

Especially adipocyte cell size seems to play an important role in the pathogenesis of the inflammatory alterations, which contribute to the development of the metabolic syndrome [9, 15, 29, 184]. Thus, adequate methods for quantitative morphological analysis of adipose tissue samples are of great importance to gain valuable insights in the pathogenesis of relevant quantitative morphological alterations in adipocyte growth patterns.

For the analysis of quantitative morphological adipocyte parameters, several different approaches are possible. Methods such as the Coulter Counter or flow cytometry to determine adipocyte volumes and numbers are performed on isolated fat cells [183, 273, 274, 278]. The liberation of the fat cells from the adipose tissue

can be easily achieved by, for example, enzyme digestion or osmium tetroxide [183, 271]. However, rupture, especially of large, fragile adipocytes, or swelling of fat cells may occur, which lead to biased results in subsequent analyses [29, 183, 271, 274, 280]. Furthermore, isolated fat cells in solution display a different shape (approximately spherical) than adipocytes observed in histological sections (icosahedral/tetracaidecahedronic) from adipose tissue samples [183, 276].

In addition to the examination of isolated fat cells, adipocyte section profiles in histological tissue sections are quantitatively analysed in a large number of (translational) obesity studies on human and animal adipose tissue. This can be performed precisely and quickly using manual or software-assisted (*e.g.,* ImageJ) planimetric analysis methods [271]. Two-dimensional quantitative morphometric parameters obtained by these analyses, such as mean adipocyte section area/diameter or the number of adipocyte section profiles per section area, are used to describe possible (pathogenesis-relevant) alterations in adipocyte morphology. However, relevant 3D adipocyte parameters such as mean volumes and numbers are neither equivalent to these 2D parameters nor can they be directly deduced from them [21, 284, 296]. It is also not possible to derive information about individual adipocyte volumes or fat cell size distributions in the respective reference compartment from two-dimensional morphometric parameters obtained in single histological sections [297]. For example, the orientation of the section plane to anisotropic structures influences the shape and size of the corresponding section profiles [23, 285]. Additionally, the larger the volume of a tissue structure, the greater the probability that it will be hit by an arbitrarily oriented section plane, which can lead to an overrepresentation of large section profiles in the histological section [296]. The generation of histological tissue sections is also accompanied by a dimensional reduction (3D to 2D) and thus a loss of information [284, 293, 294]. In addition, embedding-related tissue shrinkage may occur [282]. Therefore, an unbiased determination of the 3D fat cell parameters mean adipocyte volume and total adipocyte number needed to characterise the obesity-associated adipocyte growth pattern (*i.e.,* hypertrophy and/or hyperplasia), as well as individual adipocyte volume, is not possible by measurement of two-dimensional quantitative morphometric parameters (*e.g.,* areas of adipocyte section profiles) in single histological sections [20, 21, 285, 296, 297].

To obtain these parameters, unbiased, design-based quantitative stereological methods are required, which represent the gold standard for quantitative morphological analyses in histological tissue sections [20, 21, 284, 293, 298]. In contrast to model-based quantitative stereology, which is based on assumptions about *inter alia* the shape, orientation and distribution of tissue structures of interest and is therefore principally considered biased, design-based quantitative stereology solely relies on statistical sampling principles and stochastic geometry that guarantee unbiased estimation of three-dimensional quantitative parameters in two-dimensional tissue sections with statistically defined and tolerable error probabilities [20, 23, 300]. The application of (systematic) random sampling designs on each sampling level, which guarantees that every sampled tissue specimen/-section, field of view *etc.* is a representative of the reference compartment, is a key prerequisite for unbiased quantitative stereological analyses [20, 21, 23, 301].

The three-dimensional morphological parameters determined by quantitative stereological analyses are estimates of their corresponding density values such as volume- and numerical volume densities (*i.e.,* the proportional volume and number of structures within the respective reference compartment) [23, 28]. Different stereological probes ensure unbiased analyses despite the loss of dimensional information that occurs when a two-dimensional tissue section is generated from a three-dimensional tissue sample [293, 294]. Volume densities can be determined in single two-dimensional tissue sections using points as stereological probe, whereas the estimation of mean volumes and numerical volume densities requires three-dimensional stereological probes (*e.g.,* physical disector) as well as consideration of embedding related tissue shrinkage [20, 21, 293]. To guarantee a random interaction with the structure of interest, all stereological probes must be placed at random onto the histological tissue sections and when determining surfaces area- and lengths densities, the section plane orientation must be randomised as well [20, 23, 28, 285]. Since all quantitative stereological parameters can be estimated in IUR sections, it might be beneficial to prepare such sections irrespective of the actual quantitative stereological parameter in question, as this enables subsequent analyses of additional IUR or VUR section dependent parameters [20, 21, 305]. The estimated relative values must be corrected for embedding-related tissue shrinkage (in case of shrinkage-sensitive parameters) and multiplied with the total volume of the corresponding reference compartment (except for fractionator designs) to obtain

unbiased absolute values, thereby avoiding the reference trap [20, 28, 285, 308]. To unbiasedly determine individual cell volumes following the principle of Cavalieri, analyses of cell section profile areas in exhaustive parallel equidistant serial sections are required. In the case of unilocular adipocytes, for example, which are comparatively large cells, a high number of serial sections would be needed [21, 23, 301]. Together with the identification of corresponding cell section profiles becoming increasingly difficult with higher vertical distances between two examined sections, this quantitative stereological analysis method is quite time consuming and laborious.

In the present work, subcutaneous and visceral adipose tissue depot samples of the DIO minipig model were analysed to characterise obesity-associated depot-specific quantitative morphological alterations. The samples required for unbiased quantitative stereological analysis and LSFM-based analysis, respectively, of adipocyte volumes, numbers, and mean volumes were SUR-sampled to ensure the unbiasedness and comparability of the results obtained by both analysis methods. Since in adipose tissue differential shrinkage is irrelevant, volume densities of adipocytes are independent of the extent of embedding-related tissue shrinkage and were determined with little effort in arbitrarily oriented paraffin sections of the SUR-sampled fat tissue specimens using point counting. Importantly, the analysis of this parameter can also be performed, for example, on sections of plastic embedded (adipose) tissue samples or even in digital two-dimensional optical LSFM sections. Quantitative stereological analyses of the numerical volume density of the adipocytes in the respective depots as well as the mean adipocyte volume were performed in GMA/MMA sections. This embedding method was chosen, because it allows for the preparation of very thin histological sections and results only in a low, uniform, reproducible and, above all, precisely determinable tissue shrinkage [20, 282, 315]. Adipocytes analysed by unbiased quantitative stereology (and LSFM analysis) were sampled using the physical disector method [21, 314] to guarantee an unbiased, number weighted sampling. Subsequently, the same stereological tool was used to determine the numerical volume density of adipocytes in the respective adipose tissue depots. Compared to other methods, such as fractionator designs, the physical disector is considered technically complex and time-consuming, however, in this study it was found absolutely suitable, at least subjectively [20, 21]. The thin tissue sections generated for the physical disector allow for complete stain

penetration, which is required to clearly identify all tissue components, and reduce bias due to overprojection effects [20, 23]. Additionally, the sampling or counting of adipocytes with this method was subjectively found easier and more reliable, as it is strictly decided by the presence/absence of their cell nuclei section profile in the reference respectively lookup section and not, as for example with the optical disector, whether particles are clearly focused or not (*i.e.,* in or out of the focal plane). For accurate estimation of mean particle volume and number using the physical disector, precise knowledge of the section thickness (for calculating the disector volume) and the embedding-related tissue shrinkage is essential [303, 315]. Therefore, the factual section thickness of the GMA/MMA sections was determined by means of reflectometric measurement analysis [315]. The embedding-related tissue shrinkage, which was determined using established volumetric measurement methods [283, 303], displayed a low standard deviation between individual samples, confirming the uniform extent of three-dimensional GMA/MMA embedding-related tissue shrinkage. The mean volume was calculated from the volume density of adipocytes per adipose tissue depot and the shrinkage corrected numerical volume density of adipocytes per adipose tissue depot. All estimated relative values were multiplied with the total volume of the respective adipose tissue depot to obtain the corresponding absolute values and avoid the reference trap [20, 28, 285, 308].

The unbiased quantitative stereological analysis methods, which have been applied in the present study, allow for an accurate estimation of relevant morphological parameters such as (fat) cell volumes and numbers. However, their application remains complex and time consuming. Furthermore, the application of strict sampling designs throughout the entire examination and the almost always (except for fractionator designs) required knowledge of the total volume of the tissue/organ analysed (*i.e.,* the reference compartment) render the retrospective application of stereological methods on arbitrarily sampled specimen impossible [23, 28, 285, 297].

3D (laser) light sheet fluorescence microscopy (LSFM) of optically cleared adipose tissue samples might be a simple, fast, and elegant alternative. Its applicability for quantitative morphological analyses of optically cleared adipose tissue samples was therefore comparatively tested in the present work. As unbiased quantitative stereological analysis techniques represent the gold standard for estimation of

quantitative morphological parameters in histological tissue sections, they were used to verify the results of the LSFM-based quantitative morphological analyses [20-22]. Both analysis methods were performed on SUR-sampled adipose tissue specimen from identical adipose tissue depots of the same pigs. This way, the comparability of the results of LSFM-based quantitative morphologic analyses of cleared adipose tissue samples and unbiased quantitative stereological methods was guaranteed.

For LSFM-based quantitative morphologic analyses, the fat tissue samples of the subcutaneous and visceral adipose tissue depots were optically cleared using the 3DISCO protocol [325]. With this technique, tissue samples up to several cm^3 can be cleared, which become firm and dimensionally stable, but still easy to cut. Especially the dimensional stability of the cleared adipose tissue samples was a decisive factor in the choice of this clearing protocol. In contrast to other solvent-based clearing protocols, such as iDISCO+ or Adipo-Clear, a considerable tissue shrinkage is associated with the clearing and staining procedure of the 3DISCO protocol [334, 351, 352]. In the present work, the clearing and staining-associated tissue shrinkage was determined using appropriate volumetric measurement methods, and interestingly corresponded approximately the GMA/MMA embedding-related tissue shrinkage of the adipose tissue samples. However, for quantitative morphological analyses of adipose tissue samples, other tissue clearing protocols such as Adipo-Clear and iDISCO+ might represent a suitable alternative and have already been successfully used to clear and subsequently image adipose tissue samples [334, 351, 352].

Individual adipocyte volumes were determined by automatic digital image analysis in three-dimensional reconstructions of the optically cleared fat tissue samples. This method relies on the distinguishability of cell membrane (auto)fluorescence signals and the unstained (*i.e.,* optically empty) centre of the cell. Since the number of voxels within the centre of the fat cell is used to calculate the volume of the individual adipocyte, continuous cell membrane fluorescence signals are therefore essential [347]. Following 3DISCO clearing, the adipocyte cell membranes showed a variably strong autofluorescence at a wavelength of 520/40 nm (excitation range) and 585/40 nm (emission range). However, the cell membrane fluorescence signals of individual adipocytes were often not completely detectable, *i.e.,* interrupted, causing

neighbouring cells to be recognised as one single cell, which would falsify the individual cell volume. Therefore, the adipose tissue samples were stained with eosin following 3DISCO clearing to enhance the autofluorescence signal of the cell membrane, which resulted in a reliable and sufficiently strong cell membrane labelling. Other methods for fluorescence-labelling of adipocyte membranes, such as the use of fluorescence-labelled antibodies, would have been far more elaborate, time and cost-intense. As the LSFM-analysis approach aims for an easy, fast and reliable detection of continuously labelled adipocyte cell membranes in cleared adipose tissue samples, the eosin-enhanced autofluorescence of adipocyte membranes was considered more than sufficient. The samples were imaged at 585/40 nm wavelength (emission range), with a 0.63-10 magnification and a vertical resolution (*i.e.,* z-step height) of 5 µm. The three-dimensional digital reconstruction of the imaged samples was carried out using the arivis Vision 4D software [347]. Although fat cells were only identified by the autofluorescence signal of their cell membrane and were therefore only distinguished from other tissue structures (*e.g.,* connective tissue, vessels, other cell types) by their characteristic shape, incorrect identification was ruled out by visualising questionable structures in 3D.

In LSFM (and 3D fluorescence microscopy in general), the accurate determination of individual adipocyte volumes (and object volumes in general) requires an accurate reconstruction of the 3D image from the z-stacks (*i.e.,* the digital reconstruction must precisely reflect the volume of the imaged object). A nonconformity between the nominal and factual z-step size and imaging artifacts due to spherical aberration may cause distortion of object shapes and their corresponding volumes in the reconstructed 3D images, which can be prevented by the use of appropriate technical equipment and a precise adjustment of the instrument settings [348]. Such precautions were also taken in the present work. For the objective, an optimized dipping cap was used, and the same medium was used as clearing solvent and submersion medium to avoid imaging artifacts caused by spherical aberration [326, 348]. Additionally, the z-step advance, the instrument settings as well as the image scaling were strictly controlled. The accuracy of the reconstructed 3D images of the adipose tissue samples and thus the correctness of the measurement results (*i.e.,* the successful prevention of volumetric measurement errors) was confirmed using fluorescent labelled, spherical polystyrene beads with a defined size (comparable to the size/volume of the analysed adipocytes), which

were immobilized in agar, fixed in 4% neutrally buffered formaldehyde solution, subjected to 3DISCO clearing and subsequently imaged and volumetric analysed with the identical LSFM settings as the fat tissue samples. The diameters and volumes of the test objects determined in the digital z-stack images and the corresponding 3D reconstruction matched precisely the “true” values of the polystyrene beads (see **Supplemental Figure S4** of publication). To ensure accuracy and reproducibility of measurement results, quantitative morphological analyses should in general be performed on identically prepared tissue samples, the same LSFM instruments and analysis settings should be used, and the accuracy of the reconstructed 3D images should be validated (*e.g.,* using standardized test objects as - to our knowledge - first described in the present study for LSFM-based quantitative morphologic analyses of cleared adipose tissue samples). With regard to the comparability and reproducibility of such studies in different laboratories, it must be borne in mind that there are currently no standardised LSFM platforms, *i.e.,* they differ *inter alia* in terms of equipment and configuration. Therefore, in quantitative morphological studies using LSFM, all relevant technical details should be provided accurately, which was done accordingly in the present publication.

For the LSFM-based analysis of adipocyte volumes and numbers in subcutaneous and visceral adipose tissue samples of the porcine DIO model, the same stereological probe (*i.e.,* physical disector in SUR-sampled FOV) as in the unbiased quantitative stereological analysis approach was applied to ensure an unbiased measurement of these fat cell parameters. The resulting shrinkage corrected fat cell volumes and numbers were compared to the results of the unbiased stereological analysis in GMA/MMA adipose tissue sections. The measurement data were virtually equal, which proved that LSFM-based analyses are suitable for the accurate and unbiased determination of relevant quantitative morphological adipocyte parameters.

The LSFM-based analysis of adipose tissue samples was overall, *i.e.,* from tissue clearing to digital quantitative morphological analysis, found to be significantly less complex and time-consuming than unbiased quantitative stereological analyses in two-dimensional histological tissue sections using the physical disector (including elaborate tissue processing and analysis steps). The sampling and subsequent counting of the adipocytes with the disector method, for example, was, at least

subjectively, a lot easier to carry out in the virtual three-dimensional adipose tissue and more reliable than in physical disector section pairs. Most strikingly, LSFM-based analysis additionally allowed for a fast and efficient unbiased determination of individual adipocyte volumes. This is a considerable advantage, as the determination of this parameter in two-dimensional adipose tissue sections is only possible with an almost unjustifiable technical effort. As a result, the size distribution of adipocytes in different adipose tissue depots, which may not cause a net change in mean adipocyte volume, can now be determined for the first time in intact adipose tissue samples. This can help to identify, for example, adipocyte subpopulations with different growth patterns that may contribute to the metabolic changes associated with obesity [29].

Göttingen minipigs of the DIO model showed a strong obesity-associated volume increase of both subcutaneous and visceral adipose tissue depots, which was objectively attributed to depot-specific growth reaction patterns of adipocytes by the results of the present work. In the subcutaneous adipose tissue depot of the obese minipigs, a balanced proportion of adipocyte hyperplasia and hypertrophy occurred, whereas the increase in visceral adipose tissue in these animals was the result of a disproportionate increase in mean fat cell volume with hardly any appreciable increase in the total number of adipocytes. The massive enlargement of visceral adipocytes might explain the multifocal adipose tissue inflammation exclusively occurring in this adipose tissue depot. Reaching the expansion limit may cause cellular stress and might expose the enlarged adipocytes to an increased shear stress [29, 184, 186, 353, 354]. As a consequence, altered adipokine secretion might occur, contributing to a pro-inflammatory milieu in the adipose tissue [29]. Increased inflammatory response in hypertrophic adipose tissue has already been associated in previous studies with the expression of inflammatory genes and increased secretion of pro-inflammatory adipokines with a concomitant decrease in the secretion of anti-inflammatory adipokines [221, 222, 355, 356]. Additionally, hypertrophic adipocytes become insulin resistant, which reduces the antilipolytic effect of insulin, resulting in an increased lipolysis [89, 95].

Interestingly, the metabolism and pro-inflammatory properties of increased proportions of small fat cells with impaired adipogenesis and/or terminal differentiation are altered in obesity as well [357-359]. In lean and obese minipigs of

the DIO model, there was no noteworthy variation in the relative size distribution patterns of subcutaneous or visceral adipocytes, which indicated a mainly homogenous, hypertrophy-mediated increase of the volume of individual visceral fat cells during the development of obesity. In the subcutaneous adipose tissue of obese pigs, however, an equilibrated hyperplastic and hypertrophic growth of fat cells maintained the normal distribution of individual subcutaneous adipocyte volumes. These results clearly demonstrate that despite significant changes in either (fat) cell volumes or (fat) cell numbers, there is not always an altered size distribution, or *vice versa*.

It is important to mention, that although the present work describes an LSFM-approach for quantitative morphological adipocyte volume and number analysis in a porcine DIO-model, this method is principally also possible in murine or human adipose tissue samples but requires an adaption of the used (SUR)-sampling regime to the respective volume of the examined adipose tissue depots and the corresponding numbers of sampled tissue locations. Moreover, the 3DISCO clearing protocol used in the present study does not preclude subsequent tissue-based analyses such as histology or mass spectrometry imaging [30].

In conclusion, analyses based on laser light sheet fluorescence microscopy were found to be a fashionable and efficient approach for unbiased determination of (individual) adipocyte volumes and numbers. In future studies, LSFM offers the possibility to comprehensively characterise adipocyte morphology by analysing additional qualitative and quantitative morphological fat cell parameters (*e.g.,* shape, surface, and isotropy), which might also be relevant for adipocyte (dys)function in obesity. The potential to combine the described LSFM approach with various specific fluorescence markers may further allow for the selective visualization and quantitative analysis of distinct cell (sub)populations in different adipose tissue depots, such as brown/beige adipocytes or inflammatory cells. Complementing the obtained quantitative morphological adipocyte parameters with functional data from transcript profiling, proteomic, lipidomic or metabolomic analyses and/or clinical outcomes could further help to relate obesity-associated morphological adipocyte alterations to potentially concomitant alterations in adipocyte function, thereby significantly increasing the effectiveness of a study.

VI Summary

Worldwide, the prevalence of overweight and obesity has been rising for years. Alongside with obesity, different obesity-associated diseases, like type 2 diabetes mellitus, cardiovascular diseases and depression are continuously increasing. The elevated risk of developing these chronic diseases is primarily caused by obesity-associated metabolic alterations which, when occurring together, are referred to as metabolic syndrome. These changes are much more correlated to the regional adipose tissue distribution than the total fat mass. Especially accumulation of visceral adipose tissue enhances the risk of metabolic alterations. Different growth patterns of the adipocytes seem to play a causal role in the development of metabolic alterations associated with individual adipose tissue depots. Therefore, an objective assessment of adipocyte volumes and numbers in different fat tissue depots is essential to characterise obesity-associated histomorphological alterations in the adipose tissue and to evaluate the efficacies of experimental medicinal or dietetic interventions.

Although two-dimensional section-based quantitative stereological analyses allow for the unbiased estimation of relevant three-dimensional parameters of adipocyte morphology and are currently considered the gold standard, they often involve elaborate tissue processing and analysis procedures. Therefore, the present work was designed to evaluate the applicability of laser light sheet fluorescence microscopy (LSFM)-based quantitative morphological analyses of optical cleared adipose tissue samples as an efficient alternative to quantitative stereological analyses (specifically the physical disector method) to objectively quantify and characterise obesity-related growth patterns and alterations of the adipocyte morphology in subcutaneous and visceral adipose tissue depots of an established porcine large-animal model of diet-induced obesity. The results of this work were published in the journal *PLoS One* in 2021 [38].

The measurement data obtained by LSFM-based quantitative morphological analysis did not significantly differ from the corresponding estimates determined by quantitative stereological analysis techniques performed on adipose tissue specimen SUR-sampled from the same adipose tissue depots of the identical pigs.

The key findings of adipose tissue morphology in DIO-Göttingen minipigs were:

- Subcutaneous and visceral adipose tissue depots showed depot-specific adipocyte growth reaction patterns
- Subcutaneous adipocytes displayed a comparatively balanced ratio of hyperplastic and hypertrophic volume increase
- Visceral adipocytes displayed mainly hypertrophic volume increase, with negligibly presence of hyperplasia
- Relative size-distribution patterns of individual adipocytes in both depots did not vary between lean and obese Göttingen minipigs

The LSFM-based analysis of optically cleared subcutaneous and visceral adipose tissue samples has been found to be considerably less complex and time-consuming than 2D section-based unbiased quantitative stereological analyses by the physical disector method. The results thus obtained significantly contribute to the characterisation of the porcine DIO-model. A particularly noteworthy advantage of the LSFM-based analysis is the possibility to unbiasedly determine individual adipocyte volumes with significantly less technical effort compared to the determination of this parameter in (serial) 2D tissue sections. Knowledge of the individual adipocyte volume now enables to determine not only changes in mean adipocyte volume, but also in the size distribution of fat cells in different adipose tissue depots and thus detect distinct, possibly pathogenesis-relevant adipocyte subpopulations. Furthermore, samples optically cleared for LSFM analyses can be (re-)embedded in, for example, paraffin and subjected to other tissue-based analyses such as immunohistochemistry or mass spectrometry imaging.

In conclusion, the expeditious acquisition of unbiased pathogenetically relevant morphological key parameters of adipocytes using LSFM-based analyses can significantly contribute to increase the effectiveness of future studies on translational obesity models or in human tissue samples, respectively.

VII Zusammenfassung

Die Prävalenz von Übergewicht und Obesitas steigt weltweit seit Jahren an. In Assoziation mit Obesitas nehmen verschiedene Erkrankungen wie Diabetes mellitus Typ 2, Herz-Kreislauf-Erkrankungen und Depressionen kontinuierlich zu. Das erhöhte Risiko, diese chronischen Krankheiten zu erleiden, wird vor allem durch Obesitas-assoziierte Stoffwechselveränderungen verursacht, die, wenn sie gemeinsam auftreten, als Metabolisches Syndrom bezeichnet werden. Diese Veränderungen sind viel stärker mit der regionalen Fettgewebeverteilung korreliert als mit der Gesamtfettmasse. Insbesondere die Akkumulation von viszeralem Fettgewebe erhöht das Risiko für metabolische Veränderungen. Unterschiedliche Wachstumsmuster der Adipozyten scheinen eine wesentliche Rolle bei der Entstehung der Stoffwechselveränderungen zu spielen, die mit einzelnen Fettgewebedepots assoziiert sind. Daher ist eine objektive Bewertung der Adipozytenvolumina und -zahlen in verschiedenen Fettgewebedepots unerlässlich, um die mit Obesitas in Zusammenhang stehenden histomorphologischen Veränderungen im Fettgewebe zu charakterisieren und die Wirksamkeit experimenteller medikamentöser oder diätetischer Interventionen zu bewerten.

Obwohl auf 2D-Schnitten basierende quantitativ-stereologische Analysen erwartungstreue Schätzungen relevanter 3D-Parameter der Fettzellmorphologie ermöglichen und derzeit als Goldstandard gelten, beinhalten sie oft komplexe und zeitaufwändige Gewebeaufbereitungs- und Analyseschritte. Daher wurde in der vorliegenden Arbeit die Eignung von auf Laser-Lichtblattfluoreszenzmikroskopie (LSFM) basierenden quantitativ-morphologischen Analysen an optisch geklärten Fettgewebeproben als eine effiziente Alternative zu quantitativ-stereologischen Analysen (konkret dem physikalischen Disektor) evaluiert, um Adipositas-bedingte Wachstumsmuster und Veränderungen der Fettzellmorphologie in verschiedenen Fettgewebedepots eines etablierten porzinen Großtiermodells für diätinduzierte Obesitas objektiv zu quantifizieren und charakterisieren. Die Ergebnisse dieser Arbeit wurden 2021 in der Zeitschrift PLoS One veröffentlicht [38].

Die mittels LSFM-basierten quantitativ-morphologischen Analysen gewonnenen Messwerte sind nicht signifikant unterschiedlich zu den entsprechenden Schätzwerten, die mit quantitativ-stereologischen Analysen an systematisch zufällig gewonnenen Fettgewebeproben derselben Depots und Schweine ermittelt wurden.

Die Hauptbefunde der Fettgewebsmorphologie bei DIO-Göttinger Minischweinen waren:

- Subkutane und viszerale Fettgewebedepots zeigten Depot-spezifische Fettzellwachstumsmuster
- Subkutane Adipozyten zeigten ein vergleichsweise ausgewogenes Verhältnis von hyperplastischem und hypertrophem Wachstum
- Viszerale Adipozyten zeigten hauptsächlich eine hypertrophe Volumenzunahme mit zu vernachlässigender Hyperplasie
- Relative Größenverteilungsmuster individueller Adipozyten in beiden Depots unterschieden sich nicht zwischen normalgewichtigen und adipösen Göttinger Minischweinen

Die LSFM-basierte Analyse von optisch geklärten subkutanen und viszeralen Fettgewebeproben erwies sich als erheblich unkomplizierter und weniger zeitaufwändig als die auf 2D-Schnitten basierende erwartungstreue quantitativ-stereologische Analyse mit der physikalischen Disektormethode. Die so gewonnenen Ergebnisse tragen wesentlich zur Charakterisierung des porzinen DIO-Modells bei. Ein besonders hervorzuhebender Vorteil der LSFM-basierten Analyse ist die Möglichkeit, individuelle Adipozytenvolumina mit deutlich weniger technischem Aufwand erwartungstreu zu ermitteln als im Vergleich zur Bestimmung dieses Parameters in (seriellen) 2D-Gewebeschnitten. Die Kenntnis des individuellen Fettzellvolumens ermöglicht es nun, nicht nur Veränderungen des mittleren Adipozytenvolumens, sondern auch der Größenverteilung der Fettzellen in verschiedenen Fettgewebedepots festzustellen und so unterschiedliche, möglicherweise Pathogenese-relevante Fettzellsubpopulationen zu erkennen. Darüber hinaus können die für LSFM Analysen optisch gereinigten Proben z. B. in Paraffin (wieder) eingebettet und anderen gewebebasierten Analysen wie Immunhistochemie oder bildgebender Massenspektrometrie unterzogen werden.

Abschließend ist hervorzuheben, dass die zügige Erfassung erwartungstreuer, pathogenetisch relevanter morphologischer Schlüsselparameter von Adipozyten mittels LSFM-basierter Analysen wesentlich dazu beitragen kann, die Effektivität zukünftiger Studien an translationalen Adipositasmodellen bzw. an menschlichen Gewebeproben zu erhöhen.

VIII References

1. Zhang ZY, Wang MW. Obesity, a health burden of a global nature. Acta Pharmacol Sin. 2012;33(2):145-7.
2. World Health Organization. Obesity and Overweight 2020 [Access Date 08.05.2020]. Available from: https://www.who.int/news-room/fact-sheets/detail/obesity-and-overweight.
3. Kelly T, Yang W, Chen CS, Reynolds K, He J. Global burden of obesity in 2005 and projections to 2030. Int J Obes (Lond). 2008;32(9):1431-7.
4. Grundy SM, Cleeman JI, Daniels SR, Donato KA, Eckel RH, Franklin BA, Gordon DJ, Krauss RM, Savage PJ, Smith SC, Jr., Spertus JA, Costa F, American Heart Association, National Heart, Lung, and Blood Institute. Diagnosis and management of the metabolic syndrome: an American Heart Association/National Heart, Lung, and Blood Institute Scientific Statement. Circulation. 2005;112(17):2735-52.
5. O'Neill S, O'Driscoll L. Metabolic syndrome: a closer look at the growing epidemic and its associated pathologies. Obes Rev. 2015;16(1):1-12.
6. de Heredia FP, Gomez-Martinez S, Marcos A. Obesity, inflammation and the immune system. Proc Nutr Soc. 2012;71(2):332-8.
7. Puhl RM, Heuer CA. Obesity stigma: important considerations for public health. Am J Public Health. 2010;100(6):1019-28.
8. Dobner J, Kaser S. Body mass index and the risk of infection - from underweight to obesity. Clin Microbiol Infect. 2018;24(1):24-8.
9. Goossens GH. The metabolic phenotype in obesity: fat mass, body fat distribution, and adipose tissue function. Obes Facts. 2017;10(3):207-15.
10. Ridker PM, Buring JE, Cook NR, Rifai N. C-reactive protein, the metabolic syndrome, and risk of incident cardiovascular events: an 8-year follow-up of 14 719 initially healthy American women. Circulation. 2003;107(3):391-7.
11. Manna P, Jain SK. Obesity, oxidative stress, adipose tissue dysfunction, and the associated health risks: causes and therapeutic strategies. Metab Syndr Relat Disord. 2015;13(10):423-44.
12. Despres JP, Moorjani S, Lupien PJ, Tremblay A, Nadeau A, Bouchard C. Regional distribution of body fat, plasma lipoproteins, and cardiovascular disease. Arteriosclerosis. 1990;10(4):497-511.
13. Snijder MB, Zimmet PZ, Visser M, Dekker JM, Seidell JC, Shaw JE. Independent and opposite associations of waist and hip circumferences with diabetes, hypertension and dyslipidemia: the AusDiab Study. Int J Obes Relat Metab Disord. 2004;28(3):402-9.

14. Yusuf S, Hawken S, Ounpuu S, Bautista L, Franzosi MG, Commerford P, Lang CC, Rumboldt Z, Onen CL, Lisheng L, Tanomsup S, Wangai P, Jr., Razak F, Sharma AM, Anand SS, Investigators IS. Obesity and the risk of myocardial infarction in 27,000 participants from 52 countries: a case-control study. Lancet. 2005;366(9497):1640-9.

15. Joe AW, Yi L, Even Y, Vogl AW, Rossi FM. Depot-specific differences in adipogenic progenitor abundance and proliferative response to high-fat diet. Stem Cells. 2009;27(10):2563-70.

16. Pellegrinelli V, Carobbio S, Vidal-Puig A. Adipose tissue plasticity: how fat depots respond differently to pathophysiological cues. Diabetologia. 2016;59(6):1075-88.

17. Fuchs T, Loureiro MP, Macedo LE, Nocca D, Nedelcu M, Costa-Casagrande TA. Animal models in metabolic syndrome. Rev Col Bras Cir. 2018;45(5):e1975.

18. Aigner B, Renner S, Kessler B, Klymiuk N, Kurome M, Wünsch A, Wolf E. Transgenic pigs as models for translational biomedical research. Journal of Molecular Medicine. 2010;88(7):653-64.

19. Klymiuk N, Seeliger F, Bohlooly YM, Blutke A, Rudmann DG, Wolf E. Tailored pig models for preclinical efficacy and safety testing of targeted therapies. Toxicol Pathol. 2016;44(3):346-57.

20. Gundersen HJG, Mirabile R, Brown D, Boyce RW. Stereological principles and sampling procedures for toxicologic pathologists. In: Haschek WM, Rousseaux CG, Wallig MA, editors. Haschek and Rousseaux´s Handbook of Toxicologic Pathology. 3 ed. London, UK: Academic Press. INC.; 2013. pp. 215-86.

21. Howard CV, Reed MG. Unbiased stereology. 2 ed. Coleraine, UK: QTP Publications; 2005. 278 p.

22. Madsen KM. The art of counting. J Am Soc Nephrol. 1999;10(5):1124-5.

23. Boyce RW, Dorph-Petersen KA, Lyck L, Gundersen HJ. Design-based stereology: introduction to basic concepts and practical approaches for estimation of cell number. Toxicol Pathol. 2010;38(7):1011-25.

24. Blutke A, Schneider MR, Wolf E, Wanke R. Growth hormone (GH)-transgenic insulin-like growth factor 1 (IGF1)-deficient mice allow dissociation of excess GH and IGF1 effects on glomerular and tubular growth. Physiological reports. 2016;4(5):e12709.

25. Hoeflich A, Weber MM, Fisch T, Nedbal S, Fottner C, Elmlinger MW, Wanke R, Wolf E. Insulin-like growth factor binding protein 2 (IGFBP-2) separates hypertrophic and hyperplastic effects of growth hormone (GH)/IGF-I excess on adrenocortical cells in vivo. FASEB J. 2002;16(13):1721-31.

26. Cuellar E, Solis L. First use of stereology to quantify the survival of fat autografts. Image Anal Stereol 2005;24:187-93.

27. Aslan H, Altunkaynak BZ, Altunkaynak ME, Vuraler O, Kaplan S, Unal B. Effect of a high fat diet on quantitative features of adipocytes in the omentum: an experimental, stereological and ultrastructural study. Obes Surg. 2006;16(11):1526-34.

28. Tschanz S, Schneider JP, Knudsen L. Design-based stereology: planning, volumetry and sampling are crucial steps for a successful study. Ann Anat. 2014;196(1):3-11.

29. Stenkula KG, Erlanson-Albertsson C. Adipose cell size: importance in health and disease. Am J Physiol Regul Integr Comp Physiol. 2018;315(2):R284-R95.

30. Blutke A, Sun N, Xu Z, Buck A, Harrison L, Schriever SC, Pfluger PT, Wiles D, Kunzke T, Huber K, Schlegel J, Aichler M, Feuchtinger A, Matiasek K, Hauck SM, Walch A. Light sheet fluorescence microscopy guided MALDI-imaging mass spectrometry of cleared tissue samples. Sci Rep. 2020;10(1):14461.

31. Feuchtinger A, Walch A, Dobosz M. Deep tissue imaging: a review from a preclinical cancer research perspective. Histochem Cell Biol. 2016;146(6):781-806.

32. Kennel P, Dichamp J, Barreau C, Guissard C, Teyssedre L, Rouquette J, Colombelli J, Lorsignol A, Casteilla L, Plouraboue F. From whole-organ imaging to in-silico blood flow modeling: a new multi-scale network analysis for revisiting tissue functional anatomy. PLoS Comput Biol. 2020;16(2):e1007322.

33. Lugo-Hernandez E, Squire A, Hagemann N, Brenzel A, Sardari M, Schlechter J, Sanchez-Mendoza EH, Gunzer M, Faissner A, Hermann DM. 3D visualization and quantification of microvessels in the whole ischemic mouse brain using solvent-based clearing and light sheet microscopy. J Cereb Blood Flow Metab. 2017;37(10):3355-67.

34. Fiedler S, Wunnemann H, Hofmann I, Theobalt N, Feuchtinger A, Walch A, Schwaiger J, Wanke R, Blutke A. A practical guide to unbiased quantitative morphological analyses of the gills of rainbow trout (Oncorhynchus mykiss) in ecotoxicological studies. PLoS One. 2020;15(12):e0243462.

35. Klingberg A, Hasenberg A, Ludwig-Portugall I, Medyukhina A, Mann L, Brenzel A, Engel DR, Figge MT, Kurts C, Gunzer M. Fully automated evaluation of total glomerular number and capillary tuft size in nephritic kidneys using lightsheet microscopy. J Am Soc Nephrol. 2017;28(2):452-9.

36. Amich J, Mokhtari Z, Strobel M, Vialetto E, Sheta D, Yu Y, Hartweg J, Kalleda N, Jarick KJ, Brede C, Jordan-Garrote AL, Thusek S, Schmiedgen K, Arslan B, Pinnecker J, Thornton CR, Gunzer M, Krappmann S, Einsele H, Heinze KG,

Beilhack A. Three-dimensional light sheet fluorescence microscopy of lungs to dissect local host immune-Aspergillus fumigatus interactions. mBio. 2020;11(1):e02752-19.

37. Renner S, Blutke A, Dobenecker B, Dhom G, Muller TD, Finan B, Clemmensen C, Bernau M, Novak I, Rathkolb B, Senf S, Zols S, Roth M, Gotz A, Hofmann SM, Hrabě de Angelis M, Wanke R, Kienzle E, Scholz AM, DiMarchi R, Ritzmann M, Tschop MH, Wolf E. Metabolic syndrome and extensive adipose tissue inflammation in morbidly obese Gottingen minipigs. Mol Metab. 2018;16:180-90.

38. Theobalt N, Hofmann I, Fiedler S, Renner S, Dhom G, Feuchtinger A, Walch A, Hrabě de Angelis M, Wolf E, Wanke R, Blutke A. Unbiased analysis of obesity related, fat depot specific changes of adipocyte volumes and numbers using light sheet fluorescence microscopy. PLoS One. 2021;16(3):e0248594.

39. World Health Organization. Body mass index - BMI [Access Date 19.11.2020]. Available from: https://www.euro.who.int/en/health-topics/disease-prevention/nutrition/a-healthy-lifestyle/body-mass-index-bmi.

40. Apovian CM. Obesity: definition, comorbidities, causes, and burden. Am J Manag Care. 2016;22(7 Suppl):s176-85.

41. Engin A. The definition and prevalence of obesity and metabolic syndrome. Adv Exp Med Biol. 2017;960:1-17.

42. Jablonowska-Lietz B, Wrzosek M, Wlodarczyk M, Nowicka G. New indexes of body fat distribution, visceral adiposity index, body adiposity index, waist-to-height ratio, and metabolic disturbances in the obese. Kardiol Pol. 2017;75(11):1185-91.

43. Chooi YC, Ding C, Magkos F. The epidemiology of obesity. Metabolism. 2019;92:6-10.

44. World Health Organization. Regional Office for the Western Pacific. The Asia-Pacific perspective: redefining obesity and its treatment: Sydney, Australia: Health Communications Australia; 2000.

45. Bergman RN, Stefanovski D, Buchanan TA, Sumner AE, Reynolds JC, Sebring NG, Xiang AH, Watanabe RM. A better index of body adiposity. Obesity (Silver Spring). 2011;19(5):1083-9.

46. Freedman DS, Thornton JC, Pi-Sunyer FX, Heymsfield SB, Wang J, Pierson RN, Jr., Blanck HM, Gallagher D. The body adiposity index (hip circumference / height(1.5)) is not a more accurate measure of adiposity than is BMI, waist circumference, or hip circumference. Obesity (Silver Spring). 2012;20(12):24 38-44.

47. Liebich HG. Funktionelle Histologie der Haussäugetiere und Vögel: Lehrbuch und Farbatlas für Studium und Praxis. 5 ed. Stuttgart, Germany: Schattauer; 2010. 442 p.

48. Müller F. Lehrbuch der Anatomie der Haussäugethiere: Mit besonderer Berücksichtigung des Pferdes und Physiologischen Bemerkungen. 2 ed. Wien, Austria: W. Braumüller; 1871. 551 p.

49. Shiffman MA. Autologous fat transfer: art, science, and clinical practice. 1 ed. Berlin Heidelberg, Germany: Springer-Verlag Berlin Heidelberg; 2009. 471 p.

50. Avram AS, Avram MM, James WD. Subcutaneous fat in normal and diseased states: 2. Anatomy and physiology of white and brown adipose tissue. J Am Acad Dermatol. 2005;53(4):671-83.

51. Napolitano L. The differentiation of white adipose cells. An electron microscope study. J Cell Biol. 1963;18:663-79.

52. Betz MJ, Enerback S. Targeting thermogenesis in brown fat and muscle to treat obesity and metabolic disease. Nat Rev Endocrinol. 2018;14(2):77-87.

53. Cypess AM, Lehman S, Williams G, Tal I, Rodman D, Goldfine AB, Kuo FC, Palmer EL, Tseng YH, Doria A, Kolodny GM, Kahn CR. Identification and importance of brown adipose tissue in adult humans. N Engl J Med. 2009;360(15):1509-17.

54. van Marken Lichtenbelt WD, Vanhommerig JW, Smulders NM, Drossaerts JM, Kemerink GJ, Bouvy ND, Schrauwen P, Teule GJ. Cold-activated brown adipose tissue in healthy men. N Engl J Med. 2009;360(15):1500-8.

55. Saito M, Okamatsu-Ogura Y, Matsushita M, Watanabe K, Yoneshiro T, Nio-Kobayashi J, Iwanaga T, Miyagawa M, Kameya T, Nakada K, Kawai Y, Tsujisaki M. High incidence of metabolically active brown adipose tissue in healthy adult humans: effects of cold exposure and adiposity. Diabetes. 2009;58(7):1526-31.

56. Virtanen KA, Lidell ME, Orava J, Heglind M, Westergren R, Niemi T, Taittonen M, Laine J, Savisto NJ, Enerback S, Nuutila P. Functional brown adipose tissue in healthy adults. N Engl J Med. 2009;360(15):1518-25.

57. Heaton JM. The distribution of brown adipose tissue in the human. J Anat. 1972;112(Pt 1):35-9.

58. Becker AS, Nagel HW, Wolfrum C, Burger IA. Anatomical grading for metabolic activity of brown adipose tissue. PLoS One. 2016;11(2):e0149458.

59. Cannon B, Nedergaard J. Brown adipose tissue: function and physiological significance. Physiol Rev. 2004;84(1):277-359.

60. Sarjeant K, Stephens JM. Adipogenesis. Cold Spring Harb Perspect Biol. 2012;4(9):a008417.

61. Renner S, Blutke A, Clauss S, Deeg CA, Kemter E, Merkus D, Wanke R, Wolf E. Porcine models for studying complications and organ crosstalk in diabetes mellitus. Cell Tissue Res. 2020;380(2):341-78.

62. Peirce V, Carobbio S, Vidal-Puig A. The different shades of fat. Nature. 2014;510(7503):76-83.

63. Fyda TJ, Spencer C, Jastroch M, Gaudry MJ. Disruption of thermogenic UCP1 predated the divergence of pigs and peccaries. J Exp Biol. 2020;223(Pt 15).

64. Lin J, Cao C, Tao C, Ye R, Dong M, Zheng Q, Wang C, Jiang X, Qin G, Yan C, Li K, Speakman JR, Wang Y, Jin W, Zhao J. Cold adaptation in pigs depends on UCP3 in beige adipocytes. J Mol Cell Biol. 2017;9(5):364-75.

65. Berg F, Gustafson U, Andersson L. The uncoupling protein 1 gene (UCP1) is disrupted in the pig lineage: a genetic explanation for poor thermoregulation in piglets. PLoS Genet. 2006;2(8):e129.

66. Fuller-Jackson JP, Henry BA. Adipose and skeletal muscle thermogenesis: studies from large animals. J Endocrinol. 2018;237(3):R99-R115.

67. Nowack J, Vetter SG, Stalder G, Painer J, Kral M, Smith S, Le MH, Jurcevic P, Bieber C, Arnold W, Ruf T. Muscle nonshivering thermogenesis in a feral mammal. Sci Rep. 2019;9(1):6378.

68. Periasamy M, Huke S. SERCA pump level is a critical determinant of Ca(2+)homeostasis and cardiac contractility. J Mol Cell Cardiol. 2001;33(6):1053-63.

69. Maurya SK, Bal NC, Sopariwala DH, Pant M, Rowland LA, Shaikh SA, Periasamy M. Sarcolipin is a key determinant of the basal metabolic rate, and its overexpression enhances energy expenditure and resistance against diet-induced obesity. J Biol Chem. 2015;290(17):10840-9.

70. Mall S, Broadbridge R, Harrison SL, Gore MG, Lee AG, East JM. The presence of sarcolipin results in increased heat production by Ca(2+)-ATPase. J Biol Chem. 2006;281(48):36597-602.

71. de Meis L. Uncoupled ATPase activity and heat production by the sarcoplasmic reticulum Ca2+-ATPase. Regulation by ADP. J Biol Chem. 2001;276(27):25078-87.

72. Zheng Q, Lin J, Huang J, Zhang H, Zhang R, Zhang X, Cao C, Hambly C, Qin G, Yao J, Song R, Jia Q, Wang X, Li Y, Zhang N, Piao Z, Ye R, Speakman JR, Wang H, Zhou Q, Wang Y, Jin W, Zhao J. Reconstitution of UCP1 using CRISPR/Cas9 in the white adipose tissue of pigs decreases fat deposition and improves thermogenic capacity. Proc Natl Acad Sci USA. 2017;114(45):E947 4-E82.

73. Herz CT, Kiefer FW. Adipose tissue browning in mice and humans. J Endocrinol. 2019;241(3):R97-R109.

74. Giralt M, Villarroya F. White, brown, beige/brite: different adipose cells for different functions? Endocrinology. 2013;154(9):2992-3000.

75. Petrovic N, Walden TB, Shabalina IG, Timmons JA, Cannon B, Nedergaard J. Chronic peroxisome proliferator-activated receptor gamma (PPARgamma) activation of epididymally derived white adipocyte cultures reveals a population of thermogenically competent, UCP1-containing adipocytes molecularly distinct from classic brown adipocytes. J Biol Chem. 2010;285(10):7153-64.

76. Young P, Arch JR, Ashwell M. Brown adipose tissue in the parametrial fat pad of the mouse. FEBS Lett. 1984;167(1):10-4.

77. Zoico E, Rubele S, De Caro A, Nori N, Mazzali G, Fantin F, Rossi A, Zamboni M. Brown and beige adipose tissue and aging. Front Endocrinol (Lausanne). 2019;10:368.

78. Lizcano F. The beige adipocyte as a therapy for metabolic diseases. Int J Mol Sci. 2019;20(20):5058.

79. Choe SS, Huh JY, Hwang IJ, Kim JI, Kim JB. Adipose tissue remodeling: its role in energy metabolism and metabolic disorders. Front Endocrinol (Lausanne). 2016;7:30.

80. Yang A, Mottillo EP. Adipocyte lipolysis: from molecular mechanisms of regulation to disease and therapeutics. Biochem J. 2020;477(5):985-1008.

81. Song Z, Xiaoli AM, Yang F. Regulation and metabolic significance of de novo lipogenesis in adipose tissues. Nutrients. 2018;10(10):1383.

82. Wong RH, Sul HS. Insulin signaling in fatty acid and fat synthesis: a transcriptional perspective. Curr Opin Pharmacol. 2010;10(6):684-91.

83. Wajchenberg BL. Subcutaneous and visceral adipose tissue: their relation to the metabolic syndrome. Endocr Rev. 2000;21(6):697-738.

84. Ailhaud G. L'adipocyte, cellule sécrétrice et endocrine. Med Sci (Paris). 1998;14:858-64.

85. Wang H, Eckel RH. Lipoprotein lipase: from gene to obesity. Am J Physiol Endocrinol Metab. 2009;297(2):E271-88.

86. Raynolds MV, Awald PD, Gordon DF, Gutierrez-Hartmann A, Rule DC, Wood WM, Eckel RH. Lipoprotein lipase gene expression in rat adipocytes is regulated by isoproterenol and insulin through different mechanisms. Mol Endocrinol. 1990;4(9):1416-22.

87. Farese RV, Jr., Yost TJ, Eckel RH. Tissue-specific regulation of lipoprotein lipase activity by insulin/glucose in normal-weight humans. Metabolism. 1991;40(2):214-6.

88. Horn F. Biochemie des Menschen: das Lehrbuch für das Medizinstudium. 4 ed. Stuttgart, Germany: Georg Thieme Verlag; 2009. 643 p.

89. Tchkonia T, Thomou T, Zhu Y, Karagiannides I, Pothoulakis C, Jensen MD, Kirkland JL. Mechanisms and metabolic implications of regional differences among fat depots. Cell Metab. 2013;17(5):644-56.

90. Jensen MD, Sarr MG, Dumesic DA, Southorn PA, Levine JA. Regional uptake of meal fatty acids in humans. Am J Physiol Endocrinol Metab. 2003;285(6):E1282-8.

91. Romanski SA, Nelson RM, Jensen MD. Meal fatty acid uptake in adipose tissue: gender effects in nonobese humans. Am J Physiol Endocrinol Metab. 2000;279(2):E455-62.

92. Santosa S, Hensrud DD, Votruba SB, Jensen MD. The influence of sex and obesity phenotype on meal fatty acid metabolism before and after weight loss. Am J Clin Nutr. 2008;88(4):1134-41.

93. Votruba SB, Mattison RS, Dumesic DA, Koutsari C, Jensen MD. Meal fatty acid uptake in visceral fat in women. Diabetes. 2007;56(10):2589-97.

94. Souza SC, de Vargas LM, Yamamoto MT, Lien P, Franciosa MD, Moss LG, Greenberg AS. Overexpression of perilipin A and B blocks the ability of tumor necrosis factor alpha to increase lipolysis in 3T3-L1 adipocytes. J Biol Chem. 1998;273(38):24665-9.

95. Laurencikiene J, Skurk T, Kulyte A, Heden P, Astrom G, Sjolin E, Ryden M, Hauner H, Arner P. Regulation of lipolysis in small and large fat cells of the same subject. J Clin Endocrinol Metab. 2011;96(12):E2045-9.

96. Klein S, Fontana L, Young VL, Coggan AR, Kilo C, Patterson BW, Mohammed BS. Absence of an effect of liposuction on insulin action and risk factors for coronary heart disease. N Engl J Med. 2004;350(25):2549-57.

97. Matarasso A, Kim RW, Kral JG. The impact of liposuction on body fat. Plast Reconstr Surg. 1998;102(5):1686-9.

98. Lambert EV, Hudson DA, Bloch CE, Koeslag JH. Metabolic response to localized surgical fat removal in nonobese women. Aesthetic Plast Surg. 1991;15(2):105-10.

99. Burguera B, Proctor D, Dietz N, Guo Z, Joyner M, Jensen MD. Leg free fatty acid kinetics during exercise in men and women. Am J Physiol Endocrinol Metab. 2000;278(1):E113-7.

100. Marin P, Andersson B, Ottosson M, Olbe L, Chowdhury B, Kvist H, Holm G, Sjostrom L, Bjorntorp P. The morphology and metabolism of intraabdominal adipose tissue in men. Metabolism. 1992;41(11):1242-8.

101. Hoffstedt J, Arner P, Hellers G, Lonnqvist F. Variation in adrenergic regulation of lipolysis between omental and subcutaneous adipocytes from obese and non-obese men. J Lipid Res. 1997;38(4):795-804.

102. Jepson CA, Yeaman SJ. Inhibition of hormone-sensitive lipase by intermediary lipid metabolites. FEBS Lett. 1992;310(2):197-200.

103. Fain JN, Madan AK, Hiler ML, Cheema P, Bahouth SW. Comparison of the release of adipokines by adipose tissue, adipose tissue matrix, and adipocytes from visceral and subcutaneous abdominal adipose tissues of obese humans. Endocrinology. 2004;145(5):2273-82.

104. Nguyen MT, Satoh H, Favelyukis S, Babendure JL, Imamura T, Sbodio JI, Zalevsky J, Dahiyat BI, Chi NW, Olefsky JM. JNK and tumor necrosis factor-alpha mediate free fatty acid-induced insulin resistance in 3T3-L1 adipocytes. J Biol Chem. 2005;280(42):35361-71.

105. van Hall G, Steensberg A, Sacchetti M, Fischer C, Keller C, Schjerling P, Hiscock N, Moller K, Saltin B, Febbraio MA, Pedersen BK. Interleukin-6 stimulates lipolysis and fat oxidation in humans. J Clin Endocrinol Metab. 2003;88(7):3005-10.

106. Samuel VT, Shulman GI. The pathogenesis of insulin resistance: integrating signaling pathways and substrate flux. J Clin Invest. 2016;126(1):12-22.

107. Bikman BT, Summers SA. Ceramides as modulators of cellular and whole-body metabolism. J Clin Invest. 2011;121(11):4222-30.

108. Tchkonia T, Corkey BE, Kirkland JL. Current views of the fat cell as an endocrine cell: lipotoxicity. In: Bray GA, Ryan DH, editors. Overweight and the metabolic syndrome: from bench to bedside. 1 ed. Boston, MA: Springer US; 2006. pp. 105-23.

109. Longo M, Zatterale F, Naderi J, Parrillo L, Formisano P, Raciti GA, Beguinot F, Miele C. Adipose tissue dysfunction as determinant of obesity-associated metabolic complications. Int J Mol Sci. 2019;20(9):2358.

110. Gaborit B, Abdesselam I, Kober F, Jacquier A, Ronsin O, Emungania O, Lesavre N, Alessi MC, Martin JC, Bernard M, Dutour A. Ectopic fat storage in the pancreas using 1H-MRS: importance of diabetic status and modulation with bariatric surgery-induced weight loss. Int J Obes (Lond). 2015;39(3):480-7.

111. Bahary N, Leibel RL, Joseph L, Friedman JM. Molecular mapping of the mouse db mutation. Proc Natl Acad Sci USA. 1990;87(21):8642-6.

112. Halaas JL, Gajiwala KS, Maffei M, Cohen SL, Chait BT, Rabinowitz D, Lallone RL, Burley SK, Friedman JM. Weight-reducing effects of the plasma protein encoded by the obese gene. Science. 1995;269(5223):543-6.

113. Zhang Y, Proenca R, Maffei M, Barone M, Leopold L, Friedman JM. Positional cloning of the mouse obese gene and its human homologue. Nature. 1994;372(6505):425-32.

114. Galic S, Oakhill JS, Steinberg GR. Adipose tissue as an endocrine organ. Mol Cell Endocrinol. 2010;316(2):129-39.

115. Hotamisligil GS, Shargill NS, Spiegelman BM. Adipose expression of tumor necrosis factor-alpha: direct role in obesity-linked insulin resistance. Science. 1993;259(5091):87-91.

116. Kwon O, Kim KW, Kim MS. Leptin signalling pathways in hypothalamic neurons. Cell Mol Life Sci. 2016;73(7):1457-77.

117. Lonnqvist F, Nordfors L, Jansson M, Thorne A, Schalling M, Arner P. Leptin secretion from adipose tissue in women. Relationship to plasma levels and gene expression. J Clin Invest. 1997;99(10):2398-404.

118. Fried SK, Ricci MR, Russell CD, Laferrere B. Regulation of leptin production in humans. J Nutr. 2000;130(12):3127S-31S.

119. Izquierdo AG, Crujeiras AB, Casanueva FF, Carreira MC. Leptin, obesity, and leptin resistance: where are we 25 years later? Nutrients. 2019;11(11):2704.

120. Westerterp-Plantenga MS, Saris WH, Hukshorn CJ, Campfield LA. Effects of weekly administration of pegylated recombinant human OB protein on appetite profile and energy metabolism in obese men. Am J Clin Nutr. 2001;74(4):426-34.

121. Watt MJ, Dzamko N, Thomas WG, Rose-John S, Ernst M, Carling D, Kemp BE, Febbraio MA, Steinberg GR. CNTF reverses obesity-induced insulin resistance by activating skeletal muscle AMPK. Nat Med. 2006;12(5):541-8.

122. Steinberg GR, McAinch AJ, Chen MB, O'Brien PE, Dixon JB, Cameron-Smith D, Kemp BE. The suppressor of cytokine signaling 3 inhibits leptin activation of AMP-kinase in cultured skeletal muscle of obese humans. J Clin Endocrinol Metab. 2006;91(9):3592-7.

123. Martin TL, Alquier T, Asakura K, Furukawa N, Preitner F, Kahn BB. Diet-induced obesity alters AMP kinase activity in hypothalamus and skeletal muscle. J Biol Chem. 2006;281(28):18933-41.

124. Banks WA, DiPalma CR, Farrell CL. Impaired transport of leptin across the blood-brain barrier in obesity. Peptides. 1999;20(11):1341-5.

125. Banks WA, Farrell CL. Impaired transport of leptin across the blood-brain barrier in obesity is acquired and reversible. Am J Physiol Endocrinol Metab. 2003;285(1):E10-5.

126. Wang ZV, Scherer PE. Adiponectin, the past two decades. J Mol Cell Biol. 2016;8(2):93-100.

127. Scherer PE, Williams S, Fogliano M, Baldini G, Lodish HF. A novel serum protein similar to C1q, produced exclusively in adipocytes. J Biol Chem. 1995;270(45):26746-9.

128. Hu E, Liang P, Spiegelman BM. AdipoQ is a novel adipose-specific gene dysregulated in obesity. J Biol Chem. 1996;271(18):10697-703.

129. Yamauchi T, Kamon J, Waki H, Terauchi Y, Kubota N, Hara K, Mori Y, Ide T, Murakami K, Tsuboyama-Kasaoka N, Ezaki O, Akanuma Y, Gavrilova O, Vinson C, Reitman ML, Kagechika H, Shudo K, Yoda M, Nakano Y, Tobe K, Nagai R, Kimura S, Tomita M, Froguel P, Kadowaki T. The fat-derived hormone adiponectin reverses insulin resistance associated with both lipoatrophy and obesity. Nat Med. 2001;7(8):941-6.

130. Yamauchi T, Kamon J, Minokoshi Y, Ito Y, Waki H, Uchida S, Yamashita S, Noda M, Kita S, Ueki K, Eto K, Akanuma Y, Froguel P, Foufelle F, Ferre P, Carling D, Kimura S, Nagai R, Kahn BB, Kadowaki T. Adiponectin stimulates glucose utilization and fatty-acid oxidation by activating AMP-activated protein kinase. Nat Med. 2002;8(11):1288-95.

131. Kubota N, Yano W, Kubota T, Yamauchi T, Itoh S, Kumagai H, Kozono H, Takamoto I, Okamoto S, Shiuchi T, Suzuki R, Satoh H, Tsuchida A, Moroi M, Sugi K, Noda T, Ebinuma H, Ueta Y, Kondo T, Araki E, Ezaki O, Nagai R, Tobe K, Terauchi Y, Ueki K, Minokoshi Y, Kadowaki T. Adiponectin stimulates AMP-activated protein kinase in the hypothalamus and increases food intake. Cell Metab. 2007;6(1):55-68.

132. Tomas E, Tsao TS, Saha AK, Murrey HE, Zhang Cc C, Itani SI, Lodish HF, Ruderman NB. Enhanced muscle fat oxidation and glucose transport by ACRP30 globular domain: acetyl-CoA carboxylase inhibition and AMP-activated protein kinase activation. Proc Natl Acad Sci USA. 2002;99(25):16309-13.

133. Wang C, Mao X, Wang L, Liu M, Wetzel MD, Guan KL, Dong LQ, Liu F. Adiponectin sensitizes insulin signaling by reducing p70 S6 kinase-mediated serine phosphorylation of IRS-1. J Biol Chem. 2007;282(11):7991-6.

134. Fang H, Judd RL. Adiponectin regulation and function. Compr Physiol. 2018;8(3):1031-63.

135. Kumada M, Kihara S, Ouchi N, Kobayashi H, Okamoto Y, Ohashi K, Maeda K, Nagaretani H, Kishida K, Maeda N, Nagasawa A, Funahashi T, Matsuzawa

Y. Adiponectin specifically increased tissue inhibitor of metalloproteinase-1 through interleukin-10 expression in human macrophages. Circulation. 2004;109(17):2046-9.

136. Dietze-Schroeder D, Sell H, Uhlig M, Koenen M, Eckel J. Autocrine action of adiponectin on human fat cells prevents the release of insulin resistance-inducing factors. Diabetes. 2005;54(7):2003-11.

137. Wolf AM, Wolf D, Rumpold H, Enrich B, Tilg H. Adiponectin induces the anti-inflammatory cytokines IL-10 and IL-1RA in human leukocytes. Biochem Biophys Res Commun. 2004;323(2):630-5.

138. Yokota T, Oritani K, Takahashi I, Ishikawa J, Matsuyama A, Ouchi N, Kihara S, Funahashi T, Tenner AJ, Tomiyama Y, Matsuzawa Y. Adiponectin, a new member of the family of soluble defense collagens, negatively regulates the growth of myelomonocytic progenitors and the functions of macrophages. Blood. 2000;96(5):1723-32.

139. Ohashi K, Parker JL, Ouchi N, Higuchi A, Vita JA, Gokce N, Pedersen AA, Kalthoff C, Tullin S, Sams A, Summer R, Walsh K. Adiponectin promotes macrophage polarization toward an anti-inflammatory phenotype. J Biol Chem. 2010;285(9):6153-60.

140. Weisberg SP, McCann D, Desai M, Rosenbaum M, Leibel RL, Ferrante AW, Jr. Obesity is associated with macrophage accumulation in adipose tissue. J Clin Invest. 2003;112(12):1796-808.

141. Stephens JM, Lee J, Pilch PF. Tumor necrosis factor-alpha-induced insulin resistance in 3T3-L1 adipocytes is accompanied by a loss of insulin receptor substrate-1 and GLUT4 expression without a loss of insulin receptor-mediated signal transduction. J Biol Chem. 1997;272(2):971-6.

142. Cai D, Yuan M, Frantz DF, Melendez PA, Hansen L, Lee J, Shoelson SE. Local and systemic insulin resistance resulting from hepatic activation of IKK-beta and NF-kappaB. Nat Med. 2005;11(2):183-90.

143. Hirosumi J, Tuncman G, Chang L, Gorgun CZ, Uysal KT, Maeda K, Karin M, Hotamisligil GS. A central role for JNK in obesity and insulin resistance. Nature. 2002;420(6913):333-6.

144. Steinberg GR, Michell BJ, van Denderen BJ, Watt MJ, Carey AL, Fam BC, Andrikopoulos S, Proietto J, Gorgun CZ, Carling D, Hotamisligil GS, Febbraio MA, Kay TW, Kemp BE. Tumor necrosis factor alpha-induced skeletal muscle insulin resistance involves suppression of AMP-kinase signaling. Cell Metab. 2006;4(6):465-74.

145. Yu C, Chen Y, Cline GW, Zhang D, Zong H, Wang Y, Bergeron R, Kim JK, Cushman SW, Cooney GJ, Atcheson B, White MF, Kraegen EW, Shulman GI. Mechanism by which fatty acids inhibit insulin activation of insulin receptor

substrate-1 (IRS-1)-associated phosphatidylinositol 3-kinase activity in muscle. J Biol Chem. 2002;277(52):50230-6.

146. Ruan H, Miles PD, Ladd CM, Ross K, Golub TR, Olefsky JM, Lodish HF. Profiling gene transcription in vivo reveals adipose tissue as an immediate target of tumor necrosis factor-alpha: implications for insulin resistance. Diabetes. 2002;51(11):3176-88.

147. Green A, Dobias SB, Walters DJ, Brasier AR. Tumor necrosis factor increases the rate of lipolysis in primary cultures of adipocytes without altering levels of hormone-sensitive lipase. Endocrinology. 1994;134(6):2581-8.

148. Hammarstedt A, Gogg S, Hedjazifar S, Nerstedt A, Smith U. Impaired adipogenesis and dysfunctional adipose tissue in human hypertrophic obesity. Physiol Rev. 2018;98(4):1911-41.

149. Lebensztejn DM, Flisiak-Jackiewicz M, Bialokoz-Kalinowska I, Bobrus-Chociej A, Kowalska I. Hepatokines and non-alcoholic fatty liver disease. Acta Biochim Pol. 2016;63(3):459-67.

150. Mohamed-Ali V, Goodrick S, Rawesh A, Katz DR, Miles JM, Yudkin JS, Klein S, Coppack SW. Subcutaneous adipose tissue releases interleukin-6, but not tumor necrosis factor-alpha, in vivo. J Clin Endocrinol Metab. 1997;82(12):4196-200.

151. Bora P, Majumdar AS. Adipose tissue-derived stromal vascular fraction in regenerative medicine: a brief review on biology and translation. Stem Cell Res Ther. 2017;8(1):145.

152. Rehman K, Akash MSH, Liaqat A, Kamal S, Qadir MI, Rasul A. Role of interleukin-6 in development of insulin resistance and type 2 diabetes mellitus. Crit Rev Eukaryot Gene Expr. 2017;27(3):229-36.

153. Fried SK, Bunkin DA, Greenberg AS. Omental and subcutaneous adipose tissues of obese subjects release interleukin-6: depot difference and regulation by glucocorticoid. J Clin Endocrinol Metab. 1998;83(3):847-50.

154. Rotter V, Nagaev I, Smith U. Interleukin-6 (IL-6) induces insulin resistance in 3T3-L1 adipocytes and is, like IL-8 and tumor necrosis factor-alpha, overexpressed in human fat cells from insulin-resistant subjects. J Biol Chem. 2003;278(46):45777-84.

155. Starr R, Willson TA, Viney EM, Murray LJ, Rayner JR, Jenkins BJ, Gonda TJ, Alexander WS, Metcalf D, Nicola NA, Hilton DJ. A family of cytokine-inducible inhibitors of signalling. Nature. 1997;387(6636):917-21.

156. Senn JJ, Klover PJ, Nowak IA, Zimmers TA, Koniaris LG, Furlanetto RW, Mooney RA. Suppressor of cytokine signaling-3 (SOCS-3), a potential mediator of interleukin-6-dependent insulin resistance in hepatocytes. J Biol Chem. 2003;278(16):13740-6.

157. Rosen ED, MacDougald OA. Adipocyte differentiation from the inside out. Nat Rev Mol Cell Biol. 2006;7(12):885-96.

158. Farmer SR. Molecular determinants of brown adipocyte formation and function. Genes Dev. 2008;22(10):1269-75.

159. Gesta S, Tseng YH, Kahn CR. Developmental origin of fat: tracking obesity to its source. Cell. 2007;131(2):242-56.

160. Huang H, Song TJ, Li X, Hu L, He Q, Liu M, Lane MD, Tang QQ. BMP signaling pathway is required for commitment of C3H10T1/2 pluripotent stem cells to the adipocyte lineage. Proc Natl Acad Sci USA. 2009;106(31):12670-5.

161. Tang QQ, Otto TC, Lane MD. Commitment of C3H10T1/2 pluripotent stem cells to the adipocyte lineage. Proc Natl Acad Sci USA. 2004;101(26):9607-11.

162. Lin CS, Xin ZC, Deng CH, Ning H, Lin G, Lue TF. Defining adipose tissue-derived stem cells in tissue and in culture. Histol Histopathol. 2010;25(6):807-15.

163. Tang QQ, Lane MD. Adipogenesis: from stem cell to adipocyte. Annu Rev Biochem. 2012;81:715-36.

164. Seale P, Bjork B, Yang W, Kajimura S, Chin S, Kuang S, Scime A, Devarakonda S, Conroe HM, Erdjument-Bromage H, Tempst P, Rudnicki MA, Beier DR, Spiegelman BM. PRDM16 controls a brown fat/skeletal muscle switch. Nature. 2008;454(7207):961-7.

165. Bowers RR, Kim JW, Otto TC, Lane MD. Stable stem cell commitment to the adipocyte lineage by inhibition of DNA methylation: role of the BMP-4 gene. Proc Natl Acad Sci USA. 2006;103(35):13022-7.

166. Bowers RR, Lane MD. Wnt signaling and adipocyte lineage commitment. Cell Cycle. 2008;7(9):1191-6.

167. Ross SE, Hemati N, Longo KA, Bennett CN, Lucas PC, Erickson RL, MacDougald OA. Inhibition of adipogenesis by Wnt signaling. Science. 2000;289(5481):950-3.

168. Zehentner BK, Leser U, Burtscher H. BMP-2 and sonic hedgehog have contrary effects on adipocyte-like differentiation of C3H10T1/2 cells. DNA Cell Biol. 2000;19(5):275-81.

169. Farmer SR. Transcriptional control of adipocyte formation. Cell Metab. 2006;4(4):263-73.

170. Linhart HG, Ishimura-Oka K, DeMayo F, Kibe T, Repka D, Poindexter B, Bick RJ, Darlington GJ. C/EBPalpha is required for differentiation of white, but not brown, adipose tissue. Proc Natl Acad Sci USA. 2001;98(22):12532-7.

171. Seale P, Kajimura S, Yang W, Chin S, Rohas LM, Uldry M, Tavernier G, Langin D, Spiegelman BM. Transcriptional control of brown fat determination by PRDM16. Cell Metab. 2007;6(1):38-54.

172. Kajimura S, Seale P, Tomaru T, Erdjument-Bromage H, Cooper MP, Ruas JL, Chin S, Tempst P, Lazar MA, Spiegelman BM. Regulation of the brown and white fat gene programs through a PRDM16/CtBP transcriptional complex. Genes Dev. 2008;22(10):1397-409.

173. Student AK, Hsu RY, Lane MD. Induction of fatty acid synthetase synthesis in differentiating 3T3-L1 preadipocytes. J Biol Chem. 1980;255(10):4745-50.

174. Barbatelli G, Murano I, Madsen L, Hao Q, Jimenez M, Kristiansen K, Giacobino JP, De Matteis R, Cinti S. The emergence of cold-induced brown adipocytes in mouse white fat depots is determined predominantly by white to brown adipocyte transdifferentiation. Am J Physiol Endocrinol Metab. 2010;298(6):E 1244-53.

175. Lee YH, Petkova AP, Mottillo EP, Granneman JG. In vivo identification of bipotential adipocyte progenitors recruited by beta3-adrenoceptor activation and high-fat feeding. Cell Metab. 2012;15(4):480-91.

176. Song T, Kuang S. Adipocyte dedifferentiation in health and diseases. Clin Sci (Lond). 2019;133(20):2107-19.

177. Bielczyk-Maczynska E. White adipocyte plasticity in physiology and disease. Cells. 2019;8(12):1507.

178. Bochet L, Lehuede C, Dauvillier S, Wang YY, Dirat B, Laurent V, Dray C, Guiet R, Maridonneau-Parini I, Le Gonidec S, Couderc B, Escourrou G, Valet P, Muller C. Adipocyte-derived fibroblasts promote tumor progression and contribute to the desmoplastic reaction in breast cancer. Cancer Res. 2013;73(18):5657-68.

179. Jopling C, Boue S, Izpisua Belmonte JC. Dedifferentiation, transdifferentiation and reprogramming: three routes to regeneration. Nat Rev Mol Cell Biol. 2011;12(2):79-89.

180. Wang QA, Song A, Chen W, Schwalie PC, Zhang F, Vishvanath L, Jiang L, Ye R, Shao M, Tao C, Gupta RK, Deplancke B, Scherer PE. Reversible de-differentiation of mature white adipocytes into preadipocyte-like precursors during lactation. Cell Metab. 2018;28(2):282-8.e3.

181. Spalding KL, Arner E, Westermark PO, Bernard S, Buchholz BA, Bergmann O, Blomqvist L, Hoffstedt J, Naslund E, Britton T, Concha H, Hassan M, Ryden M, Frisen J, Arner P. Dynamics of fat cell turnover in humans. Nature. 2008;453(7196):783-7.

182. Arner E, Westermark PO, Spalding KL, Britton T, Ryden M, Frisen J, Bernard S, Arner P. Adipocyte turnover: relevance to human adipose tissue morphology. Diabetes. 2010;59(1):105-9.

183. Hirsch J, Gallian E. Methods for the determination of adipose cell size in man and animals. J Lipid Res. 1968;9(1):110-9.

184. Ghaben AL, Scherer PE. Adipogenesis and metabolic health. Nat Rev Mol Cell Biol. 2019;20(4):242-58.

185. van Baak MA, Mariman ECM. Mechanisms of weight regain after weight loss - the role of adipose tissue. Nat Rev Endocrinol. 2019;15(5):274-87.

186. Khan T, Muise ES, Iyengar P, Wang ZV, Chandalia M, Abate N, Zhang BB, Bonaldo P, Chua S, Scherer PE. Metabolic dysregulation and adipose tissue fibrosis: role of collagen VI. Mol Cell Biol. 2009;29(6):1575-91.

187. Kim JI, Huh JY, Sohn JH, Choe SS, Lee YS, Lim CY, Jo A, Park SB, Han W, Kim JB. Lipid-overloaded enlarged adipocytes provoke insulin resistance independent of inflammation. Mol Cell Biol. 2015;35(10):1686-99.

188. Cotillard A, Poitou C, Torcivia A, Bouillot JL, Dietrich A, Kloting N, Gregoire C, Lolmede K, Bluher M, Clement K. Adipocyte size threshold matters: link with risk of type 2 diabetes and improved insulin resistance after gastric bypass. J Clin Endocrinol Metab. 2014;99(8):E1466-70.

189. Huh JY, Park YJ, Ham M, Kim JB. Crosstalk between adipocytes and immune cells in adipose tissue inflammation and metabolic dysregulation in obesity. Mol Cells. 2014;37(5):365-71.

190. Kuroda M, Sakaue H. Adipocyte death and chronic inflammation in obesity. J Med Invest. 2017;64(3.4):193-6.

191. Sung HK, Doh KO, Son JE, Park JG, Bae Y, Choi S, Nelson SM, Cowling R, Nagy K, Michael IP, Koh GY, Adamson SL, Pawson T, Nagy A. Adipose vascular endothelial growth factor regulates metabolic homeostasis through angiogenesis. Cell Metab. 2013;17(1):61-72.

192. Alkhouri N, Gornicka A, Berk MP, Thapaliya S, Dixon LJ, Kashyap S, Schauer PR, Feldstein AE. Adipocyte apoptosis, a link between obesity, insulin resistance, and hepatic steatosis. J Biol Chem. 2010;285(5):3428-38.

193. Knittle JL, Timmers K, Ginsberg-Fellner F, Brown RE, Katz DP. The growth of adipose tissue in children and adolescents. Cross-sectional and longitudinal studies of adipose cell number and size. J Clin Invest. 1979;63(2):239-46.

194. Salans LB, Horton ES, Sims EA. Experimental obesity in man: cellular character of the adipose tissue. J Clin Invest. 1971;50(5):1005-11.

195. Bjorntorp P, Sjostrom L. Number and size of adipose tissue fat cells in relation to metabolism in human obesity. Metabolism. 1971;20(7):703-13.

196. Hirsch J, Batchelor B. Adipose tissue cellularity in human obesity. Clin Endocrinol Metab. 1976;5(2):299-311.

197. Wang QA, Tao C, Gupta RK, Scherer PE. Tracking adipogenesis during white adipose tissue development, expansion and regeneration. Nat Med. 2013;19(10):1338-44.

198. Andersson DP, Eriksson Hogling D, Thorell A, Toft E, Qvisth V, Naslund E, Thorne A, Wiren M, Lofgren P, Hoffstedt J, Dahlman I, Mejhert N, Ryden M, Arner E, Arner P. Changes in subcutaneous fat cell volume and insulin sensitivity after weight loss. Diabetes Care. 2014;37(7):1831-6.

199. Maclean PS, Bergouignan A, Cornier MA, Jackman MR. Biology's response to dieting: the impetus for weight regain. Am J Physiol Regul Integr Comp Physiol. 2011;301(3):R581-600.

200. Vink RG, Roumans NJ, Arkenbosch LA, Mariman EC, van Baak MA. The effect of rate of weight loss on long-term weight regain in adults with overweight and obesity. Obesity (Silver Spring). 2016;24(2):321-7.

201. Vink RG, Roumans NJ, Mariman EC, van Baak MA. Dietary weight loss-induced changes in RBP4, FFA, and ACE predict weight regain in people with overweight and obesity. Physiological reports. 2017;5(21):e13450.

202. Liu Z, Wu KKL, Jiang X, Xu A, Cheng KKY. The role of adipose tissue senescence in obesity- and ageing-related metabolic disorders. Clin Sci (Lond). 2020;134(2):315-30.

203. Minamino T, Orimo M, Shimizu I, Kunieda T, Yokoyama M, Ito T, Nojima A, Nabetani A, Oike Y, Matsubara H, Ishikawa F, Komuro I. A crucial role for adipose tissue p53 in the regulation of insulin resistance. Nat Med. 2009;15(9):1082-7.

204. Munoz-Espin D, Serrano M. Cellular senescence: from physiology to pathology. Nat Rev Mol Cell Biol. 2014;15(7):482-96.

205. Tchkonia T, Morbeck DE, Von Zglinicki T, Van Deursen J, Lustgarten J, Scrable H, Khosla S, Jensen MD, Kirkland JL. Fat tissue, aging, and cellular senescence. Aging Cell. 2010;9(5):667-84.

206. Eckel RH, Grundy SM, Zimmet PZ. The metabolic syndrome. Lancet. 2005;365(9468):1415-28.

207. World Health Organization. Definition, diagnosis and classification of diabetes mellitus and its complications: report of a WHO consultation. Part 1, Diagnosis and classification of diabetes mellitus. Geneva, Switzerland: World Health Organization; 1999. p. 59.

208. Gierach M, Gierach J, Ewertowska M, Arndt A, Junik R. Correlation between body mass index and waist circumference in patients with metabolic syndrome. ISRN Endocrinol. 2014;2014:514589.

209. Ford ES, Giles WH, Dietz WH. Prevalence of the metabolic syndrome among US adults: findings from the third National Health and Nutrition Examination Survey. JAMA. 2002;287(3):356-9.

210. Azizi F, Salehi P, Etemadi A, Zahedi-Asl S. Prevalence of metabolic syndrome in an urban population: Tehran Lipid and Glucose Study. Diabetes Res Clin Pract. 2003;61(1):29-37.

211. Cameron AJ, Shaw JE, Zimmet PZ. The metabolic syndrome: prevalence in worldwide populations. Endocrinol Metab Clin North Am. 2004;33(2):351-75.

212. Kahn BB, Flier JS. Obesity and insulin resistance. J Clin Invest. 2000;106(4):473-81.

213. Lawler HM, Underkofler CM, Kern PA, Erickson C, Bredbeck B, Rasouli N. Adipose tissue hypoxia, inflammation, and fibrosis in obese insulin-sensitive and obese insulin-resistant subjects. J Clin Endocrinol Metab. 2016;101(4):1422-8.

214. Sun K, Kusminski CM, Scherer PE. Adipose tissue remodeling and obesity. J Clin Invest. 2011;121(6):2094-101.

215. Trayhurn P, Wood IS. Adipokines: inflammation and the pleiotropic role of white adipose tissue. Br J Nutr. 2004;92(3):347-55.

216. Kabon B, Nagele A, Reddy D, Eagon C, Fleshman JW, Sessler DI, Kurz A. Obesity decreases perioperative tissue oxygenation. Anesthesiology. 2004;100(2):274-80.

217. Virtanen KA, Lonnroth P, Parkkola R, Peltoniemi P, Asola M, Viljanen T, Tolvanen T, Knuuti J, Ronnemaa T, Huupponen R, Nuutila P. Glucose uptake and perfusion in subcutaneous and visceral adipose tissue during insulin stimulation in nonobese and obese humans. J Clin Endocrinol Metab. 2002;87(8):3902-10.

218. Mancuso P. The role of adipokines in chronic inflammation. Immunotargets Ther. 2016;5:47-56.

219. Fasshauer M, Bluher M. Adipokines in health and disease. Trends Pharmacol Sci. 2015;36(7):461-70.

220. Kloting N, Bluher M. Adipocyte dysfunction, inflammation and metabolic syndrome. Rev Endocr Metab Disord. 2014;15(4):277-87.

221. Hosogai N, Fukuhara A, Oshima K, Miyata Y, Tanaka S, Segawa K, Furukawa S, Tochino Y, Komuro R, Matsuda M, Shimomura I. Adipose tissue hypoxia in

obesity and its impact on adipocytokine dysregulation. Diabetes. 2007;56(4):901-11.

222. Skurk T, Alberti-Huber C, Herder C, Hauner H. Relationship between adipocyte size and adipokine expression and secretion. J Clin Endocrinol Metab. 2007;92(3):1023-33.

223. Maury E, Brichard SM. Adipokine dysregulation, adipose tissue inflammation and metabolic syndrome. Mol Cell Endocrinol. 2010;314(1):1-16.

224. Loffreda S, Yang SQ, Lin HZ, Karp CL, Brengman ML, Wang DJ, Klein AS, Bulkley GB, Bao C, Noble PW, Lane MD, Diehl AM. Leptin regulates proinflammatory immune responses. FASEB J. 1998;12(1):57-65.

225. Strissel KJ, Stancheva Z, Miyoshi H, Perfield JW 2nd, DeFuria J, Jick Z, Greenberg AS, Obin MS. Adipocyte death, adipose tissue remodeling, and obesity complications. Diabetes. 2007;56(12):2910-8.

226. Giordano A, Murano I, Mondini E, Perugini J, Smorlesi A, Severi I, Barazzoni R, Scherer PE, Cinti S. Obese adipocytes show ultrastructural features of stressed cells and die of pyroptosis. J Lipid Res. 2013;54(9):2423-36.

227. Cinti S, Mitchell G, Barbatelli G, Murano I, Ceresi E, Faloia E, Wang S, Fortier M, Greenberg AS, Obin MS. Adipocyte death defines macrophage localization and function in adipose tissue of obese mice and humans. J Lipid Res. 2005;46(11):2347-55.

228. Sims GP, Rowe DC, Rietdijk ST, Herbst R, Coyle AJ. HMGB1 and RAGE in inflammation and cancer. Annu Rev Immunol. 2010;28:367-88.

229. Chawla A, Nguyen KD, Goh YP. Macrophage-mediated inflammation in metabolic disease. Nat Rev Immunol. 2011;11(11):738-49.

230. Shulman GI. Cellular mechanisms of insulin resistance. J Clin Invest. 2000;106(2):171-6.

231. Laiglesia LM, Lorente-Cebrian S, Lopez-Yoldi M, Lanas R, Sainz N, Martinez JA, Moreno-Aliaga MJ. Maresin 1 inhibits TNF-alpha-induced lipolysis and autophagy in 3T3-L1 adipocytes. J Cell Physiol. 2018;233(3):2238-46.

232. Ryden M, Arvidsson E, Blomqvist L, Perbeck L, Dicker A, Arner P. Targets for TNF-alpha-induced lipolysis in human adipocytes. Biochem Biophys Res Commun. 2004;318(1):168-75.

233. Wueest S, Rapold RA, Rytka JM, Schoenle EJ, Konrad D. Basal lipolysis, not the degree of insulin resistance, differentiates large from small isolated adipocytes in high-fat fed mice. Diabetologia. 2009;52(3):541-6.

234. Lee JY, Sohn KH, Rhee SH, Hwang D. Saturated fatty acids, but not unsaturated fatty acids, induce the expression of cyclooxygenase-2 mediated through Toll-like receptor 4. J Biol Chem. 2001;276(20):16683-9.

235. Castoldi A, Naffah de Souza C, Camara NO, Moraes-Vieira PM. The macrophage switch in obesity development. Front Immunol. 2015;6:637.

236. Shoelson SE, Lee J, Goldfine AB. Inflammation and insulin resistance. J Clin Invest. 2006;116(7):1793-801.

237. Shi H, Kokoeva MV, Inouye K, Tzameli I, Yin H, Flier JS. TLR4 links innate immunity and fatty acid-induced insulin resistance. J Clin Invest. 2006;116(11):3015-25.

238. Pasarica M, Sereda OR, Redman LM, Albarado DC, Hymel DT, Roan LE, Rood JC, Burk DH, Smith SR. Reduced adipose tissue oxygenation in human obesity: evidence for rarefaction, macrophage chemotaxis, and inflammation without an angiogenic response. Diabetes. 2009;58(3):718-25.

239. Lee YS, Kim JW, Osborne O, Oh DY, Sasik R, Schenk S, Chen A, Chung H, Murphy A, Watkins SM, Quehenberger O, Johnson RS, Olefsky JM. Increased adipocyte O2 consumption triggers HIF-1alpha, causing inflammation and insulin resistance in obesity. Cell. 2014;157(6):1339-52.

240. Palazon A, Goldrath AW, Nizet V, Johnson RS. HIF transcription factors, inflammation, and immunity. Immunity. 2014;41(4):518-28.

241. Sherling DH, Perumareddi P, Hennekens CH. Metabolic syndrome. J Cardiovasc Pharmacol Ther. 2017;22(4):365-7.

242. Pi-Sunyer FX. Pathophysiology and long-term management of the metabolic syndrome. Obes Res. 2004;12 Suppl:174S-80S.

243. van Vliet-Ostaptchouk JV, Nuotio ML, Slagter SN, Doiron D, Fischer K, Foco L, Gaye A, Gogele M, Heier M, Hiekkalinna T, Joensuu A, Newby C, Pang C, Partinen E, Reischl E, Schwienbacher C, Tammesoo ML, Swertz MA, Burton P, Ferretti V, Fortier I, Giepmans L, Harris JR, Hillege HL, Holmen J, Jula A, Kootstra-Ros JE, Kvaloy K, Holmen TL, Mannisto S, Metspalu A, Midthjell K, Murtagh MJ, Peters A, Pramstaller PP, Saaristo T, Salomaa V, Stolk RP, Uusitupa M, van der Harst P, van der Klauw MM, Waldenberger M, Perola M, Wolffenbuttel BH. The prevalence of metabolic syndrome and metabolically healthy obesity in Europe: a collaborative analysis of ten large cohort studies. BMC Endocr Disord. 2014;14:9.

244. Rey-Lopez JP, de Rezende LF, Pastor-Valero M, Tess BH. The prevalence of metabolically healthy obesity: a systematic review and critical evaluation of the definitions used. Obes Rev. 2014;15(10):781-90.

245. Karelis AD, St-Pierre DH, Conus F, Rabasa-Lhoret R, Poehlman ET. Metabolic and body composition factors in subgroups of obesity: what do we know? J Clin Endocrinol Metab. 2004;89(6):2569-75.

246. Bray GA, Kim KK, Wilding JPH, World Obesity Federation. Obesity: a chronic relapsing progressive disease process. A position statement of the World Obesity Federation. Obes Rev. 2017;18(7):715-23.

247. Appleton SL, Seaborn CJ, Visvanathan R, Hill CL, Gill TK, Taylor AW, Adams RJ, North West Adelaide Health Study T. Diabetes and cardiovascular disease outcomes in the metabolically healthy obese phenotype: a cohort study. Diabetes Care. 2013;36(8):2388-94.

248. Bell JA, Kivimaki M, Hamer M. Metabolically healthy obesity and risk of incident type 2 diabetes: a meta-analysis of prospective cohort studies. Obes Rev. 2014;15(6):504-15.

249. Durward CM, Hartman TJ, Nickols-Richardson SM. All-cause mortality risk of metabolically healthy obese individuals in NHANES III. J Obes. 2012;2012:460321.

250. Chaput J-P, Arguin H, Gagnon C, Tremblay A. Increase in depression symptoms with weight loss: association with glucose homeostasis and thyroid function. Applied Physiology, Nutrition & Metabolism. 2008;33(1):86-92.

251. Lee SH, Han K, Yang HK, Kim HS, Cho JH, Kwon HS, Park YM, Cha BY, Yoon KH. A novel criterion for identifying metabolically obese but normal weight individuals using the product of triglycerides and glucose. Nutr Diabetes. 2015;5:e149.

252. Wehling M. Translational medicine: science or wishful thinking? J Transl Med. 2008;6:31.

253. Lutz TA, Woods SC. Overview of animal models of obesity. Curr Protoc Pharmacol. 2012;58(1):5.61.1-5.18.

254. Nilsson C, Raun K, Yan FF, Larsen MO, Tang-Christensen M. Laboratory animals as surrogate models of human obesity. Acta Pharmacol Sin. 2012;33(2):173-81.

255. Renner S, Dobenecker B, Blutke A, Zols S, Wanke R, Ritzmann M, Wolf E. Comparative aspects of rodent and nonrodent animal models for mechanistic and translational diabetes research. Theriogenology. 2016;86(1):406-21.

256. King AJ. The use of animal models in diabetes research. Br J Pharmacol. 2012;166(3):877-94.

257. Chen H, Charlat O, Tartaglia LA, Woolf EA, Weng X, Ellis SJ, Lakey ND, Culpepper J, Moore KJ, Breitbart RE, Duyk GM, Tepper RI, Morgenstern JP. Evidence that the diabetes gene encodes the leptin receptor: identification of a mutation in the leptin receptor gene in db/db mice. Cell. 1996;84(3):491-5.

258. Bates SH, Stearns WH, Dundon TA, Schubert M, Tso AWK, Wang Y, Banks AS, Lavery HJ, Haq AK, Maratos-Flier E, Neel BG, Schwartz MW, Myers MG.

STAT3 signalling is required for leptin regulation of energy balance but not reproduction. Nature. 2003;421(6925):856-9.

259. Rojas JM, Bolze F, Thorup I, Nowak J, Dalsgaard CM, Skydsgaard M, Berthelsen LO, Keane KA, Soeborg H, Sjogren I, Jensen JT, Fels JJ, Offenberg HK, Andersen LW, Dalgaard M. The effect of diet-induced obesity on toxicological parameters in the polygenic Sprague-Dawley rat model. Toxicol Pathol. 2018;46(7):777-98.

260. Marques C, Meireles M, Norberto S, Leite J, Freitas J, Pestana D, Faria A, Calhau C. High-fat diet-induced obesity rat model: a comparison between Wistar and Sprague-Dawley rat. Adipocyte. 2016;5(1):11-21.

261. Kwitek AE. Rat models of metabolic syndrome. Methods Mol Biol. 2019;2018:269-85.

262. Brower M, Grace M, Kotz CM, Koya V. Comparative analysis of growth characteristics of Sprague Dawley rats obtained from different sources. Lab Anim Res. 2015;31(4):166-73.

263. Kleinert M, Clemmensen C, Hofmann SM, Moore MC, Renner S, Woods SC, Huypens P, Beckers J, de Angelis MH, Schürmann A, Bakhti M, Klingenspor M, Heiman M, Cherrington AD, Ristow M, Lickert H, Wolf E, Havel PJ, Müller TD, Tschöp MH. Animal models of obesity and diabetes mellitus. Nature Reviews Endocrinology. 2018;14(3):140-62.

264. Panchal SK, Brown L. Rodent models for metabolic syndrome research. Journal of Biomedicine and Biotechnology. 2011;2011:351982.

265. Tschöp M, Heiman ML. Rodent obesity models: an overview. Exp Clin Endocrinol Diabetes. 2001;109(6):307-19.

266. Lunney JK. Advances in swine biomedical model genomics. Int J Biol Sci. 2007;3(3):179-84.

267. Koopmans SJ, Schuurman T. Considerations on pig models for appetite, metabolic syndrome and obese type 2 diabetes: from food intake to metabolic disease. Eur J Pharmacol. 2015;759:231-9.

268. Neeb ZP, Edwards JM, Alloosh M, Long X, Mokelke EA, Sturek M. Metabolic syndrome and coronary artery disease in Ossabaw compared with Yucatan swine. Comp Med. 2010;60(4):300-15.

269. Gerstein HC, Waltman L. Why don't pigs get diabetes? Explanations for variations in diabetes susceptibility in human populations living in a diabetogenic environment. CMAJ. 2006;174(1):25-6.

270. Whitfield J. Fat pigs ape obese humans. Nature. 2003.

271. Parlee SD, Lentz SI, Mori H, MacDougald OA. Quantifying size and number of adipocytes in adipose tissue. Methods Enzymol. 2014;537:93-122.

272. Bradshaw AD, Graves DC, Motamed K, Sage EH. SPARC-null mice exhibit increased adiposity without significant differences in overall body weight. Proc Natl Acad Sci USA. 2003;100(10):6045-50.

273. Lee YH, Chen SY, Wiesner RJ, Huang YF. Simple flow cytometric method used to assess lipid accumulation in fat cells. J Lipid Res. 2004;45(6):1162-7.

274. Maroni BJ, Haesemeyer R, Wilson LK, DiGirolamo M. Electronic determination of size and number in isolated unfixed adipocyte populations. J Lipid Res. 1990;31(9):1703-9.

275. Rodbell M. Metabolism of isolated fat cells. I. Effects of hormones on glucose metabolism and lipolysis. J Biol Chem. 1964;239:375-80.

276. Di Girolamo M, Mendlinger S, Fertig JW. A simple method to determine fat cell size and number in four mammalian species. Am J Physiol. 1971;221(3):850-8.

277. Bernstein RL, Hyun WC, Davis JH, Fulwyler MJ, Pershadsingh HA. Flow cytometric analysis of mature adipocytes. Cytometry. 1989;10(4):469-74.

278. Hagberg CE, Li Q, Kutschke M, Bhowmick D, Kiss E, Shabalina IG, Harms MJ, Shilkova O, Kozina V, Nedergaard J, Boucher J, Thorell A, Spalding KL. Flow cytometry of mouse and human adipocytes for the analysis of browning and cellular heterogeneity. Cell Rep. 2018;24(10):2746-56.e5.

279. McKinnon KM. Flow cytometry: an overview. Curr Protoc Immunol. 2018;120:5.1.-5.1.11.

280. Majka SM, Miller HL, Helm KM, Acosta AS, Childs CR, Kong R, Klemm DJ. Analysis and isolation of adipocytes by flow cytometry. Methods Enzymol. 2014;537:281-96.

281. Berry R, Church CD, Gericke MT, Jeffery E, Colman L, Rodeheffer MS. Imaging of adipose tissue. Methods Enzymol. 2014;537:47-73.

282. Dorph-Petersen KA, Nyengaard JR, Gundersen HJ. Tissue shrinkage and unbiased stereological estimation of particle number and size. J Microsc. 2001;204(Pt 3):232-46.

283. Blutke A, Wanke R. Sampling strategies and processing of biobank tissue samples from porcine biomedical models. J Vis Exp. 2018(133):57276.

284. Wanke R. Stereology-benefits and pitfalls. Experimental and toxicologic pathology. 2002;54(2):163-4.

285. Wanke R. Quantifizierung in der Morphologie - Wozu und wie? Nova Acta Leopoldina. 2016;NF 121(409):59-81.

286. de Groot DMG, Hartgring S, van de Horst L, Moerkens M, Otto M, Bos-Kuijpers MHM, Kaufmann WSH, Lammers JHCM, O'Callaghan JP, Waalkens-

Berendsen IDH, Pakkenberg B, Gundersen HG. 2D and 3D assessment of neuropathology in rat brain after prenatal exposure to methylazoxymethanol, a model for developmental neurotoxicty. Reproductive Toxicology. 2005;20(3):417-32.

287. Brown DL. Practical stereology applications for the pathologist. Vet Pathol. 2017;54(3):358-68.

288. Baak JPA, ten Kate FJW, Offerhaus GJA, van Lanschot JJ, Meijer GA. Routine morphometrical analysis can improve reproducibility of dysplasia grade in Barrett's oesophagus surveillance biopsies. J Clin Pathol. 2002;55(12):910-6.

289. Franzén LE, Ekstedt M, Kechagias S, Bodin L. Semiquantitative evaluation overestimates the degree of steatosis in liver biopsies: a comparison to stereological point counting. Modern Pathology. 2005;18(7):912-6.

290. Osman OS, Selway JL, Kepczynska MA, Stocker CJ, O'Dowd JF, Cawthorne MA, Arch JR, Jassim S, Langlands K. A novel automated image analysis method for accurate adipocyte quantification. Adipocyte. 2013;2(3):160-4.

291. O'Connell J, Lynch L, Cawood TJ, Kwasnik A, Nolan N, Geoghegan J, McCormick A, O'Farrelly C, O'Shea D. The relationship of omental and subcutaneous adipocyte size to metabolic disease in severe obesity. PLoS One. 2010;5(4):e9997.

292. Lee YB, Kauffman RG, Grummer RH. Effect of early nutrition on the development of adipose tissue in the pig. II. Weight constant basis. Journal of Animal Science. 1973;37(6):1319-25.

293. West MJ. Introduction to stereology. Cold Spring Harb Protoc. 2012;2012(8).

294. Ochs M. Morphometrie in der Mikroskopie: stereologische Methoden. In: Mulisch M, Welsch U, editors. Romeis - Mikroskopische Technik. 18 ed. Berlin Heidelberg, Germany: Springer-Verlag Berlin Heidelberg; 2015. pp. 515-24.

295. Schneider JP, Ochs M. Alterations of mouse lung tissue dimensions during processing for morphometry: a comparison of methods. Am J Physiol Lung Cell Mol Physiol. 2014;306(4):L341-50.

296. Slomianka L. Basic quantitative morphological methods applied to the central nervous system. J Comp Neurol. 2021;529(4):694-756.

297. Brown DL. Bias in image analysis and its solution: unbiased stereology. J Toxicol Pathol. 2017;30(3):183-91.

298. Weibel ER. Stereological methods. I. Practical methods for biological morphometry. 1 ed. London, UK: Academic Press; 1979.

299. Mattfeld T. Stereologische Methoden in der Pathologie. Doerr W, Leonhardt H, editors. 1 ed. Stuttgart-New York: Georg Thieme Verlag; 1990. 75 p.

300. Nyengaard JR. Stereologic methods and their application in kidney research. J Am Soc Nephrol. 1999;10(5):1100-23.

301. Gundersen HJ, Jensen EB. The efficiency of systematic sampling in stereology and its prediction. J Microsc. 1987;147(Pt 3):229-63.

302. Kayser K, Schultz H, Goldmann T, Gortler J, Kayser G, Vollmer E. Theory of sampling and its application in tissue based diagnosis. Diagn Pathol. 2009;4:6.

303. Albl B, Haesner S, Braun-Reichhart C, Streckel E, Renner S, Seeliger F, Wolf E, Wanke R, Blutke A. Tissue sampling guides for porcine biomedical models. Toxicol Pathol. 2016;44(3):414-20.

304. Mattfeldt T, Mall G, Gharehbaghi H, Moller P. Estimation of surface area and length with the orientator. J Microsc. 1990;159(Pt 3):301-17.

305. Nyengaard JR, Gundersen HJG. Sampling for stereology in lungs. European Respiratory Review. 2006;15(101):107-14.

306. Nyengaard JR, Gundersen HJG. The isector: a simple and direct method for generating isotropic, uniform random sections from small specimens. Journal of Microscopy. 1992;165(3):427-31.

307. Baddeley AJ, Gundersen HJ, Cruz-Orive LM. Estimation of surface area from vertical sections. J Microsc. 1986;142(Pt 3):259-76.

308. Braendgaard H, Gundersen HJ. The impact of recent stereological advances on quantitative studies of the nervous system. J Neurosci Methods. 1986;18(1-2):39-78.

309. Gundersen HJ. Stereology of arbitrary particles. A review of unbiased number and size estimators and the presentation of some new ones, in memory of William R. Thompson. J Microsc. 1986;143(Pt 1):3-45.

310. Nagel L. Quantitativ stereologische Analysen der mittleren Fettzellvolumina verschiedener Fettgewebedepots normalgewichtiger und adipöser Katzen. Dissertation. Ludwig-Maximilians Universität München; 2013.

311. Scherle W. A simple method for volumetry of organs in quantitative stereology. Mikroskopie. 1970;26(1):57-60.

312. Dorph-Petersen K-A, Pierri JN, Perel JM, Sun Z, Sampson AR, Lewis DA. The influence of chronic exposure to antipsychotic medications on brain size before and after tissue fixation: comparison of haloperidol and olanzapine in macaque monkeys. Neuropsychopharmacology. 2005;30(9):1649-61.

313. Delesse MA. Procédé mécanique pour déterminer la composition des roches. C R Acad Sci Paris 1847;25:544-5.

314. Sterio DC. The unbiased estimation of number and sizes of arbitrary particles using the disector. J Microsc. 1984;134(Pt 2):127-36.

315. Matenaers C, Popper B, Rieger A, Wanke R, Blutke A. Practicable methods for histological section thickness measurement in quantitative stereological analyses. PLoS One. 2018;13(2):e0192879.

316. Wanke R. Charakterisierung der renalen Alterationen Wachstumshormon-transgener Mäuse, ein Beitrag zur Morpho- und Pathogenese der progressiven Glomerulosklerose. Habilitation. Ludwig-Maximilians Universität München; 1996.

317. Bedi KS. A simple method of measuring the thickness of semi-thin and ultra-thin sections. J Microsc. 1987;148(Pt 1):107-11.

318. Gschwendtner A, Mairinger T. How thick is your section? The influence of section thickness on DNA-cytometry on histological sections. Anal Cell Pathol. 1995;9(1):29-37.

319. Yang GCH, Shea SM. The precise measurement of the thickness of ultrathin sections by a 're-sectioned' section technique. Journal of Microscopy. 1975;103(3):385-92.

320. von Bartheld CS. Distribution of particles in the z-axis of tissue sections: relevance for counting methods. Neuroquantology. 2012;10(1):66-75.

321. Gundersen HJ, Bagger P, Bendtsen TF, Evans SM, Korbo L, Marcussen N, Møller A, Nielsen K, Nyengaard JR, Pakkenberg B, Sørensen FB, Vesterby A, West MJ. The new stereological tools: disector, fractionator, nucleator and point sampled intercepts and their use in pathological research and diagnosis. APMIS. 1988;96(10):857-81.

322. Gundersen HJ. The nucleator. J Microsc. 1988;151(Pt 1):3-21.

323. Jensen EBV, Gundersen HJG. The rotator. Journal of Microscopy. 1993;170(1):35-44.

324. Tandrup T, Gundersen HJ, Jensen EB. The optical rotator. J Microsc. 1997;186(Pt 2):108-20.

325. Ertürk A, Becker K, Jahrling N, Mauch CP, Hojer CD, Egen JG, Hellal F, Bradke F, Sheng M, Dodt HU. Three-dimensional imaging of solvent-cleared organs using 3DISCO. Nat Protoc. 2012;7(11):1983-95.

326. Richardson DS, Lichtman JW. Clarifying tissue clearing. Cell. 2015;162(2):246-57.

327. Siedentopf H, Zsigmondy R. Uber Sichtbarmachung und Größenbestimmung ultramikoskopischer Teilchen, mit besonderer Anwendung auf Goldrubingläser. Annalen der Physik. 1902;315(1):1-39.

328. Chi J, Wu Z, Choi CHJ, Nguyen L, Tegegne S, Ackerman SE, Crane A, Marchildon F, Tessier-Lavigne M, Cohen P. Three-dimensional adipose tissue

imaging reveals regional variation in beige fat biogenesis and PRDM16-dependent sympathetic neurite density. Cell Metab. 2018;27(1):226-36.e3.

329. Geng J, Zhang X, Prabhu S, Shahoei SH, Nelson ER, Swanson KS, Anastasio MA, Smith AM. 3D microscopy and deep learning reveal the heterogeneity of crown-like structure microenvironments in intact adipose tissue. Science advances. 2021;7(8):eabe2480.

330. Dodt H-U, Leischner U, Schierloh A, Jährling N, Mauch CP, Deininger K, Deussing JM, Eder M, Zieglgänsberger W, Becker K. Ultramicroscopy: three-dimensional visualization of neuronal networks in the whole mouse brain. Nature Methods. 2007;4(4):331-6.

331. Ertürk A, Mauch CP, Hellal F, Förstner F, Keck T, Becker K, Jährling N, Steffens H, Richter M, Hübener M, Kramer E, Kirchhoff F, Dodt HU, Bradke F. Three-dimensional imaging of the unsectioned adult spinal cord to assess axon regeneration and glial responses after injury. Nature Medicine. 2012;18(1):166-71.

332. Ertürk A, Bradke F. High-resolution imaging of entire organs by 3-dimensional imaging of solvent cleared organs (3DISCO). Exp Neurol. 2013;242:57-64.

333. Ertürk A, Lafkas D, Chalouni C. Imaging cleared intact biological systems at a cellular level by 3DISCO. JoVE. 2014(89):e51382.

334. Vigouroux RJ, Belle M, Chedotal A. Neuroscience in the third dimension: shedding new light on the brain with tissue clearing. Mol Brain. 2017;10(1):33.

335. Gomez-Gaviro MV, Sanderson D, Ripoll J, Desco M. Biomedical applications of tissue clearing and three-dimensional imaging in health and disease. iScience. 2020;23(8):101432.

336. Hou B, Zhang D, Zhao S, Wei M, Yang Z, Wang S, Wang J, Zhang X, Liu B, Fan L, Li Y, Qiu Z, Zhang C, Jiang T. Scalable and DiI-compatible optical clearance of the mammalian brain. Frontiers in Neuroanatomy. 2015;9(19).

337. Ke M-T, Fujimoto S, Imai T. SeeDB: a simple and morphology-preserving optical clearing agent for neuronal circuit reconstruction. Nature Neuroscience. 2013;16(8):1154-61.

338. Hama H, Kurokawa H, Kawano H, Ando R, Shimogori T, Noda H, Fukami K, Sakaue-Sawano A, Miyawaki A. Scale: a chemical approach for fluorescence imaging and reconstruction of transparent mouse brain. Nature Neuroscience. 2011;14(11):1481-8.

339. Susaki Etsuo A, Tainaka K, Perrin D, Kishino F, Tawara T, Watanabe Tomonobu M, Yokoyama C, Onoe H, Eguchi M, Yamaguchi S, Abe T, Kiyonari H, Shimizu Y, Miyawaki A, Yokota H, Ueda Hiroki R. Whole-brain imaging with single-cell resolution using chemical cocktails and computational analysis. Cell. 2014;157(3):726-39.

340. Susaki EA, Tainaka K, Perrin D, Yukinaga H, Kuno A, Ueda HR. Advanced CUBIC protocols for whole-brain and whole-body clearing and imaging. Nature Protocols. 2015;10(11):1709-27.

341. Chung K, Wallace J, Kim S-Y, Kalyanasundaram S, Andalman AS, Davidson TJ, Mirzabekov JJ, Zalocusky KA, Mattis J, Denisin AK, Pak S, Bernstein H, Ramakrishnan C, Grosenick L, Gradinaru V, Deisseroth K. Structural and molecular interrogation of intact biological systems. Nature. 2013;497(7449):332-7.

342. Yang B, Treweek Jennifer B, Kulkarni Rajan P, Deverman Benjamin E, Chen C-K, Lubeck E, Shah S, Cai L, Gradinaru V. Single-cell phenotyping within transparent intact tissue through whole-body clearing. Cell. 2014;158(4):945-58.

343. Ueda HR, Erturk A, Chung K, Gradinaru V, Chedotal A, Tomancak P, Keller PJ. Tissue clearing and its applications in neuroscience. Nat Rev Neurosci. 2020;21(2):61-79.

344. Elisa Z, Toon B, De Smedt SC, Katrien R, Kristiaan N, Kevin B. Technical implementations of light sheet microscopy. Microsc Res Tech. 2018;81(9):941-58.

345. Remacha E, Friedrich L, Vermot J, Fahrbach FO. How to define and optimize axial resolution in light-sheet microscopy: a simulation-based approach. Biomed Opt Express. 2020;11(1):8-26.

346. Whitehead LW, McArthur K, Geoghegan ND, Rogers KL. The reinvention of twentieth century microscopy for three-dimensional imaging. Immunol Cell Biol. 2017;95(6):520-4.

347. arivis-AG. arivis Vision4D Basic Guide. 2018. p. 112.

348. Diel EE, Lichtman JW, Richardson DS. Tutorial: avoiding and correcting sample-induced spherical aberration artifacts in 3D fluorescence microscopy. Nat Protoc. 2020;15(9):2773-84.

349. Azaripour A, Lagerweij T, Scharfbillig C, Jadczak AE, Willershausen B, Van Noorden CJ. A survey of clearing techniques for 3D imaging of tissues with special reference to connective tissue. Prog Histochem Cytochem. 2016;51(2):9-23.

350. Bossolani GDP, Pintelon I, Detrez JD, Buckinx R, Thys S, Zanoni JN, De Vos WH, Timmermans JP. Comparative analysis reveals Ce3D as optimal clearing method for in toto imaging of the mouse intestine. Neurogastroenterol Motil. 2019;31(5):e13560.

351. Renier N, Adams EL, Kirst C, Wu Z, Azevedo R, Kohl J, Autry AE, Kadiri L, Umadevi Venkataraju K, Zhou Y, Wang VX, Tang CY, Olsen O, Dulac C, Osten

P, Tessier-Lavigne M. Mapping of brain activity by automated volume analysis of immediate early genes. Cell. 2016;165(7):1789-802.

352. Chi J, Crane A, Wu Z, Cohen P. Adipo-Clear: a tissue clearing method for three-dimensional imaging of adipose tissue. J Vis Exp. 2018(137):58271.

353. Drenckhan W, Hutzler S. Structure and energy of liquid foams. Adv Colloid Interface Sci. 2015;224:1-16.

354. Siber A, Ziherl P. Cellular patterns. 1 ed. Boca Raton, USA: CRC Press; 2017. 278 p.

355. Bahceci M, Gokalp D, Bahceci S, Tuzcu A, Atmaca S, Arikan S. The correlation between adiposity and adiponectin, tumor necrosis factor alpha, interleukin-6 and high sensitivity C-reactive protein levels. Is adipocyte size associated with inflammation in adults? J Endocrinol Invest. 2007;30(3):210-4.

356. Weyer C, Foley JE, Bogardus C, Tataranni PA, Pratley RE. Enlarged subcutaneous abdominal adipocyte size, but not obesity itself, predicts type II diabetes independent of insulin resistance. Diabetologia. 2000;43(12):1498-506.

357. McLaughlin T, Deng A, Yee G, Lamendola C, Reaven G, Tsao PS, Cushman SW, Sherman A. Inflammation in subcutaneous adipose tissue: relationship to adipose cell size. Diabetologia. 2010;53(2):369-77.

358. McLaughlin T, Lamendola C, Coghlan N, Liu TC, Lerner K, Sherman A, Cushman SW. Subcutaneous adipose cell size and distribution: relationship to insulin resistance and body fat. Obesity (Silver Spring). 2014;22(3):673-80.

359. McLaughlin T, Sherman A, Tsao P, Gonzalez O, Yee G, Lamendola C, Reaven GM, Cushman SW. Enhanced proportion of small adipose cells in insulin-resistant vs insulin-sensitive obese individuals implicates impaired adipogenesis. Diabetologia. 2007;50(8):1707-15.

IX Own publications and contributions on scientific congresses

Publications in peer-reviewed journals

N. Theobalt, I. Hofmann, S. Fiedler, S. Renner, G. Dhom, A. Feuchtinger, A. Walch, M. Hrabě de Angelis, E. Wolf, R. Wanke, A. Blutke (2021). Unbiased analysis of obesity related, fat depot specific changes of adipocyte volumes and numbers using light sheet fluorescence microscopy. PLoS One, 16(3):e0248594

S. Fiedler, H. Wünnemann, I. Hofmann, **N. Theobalt**, A. Feuchtinger, A. Walch, J. Schwaiger, R. Wanke, A. Blutke (2020). A practical guide to unbiased quantitative morphological analyses of the gills of rainbow trout (Oncorhynchus mykiss) in ecotoxicological studies. PLoS One, 15(12):e0243462.

I. Hofmann, E. Kemter, **N. Theobalt**, S. Fiedler, M. Bidlingmaier, A. Hinrichs, M. Aichler, K. Burkhardt, N. Klymiuk, E. Wolf, R. Wanke, A. Blutke (2020). Linkage between growth retardation and pituitary cell morphology in a dystrophin-deficient pig model of Duchenne muscular dystrophy. Growth hormone & IGF research, 51:6 – 16.

I. Hofmann, E. Kemter, S. Fiedler, **N. Theobalt**, L. Fonteyne, E. Wolf, R. Wanke, A. Blutke (2021). A new method for physical disector analyses of numbers and mean volumes of immunohistochemically labeled cells in paraffin sections. Journal of Neuroscience Methods, 361:109272.

Poster contributions on the 62nd annual meeting of the pathology division of the "Deutsche Veterinärmedizinische Gesellschaft (DVG)" in Fulda, Germany, on March 3rd, 2019

N. Theobalt, S. Renner, A. Feuchtinger, A. Walch, I. Hofmann, S. Fiedler, R. Wanke, A. Blutke (2019). Quantitative Stereologie des Fettgewebes. Tierärztliche Praxis Ausgabe Kleintiere, 47(03):217.

S. Fiedler, H. Wünnemann, J. Schwaiger, A. Feuchtinger, A. Walch, I. Hofmann, **N. Theobalt**, R. Wanke, A. Blutke (2019). Quantitative Stereologie der Kiemen von Regenbogenforellen. Tierärztliche Praxis Ausgabe Großtiere, 47(03):202.

Presentations on the 62nd annual meeting of the pathology division of the "Deutsche Veterinärmedizinische Gesellschaft (DVG)" in Fulda, Germany, on March 3rd, 2019

I. Hofmann, **N. Theobalt**, S. Fiedler, E. Wolf, R. Wanke, A. Blutke (2019). Quantitativ-morphologische Untersuchungen der Hypophyse in einem porzinen Modell der Duchenne-Muskeldystrophie. Tierärztliche Praxis Ausgabe Kleintiere, 47(03):210.

A. Blutke, I. Hofmann, **N. Theobalt**, S. Fiedler, A. Feuchtinger, A. Walch, R. Wanke (2019). Lichtblattmikroskopie in der quantitativ-morphologischen Analyse von Gewebeproben. Tierärztliche Praxis Ausgabe Kleintiere, 47(03):210.

X Danksagung

Mein erster Dank gilt meinem Doktorvater Herrn Prof. Dr. Rüdiger Wanke (Professur für Molekulare und Experimentelle Pathologie, Lehrstuhl für Allgemeine Pathologie und Pathologische Anatomie, LMU München) der mich jederzeit mit seinem beeindruckenden Fachwissen auf dem Gebiet der quantitativen Stereologie unterstützte und mir mit kompetentem Rat zur Seite stand.

Herrn Dr. Andreas Parzefall (Helmholtz Zentrum München), welcher meine Arbeit als Doktorvater bis zu seinem Wechsel als Helmholtz Zentrum München betreut hat, danke ich für die Möglichkeit in einem so spannenden Themenbereich zu promovieren. Außerdem möchte ich meinen Dank ausdrücken für all die Zeit, die er auch weit über seine Tätigkeit am Helmholtz Zentrum München hinaus damit verbracht hat, mich als seine Doktorandin engagiert und umfassend zu betreuen. Es gab kein Problem, welches er nicht mit innovativen und raffinierten Lösungsansätzen aus der Welt schaffen konnte. Dafür und für seine umfassende Inspiration bei der Idee bis hin zur Umsetzung dieser Arbeit möchte ich mich herzlich bedanken.

Des Weiteren möchte ich mich bei Frau Dr. Simone Renner und Herrn Prof. Eckhard Wolf (Lehrstuhl für Molekulare Tierzucht und Biotechnologie, LMU München) für die Möglichkeit zur spannenden Kooperation im Rahmen dieses Dissertationsprojekts bedanken. Das etablierte porzine Modell Diät-induzierter Obesitas weist wichtige Kennzeichen des Metabolischen Syndroms auf und ist damit ein wertvolles Modell bei der zur Erforschung zugrundeliegender Mechanismen und metabolischer Konsequenzen. Ich bin dankbar dafür, dass mir ein so einzigartiges Tiermodell als Basis dieser Arbeit zur Verfügung stand.

Ein besonderer Dank gilt meinen Mitdoktorandinnen am Institut für Tierpathologie Frau Isabel Hofmann, Frau Sonja Fiedler und Frau Alexandra Schubö für die herausragende Zusammenarbeit, den einzigartigen Zusammenhalt und all die schönen und humorvollen Momente, die den manchmal stressigen Forschungsalltag um einiges erleichtert haben. Darüber hinaus möchte ich mich bei allen für die zahlreichen engagierten, sorgfältigen und kompetenten Begutachtungen meiner Manuskripte von ganzem Herzen bedanken.

Danksagung

Allen Mitarbeitern des Instituts für Tierpathologie möchte ich für die angenehme Atmosphäre und die entgegengebrachte, allgegenwärtige Hilfsbereitschaft am Institut danken. Vielen Dank für die großartige Unterstützung speziell an Josef Grieser, Marold Handl, Lisa Pichl, Michaela Nützel, Doris Merl, Nadschman Rahimi, Ella Schwagerus und Sandra Aumiller. Insbesondere möchte ich mich bei Frau Marjam O´Gorman für ihr allzeit offenes Ohr, ihre kompetente Hilfe bei allen organisatorischen Angelegenheiten und das Lösen noch so unlösbar erscheinender Probleme bedanken. Für das Ermöglichen der Durchführung der Lichtblattfluoreszenz-Experimente möchte ich zudem Frau Dr. Annette Feuchtinger, Herrn Dr. Axel Walch und Frau Ulrike Buchholz (Helmholtz Zentrum München) ausdrücklich meinen Dank aussprechen.

Der Begabtenförderung der Hanns-Seidel-Stiftung e.V., unter der Leitung von Herrn Prof. Dr. Hans-Peter Niedermeier und seiner Nachfolgerin, Frau Dr. Jutta Möhringer, möchte ich mich für die großzügige Unterstützung bedanken, die dieses Dissertationsprojekt erst ermöglicht hat. Herrn Dr. Andreas Burtscheidt möchte ich für die kompetente und freundschaftliche Betreuung sowie die gelungene Organisation fachlicher Seminarveranstaltungen im Rahmen der ideellen Förderung danken.

Nicht zuletzt möchte ich mich beim Dekan unserer Fakultät Herrn Prof. Dr. Reinhard Straubinger für seine wertvolle Tätigkeit als Vertrauensdozent bedanken.

Zuletzt gilt mein großer Dank meinen Eltern Heike und Wendelin, die mir immer mit Rat und Tat zur Seite stehen und auf deren Unterstützung ich mich jederzeit verlassen kann. All meinen guten Freunden Veronika und Karsten, Fabian, Sabrina, Johanna, Jana, Vanessa, Rebecca, Stefanie, Stephanie, Irene, Johannes sowie meiner Mitbewohnerin Pauline danke ich für ihre mentale Unterstützung. Mein herzlichster Dank gilt meinem Freund Rudi, der mir vor allem in der stressigen Endphase mehr Halt gegeben hat, als er vermutet und ohne dessen offenes Ohr, tröstende Schulter, guten Rat, Süßigkeiten-Nachschub und hervorragende Kaffeemaschine „Petra“ ich aufgeschmissen gewesen wäre.